Measurement of the Analyzing Power A_N in *pp* Elastic Scattering in the CNI Region with a Polarized Atomic Hydrogen Gas Jet Target

Hiromi Okada (Iinuma)

A Dissertation Submitted in Partial Fulfillment
of the Requirements for the Degree of

Doctor of Science

DEPARTMENT OF PHYSICS
FACULTY OF SCIENCE
KYOTO UNIVERSITY

July, 2006

Abstract

A precise measurement of the single spin asymmetry, A_N, in proton-proton elastic scattering in the region of four-momentum transfer squared $0.001 < |t| < 0.032$ $(\mathrm{GeV}/c)^2$ has been performed using a polarized atomic hydrogen gas jet target and polarized proton beam with momentum 100 GeV/c at the Brookhaven National Laboratory (BNL). This kinematic region is known as the Coulomb Nuclear Interference (CNI) region. The interference of the electromagnetic spin-flip amplitude with a hadronic spin-non-flip amplitude is predicted to generate a significant A_N of 4–5%, peaking at $-t \simeq 0.003$ $(\mathrm{GeV}/c)^2$, and a presence of hadronic spin-flip amplitude would modify this calculable prediction.

The hydrogen gas jet target system provides highly polarized atomic hydrogen, $P_t = 0.924 \pm 0.018$. The system performance meets the design specifications. The recoil spectrometer, which consisted of the three left-right symmetric pairs of silicon detectors, was newly developed for this experiment. We have collected 4 million elastic *pp* events in the region of $0.001 < |t| < 0.032$ $(\mathrm{GeV}/c)^2$.

We present the first precise result of A_N in the CNI region as a function of $-t$ with a relative accuracy of $\sim 5\%$. Our data are well described by the theoretical prediction with the electromagnetic single spin-flip amplitude alone and do not support the presence of a large hadronic single spin-flip amplitude.

In addition to the physics interests, the precise measurement for A_N is extremely important for the measurement of proton beam polarization at the Relativistic Heavy Ion Collider (RHIC) spin program. The newly measured A_N data satisfy with the required accuracy.

At the same time, we have also accomplished the precise measurement of the double spin asymmetry, A_{NN}, in the same $|t|$ region for the first time. A_{NN} is sensitive to the hadronic double spin-flip amplitude but there is no solid theoretical prediction for its energy dependence nor magnitude. The results of A_{NN} for each measured points are consistent with zero within the errors. The mean value for the region of $0.001 < |t| < 0.032$ (GeV/c)^2 is $< A_{NN} >= -0.0024 \pm 0.0015$.

Our results of A_N and A_{NN} in the CNI region do not support the presence of large size of single nor double spin-flip amplitudes at this energy, and provide significant constraints to determine the poorly known hadronic single and double spin-flip amplitudes.

Contents

Chapter 1

Introduction

1.1 Importance of Elastic proton-proton Scattering

Elastic proton-proton (*pp*) scattering is one of the most fundamental reactions in particle-nuclear physics. This reaction is described in transition amplitudes by use of helicity of initial and final states. Requiring that the interaction is invariant under space inversion, time reversal and rotation in spin space, proton-proton scattering in a given spin state is described in five independent transition amplitudes. And the understanding of these amplitudes would provide crucial guidelines to investigate the reaction mechanism.

There are two kinematic regions of interest in this reaction. One is small to medium values of momentum transfer and the other is large momentum transfer. The first is in the domain of non-perturbative quantum chromodynamics (QCD) and precise prediction basing on the QCD is very difficult. On the other hand, perturbative QCD should be applicable in the latter region. In this thesis, we will focus on the spin-dependent *pp* elastic scattering at small momentum transfer and at high center-of-mass energy.

Each transition amplitude is described as a superposition of the hadronic amplitude and the electro-magnetic amplitude. Thanks to the great successes of quantum electrodynamics (QED), the electro-magnetic force is precisely described including the small momentum transfer region. On the other hand, the hadronic force is not fully described by theory. There are several theoretical approaches [1]: extrapolation of low and medium energy Regge phenomenology to high energies, models based on a hybrid of perturbative QCD and non-relativistic quark models, and models based on eikonalization techniques.

The nuclear force totally dominates the *pp* scattering process, except the certain kinematic regions where the electro-magnetic force leads to transition amplitudes that grow rapidly and eventually exceed the nuclear force. In this kinematic region, two forces become similar in strength and interfere with each other. We call this interference the Coulomb Nuclear Interference (CNI). The interference of a spin-flip amplitude and non-spin-flip amplitude leads a sizable transverse-spin dependent asymmetry, A_N which is defined by the asymmetry of cross-sections with up-down polarization for one of the protons. In the case of the elastic scattering between proton beam and proton target,

$$A_N = \frac{\sigma_{\uparrow 0} - \sigma_{\downarrow 0}}{\sigma_{\uparrow 0} + \sigma_{\downarrow 0}}, \tag{1.1}$$

where two subscripts of σ denote the beam polarization state (left) and the target polarization state (right), respectively. $\uparrow$ ($\downarrow$) in subscript denotes beam or target is polarized transverse-up (transverse-down) direction with respect to the beam direction (longitudinal axis) [1]. "0" in subscript denotes unpolarized state. Originally, A_N in the CNI region was first predicted by Schwinger from the study of neutron-nucleus. scattering in the low center-of-mass energy region in 1946 [2].

At higher center-of-mass energy, A_N is predicted to reach a maximum value of about 4–5% around the momentum transfer squared $|t| \simeq 0.003$ $(\mathrm{GeV}/c)^2$ and decreases with increasing $|t|$ [3, 4]. The prediction is based on the interference between the spin-flip electro-magnetic amplitude and the non-spin-flip hadronic amplitude assuming that the spin-flip hadronic amplitude is zero. However there is no solid ground for this assumption, and A_N will be significantly changed if it is non-zero. Therefore the measurement of the A_N will provide a crucial information on the spin-flip hadronic amplitude.

Similarly double transverse-spin dependent asymmetry A_{NN} which is defined by the asymmetry of cross-sections with up-down beam and target polarizations:

$$A_{NN} = \frac{\sigma_{\uparrow\uparrow} - \sigma_{\uparrow\downarrow}}{\sigma_{\uparrow\uparrow} + \sigma_{\uparrow\downarrow}}. \tag{1.2}$$

We call "parallel" or "anti-parallel" state where the beam and target polarization in the same or opposite direction. A_{NN} is sensitive to another type of spin-dependent transition amplitude as we will see later in this chapter. Therefore the study of the spin-dependence would be crucial in completing the picture of the forward *pp* elastic scattering.

Important polarized *pp* elastic scattering experiments were done in the 1980s – 1990s. A_N and A_{NN} had been measured using low-medium energy proton beams and polarized proton targets in the higher four-momentum transfer $0.05 < |t| < 10$ (GeV/c)^2. However, polarization-dependence at high energy has been still highly unknown. The first measurement of A_N in the CNI region had been performed by the E704 experiment at $\sqrt{s} = 19.4$ GeV with moderate precision [5]. Recently, A_N has been measured also at $\sqrt{s} = 200$ GeV by PP2PP [7], but slightly beyond the $|t|$ region of the CNI peak. Regarding A_{NN}, there has been no measurement in the CNI region because of difficulties of experiments. Therefore the measurements of A_N and A_{NN} in the CNI region are expected to be significant constraints for theoretical approaches and models.

In addition to the physics interests, the precise measurement of A_N is also extremely important for the RHIC (Relativistic Heavy Ion Collider) spin program [8]. The RHIC is located at Brookhaven National Laboratory on Long Island, New York. In addition to heavy ion collisions, the RHIC also collides intense beams of polarized protons at center-of-mass energies ranging from 50 to 500 GeV. The design luminosity and polarization for *pp* collisions are 2×10^{32} (cm^{-2} $\cdot$ sec^{-1}) and 70%, respectively. The technical challenges include the production and acceleration of the polarized beams, manipulation of the spin direction at the interaction points, and the accurate measurement of the beam polarization and related asymmetries. The roles of the RHIC-polarimeter consists of two main stages to carry out these technical challenges.

In the first stage, the polarimeter serves as a *semi on-line* feedback tool to tune up the beam acceleration. The RHIC featured one polarimeter for each ring based on proton-carbon elastic scattering in the CNI region ("*p*C-CNI-polarimeters") [9]. The *p*C-CNI-polarimeters measured the bunch-by-bunch polarization for both beams independently at beam momentum (P_{beam}) ranging from 21.4 to 100 GeV/c. Featuring elastic scattering in the CNI region, the beam polarization measurement is performed at any energy without any configuration change. Its accuracy

[1] L denotes longitudinal polarized state and N denotes transverse polarized state. See Figure 1.1

was limited to $\pm 30\%$ due to the previous experiment (BNL E950) where the polarized proton beam was extracted to be calibrated absolutely in polarization [6]. The *p*C-CNI polarimeter performed perfectly in the first stage.

In the second stage, the accurate and absolute polarization measurement becomes critical for the spin-physics results which provide detailed studies of QCD at a new level of accuracy. This relies heavily upon an accurate knowledge of the beam polarization. For example, double longitudinal-spin dependent asymmetry is defined as

$$A_{LL} = \frac{\epsilon_{LL}}{P_b^2}$$

where ϵ_{LL} is the measured *raw* asymmetry in the event yield for a particular process for parallel and anti-parallel longitudinal-spin of the protons [1]. Equal polarizations are assumed for both beams (P_b) for a simplicity. In the case that $\epsilon_{LL} \neq 0$ [2], the accuracy is given by

$$\Delta A_{LL} = \frac{\epsilon_{LL}}{P_b^2}\left(\left(\frac{\Delta\epsilon_{LL}}{\epsilon_{LL}}\right)^2 + \left(2\frac{\Delta P_b}{P_b}\right)^2\right)^{\frac{1}{2}}. \quad (1.3)$$

We refer to the uncertainty from the beam polarization as $\Delta P_b/P_b$. $\Delta P_b/P_b$ gives a contribution to the accuracy of the A_{LL} measurement and becomes more important when the accuracy of $\Delta\epsilon_{LL}/\epsilon_{LL}$ is improved with sufficient statistics. In practice, A_{LL} for the neutral pion is connected to the gluon polarization [10] which is one of the major physics goal for the RHIC-spin program. We expect to accumulate enough statistics $\Delta\epsilon_{LL}/\epsilon_{LL} \sim 0.1$. Therefore we aim to accomplish the accuracy of beam polarization $\Delta P_b/P_b < 0.05$. However the *p*C-CNI polarimeter is not sufficient for this requirement.

The accuracy of the *p*C-CNI polarimeter was limited by the absolute A_N value of *p*C elastic scattering (A_N^{pC}). The A_N^{pC} was measured at $P_{beam} = 21.7$ GeV/c with moderate precision [6] and we need to extrapolate to get A_N^{pC} at $P_{beam} = 100$ GeV/c using a theoretical calculation [11]. The uncertainty of A_N would cause a wrong scale of the measured beam polarization. Once we know the exact A_N^{pC} at $P_{beam} = 100$ GeV/c, we can correct a wrong scale and calibrate the measured beam polarizations.

Our strategy toward the goal of polarimetry at the RHIC is to use the *p*C-CNI-polarimeter as the relative polarimeter and to install a polarized hydrogen jet target (H-jet-target) to absolutely calibrate the *p*C-CNI-polarimeter. The *pp* elastic scattering process is 2-body exclusive scattering with identical particles. Therefore we can change the role of which is polarized between the target proton and the beam proton. At first we measure A_N by use of a well calibrated polarized proton target.

$$A_N = \frac{\epsilon_t}{P_t}, \quad (1.4)$$

where P_t is proton target polarization and ϵ_t is *raw* asymmetry for the *pp* elastic scattering for the transversely polarized proton **target**. Then the beam polarization is measured utilizing the A_N:

$$P_b = \frac{\epsilon_b}{A_N}, \quad (1.5)$$

[2] In the case that ϵ_{LL} is quite small and the same size as its error ($\epsilon_{LL} \simeq \Delta\epsilon_{LL}$), Equation (1.3) is rewritten as

$$\Delta A_{LL} \simeq \frac{\Delta\epsilon_{LL}}{P_b^2}\left(1 + \left(2\frac{\Delta P_b}{P_b}\right)^2\right)^{\frac{1}{2}}.$$

where ϵ_b is *raw* asymmetry for the *pp* elastic scattering for the transversely polarized proton **beam**.

Therefore, a new measurement of A_N with a precision of $\Delta A_N/A_N \sim 0.05$ is required.

In this thesis we report on a precise measurement of A_N and A_{NN} of *pp* elastic scattering in the CNI region at $\sqrt{s} = 13.7$ GeV which has been performed in 2004 at the RHIC.

The following sections in Chapter 1, we will describe the general properties of transition amplitudes of the *pp* elastic scattering process. We will describe their behavior with a brief review of existing experimental data. We also explain how to extract unknown spin-flip hadronic amplitudes from A_N and A_{NN}.

In Chapter 2, we describe setup of the experiment (H-jet-target system and the recoil spectrometer) and the RHIC high energy polarized proton beam.

Chapter 3 presents the off-line analysis.

In Chapter 4, our A_N and A_{NN} data are shown. The experimental interpretation of hadronic spin-flip amplitudes is discussed. Chapter 4 also contains the comparisons between our A_N data and past experimental results.

1.2 Transition Amplitude for Elastic *pp* Scattering

Through this thesis units are used in which $\hbar = c = 1$. We specify the kinematics in the center-of-mass frame for convenience, unless stated otherwise.

1.2.1 Introduction of helicity amplitudes

When two hadrons interact, their interaction is controlled by a mixture of strong (hadronic) and electro-magnetic forces. Several kinds of transition amplitude can be found depending on how the quantization axes and eigenstates are chosen. The helicity amplitudes are the simplest, useful and urged by the parity restrictions. Therefore we shall concentrate exclusively on them [3].

We consider a reaction of $A + B \rightarrow C + D$, where A, B, C and D are all protons. The four-momenta of them are

$$\begin{aligned} p_A &= (E, \vec{p}),\ \ p_B = (E, -\vec{p}), \\ p_C &= (E, \vec{q}),\ \ p_D = (E, -\vec{q}), \end{aligned}$$

where E is the energy. $\vec{p}$ and $\vec{q}$ are the three-momenta of coming and outgoing particles, respectively. Their absolute values are same ($|\vec{p}| = |\vec{q}|$). And those square are

$$p_i^2 = E^2 - |\vec{p}|^2 = (m_p)^2 \ \ (i = A,\ B,\ C \text{ and } D)$$

where $m_p = 0.93827$ GeV/c^2 is the proton mass. In the collision of particle A and B the total center-of-mass energy squared can be expressed in the Lorentz-invariant form

$$s = (p_A + p_B)^2 = (p_C + p_C)^2 = 4E^2.$$

The four-momentum transfer squared is

$$t = (p_A - p_C)^2 = (-p_B + p_D)^2 = -2|\vec{p}|^2(1 - \cos\theta),$$

where θ is the scattering angle between the three-momentum $\vec{p}$ and $\vec{q}$.

The scattering process is described in the center-of-mass system by a matrix ϕ in spin space, defined in such a way that the differential cross-section is given by

$$\frac{\mathrm{d}\sigma}{\mathrm{d}\Omega} = \sum_{\lambda_A,\lambda_B,\lambda_C,\lambda_D} | < \lambda_C \lambda_D | \phi | \lambda_A \lambda_B > |^2,$$

where λ_C, λ_D represent the spin state of the outgoing nucleons, λ_A, λ_B the spin states of the incoming nucleons. The matrix ϕ is a function of the total center-of-mass energy squared s and is expressed in terms of amplitudes for total angular momentum, parity and spin. Requiring that the interaction is invariant under space inversion, time reversal and rotation in spin space, we can select the following set of five independent helicity amplitudes as functions of s and t.

[3] However, in some circumstances other types of transition amplitude can be valuable, in particular transversity amplitudes, so we introduce them in Appendix A.1.

$$
\begin{aligned}
\phi_1(s,t) &= <+\frac{1}{2}+\frac{1}{2}|\phi|+\frac{1}{2}+\frac{1}{2}>, \\
\phi_2(s,t) &= <+\frac{1}{2}+\frac{1}{2}|\phi|-\frac{1}{2}-\frac{1}{2}>, \\
\phi_3(s,t) &= <+\frac{1}{2}-\frac{1}{2}|\phi|+\frac{1}{2}-\frac{1}{2}>, \\
\phi_4(s,t) &= <+\frac{1}{2}-\frac{1}{2}|\phi|-\frac{1}{2}+\frac{1}{2}>, \\
\phi_5(s,t) &= <+\frac{1}{2}+\frac{1}{2}|\phi|+\frac{1}{2}-\frac{1}{2}>.
\end{aligned}
\tag{1.6}
$$

where $\phi_1(s,t)$ and $\phi_3(s,t)$ correspond to non-spin-flip amplitudes, $\phi_5(s,t)$ corresponds to single-spin-flip amplitude and $\phi_2(s,t)$ and $\phi_4(s,t)$ correspond to double-spin-flip amplitudes, respectively.

It will be convenient to introduce following shorthand:

$$\phi_\pm(s,t) = \frac{\phi_1(s,t) \pm \phi_3(s,t)}{2}.$$

Connections between helicity amplitudes and Spin-dependent observables

There are many spin-dependent observables regarding beam and target polarization states. We define proton moves along z-axis as displayed in Figure 1.1. In the case that the polarization axis is the y-axis, the proton is polarized transversely. In the case that the polarization axis is the z-axis, the proton is polarized longitudinally.

In this section, we mainly consider only initial state transverse polarization measurements. As we have described in Equation (1.1) and (1.2), the transverse single and double spin dependent asymmetries, A_N and A_{NN}, are defined by the asymmetry of cross sections with up-down beam and target polarizations. Such cross-sections are proportional to transversity amplitude squared as shown in Figure A.2 in Appendix A.1. The relations between transversity and helicity amplitudes are described in Equation A.1.

A_N and A_{NN} are expressed using helicity amplitudes respectively [4]:

$$A_N \frac{\mathrm{d}\sigma}{\mathrm{d}t} = -\frac{4\pi}{s(s-4m_p^2)} \mathrm{Im}[\phi_5^*(s,t)\{\phi_1(s,t)+\phi_2(s,t)+\phi_3(s,t)-\phi_4(s,t)\}], \tag{1.7}$$

$$A_{NN} \frac{\mathrm{d}\sigma}{\mathrm{d}t} = \frac{4\pi}{s(s-4m_p^2)} \{2|\phi_5(s,t)|^2 + \mathrm{Re}[\phi_1^*(s,t)\phi_2(s,t)-\phi_3^*(s,t)\phi_4(s,t)]\}, \tag{1.8}$$

where $\mathrm{d}\sigma/\mathrm{d}t$ is differential cross-section which is obtained if the initial spin states are unpolarized:

$$\frac{\mathrm{d}\sigma}{\mathrm{d}t} = \frac{2\pi}{s(s-4m_p^2)}[|\phi_1(s,t)|^2 + |\phi_2(s,t)|^2 + |\phi_3(s,t)|^2 + |\phi_4(s,t)|^2 + 4|\phi_5(s,t)|^2] \tag{1.9}$$

As for the other spin-dependent asymmetries with all polarization directions, they are summarized in Appendix A.2.

In the limit of $t = 0$, the optical theorem introduces a total cross-section as follows:

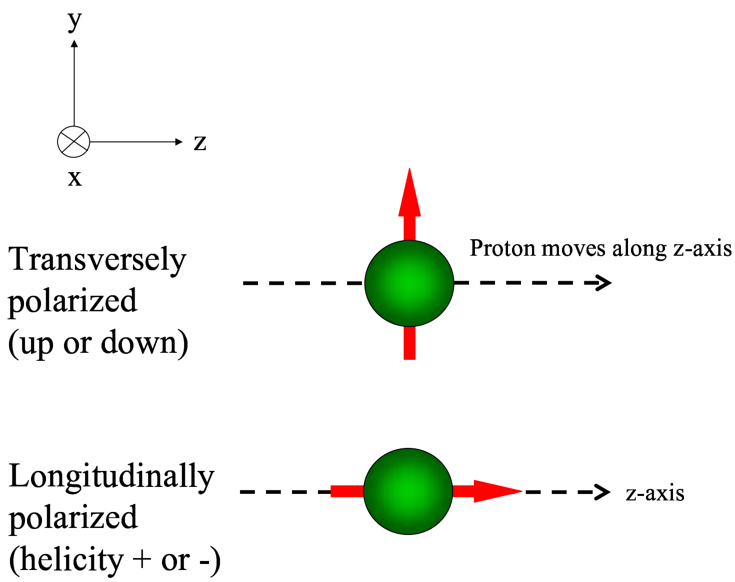

Figure 1.1: Definition of transverse-polarization and longitudinal-polarization. Red arrow represents the proton spin direction.

- Spin averaged total cross-section

$$\sigma_{tot} = \frac{8\pi}{\sqrt{s(s-4m_p^2)}}\mathrm{Im}\phi_+(s,0). \tag{1.10}$$

- Difference between total cross sections for anti-parallel and parallel spin states (transverse)

$$\Delta\sigma_T = \sigma_{\uparrow\downarrow} - \sigma_{\uparrow\uparrow} = -\frac{8\pi}{\sqrt{s(s-4m_p^2)}}\mathrm{Im}\phi_2(s,0). \tag{1.11}$$

  We would describe the connection between A_{NN} and $\Delta\sigma_T$ in the limit of $t \rightarrow 0$:

$$A_{NN} \rightarrow -\frac{\Delta\sigma_T}{\sigma_{tot}}$$

- Difference between total cross section for anti-parallel and parallel spin states (longitudinal)

$$\Delta\sigma_L = \sigma_{\rightleftarrows} - \sigma_{\rightrightarrows} = \frac{8\pi}{\sqrt{s(s-4m_p^2)}}\mathrm{Im}\phi_-(s,0). \tag{1.12}$$

The $\sqrt{s}$ dependence of $\mathrm{Im}\phi_+(s,0), \mathrm{Im}\phi_2(s,0)$ and $\mathrm{Im}\phi_-(s,0)$ have been studied experimentally and theoretically, as discussed later.

Parameterization of helicity amplitudes at very small t

We will concentrate on describing the properties of helicity amplitudes at very small momentum transfer squared $|t| < 0.05$ (GeV/c)^2 and high energy $\sqrt{s}$ ($\gg m_p$) in the following discussions. At small $|t| \approx 0.003$ (GeV/c)^2, the electro-magnetic-force and hadronic-force become similar in strength and interfere with each other. The lowest order in α, the fine structure constant, ϕ_i ($i = 1-5$) can be approximated as a sum of the one-photon exchange amplitude and the hadronic amplitude decomposed as;

$$\phi_i(s,t) = \phi_i^{had}(s,t) + \phi_i^{em}(s,t)e^{i\delta_C}. \tag{1.13}$$

The Coulomb phase δ_C reflects the distortion of the pure amplitudes $\phi_+^{em}(s,t)$ and $\phi_+^{had}(s,t)$ due to the simultaneous presence of both hadronic and Coulomb scattering. Here, δ_C is approximately independent of helicity [4, 12]

$$\delta_C = \alpha \ln \frac{-2}{t(B + 8/\Lambda^2)} - \alpha\gamma. \tag{1.14}$$

where B, often called "the slope", is the logarithmic derivative of the differential cross-section at $-t = 0$, a number about 12 (GeV/c)$^{-2}$ and increasing above $\sqrt{s} = 10$ GeV. γ is Euler's constant $\gamma = 0.5772$ and Λ is introduced phenomenological way as energy scale $\Lambda^2 = 0.71$ GeV^2.

The electro-magnetic part of helicity amplitude The electro-magnetic force is well understood in QED and electro-magnetic amplitudes are given exactly [4]. We are interested in their *leading terms at high energies*;

$$\phi_1^{em}(s,t) = \phi_3^{em}(s,t) = \phi_+^{em}(s,t) \cong \frac{\alpha s}{t}, \tag{1.15}$$

$$\phi_2^{em}(s,t) = -\phi_4^{em}(s,t) \cong \frac{\alpha s \kappa^2}{4m_p^2}, \tag{1.16}$$

$$\phi_5^{em}(s,t) \cong -\frac{\alpha s \kappa}{2m_p\sqrt{-t}}. \tag{1.17}$$

where $\mu_p = \kappa + 1 = 2.79285\mu_N$ is the proton magnetic moment. κ refers to the *anomalous* magnetic moment. μ_N is the nuclear magneton.

The amplitudes $\phi_+^{em}(s,t)$ and $\phi_5^{em}(s,t)$ are all singular as $|t| \rightarrow 0$. The amplitudes $\phi_2^{em}(s,t)$ and $\phi_4^{em}(s,t)$ are non-singular as $|t| \rightarrow 0$.

The hadronic part of helicity amplitude At very small t in the forward limit ($\theta \rightarrow 0$) and the domain of non-perturbative QCD, there are no precise theoretical predictions. However, the behaviors of hadronic amplitudes are assumed from a consequence of angular momentum conservation:

$$\phi_1^{had}(s,t) \propto \cos\theta \rightarrow 1, \tag{1.18}$$

$$\phi_2^{had}(s,t) \propto \cos\theta \rightarrow 1, \tag{1.19}$$

$$\phi_3^{had}(s,t) \propto \frac{1}{2}\cos\theta(1+\cos\theta) \rightarrow 1, \tag{1.20}$$

$$\phi_4^{had}(s,t) \propto \frac{1}{2}\cos\theta(1-\cos\theta)\cos\theta \rightarrow |t|, \tag{1.21}$$

$$\phi_5^{had}(s,t) \propto -\frac{1}{\sqrt{2}}\cos\theta\sqrt{1-\cos\theta^2} \rightarrow \sqrt{-t} \tag{1.22}$$

Thus, as $|t| \to 0$ the hadronic amplitude $\phi_1^{had}(s,t), \phi_2^{had}(s,t)$ and $\phi_3^{had}(s,t)$ go to a possibly nonzero constant while $\phi_4^{had}(s,t) \propto |t|$ and $\phi_5^{had}(s,t) \propto \sqrt{-t}$. All $\phi_i^{had}(s,t)$ are non-singular at $|t| \to 0$.

From another aspect of Regge pole theory, the factorization of helicity amplitudes should hold to a good approximation at high energies [1, 13],

$$\phi_1^{had}(s,t) = \phi_3^{had}(s,t), \tag{1.23}$$

$$\phi_2^{had}(s,t) = -\frac{\{\phi_5(s,t)\}^2}{\phi_+(s,t)}. \tag{1.24}$$

The interpretation of $\phi_2^{had}(s,t)$ from the property of factorization [14] runs counter to Equation (1.19). However it is generally expected that double spin flip amplitude $\phi_2^{had}(s,t)$ is negligible as $|t| \to 0$. Thus,

$$\phi_-^{had}(s,t) \to 0 \tag{1.25}$$

$$\phi_2^{had}(s,t) \propto |t| \to 0. \tag{1.26}$$

We would describe the expected magnitude of the hadronic helicity amplitudes in the region $|t| < 0.05$ (GeV/c)^2 at $\sqrt{s} \gg m_p$,

$$(|\phi_1^{had}(s,t)| \cong |\phi_3^{had}(s,t)|) \gg (|\phi_5^{had}(s,t)| \propto \sqrt{-t}) > (|\phi_4^{had}(s,t)| \propto |t|). \tag{1.27}$$

For example, in the middle of CNI region $-t = 0.003$ (GeV/c)^2, the size of $\phi_1^{had}(s,t)$ and $\phi_3^{had}(s,t)$ are three hundred times lager than those of $\phi_4^{had}(s,t)$, and twenty times lager than $\phi_5^{had}(s,t)$, respectively.

As we have introduced before, $\phi_2(s,0)$ is related to $\Delta\sigma_T$ directly in Equation (1.11) and $\phi_-(s,0)$ is related to $\Delta\sigma_L$ directly in Equation (1.12). There are some measurements from the past experiments for $\Delta\sigma_T$ and $\Delta\sigma_L$ (Figure 1.5 and 1.6 in the next section). In particular, $\Delta\sigma_L$ is decreasing in magnitude fast with energy and it is quite compatible with Equation (1.23).

1.2.2 The current constraints on hadronic amplitudes

In the 1980s-1990s many polarized and unpolarized *pp* collisions in the CNI and higher t region have been measured. Consequently, hadronic non-spin-flip amplitudes are understood very well.

On the other hand, hadronic spin-flip amplitudes ($\phi_2^{had}(s,t)$, $\phi_4^{had}(s,t)$ and $\phi_5^{had}(s,t)$) are not well understood. There are only two experiments in the CNI region, so far. A first measurement of A_N in CNI region at $\sqrt{s} = 19.4$ GeV had been performed by the E704 experiment at Fermi National Accelerator Laboratory (FNAL) using the 200 GeV/c polarized proton beam obtained from the decay of Λ hyperons [5]. Recently, A_N has been measured also at $\sqrt{s} = 200$ GeV by colliding the RHIC polarized proton beams [7]. However, the former measurement is much less precise and the recent measurement is slightly higher than the CNI region, they are not enough in resolving the unknown hadronic spin-flip amplitudes.

At large $|t| > 0.1$ (GeV/c)^2, many A_N and A_{NN} data been measured in the 1980s – the 1990s for the broad center-of-mass energy region. In this region, A_N is expected to vanish by theory. However there are some contradictions between theory and experiment. Therefore, the spin dependence of helicity amplitudes ($\phi_2^{had}(s,t)$, $\phi_4^{had}(s,t)$ and $\phi_5^{had}(s,t)$) are not well understood for all t and center-of-mass energies.

In the rest of the subsections, we will describe the best knowledge of helicity amplitudes in the CNI region from the past measurements for unpolarized and polarized cases.

$\phi_+^{had}(s,t)$ from unpolarized *pp* elastic scattering experiments

There are many total cross-section and differential cross-section data of unpolarized *pp* elastic scattering with precise and broad energy range. Figure 1.2 displays the total cross-section (σ_{tot}) as a function of total center-of-mass energy. The high energy behavior of σ_{tot}, which is flat up to $\sqrt{s} \sim 20$ GeV, is a value of 38 mb and then grows to 43 mb at $\sqrt{s} = 63$ GeV increasing further to about 62 mb at the CERN Super Proton Synchrotron (S$p\bar{p}$S) collider ($\sqrt{s} = 546$GeV). Especially for the high energy region, more than $\sqrt{s} \sim 20$ GeV, the cross-section was found to be rising approximately as $\ln^2 s$. Regge theory [15] describes the data and suggests the form of $\phi_+(s,0)$ as the Froissart-Martin bound [16].

$$|\phi_+(s,0)| \leq \text{const.} s \ln^2 s \text{ as } s \rightarrow \infty.$$

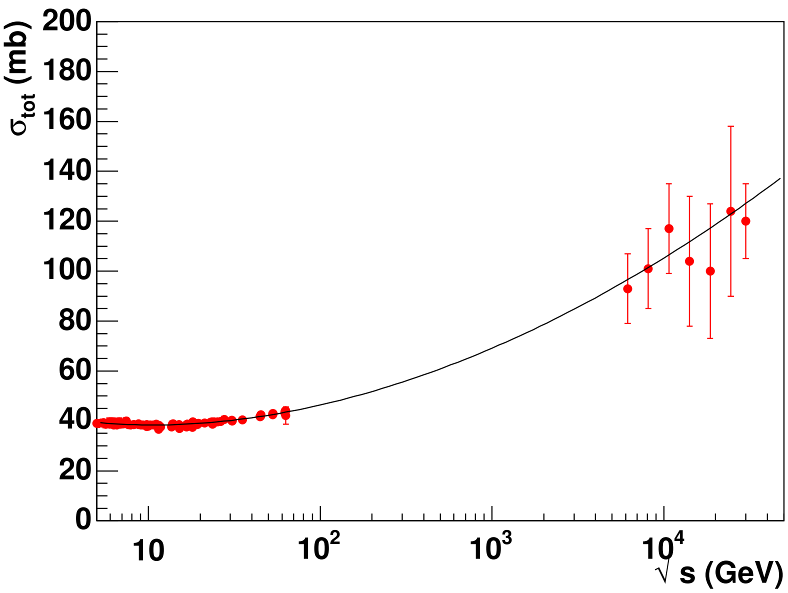

Figure 1.2: Total cross-section for *pp* collision as a function of center-of-mass energy [17]. The solid curve shows the results of the fitted function using Equation (1.9) [18] suggested by Regge theory.

Figure 1.3 displays the differential cross-section measured by experiment the UA6 at $\sqrt{s} = 24.3$ GeV [19] and the solid curve shows the results of the fitted function using Equation (1.9). In this small $|t|$ region, Equation (1.27) tells us the dominant components are $\phi_1^{had}(s,t)$ and $\phi_3^{had}(s,t)$. Since we are interested in very high energy $\sqrt{s}$, we will generally neglect m_p with respect to $\sqrt{s}$ to simplify the presentation of the formulas which follow. For example, $s(s-$

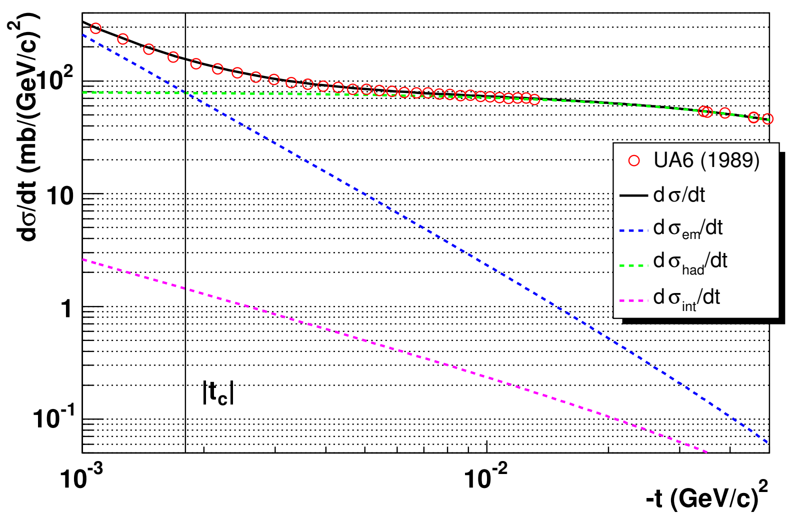

Figure 1.3: An experimental plot of $\mathrm{d}\sigma/\mathrm{d}t$ vs. $-t$ for *pp* elastic scattering at $\sqrt{s} = 24.3$ GeV. The horizontal and vertical axes are logarithmic scales. The solid curve used the parameterization of Equation (1.29). Parameters from fitting results [19] are $\sigma_{tot} = 39.46 \pm 0.04$ mb, $\rho = 0.009 \pm 0.010 \pm 0.006$ and $B = 11.4 \pm 0.5 \pm 0.07$ (GeV/c)$^{-2}$. We input $\delta_C = 0.02$. The dashed lines corresponds to $\mathrm{d}\sigma_{em}/\mathrm{d}t$ (blue), $\mathrm{d}\sigma_{had}/\mathrm{d}t$ (green) and $\mathrm{d}\sigma_{int}/\mathrm{d}t$ (pink).

$4m_p^2) \cong s^2$. Then Equation (1.9) is rewritten as below:

$$\frac{\mathrm{d}\sigma}{\mathrm{d}t} \simeq \frac{2\pi}{s^2} 2|\phi_+(s,t)|^2 \tag{1.28}$$

$$\cong 4\pi \left| \frac{\alpha}{|t|} e^{i\delta_C} + (\rho + i)\frac{\sigma_{tot}}{8\pi} e^{Bt/2} \right|^2$$

$$\cong \frac{d\sigma_{had}}{\mathrm{d}t} + \frac{d\sigma_{em}}{\mathrm{d}t} + \frac{\mathrm{d}\sigma_{int}}{\mathrm{d}t}, \tag{1.29}$$

where we used the optical theorem (1.10) at the last step.

As we will discuss in Subsection 1.3.1, the parameters (ρ, B, σ_{tot} and δ_C) in the explicit expression for $\phi_+^{had}(s,t)$ are related the accuracy of the theoretical prediction of A_N. ρ is real-to-imaginary ratio of ϕ_+^{had},

$$\rho = \frac{\mathrm{Re}\phi_+^{had}(s,0)}{\mathrm{Im}\phi_+^{had}(s,0)}. \tag{1.30}$$

We assume that ρ is small and varies negligible over the very small $|t|$ region of our interest.

B and δ_C have been introduced in Equation (1.14). The two parameters are obtained from experimental data as displayed Figure A.3 and Figure A.4. (For example, $\rho = -0.08 \pm 0.02$ and $B = 12.0 \pm 0.1$ (GeV/c)$^{-2}$ at at $\sqrt{s} = 13.7$ GeV.)

Coulomb-Nuclear-Interference The importance of the interference between coulomb force and nuclear force, defined $\mathrm{d}\sigma_{int}/\mathrm{d}t$ in Equation (1.29), is clearly maximal when $|\phi_+^{had}| = |\phi_+^{em}|$.

The interference term is of maximum significance when $|t| = |t_c|$,

$$|t_c| \cong \frac{8\pi\alpha}{\sigma_{tot}} \cong \frac{0.071}{\sigma_{tot}(\mathrm{mb})}. \tag{1.31}$$

In this small $-t$ region, the behavior of $\mathrm{d}\sigma/\mathrm{d}t$ changes dramatically. The coulomb scattering dominates in the region of $|t| \ll |t_c|$ and $\mathrm{d}\sigma/\mathrm{d}t$ goes nearly as $1/|t|^2$. The nuclear scattering dominates in the region for $|t| \gg |t_c|$ and $\mathrm{d}\sigma/\mathrm{d}t$ goes nearly as e^{Bt}. Between the two region at $|t| \simeq |t_c|$, the electro-magnetic amplitude and hadronic amplitude become similar in strength and interfere with each other. We refer to this region as the Coulomb-Nuclear-Interference (CNI) region ($|t| < 0.05$ (GeV/c)^2). $|t_c|$ is obtained to be ~ 0.002 (GeV/c)^2 at $\sqrt{s} = 10$–200 GeV. Figure 1.3 displays the coulomb, nuclear and interference components of the differential cross-section in these three $|t|$ regions. The dashed lines corresponds to $\mathrm{d}\sigma_{em}/\mathrm{d}t$ (blue), $\mathrm{d}\sigma_{had}/\mathrm{d}t$ (green) and $\mathrm{d}\sigma_{int}/\mathrm{d}t$ (pink).

$\phi_2^{had}(s,t)$ and $\phi_5^{had}(s,t)$ from polarized *pp* elastic scattering experiments

There is a huge amount of spin-dependent data at low to medium energies and higher $|t|$ (> 0.05), but little understanding of mechanisms at work. Because of the lack of clear-cut theoretical ideas and because of the difficulty of experiments there has generally been a lack of experimental effort since the middle 1980s. In particular, there are few experimental data at high energy and in the CNI region for A_N.

A first measurement of A_N at $\sqrt{s} = 19.4$ GeV and in the CNI peak region had been performed by the E704 experiment at FNAL in 1990 [5]. Recently, new A_N data has been measured at $\sqrt{s} = 200$ GeV by the PP2PP experiment [7] with the advent of polarized proton collider experiments at BNL. Both results are displayed in Figure 1.4 as a function of $-t$. However, the former measurement is much less precise and the recent measurement is slightly beyond the CNI peak region, they are not decisive results in resolving the unknown hadronic spin-flip amplitudes.

We would introduce the data in several t regions at low to medium beam energies briefly: $-t = 0, 0.15$ and 0.1 – 10 (GeV/c)^2.

Figure 1.5 and 1.6 display the results of measurements of $\Delta\sigma_T$ [32] and $\Delta\sigma_L$ [33]. As they have been introduced in Equation (1.11) and (1.12), these data are in the limit of $-t = 0$ (GeV/c)^2. $\Delta\sigma_T$ is certainly not zero in the low to medium energy region, but the limited data do suggest that it is decreasing rapidly with energy. $\Delta\sigma_L$ is a complicated structure at low-to-medium energies but is decreasing in magnitude fast with energy.

Away from the very small t in the CNI region, the data for fixed $-t = 0.15$ (GeV/c)^2 (or interpolated from nearby values) are displayed in Figure 1.7 and indicate that A_N in *pp* elastic scattering falls very fast with the center-of-mass energy. This data has sometimes led to the conclusion that $\phi_5(s,t)$ would vanish as a power of s as $s \rightarrow \infty$ [34]. The solid line is a fitted function suggested by Regge poles, namely, $A_N = a_1 + a_2/\sqrt{P_{beam}} + a_3/P_{beam}$ [35]. a_1, a_2 and a_3 are free parameters.

Figure 1.8 and 1.9 display the results of measurements of A_N [36, 37, 38, 39, 40] and A_{NN} [41, 42] at higher $-t$ and low beam momenta.

The results of A_N and A_{NN} data at even higher $-t$ are quite contrary to the theoretical prediction from helicity conservation at high energy. It is believed that the single spin-flip amplitude $\phi_5(s,t)$, where the initial helicity (=1) is not equal to the final total helicity (=0), should vanish. The same for the double spin-flip amplitude $\phi_2(s,t)$. It should vanish because the initial helicity (=1) is not equal to the final total helicity (=-1). Therefore A_N and A_{NN} must go to

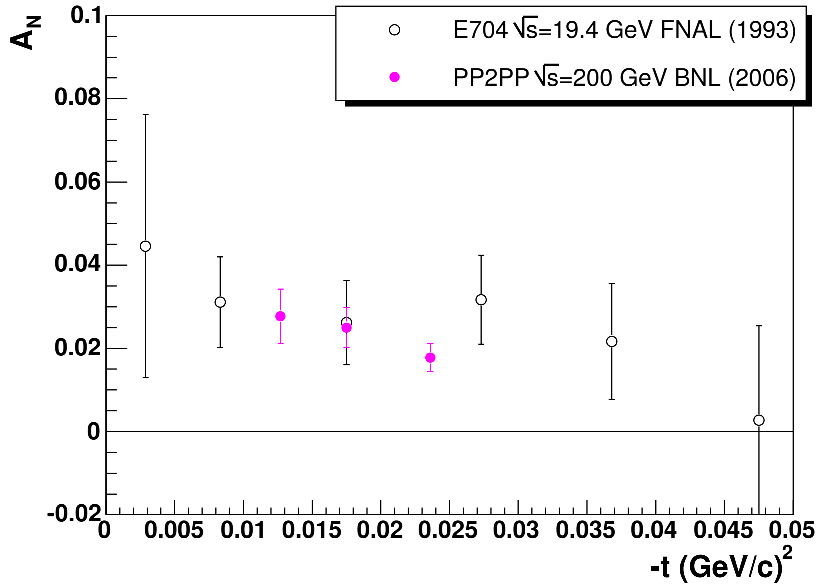

Figure 1.4: A_N data as a function of momentum transfer squared t at large $\sqrt{s}$ [5, 7].

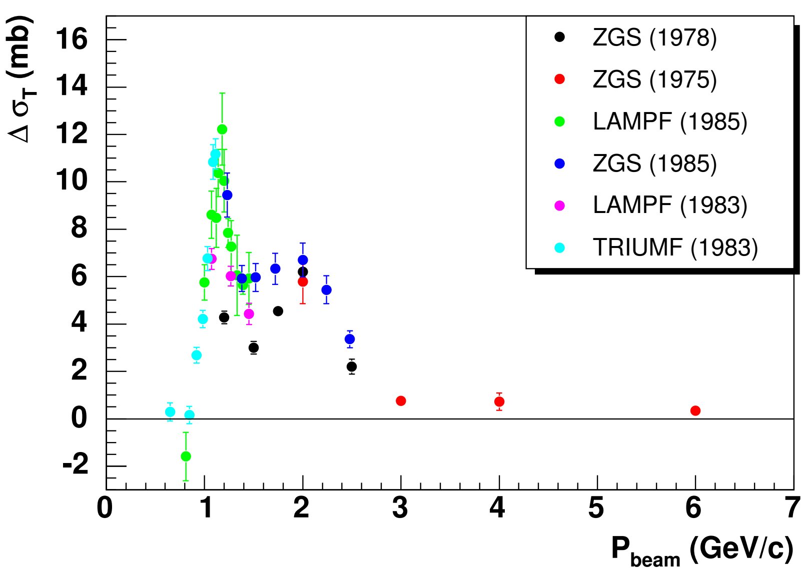

Figure 1.5: $\Delta\sigma_T$ for *pp* elastic scattering as a function of laboratory beam momentum [32].

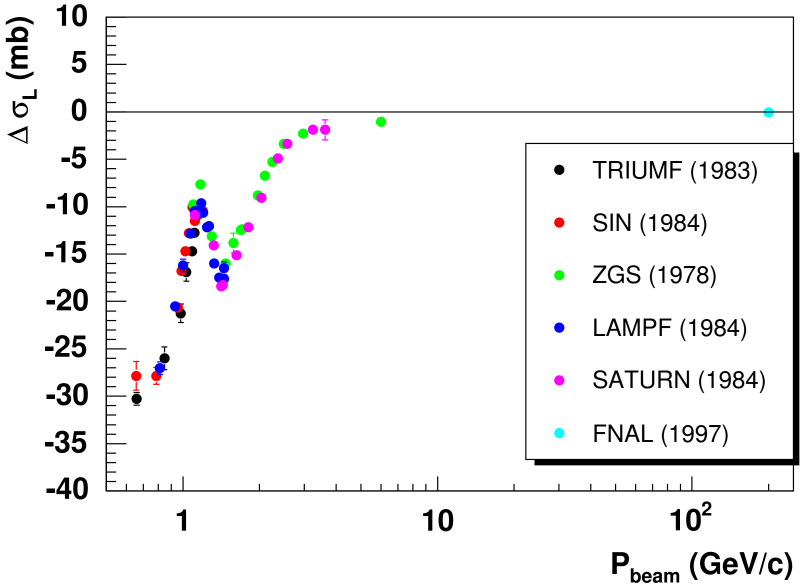

Figure 1.6: $\Delta\sigma_L$ for *pp* elastic scattering as a function of laboratory beam momentum [33].

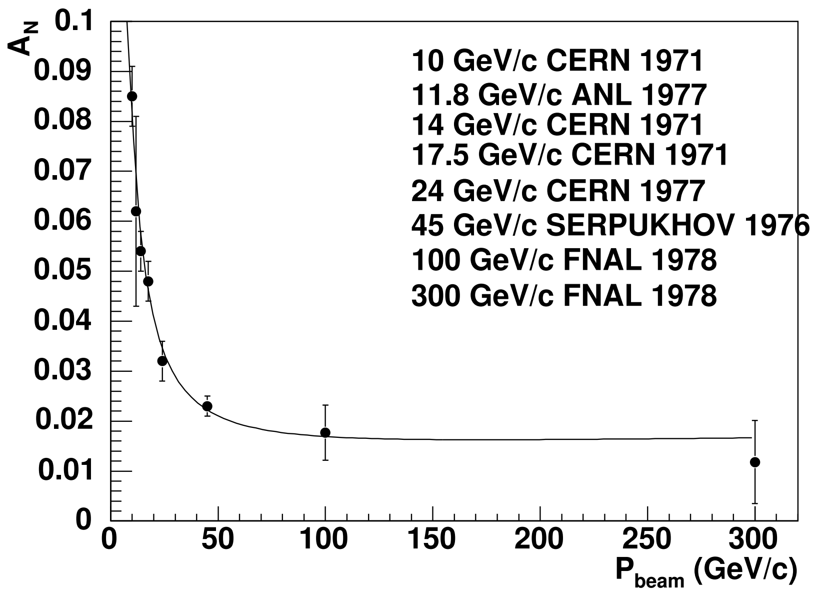

Figure 1.7: A_N for *pp* elastic scattering at $-t = 0.15$ (GeV/c)^2 as a function of laboratory beam momentum. The solid line is a fitted function suggested by Regge poles, namely, $A_N = a_1 + a_2/\sqrt{P_{beam}} + a_3/P_{beam}$ [35]. a_1, a_2 and a_3 are free parameters.

zero because they are proportional to $\phi_5(s,t)$ and $\phi_2(s,t)$. These contradictions between theory and experiment are not understood, except for the statement that $-t$ is too small to expect the asymptotic predictions to hold. But if the trend in A_N and A_{NN} continues to much larger values of $-t$ we will seriously have to question whether QCD picture of the strong interaction is really correct.

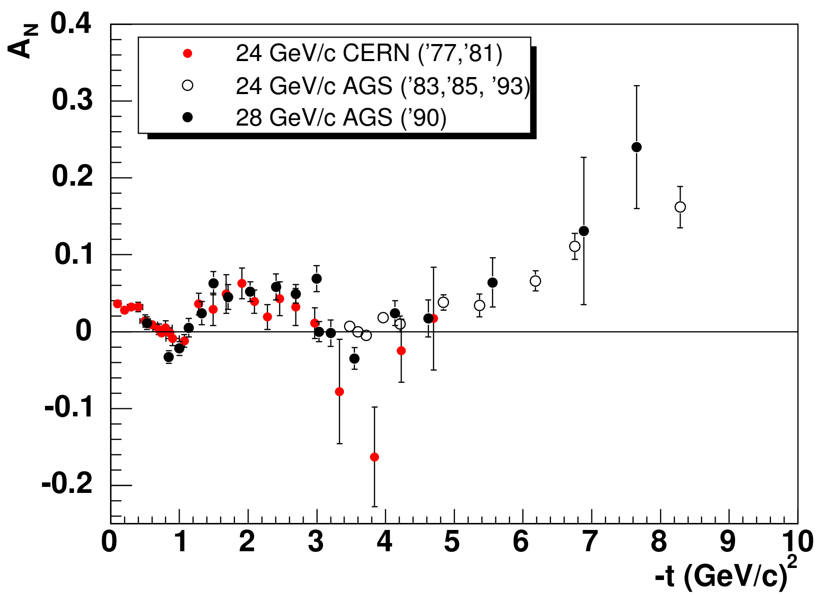

Figure 1.8: A_N for *pp* elastic scattering as a function of $-t$ at $P_{beam} = 24$ GeV/c and $P_{beam} = 28$ GeV/c. These A_N data at large $-t$ are measured in 1977 - 1993 [36, 37, 38, 39, 40]

.

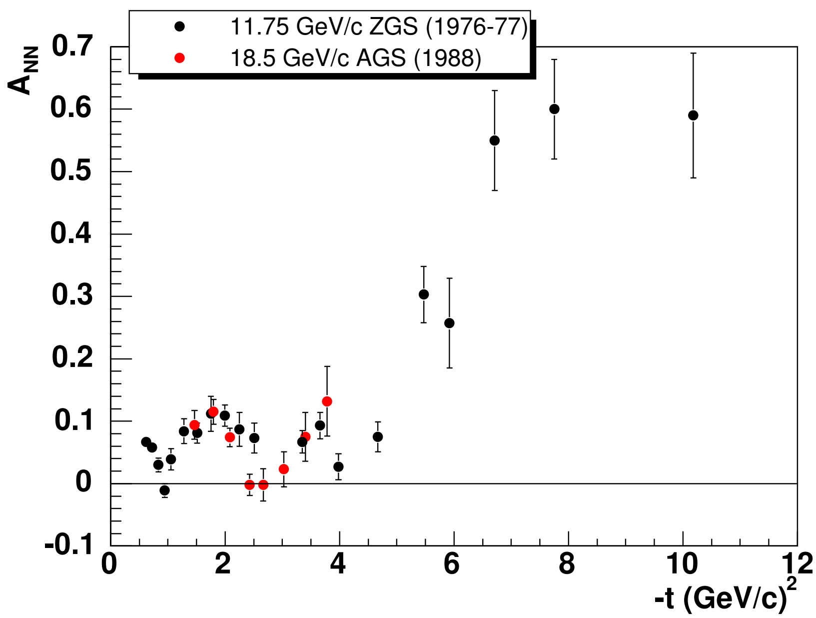

Figure 1.9: A_{NN} for *pp* elastic scattering as a function of $-t$ at beam momentum in the laboratory frame $P_{beam} = 11.75$ GeV/c [41] and 18.5 GeV/c [42].

1.3 Experimental approach to $\phi_2^{had}(s,t)$ and $\phi_5^{had}(s,t)$

In principle we can approach to the unknown hadronic spin-flip amplitudes by measuring several observable with proper initial spin states as referred in Equation (1.7) and (1.8). In this section, the more dedicated experimental approach to extract the contributions of hadronic spin-flip amplitudes from the measured A_N and A_{NN} are discussed .

1.3.1 $\phi_5^{had}(s,t)$ and A_N

In the CNI region, the known electro-magnetic amplitudes and the hadronic amplitudes are comparable in size. Although the hadronic amplitudes cannot be calculated from QCD at the same time they are expected to have smooth finite limits as $|t| \rightarrow 0$. Therefore, a knowledge of the electro-magnetic amplitudes together with some limited information on the hadronic amplitudes may allow us to anticipate the the form of A_N and the position of its maximum in terms of t.

For understanding the $|t|$ dependence of the dominant A_N form, we will ignore the second and higher order of $\phi_2^{had}(s,t)$ and $\phi_4^{had}(s,t)$ because they are negligible with respect to $\phi_+^{had}(s,t)$. Their magnitudes are explained in Equation (1.27). Using Equation (1.7) and (1.9), A_N becomes

$$\begin{aligned} A_N &= \frac{-2\text{Im}[\phi_5^*(s,t)\{\phi_1(s,t)+\phi_2(s,t)+\phi_3(s,t)-\phi_4(s,t)\}]}{|\phi_1(s,t)|^2+|\phi_2(s,t)|^2+|\phi_3(s,t)|^2+|\phi_4(s,t)|^2+4|\phi_5(s,t)|^2} \\ &\approx \frac{-\text{Im}[\phi_5^*(s,t)\phi_+(s,t)]}{|\phi_+(s,t)|^2}. \end{aligned} \tag{1.32}$$

$\phi_5^{had}(s,t)$ is characterized by use of relative amplitude, which is defined in the following way:

$$r_5 = \frac{m_p \phi_5^{had}(s,t)}{\sqrt{-t}\,\text{Im}\phi_+^{had}(s,t)}, \tag{1.33}$$

where r_5 is assumed to be complex and to vary with $\sqrt{s}$ but their variation with $-t$ over small region are neglected.

Equation (1.32) is rewritten as:

$$\frac{m_p A_N}{\sqrt{-t}}\frac{16\pi}{\sigma_{tot}^2}\frac{\text{d}\sigma}{\text{d}t}e^{-Bt} = [\kappa(1-\delta_C\rho)-2(\text{Im}r_5-\delta_C\text{Re}r_5)]\frac{t_c}{t} - 2\text{Re}r_5 + 2\rho\text{Im}r_5, \tag{1.34}$$

and

$$\frac{16\pi}{\sigma_{tot}^2}\frac{\text{d}\sigma}{\text{d}t}e^{-Bt} = \left(\frac{t_c}{t}\right)^2 - 2(\rho+\delta_C)\frac{t_c}{t} + (1+\rho^2). \tag{1.35}$$

The asymmetry for the CNI region can thus be expressed as a function of $\left(\frac{t_c}{t}\right)$. The position of the maximum in A_N is near t_c:

$$\frac{t_{max}}{t_c} = \sqrt{3} + \frac{8}{\kappa}(\rho\text{Im}r_5 - \text{Re}r_5) - (\rho+\delta_C). \tag{1.36}$$

The uncertain "spin-flip" relative amplitudes are apparent in these equations. Comparing this equation with the precisely measured A_N, we can extract the relative spin-flip amplitudes. A measurement of A_N in the CNI region, therefore, can be a sensitive probe for $\phi_5^{had}(s,t)$.

The presence of a hadronic spin-flip amplitude ($\phi_5^{had}(s,t)$) interfering with the electromagnetic spin-non-spin-flip one ($\phi_+^{em}(s,t)$) introduces a deviation in shape and magnitude for

A_N calculated with no hadronic spin-flip [1]. We compare the A_N data from the E704 to the theoretical prediction with no hadronic spin-flip hadronic amplitudes. We input the parameters: $\delta_C = 0.02$, $\rho = -0.03$, $\sigma_{tot} = 39.0$ mb and $B = 12$ (GeV/c)$^{-2}$ at $\sqrt{s}$=19.4 GeV. The χ^2 is 1.65 for 6 degrees of freedom. (The χ^2/ndf for a fitting with constant value is also small, χ^2/ndf = 1.94/5.)

The A_N data from the E704 are also fitted with the theoretical prediction allowing for a hadronic spin-flip contribution. The χ^2 is $1.33/4\ d.o.f$. The r_5 is obtained as:

$$\begin{aligned} \mathrm{Im} r_5 &= 0.14 \pm 0.32, \\ \mathrm{Re} r_5 &= -0.03 \pm 0.05, \end{aligned}$$

where we assume that $|\phi_2^{had}(s,t)|$ is zero. It is hard to see the form of A_N and extract the hadronic spin-flip contribution from the data points, because they are moderate precision.

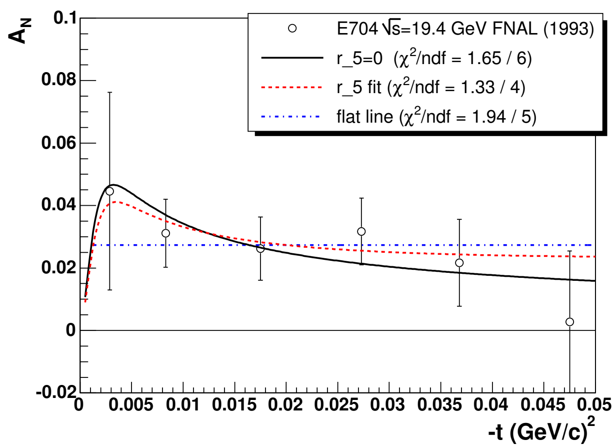

Figure 1.10: A_N as a function of $-t$ for $p^{\uparrow}p \to pp$ at $\sqrt{s} = 19.4$ GeV [5]. The data points are moderate precision and it is hard to see the form of A_N. The black line the is theoretical function with no hadronic spin-flip. The A_N data were also fitted with theoretical function which is shown in the dotted red line($|\phi_2^{had}(s,t)| = 0$) and just flat line shown in the blue dashed-dotted line.

Lastly, we will describe the r_5 dependence of the A_N form using Equation (1.34). We input the parameters: $\rho = -0.08$ and $\sigma_{tot} = 38.4$ mb and $\delta_C = 0.02$. They are obtained from the experimental results at $\sqrt{s} = 13.7$ GeV. We estimated the size of $\mathrm{Im} r_5$ and $\mathrm{Re} r_5$ from a deviation ($\Delta A_N \sim 10^{-3}$) in shape and magnitude for A_N calculated with no hadronic spin-flip amplitude.

Figure 1.11 and 1.12 display the deviation in shape and magnitude for A_N calculated with different non-spin-flip amplitudes. The solid black line in the Figure 1.11 and 1.12 is the A_N with no hadronic spin-flip ($|r_5| = 0$). .

The solid black line, dashed red line and dashed-dotted pink line in Figure 1.11 are the case of $\mathrm{Im} r_5 = 0$, $\mathrm{Im} r_5 = 0.02$ and $\mathrm{Im} r_5 = -0.02$, respectively.

The solid black line, dashed red line and dashed-dotted pink line in Figure 1.12 are the case of $\mathrm{Re} r_5 = 0$, $\mathrm{Re}\ r_5 = 0.02$ and $\mathrm{Re}\ r_5 = -0.02$, respectively.

We can anticipate that the height of the peak is mainly sensitive $\mathrm{Im} r_5$, while the shape depends mainly on $\mathrm{Re} r_5$. The deviation which comes from non-zero $\mathrm{Re}\ r_5$ will be bigger than that

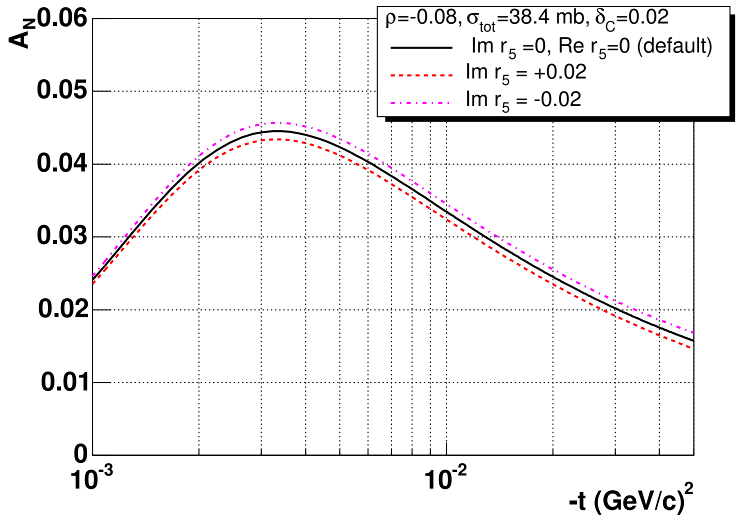

Figure 1.11: A_N for $\mathrm{Im}r_5 = 0.00, 0.02, -0.02$.

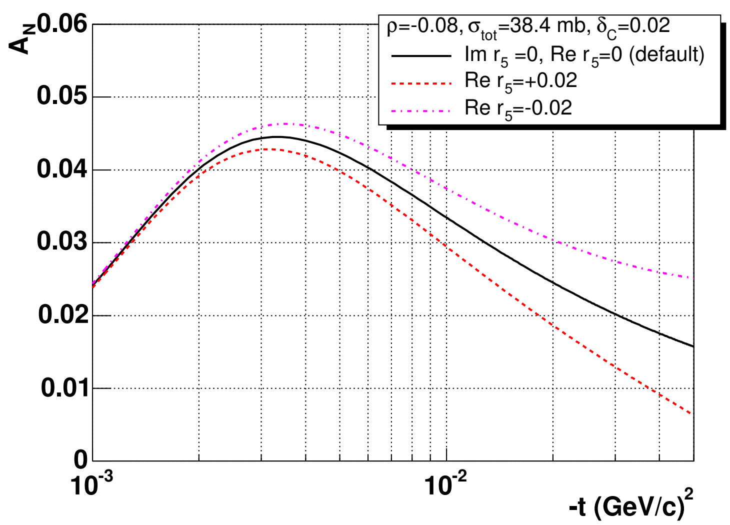

Figure 1.12: A_N for $\mathrm{Re}r_5 = 0.00, 0.02, -0.02$.

of Im r_5. This means that the A_N measurement is more sensitive to Re r_5 than Im r_5. Thus, comparing new measurement of A_N data , which are required to be better than $\Delta A_N \ < \ 10^{-3}$ ($\Delta A_N / A_N \sim$ few %), to the theoretical prediction with no hadronic spin-flip, a deviation in shape and magnitude will constrain the size of the hadronic spin-flip amplitude.

Actually, the form of A_N and the position of its maximum depend on the parameters describing the hadronic amplitudes:σ_{tot}, the ratio ρ between the real and imaginary parts of the forward scattering amplitude, the Bethe phase shift δ_C, and the nuclear slope parameter B [1]. The accuracy of σ_{tot}, ρ and δ_C will limit the accuracy of the r_5 measurement and we will discuss this issue in Chapter 5.

1.3.2 $\phi_2^{had}(s,t)$ and A_{NN}

The conventional assumption, $\phi_4^{had}(s,t) \propto \ t \ \rightarrow 0$ at large $\sqrt{s}$ and small $-t$, leads to

$$\begin{aligned} A_{NN}\frac{\mathrm{d}\sigma}{\mathrm{d}t} &= \frac{4\pi}{s^2}\{2|\phi_5(s,t)|^2 + \mathrm{Re}[\phi_1^*(s,t)\phi_2(s,t) - \phi_3^*(s,t)\phi_4(s,t)]\} \\ &\cong \frac{4\pi}{s^2}\{2|\phi_5^{had}(s,t)|^2 + \mathrm{Re}[\phi_+^*(s,t)\phi_2^{had}(s,t)]\}. \end{aligned}$$

Because there is no purely one photon exchange contribution to this asymmetry, A_{NN} is sensitive to spin-flip hadronic amplitudes especially for $\phi_2^{had}(s,t)$.

This sensitivity has been studied theoretically but there is no conclusive understanding for its $-t$ dependence nor magnitude to $\phi_+^{had}(s,t)$ [43]. Figure 1.13 illustrates the enhancement of $\phi_2^{had}(s,t)$ to A_{NN} assuming 5% magnitude to $\phi_+^{had}(s,t)$ at $-t = 0$. The three curves correspond to

$$\begin{aligned} \phi_2^{had}(s,t)/\phi_+^{had}(s,t) &= 0.05(1+i), \\ \phi_2^{had}(s,t)/\phi_+^{had}(s,t) &= 0.05, \\ \phi_2^{had}/\phi_+^{had} &= 0.05i. \end{aligned}$$

The A_{NN} shape is almost flat in the region of $-t > 0.005$ (GeV/c)^2 and the value is quite different depending on the real-to-imaginary ratio of $\phi_2^{had}(s,t)/\phi_+^{had}(s,t)$. Here, we would emphasize that assumed of 5% magnitude to $\phi_+^{had}(s,t)$ was noted as "achievable experimental accuracy of not-too-distant future", since we do not know how large the double spin-flip amplitude, if it exists. But this theoretical estimation indicates that the imaginary part of $\phi_2^{had}(s,t)$ is much sensitive to A_{NN}.

Thus, we are able to confirm the existence of hadronic spin-flip amplitudes from A_N and A_{NN} measurements. However, as we discussed in Section 1.1, there has been no measurement in the CNI region because of difficulties of experiments. Therefore the first measurement of A_{NN} as a function of $|t|$ in the CNI region is especially important and is expected to provide best knowledges of $\phi_2^{had}(s,t)$, $\Delta\sigma_T$ and Im$\phi_2(s,0)$.

1.4 Summary of Introduction

As a summary of above discussions, we summarized the theoretical and experimental understanding for elastic *pp* scattering as below:

- The *pp* elastic scattering processes are described in transition amplitudes by use of helicity of initial and final states.

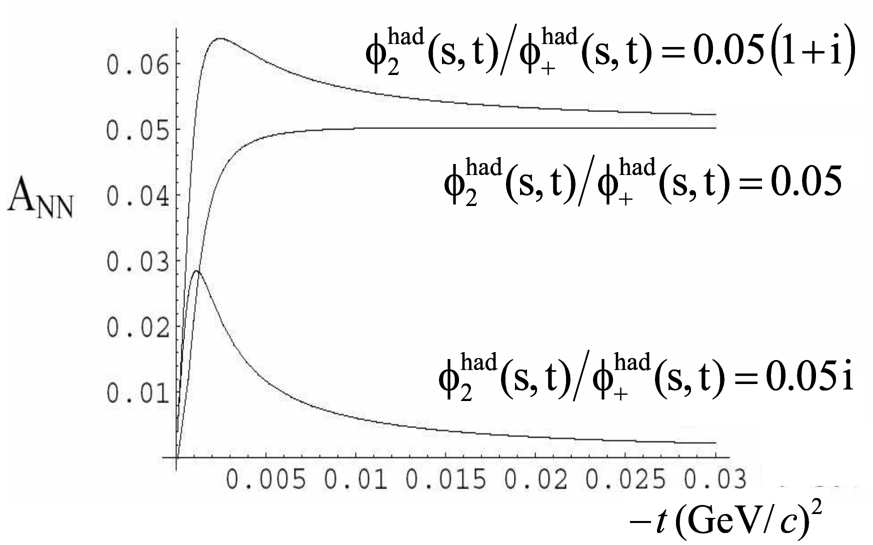

Figure 1.13: We quote this plot from [43, 66]. The plot illustrates the enhancement of $\phi_2^{had}(s,t)$ to A_{NN} due to the interference with the one-photon exchange by use of 5% magnitude at $-t = 0$. The three curves correspond to $\phi_2^{had}(s,t)/\phi_+^{had}(s,t) = 0.05i$, $\phi_2^{had}(s,t)/\phi_+^{had}(s,t) = 0.05$, $\phi_2^{had}(s,t)/\phi_+^{had}(s,t) = 0.05(1+i)$.

- Requiring that the interaction is invariant under space inversion, time reversal and rotation in isotopic spin space, we can select a set of five independent helicity amplitudes as functions of s and t ($\phi_i(s,t)$, i=$1,2,3,4,5$).
- Each helicity amplitude is described as a superposition of the hadronic amplitude $\phi_i^{had}(s,t)$ and the electro-magnetic amplitude $\phi_i^{em}(s,t)$.
- The electro-magnetic amplitudes ($\phi_i^{em}(s,t)$, i=$1,2,3,4,5$) are given exactly by QED [4].
- Non-spin-flip hadronic amplitude ($\phi_+^{had}(s,t) = (\phi_1^{had}(s,t) + \phi_3^{had}(s,t))/2$) are determined by the total cross-section phenomenological way.

We may expect the characteristics of these hadronic amplitude theoretically as $-t \to 0$:

- $\phi_-^{had}(s,t) = (\phi_1^{had}(s,t) - \phi_3^{had}(s,t))/2 \to 0$.
- $\phi_4^{had}(s,t) \to 0$

The missing pieces are $\phi_2^{had}(s,t)$ and $\phi_5^{had}(s,t)$. They correspond to double and single spin-flip amplitudes.

The precise measurements of A_N and A_{NN} will provide the best experimental constrains for r_5 and r_2, and allow us to achieve fully understanding for *pp* elastic scattering in the CNI region at $\sqrt{s} \to \infty$.

Chapter 2

Experiment

2.1 Kinematics of *pp* Elastic Scattering and Detector Design

We describe the kinematics of *pp* elastic scattering at very small $|t| < 0.035$ (GeV/c)^2 and specify the kinematics in the laboratory frame.

In the *pp* elastic scattering process, both forward-scattered particle and recoil particle are protons and there are no other particles involved nor new particles produced in the process. Therefore, the recoil particle identification and the mass measurement of all the rest particles, which we do not detect, are essential for the elastic event selection.

In order to select a 2-to-2 process, the recoil particle identification and missing particle(s) identification is needed. Since initial states are well defined, both particles can be, in principle, identified by detecting the recoil particle only. The background processes are also discussed for the comparison. Particularly the forward scattered particle identification is essential to reject the background processes. The required detector resolutions to distinguish the elastic events from those background is also described.

2.1.1 Elastic Scattering and Background Processes

Figure 2.1 displays (a) elastic *pp* scattering process *pp* → *pp* and (b) background inelastic scattering process *pp* → *Xp* for comparison.

p_1, p_2 and p_R are 4-momenta of incident proton, target proton and recoil particle, respectively. m_p is the proton mass. p_X is the four-momentum of missing particle(s) which we do not measure;

$$\begin{aligned} p_1 &= (E_1, \vec{p}_1), \\ p_2 &= (m_p, 0), \\ p_X &= (E_X, \vec{p}_X) \text{ and} \\ p_R &= (E_R, \vec{p}_R). \end{aligned} \tag{2.1}$$

Here $E_1(= 100$ GeV), E_X and E_R are the energies of the incident, undetected and recoil particles. $\vec{p}_1$, $\vec{p}_X$ and $\vec{p}_R$ are 3-momenta of incident, undetected and recoil particles. We define the scattering plane from $\vec{p}_1$ and $\vec{p}_R$. In the scattering plane, the relationship of 4-momenta between missing momenta and recoil protons are unique.

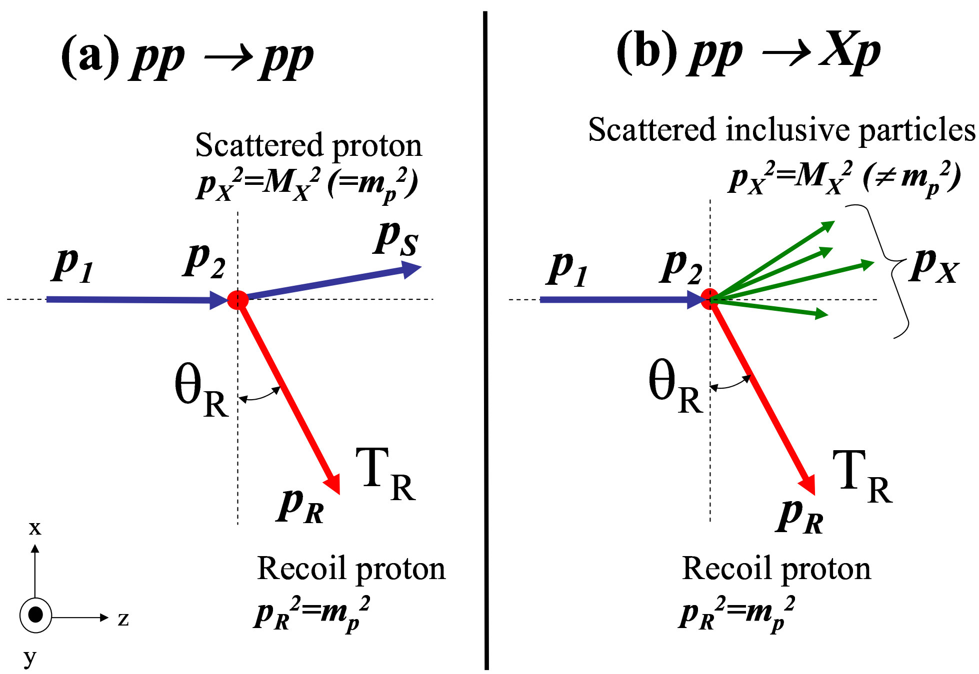

Figure 2.1: (a) Elastic scattering process and (b) Inelastic scattering process in the laboratory frame.

Four-momentum transfer squared, t is obtained measuring the kinetic energy of the recoil particle T_R:

$$t = (p_2 - p_R)^2 = (m_p - E_R, -\vec{p_R})^2 = -2m_pT_R < 0, \tag{2.2}$$

where $T_R = E_R - m_R$ is the kinetic energy of recoil particle. In the region $0.001 \leq |t| \leq 0.035$ (GeV/c)^2, the kinetic energy of the recoil proton is $0.5 \leq T_R \leq 17$ MeV.

T_R, time-of-flight (ToF) of recoil proton and flight length L satisfy the following equation :

$$ToF = L\sqrt{\frac{m_p}{2T_R}}. \tag{2.3}$$

Since we discuss very low kinetic energy region, $T_R < 17$ MeV, the nonrelativistic approximation is applicable to the kinematics.

By imposing energy-momentum conservation:

$$p_X = (p_1 + p_2 - p_R),$$

after some algebra

$$\begin{aligned} {p_X}^2 &= (p_1 + p_2 - p_R)^2 \\ {M_X}^2 &= {m_p}^2 + t - 2E_1T_R + 2|\vec{p_1}||\vec{p_R}|\sin\theta_\mathrm{R} \end{aligned} \tag{2.4}$$

where θ_R is the recoil angle with respect to the x-axis as displayed in Figure 2.1 and $M_X^2 = p_X^2$ is the invariant mass squared of the undetected particle(s). For the *pp* elastic scattering, M_X is the proton mass and recoil angle, θ_R^{pp}, and kinetic energy, T_R, are uniquely correlated by:

$$\theta_R{}^{pp} = \frac{-t + 2E_1T_R}{2|\vec{p_1}||\vec{p_R}|} \cong \frac{\sqrt{|t|}}{2m_p} \cong \sqrt{\frac{T_R}{2m_p}} \tag{2.5}$$

where $\theta_R \cong \sin\theta_R$ at high energies $E_1 \gg m_p$ and at small momentum transfer region ($|t| \ll 4{m_p}^2$). This equation corresponds to the blue line in Figure 2.2.

The possible diffractive dissociation processes (b) in Figure 2.1 are:

$$\begin{aligned} pp &\rightarrow (p + \pi)p \\ pp &\rightarrow (p + 2\pi)p \\ pp &\rightarrow N(1440)p \end{aligned}$$

Thus, the channel for diffractive dissociation opens at $M_X > m_p + m_\pi \approx 1.07$ GeV/c^2. Here, m_π is the mass of pion. The red, green and pink lines in Figure 2.2 are the angle-energy correlations of these inelastic processes.

The recoil particle identification and the mass measurement of all the rest particle(s) are essential for the event selection. This is carried out by use of

- kinetic energy, T_R,
- time of flight, *ToF*, and
- recoil angles, θ_R of the recoil particles.

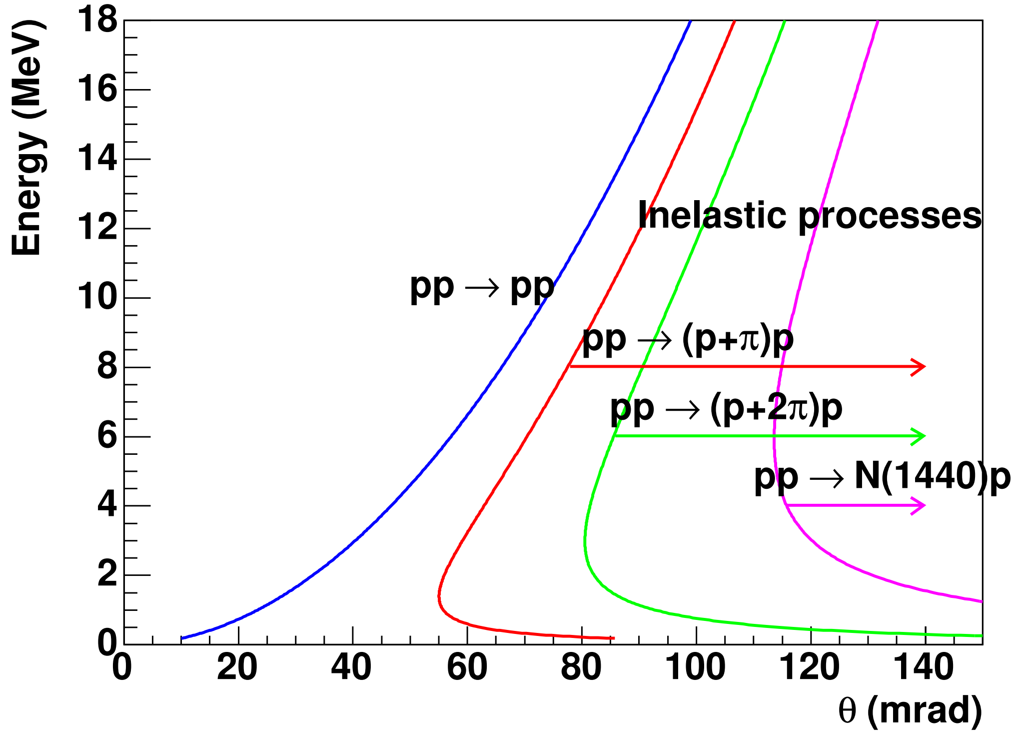

Figure 2.2: The correlations between energy and angle of recoil particle of elastic and inelastic process.

2.1.2 Required Detector Performance

Required Kinetic Energy Range and Resolution.

As we have introduced in the section 1.1, the interference between electro-magnetic force and nuclear force is predicted to generate a significant A_N of $4 \sim 5\%$, peaking at $|t| \simeq 0.003$ (GeV/c)^2. For a precise measurement of the A_N peak, the required accuracy for t and A_N are $\Delta|t| < 0.0005$ (GeV/c)^2 and $\Delta A_N < 0.001$, respectively. The recoil technique is of great advantage to achieve the very small $|t|$ region, because the resolution of $|t|$ is directly connected to the kinetic energy resolution. For example, $\Delta|t| = 0.0005$ (GeV/c)^2 corresponds to $\Delta T_R = 0.1$ MeV in terms of the kinetic energy.

In order to reach $\Delta A_N \sim 0.001$ statistically, we need to accumulate more than 10^6 *pp* elastic scattering events in the CNI region.

Here we would emphasize the advantages of our apparatus. The recoil technique using internal solid target was pioneered at Joint Institute for Nuclear Research (JINR) [44] and was later used at Serpukov [45], Felmilab [46, 47], Centre European pour la Recherche Nucleaire (CERN) [19], Indiana University Cyclotron Facility (IUCF) [48] et cetera. However there was no spin-dependent data in the CNI region from these experiments. Because the energy loss in the solid target would limit the achievable minimum kinetic energy. We employed the gas-jet target and improved the achievable minimum kinetic energy by one-fifty.

Required Recoil Angle Range and Resolution

The goal of the missing mass measurement is to distinguish ${m_p}^2$ from $(m_p + m_\pi)^2$. If we aim for a 3-σ separation, the required width of the missing mass squared $\Delta(M_X^2)$ of the *pp* elastic scattering process is:

$$\Delta(M_X^2) < \{(m_p + m_\pi)^2 - m_p^2\}\frac{2}{3} \sim 0.17(\text{GeV}/c^2)^2. \tag{2.6}$$

By using Equation (2.4), the width of M_X^2 for the *pp* elastic scattering process is estimated:

$$\Delta(M_X^2) \cong \left(-2(m_p + E_1) + \frac{p_1}{\sqrt{2m_p}}\right)\Delta T_R \oplus 2|\vec{p_1}|\sqrt{2m_pT_R}\Delta\theta_R \tag{2.7}$$

where $A \oplus B$ denotes the quadratic sum of A and B. The first term is independent of T_R but is linear in ΔT_R. ΔT_R has been required to be less than 0.1 MeV. Then, the first term is estimated to be ~ 0.01 (GeV/c^2)^2 and does not limit $\Delta(M_X^2)$.

The second term is a function of T_R. In the cases of $T_R = 5, 10$ and 17 MeV, the angle resolution is required to be $\Delta\theta_R \sim 8.8, 6.2$ and 4.8 mrad, respectively. Thus we conclude that $\Delta\theta_R \leq 4.8$ mrad is sufficient for 3-σ separation between elastic and inelastic processes.

Required Flight Length L, ToF Range and Resolution

The goal of the recoil particle identification is to distinguish protons from the huge amount of *prompt* particles, which are possibly pions from beam-related interactions upstream and are synchronized with RHIC beam bunches. The beam bunch arrives every 106 nsec with the design luminosity (110 bunches in each ring). Due to the length of the RHIC beam bunches, the collision timing spread around $\sigma \sim 2$ nsec. Considering the intrinsic time resolution and stability of the

	Range	Resolution
recoil kinetic energy T_R (MeV)	$0.5 - 20$	≤ 0.1
recoil angle θ_R (mrad)	$15 - 100$	≤ 4.8
ToF (nsec)	13–80	≤ 3.5

Table 2.1: Summary of the kinematic parameters

DAQ system, the ToF resolution can be roughly estimated to be ~ 3.5 nsec as discussed later in Section 3.4.

By assuming the velocity of the *prompt* particles is the light velocity c and requiring 3-σ separation, ToF of the fastest recoil proton is estimated. In order to have the signal protons well separated from the prompt particles of the "current" beam bunch,

$$ToF_{min} = \frac{L}{v_{max}} > \frac{L}{c} + 11 \text{ nsec},$$

where L is the flight length. The highest energy of proton is $\sim$ 20 MeV and $\beta \sim 0.2$ for our physics purpose. Therefore the minimum L is estimated to be 0.75 m.

In order to have the slowest signal protons well separated from the prompt particles of the "next" beam bunch,

$$ToF_{max} = \frac{L}{v_{min}} < \frac{L}{c} + 95 \text{ nsec}.$$

The lowest energy of proton is ~ 0.5MeV and $\beta \sim 0.03$ for our physics purpose. Therefore the maximum L should be 0.92 m.

Summary of kinematic parameters

Taking account of the above considerations, we set $L = 0.8$ m for the experiment. The required range and resolution of energy, angle and *ToF* are summarized in Table 2.1.

We will compare the required to the achieved performances in Section 2.4.

2.2 H-jet-target System and the Recoil Detector

Firstly we will describe the overview of the experimental setup. Secondly H-jet-target system is described. The basic principles of polarized atomic-beam and the performance from 2004 commissioning experiment are described. Lastly we will describe the recoil spectrometers.

2.2.1 Overview of Experimental Setup

Figure 2.3 displays the photo of the entire jet-target system at the interaction point, ”12 o’clock” (IP12). [1]

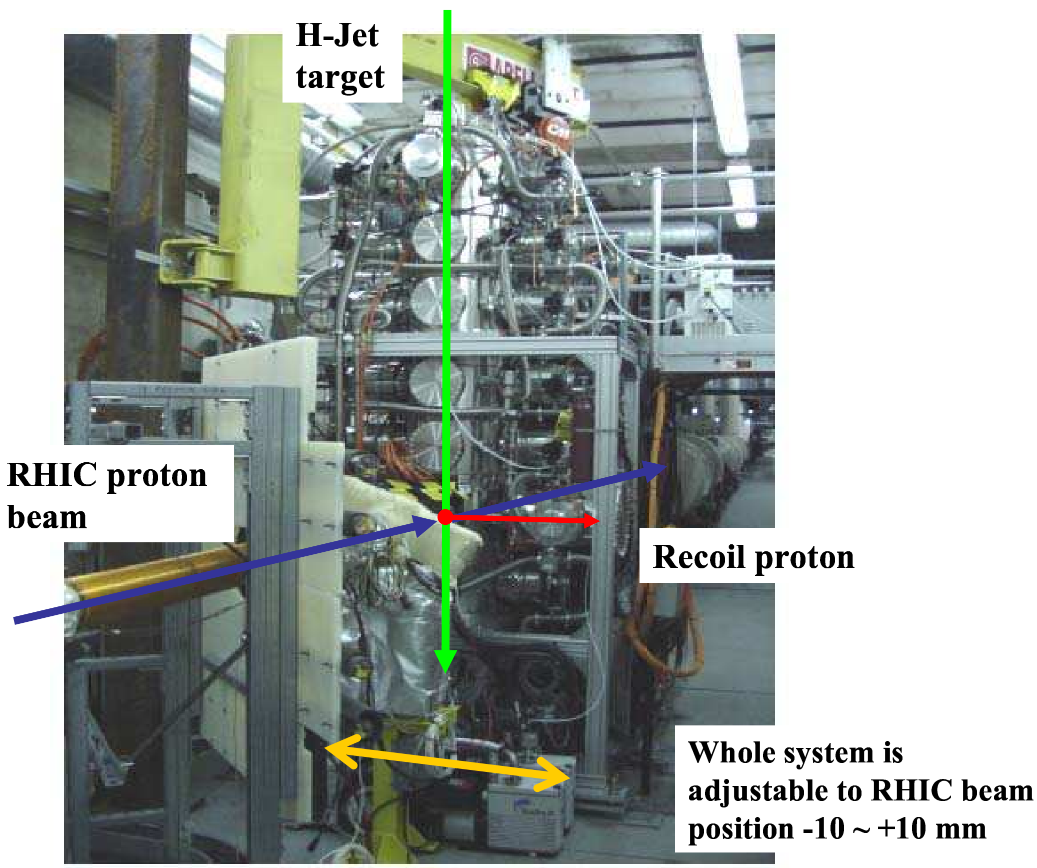

Figure 2.3: Picture of the jet-target system at IP12

The jet-target system is 3.5 m in height and about 3000 kg in weight. At IP12, the blue and yellow beams can be separated by more than 10 mm. During the commissioning run in 2004, only blue beam collided with the jet-target. The arrows in Figure 2.3 indicate the directions of the RHIC blue beam, H-Jet atomic-beam and recoil proton, respectively. The jet-target is a free

[1]The RHIC storage rings, which we will describe later in Section 2.3, are designed with six interaction points (IP’s), where beam collisions are possible. If the rings are thought of as a clock face, the system is at 12 o’clock.

atomic-beam (vertical green arrow), which crosses the RHIC beam (blue arrow). The velocity of the atomic-beam is $\sim 1560 \pm 50$ m/s [50] and negligible with respect to the RHIC beam (100 GeV/c). Therefore, we treated target proton as quiescence in the laboratory frame. The recoil proton direction is indicated with red arrow. The jet-target system was placed on the rails which are perpendicular to the beam direction (yellow arrow in Figure 2.3). The entire system is able to move to left and to right by 10 mm each, in order to adjust the jet-target center to the blue beam center.

The recoil protons were detected by the silicon detectors in both sides as shown in Figure 2.4. We use the x-, y- and z-axis, which is defined in the figure, in the following discussions.

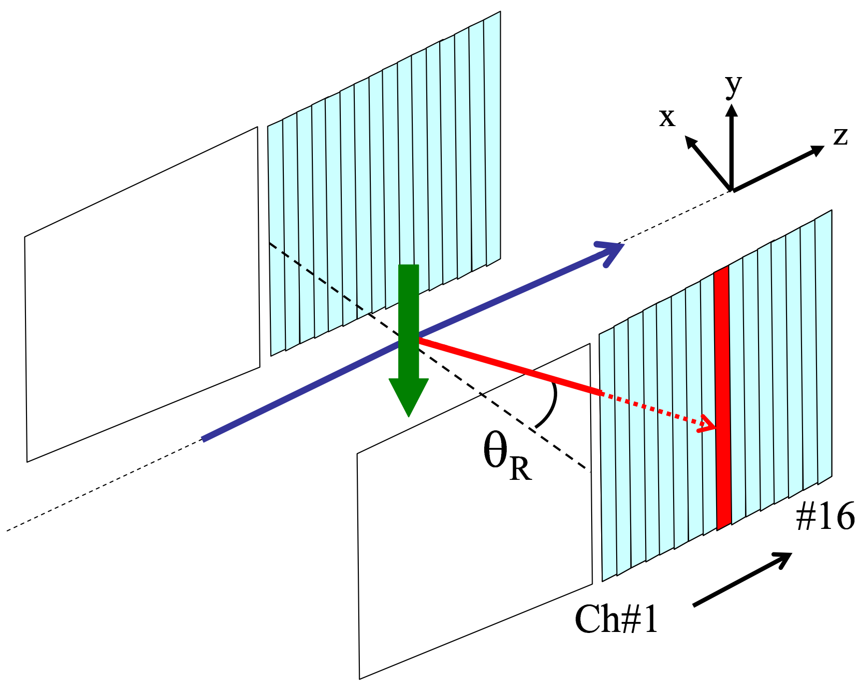

Figure 2.4: Inelastic process ($pp \rightarrow pX$) in laboratory frame

2.2.2 H-jet-target System

Figure 2.5 displays the H-jet-target system. The system consists of mainly 3 parts including nine vacuum chambers and nine differential vacuum stages:

1. Atomic Beam Source (ABS) : 1st to 5th chambers. Polarize the atomic hydrogens.

2. Scattering Chamber : 6th chamber. Collisions between the target-proton and the beam-proton are occurred.

3. Breit-Rabi Polarimeter (BRP): 7th to 9th chamber. Measure the target polarization

We will describe these below.

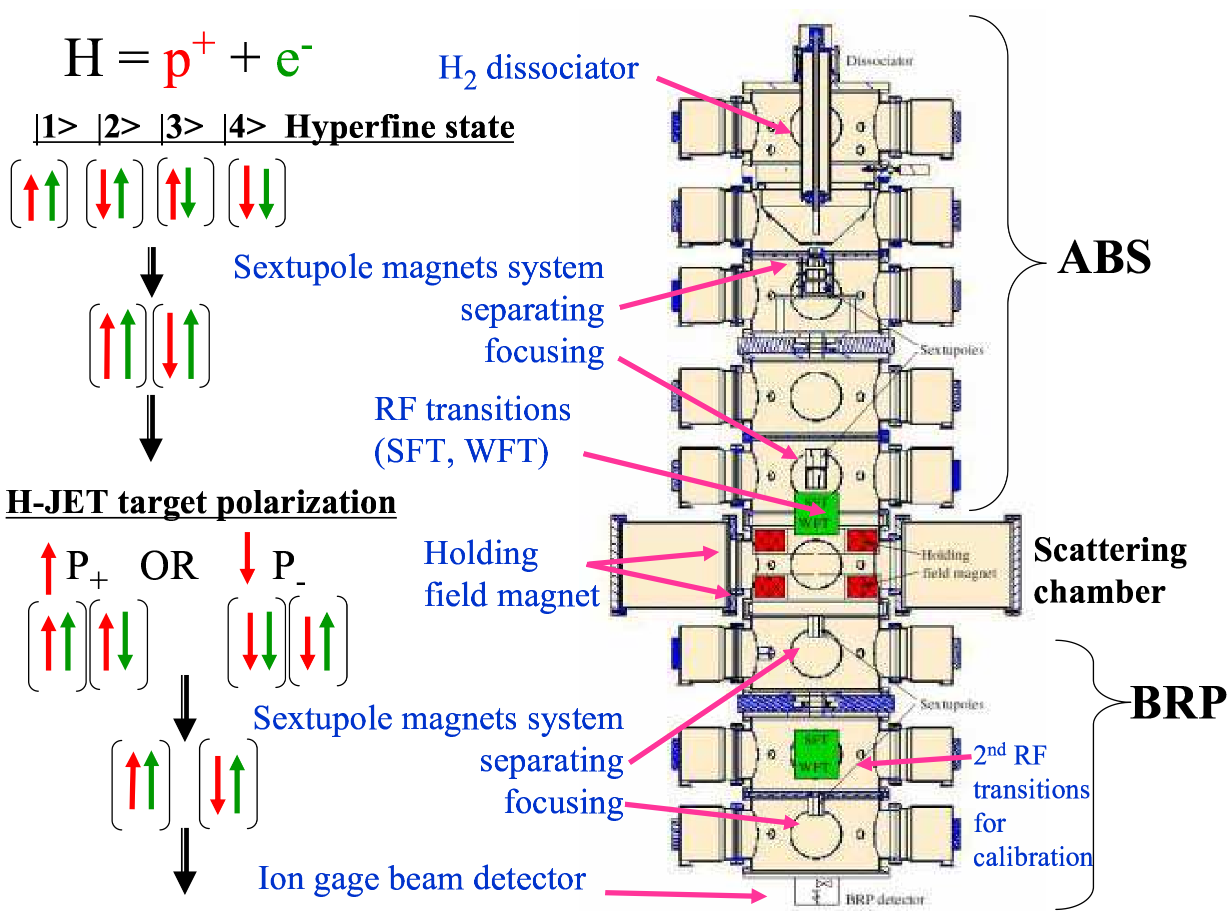

Figure 2.5: H-Jet system overview

Atomic Beam Source (ABS)

The ABS part includes five vacuum chambers and five differential vacuum stage. The five chambers consisted of H_2 dissociator, the separation-magnets (six permanent sextupole magnets), focusing-magnets (two permanent sextupole magnets), RF-transitions. The magnets are well aligned to the center of each chamber.

H$_2$ dissociator The principle for the polarized hydrogen atom is described below. H$_2$ molecules are dissociated to two hydrogen atoms by passing through RF-cavity (RF 21.6 MHz, 250 300W). The S-wave ground state of hydrogen atom is split by hyperfine states :

$$\begin{aligned} |1> &= |\uparrow\ ;+> \\ |2> &= \cos\theta|\uparrow\ ;-> + \sin\theta|\downarrow\ ;+> \\ |3> &= |\downarrow\ ;-> \\ |4> &= \cos\theta|\downarrow\ ;+> - \sin\theta|\uparrow\ ;-> \end{aligned}$$

where $\uparrow, \downarrow$ denotes the electron spin-state and $+, -$ denotes the nucleus spin-state. Both spin axes are parallel to the y-axis. And $\theta = \frac{1}{2}\arctan(\frac{B_c}{B})$, $B_c = \frac{E_{hfs}}{2\mu_B} = 50.7$ mT. E_{hfs} is the zero field hyperfine splitting. The populations of four hyperfine states are called n_1, n_2, n_3 and n_4, respectively. Figure 2.6 shows the energy levels of the four hydrogen hyperfine states as a function of applied magnetic field. The atomic-beam exiting the dissociator consists of nearly equal populations of hyperfine states, $n_1 = n_2 = n_3 = n_4$.

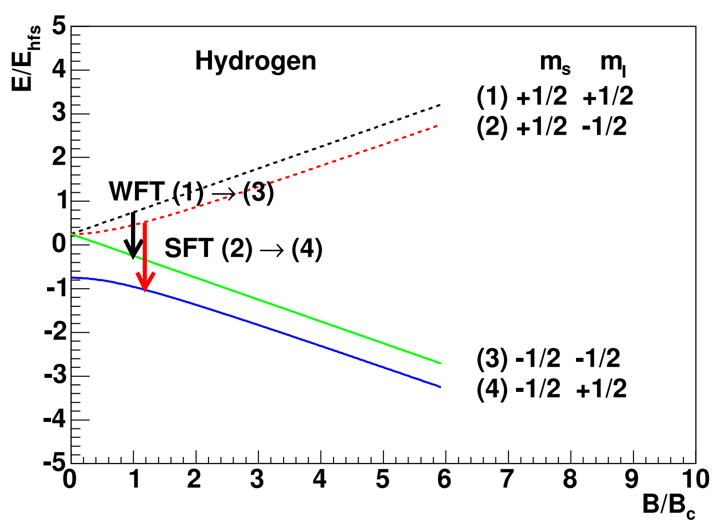

Figure 2.6: Energy level diagram for hydrogen. Energy is measured in units of E_{hfs}, the zero field hyperfine splitting. Magnetic field is measured in units of $B_c = 50.7$ mT.

Separation and Focusing magnets The inhomogeneous field acts as a Stern-Gerlach apparatus separating the atomic-beam by electron spin projection. The field strength of the separation magnet B is typically $1.6 \sim 1.7$ T. Therefore, θ in Equation (2.8) is almost zero. The four hydrogen hyperfine states become :

$$
\begin{aligned}
|1> &= |\uparrow\,;\,+> \\
|2> &= |\uparrow\,;\,-> \\
|3> &= |\downarrow\,;\,-> \\
|4> &= |\downarrow\,;\,+>
\end{aligned}
\tag{2.8}
$$

The separation magnets kick out hyperfine states $|3>$ and $|4>$ (electron spin down) and the atomic-beam exiting the last sextupole separation magnet consists of nearly equal populations, $n_1 = n_2$. Then, the *electron* spin is totally polarized to up. In case, if the $|3>$ or $|4>$ state atom goes through along the very center axis of the sextupole magnet, it would not be kicked out by magnetic field. Although the separating magnets, a set of six sextupole magnets, are aligned well to the chamber centers, but they do not aligned perfectly. Therefore, the residual atoms of state $|3>$ and $|4>$ are negligible. The focusing-magnets guide atoms in the state $|1>$ and $|2>$ to the center of scattering chamber.

RF-transitions Compact high frequency transitions are employed to create nuclear polarization of the atomic beam with high efficiency [49]. They consist of a resonator cavity in the case of the strong field transition (SFT) or a high frequency coil in the case of weak field transition (WFT). They are immersed in a static magnetic field whose strength and gradient along the atomic beam path can be individually adjusted. In principle the SFT exchanges populations of the state $|2>$ and $|4>$, the WFT exchanges populations of the state $|1>$ and $|3>$ as a function of the magnetic field. We adjust the each of magnetic fields that the SFT to move atoms in the state $|2>$ into $|4>$ and the WFT moves atoms from the state $|1>$ to $|3>$. The set of SFT and WFT is positioned between the fifth and the sixth chamber (just in front of the scattering chamber) as displayed in Figure 2.6. The ON/OFF combination of RF-transitions changes the polarity of the target.

⟨ TYPE-1 : SFT is ON and WFT is OFF ⟩ The SFT moves atoms from the state $|2>$ to $|4>$. Atoms in the state $|1>$ do not change the state. The populations of state $|1>$ and $|4>$ are nearly equal, while state $|2>$ and $|3>$ are nearly zero, $n_1 \cong n_4 \neq 0$ and $n_1 \cong n_4 \cong 0$. Thus, the *electron* spin is totally de-polarized, while the *proton* spin is now completely polarized to up direction ($P_+ = 1$).

⟨TYPE-2 : SFT is OFF and WFT is ON ⟩ The WFT moves atoms in the state $|1>$ to state $|3>$. Atoms in the state $|2>$ do not change the state. The populations of state $|2>$ and $|3>$ are nearly equal, while state $|1>$ and $|4>$ are nearly zero, $n_2 \cong n_3 \neq 0$ and $n_1 \cong n_4 \cong 0$. Thus, *electrons* spin is totally de-polarized, while the *proton* spin is now completely polarized to down direction ($P_- = -1$).

⟨TYPE-3 : Both SFT and WFT are ON at the same time ⟩ The SFT and the WFT move atoms in the state $|2>$ to $|4>$ and atoms in the state $|1>$ to $|3>$, respectively. The populations of state $|3>$ and $|4>$ are nearly equal, while state $|1>$ and $|2>$ are nearly zero, $n_3 \cong n_4 \neq 0$ and $n_1 \cong n_2 \neq 0$. Thus, *electrons* spin state changes to opposite sign, while the *protons* stays zero ($P_0 = 0$).

$\langle$**TYPE-4 : Both SFT and WFT are OFF** $\rangle$ Nothing is change. The *electron* spin state stays up, while *protons* spin state stays zero ($P_0 = 0$).

Although $P_z = 0$ state is obtained by two ways, TYPE-3 and 4, we preferred the operation that SFT and WFT are both ON (TYPE-3). The reason is discussed in section 2.2.2. The ideal target polarization is obtained if the 3 conditions are fulfilled:

- The efficiency of RF-transition are almost 100%,
- the atomic-beam entering the RF-transitions consists of nearly equal populations of hyperfine state $|1>$ and $|2>$, $n_1 \cong n_2$ and
- the presence of infinite holding magnetic field in the scattering chamber.

The efficiency of RF-transitions and the population of states are confirmed in the BRP and we will mention this later. We will mention about the holding magnetic field in the next.

Scattering Chamber

The polarization is determined by the strength of the holding field magnet located in the scattering chamber. In order to minimize the effect of the holding magnetic field on the recoil protons, we use The Nested Opposing Helmholtz-type Coils, whose fields are adjusted to keep the total y-axis (vertical) field integral along the proton paths close to zero, as shown in Figure 2.7.

Figure 2.8 shows the polarization of the four hydrogen hyperfine states as a function of applied magnetic field, $\frac{B_{hold}}{B_c}$.

This figure tells that the stronger B_{hold} we set, the higher the achievable polarization, even there are polarization saturation limit. But, in practice, the holding magnetic field was tuned to avoid De-polarization of atomic-beam by bunch field of the RHIC beam. Then, $\frac{\Delta P_\pm}{P_\pm} < 0.02$ were measured by comparison with and without RHIC beam conditions.

The holding magnetic field is measured $B_{hold} = 1200$ Gauss and high uniformity was achieved, $\frac{\Delta B_{hold}}{B_{hold}} \sim 5 \cdot 10^{-3}$ within ~ 4.0 cm center region. At the applied field, $\frac{B_{hold}}{B_c} = 2.37$, and the maximum achievable two-state atom polarization is estimated using Equation (2.9). Where,$\epsilon_{1\to3}$ and $\epsilon_{2\to4}$ are the inefficiency of the RF-transitions of WFT and SFT, respectively. In ideal case, the inefficiencies are zero and $\frac{n_2}{n_1} = 1$, the maximum achievable two-state atom polarization is ± 0.96.

$$\begin{aligned} P_+ &= \frac{1 + \frac{n_2}{n_1}\cos 2\theta - 2\frac{\mathrm{n}_2}{\mathrm{n}_1}\epsilon_{2\to4}\cos 2\theta}{1 + \frac{n_2}{n_1}} \\ P_- &= \frac{-1 - \frac{n_2}{n_1}\cos 2\theta + 2\frac{\mathrm{n}_2}{\mathrm{n}_1}\epsilon_{1\to3}}{1 + \frac{n_2}{n_1}} \\ P_0 &= \frac{-1 - \frac{n_2}{n_1}(1 - 2\epsilon_{2\to4})\cos 2\theta + 2\epsilon_{1\to3}}{1 + \frac{n_2}{n_1}} \\ 2\theta &= \tan^{-1}\frac{B_c}{B_{hold}} \\ \cos 2\theta &\sim 0.921. \end{aligned} \tag{2.9}$$

where, $\frac{n_2}{n_1}$, $\epsilon_{1\to3}$ and $\epsilon_{2\to4}$ are measured by BRP and we will describe in the next section.

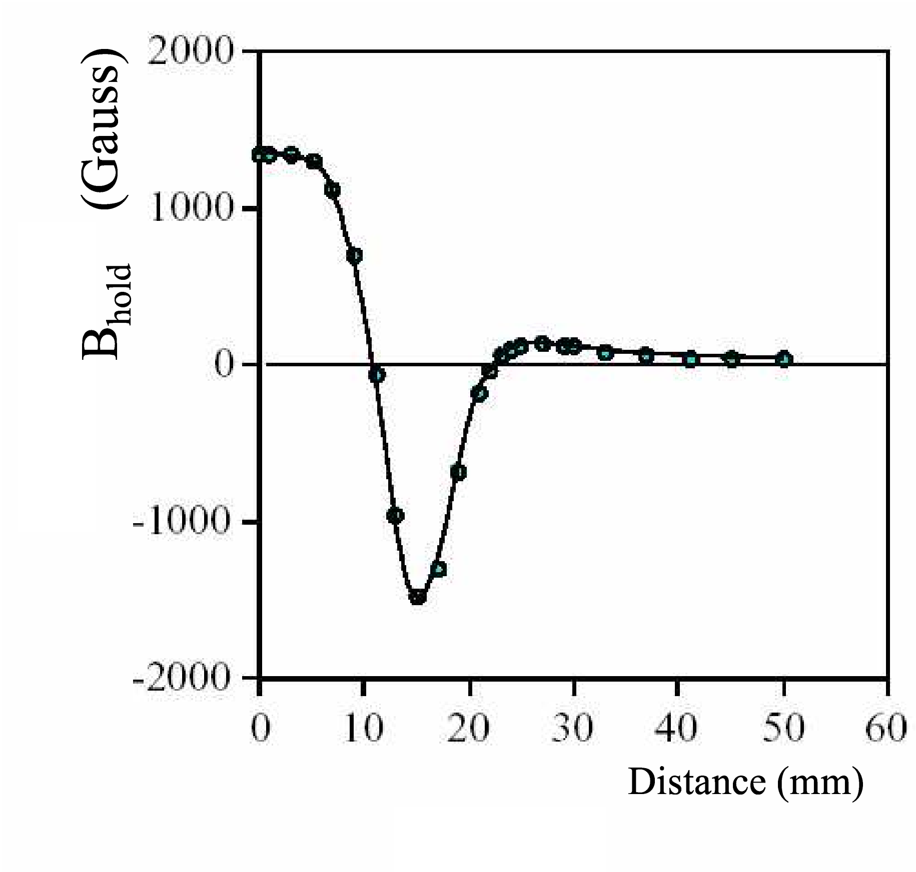

Figure 2.7: The holding magnetic field as a function of distance from the chamber center on the x-z plane. The fields are adjusted to keep the total y-axis (vertical) field integral along the proton paths close to zero. The Nested Opposing Helmholtz-type Coils are used.

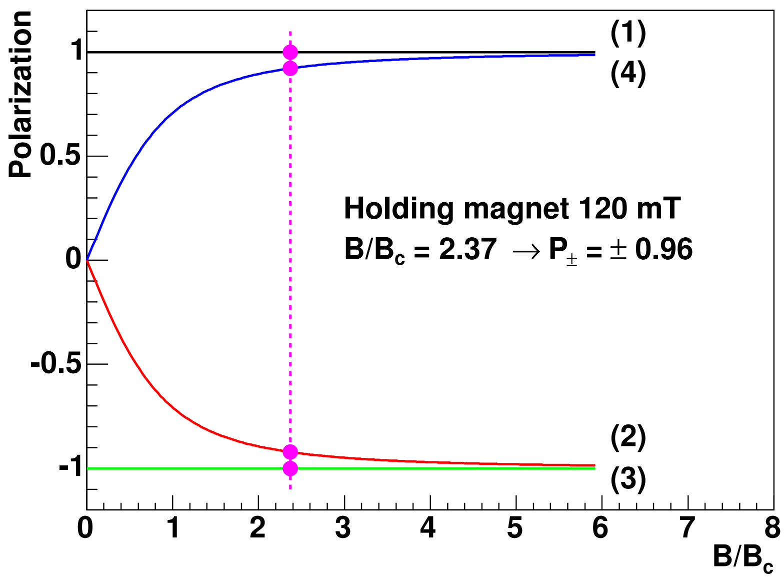

Figure 2.8: Holding magnetic field strength vs. proton polarization

Breit-Rabi Polarimeter (BRP)

BRP measures the transition inefficiencies $\epsilon_{1\to3}$ and $\epsilon_{2\to4}$ and the ratio of n_2/n_1. This part includes the sextupole magnet system (separating and focusing sextuple magnets), ion gage atomic-beam detector and the same type of SFT and WFT. In order to achieve the best accuracy of the measurement of RF-transition inefficiencies, SFT and WFT are used for the purpose of redundancy check.

As described in the previous section, the target polarization P_0 is obtained by two ways in principle.

- TYPE-3 : Both SFT and WFT are **ON**, the ion gage atomic-beam detector will measure the population $N_{\rm ON} = (n_1 \cdot \epsilon_{1\to3} + n_2 \cdot \epsilon_{2\to4})$.
- TYPE-4 : Both SFT and WFT are **OFF**, the ion gage atomic-beam detector will measure the population $N_{\rm OFF}$= $(n_1 + n_2)$.

Figure 2.9 displays the population of atom for several target spin-states. In this figure, $N_{\rm ON}$ is smaller than $N_{\rm OFF}$ the order of thousand. Thus $\epsilon_{1\to3}$ and $\epsilon_{2\to2}$ are measured to be ~ 0.003 or less. The measurement time of ion gage atomic-beam detector is proportional to the population of atom. During the experiment, the target polarity was changed periodically, every 5 minutes, to reduce the systematic errors of asymmetry measurements. Between spin-up and spin-down period, the spin-zero period was needed for system requirement but spin-zero period was *dead-time* for experimental purpose. To reduce *dead-time* during data taking period, the operation TYPE-3 was employed.

Results from commissioning RUN in 2004

Figure 2.10 displays a sample of the measured $P_\pm$ in 2004 commissioning run [51]. We had

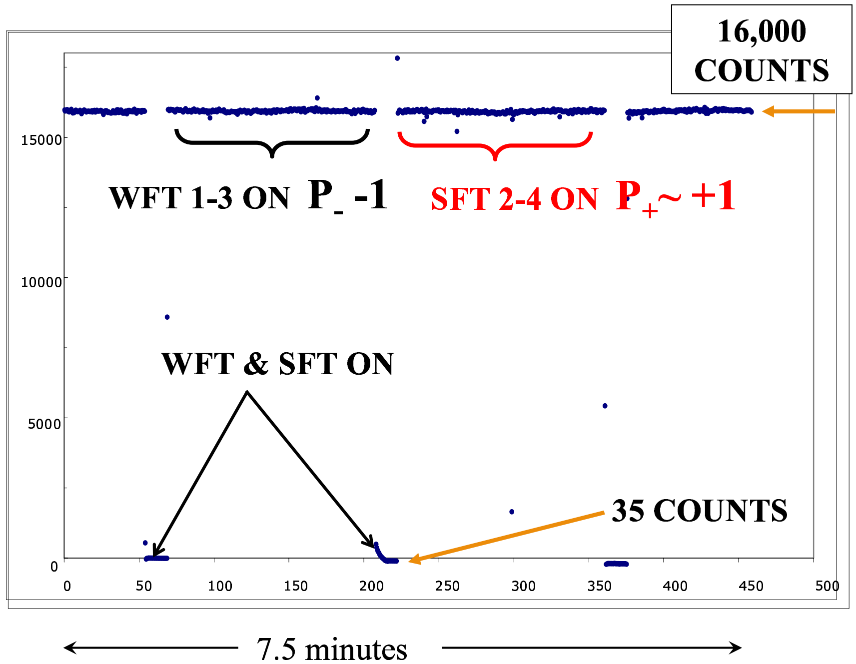

Figure 2.9: The population of atom for several spin-states measured by the ion gage atomic-beam detector.

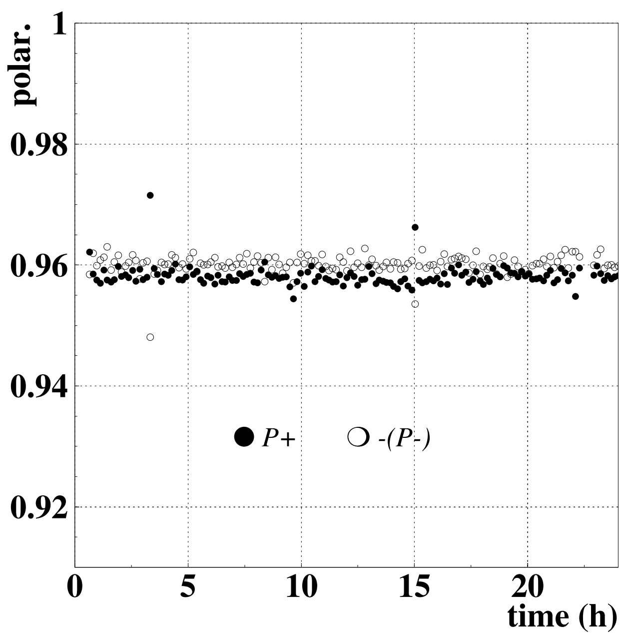

Figure 2.10: The jet-target polarization in 2004.

measured quite stable behavior over the whole 2004 run, mean values for nuclear polarization of the atoms:

$$|P_{\pm}| = 0.958 \pm 0.001. \tag{2.10}$$

Here we describe the dilution correction from hydrogen molecules. Actually, there were still some hydrogen molecules in the scattering chamber and the estimated was $H_2/H \sim 0.015$. This means that the dilution is about 3% in terms of hydrogen atoms. BRP can measure only **proton** polarization, therefore we have corrected the effect on the polarization from the hydrogen molecules.

Finally, the target polarization in 2004 commissioning run was $|P_{\pm}| = 0.924 \pm 0.018$.

Profile and Thickness of Atomic-beam

We have discussed about the target polarization in the previous sections. Here, the profile and the density of atomic-beam are mentioned briefly. The atomic-beam profile was measured with a 2mm in diameter compression tube. The results are displayed in Figure 2.11. At the center of the scattering chamber, the FWHM of the atomic-beam was 6.5mm.

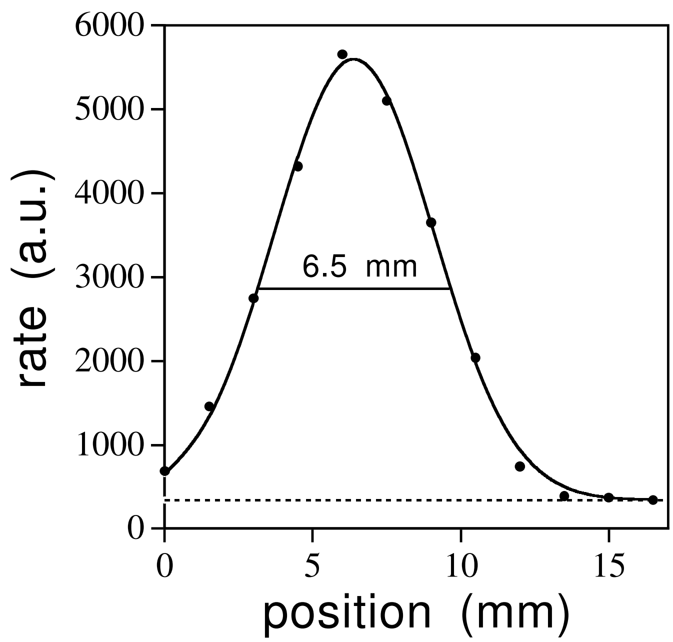

Figure 2.11: Atomic-beam profile at the target

The measured profile satisfied the designed value and guarantee the required angle resolution, $\Delta\theta_R \sim 5$ mrad, discussed in Subsection 2.1.2. Furthermore, we measured target profile by scanning with the RHIC beam and the recoil spectrometer during commissioning run period. We will mention this measurement in the later section, but the results of both ways agree very well.

The total atomic-beam intensity in the collision chamber was measured to be $(1.2 \pm 0.2) \cdot 10^{17}$ atoms/cm^2 [51]. Taking the measured atomic-beam intensity, velocity (1560 $\pm$ 50) m/s [50] and profile, the areal target thickness along RHIC beam axis was calculated to be $(1.3 \pm 0.2) \cdot 10^{12} \text{atoms/cm}^2$.

2.2.3 Recoil Spectrometer Setup

The spectrometer employed for the experiment was silicon detector to measure the kinetic energy of recoil proton precisely. We will look briefly at the overview of the recoil spectrometer at first. Figure 2.12 displays the picture of scattering chamber. The RHIC blue beam goes from left to right horizontally (along the x-axis) and the atomic-beam goes vertically (along the y-axis). The recoil protons come out almost perpendicular to the y-z plane and were detected by silicon detectors. The detectors were mounted on the flanges of scattering chamber as shown in Figure 2.13. Flanges are parallel to the y-z plane.

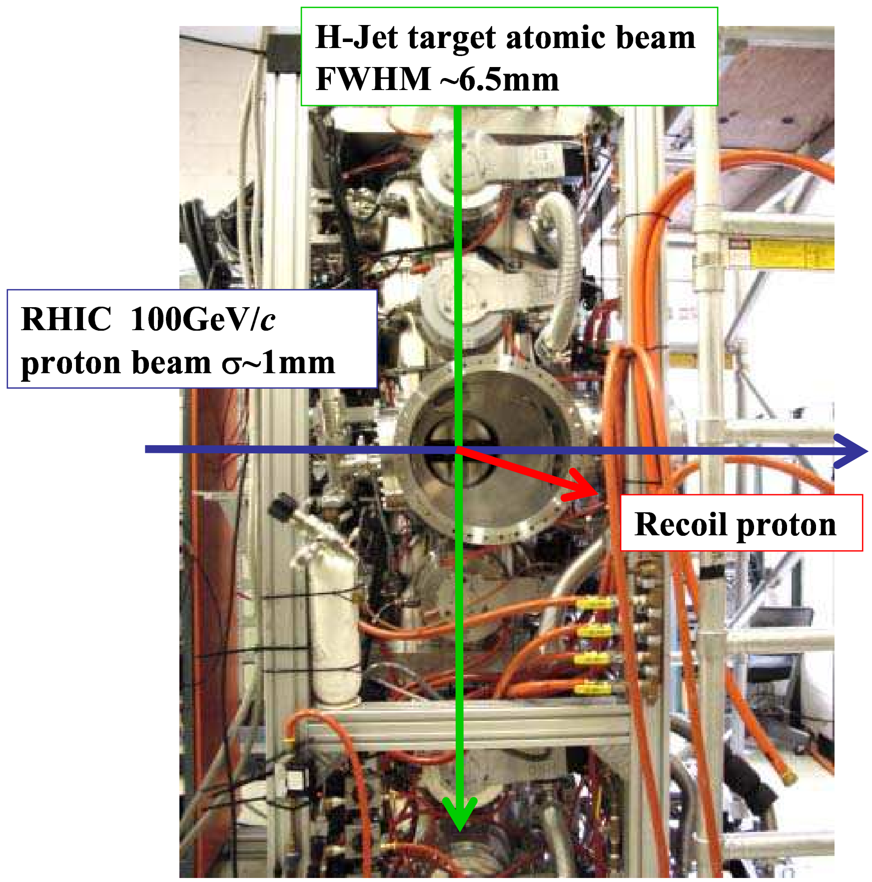

Figure 2.12: Relationships of the RHIC-beam and the jet-target atomic-beam directions superimposed on the scattering chamber.

The required resolutions for kinetic values have been discussed in Subsection 2.1.2. In this section, we will compare the kinetic values between the **required** and the **achieved** one-by-one.

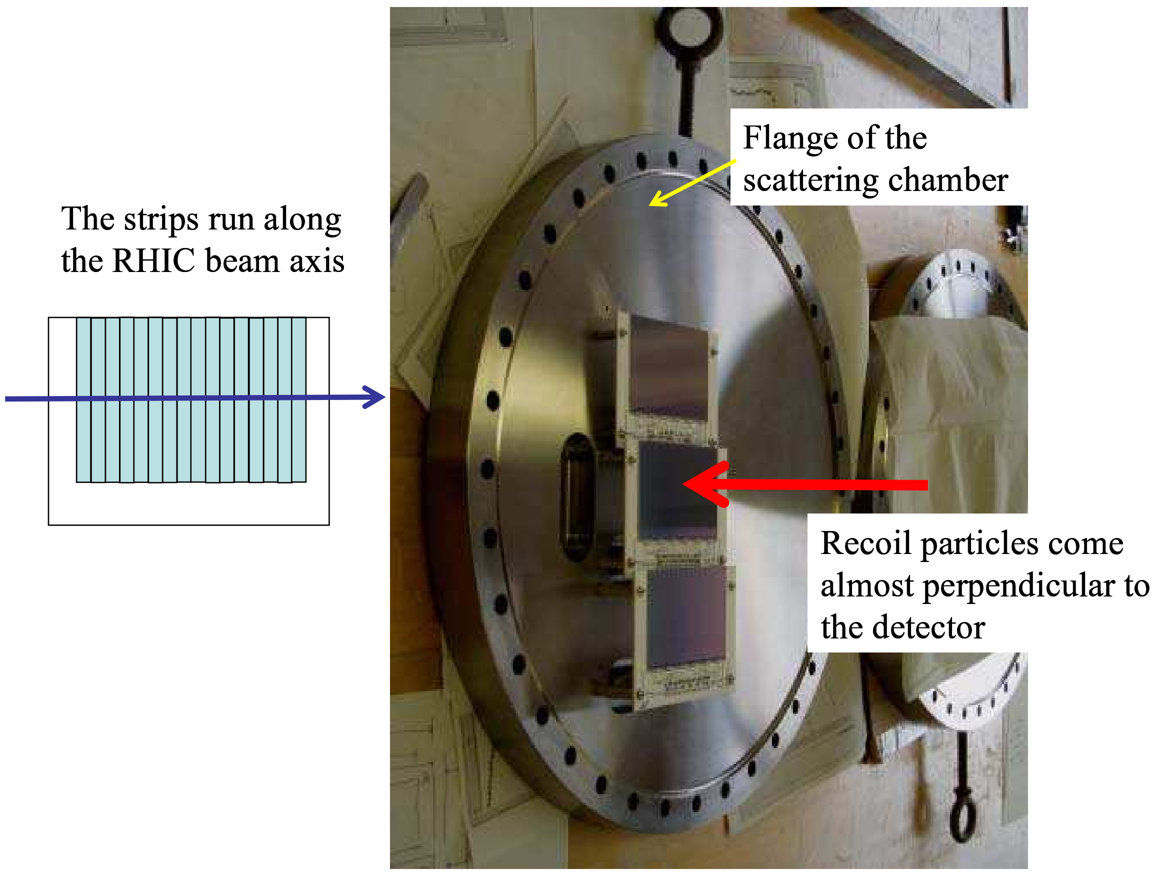

Figure 2.13: The silicon detectors mounted on the flange

Achieved acceptance and angle resolution

Taking account of the flight length $L = 0.8$ m and the required angular range and resolution, the objective size and fineness of the detector are obtained.

- The detector length along with beam direction should be more than 6 cm in order to cover the required angular range.
- The read-out pitch should be less than 6.4 mm in order to meet the required angular resolution.

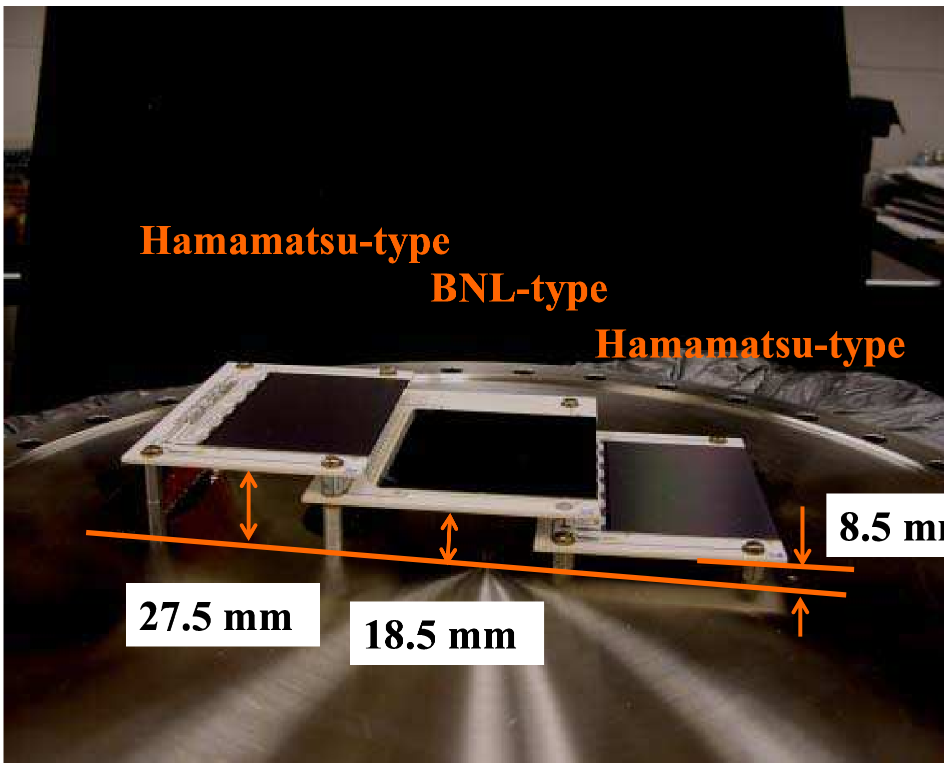

Figure 2.14: The picture of silicon detectors mounted on the one of the flange.

Figure 2.15 displays the schematic view of the atomic beam of the jet-target, the RHIC-beam and three-pairs of silicon detectors. Three pairs of silicon detectors were located in left-right sides to gain the azimuthal acceptance for statistics. One arm covered 0.205 rad in azimuth angle.

Figure 2.16 displays the picture of silicon detectors mounted on one side of the flange. We used two different types of silicon detectors and we will discuss details in Subsection 2.2.3.

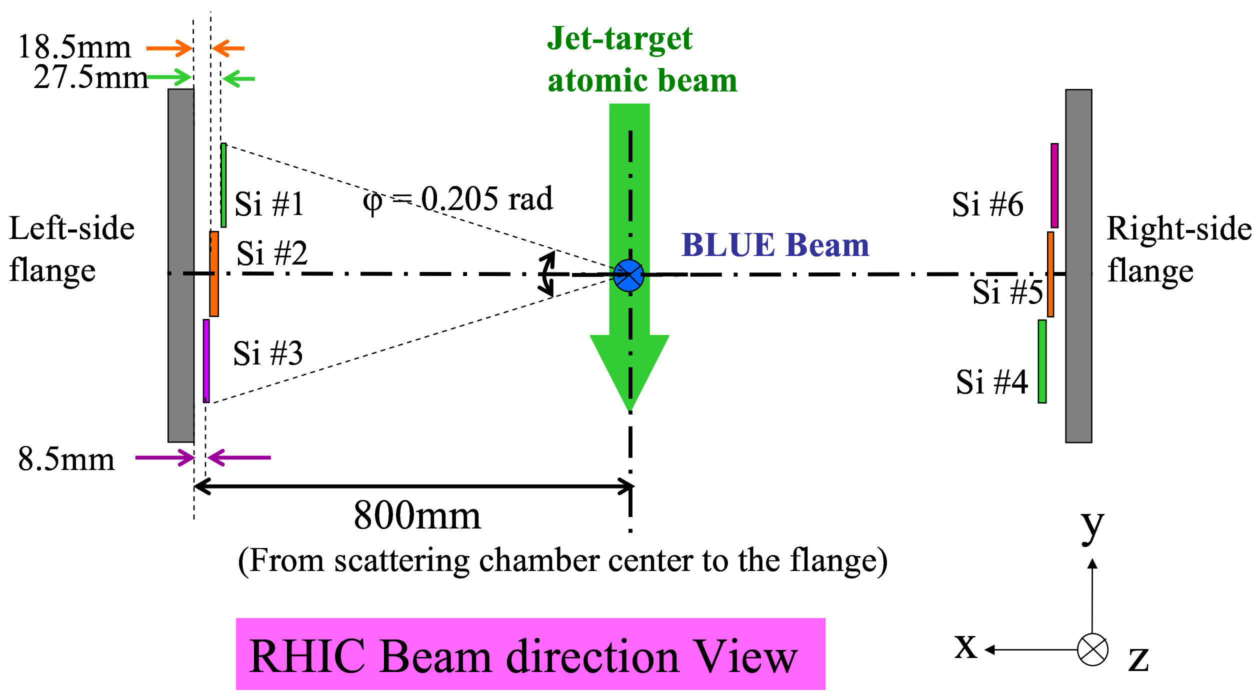

Figure 2.15: Schematic view of the atomic-beam of the jet-target, RHIC-beam and six silicon detectors

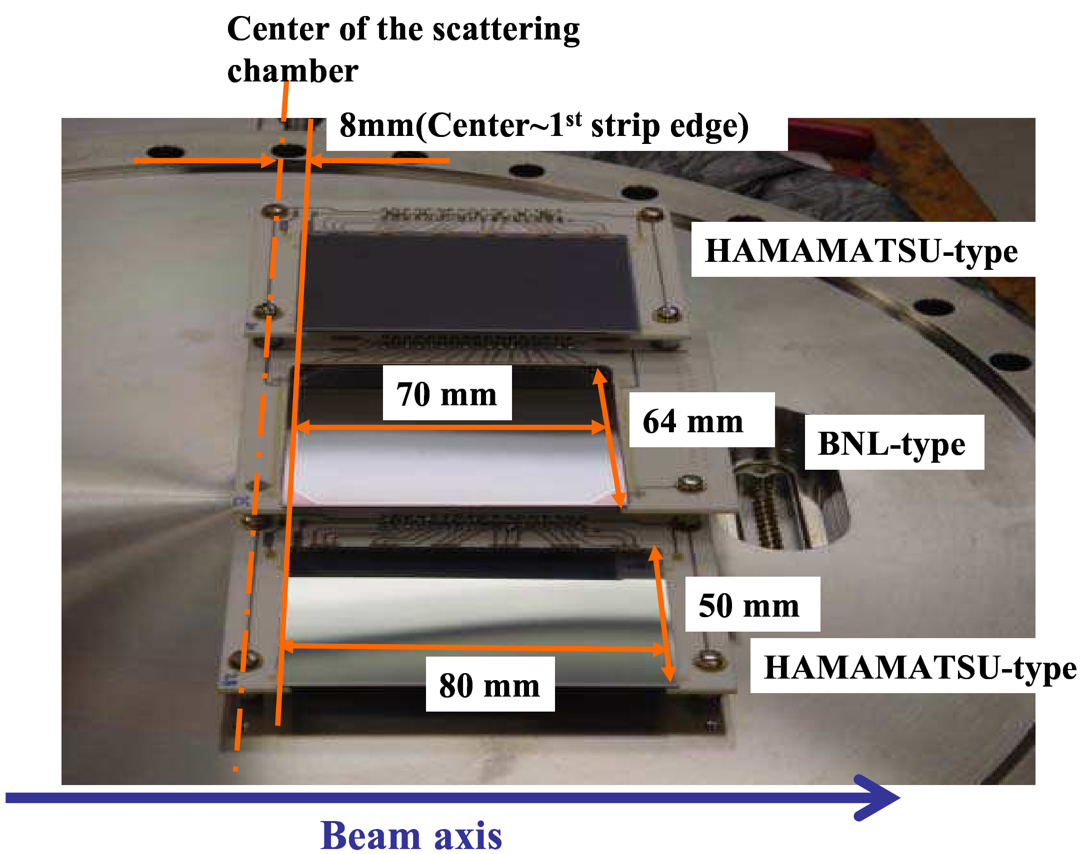

Figure 2.16: The silicon detectors mounted on the flange

Figure 2.17 displays the schematic view of three pairs of silicon detectors from top view. The silicon strip runs along the incident RHIC-beam direction (we set it as the z-axis). Therefore, the hit position, Z, is obtained from the channel-number.

$$Z = Z_0 + channel\# \times dZ$$

where, $Z_0 = 8$ mm, $dZ = 4$ mm (See Figure 2.17). The recoil angle and its resolution are obtained as:

$$\theta_R = \frac{Z}{L}, \tag{2.11}$$

$$\Delta\theta_R = \frac{dZ}{L}, \tag{2.12}$$

where, $L \sim 800$ mm (See Figure 2.17). Thus the acceptance of one arm is $10 \sim 100$ mrad in recoil proton angle. and each read-out channel covered 5.5 mrad. And the recoil angle resolution is estimated to be 5.5mrad from readout single channel size.

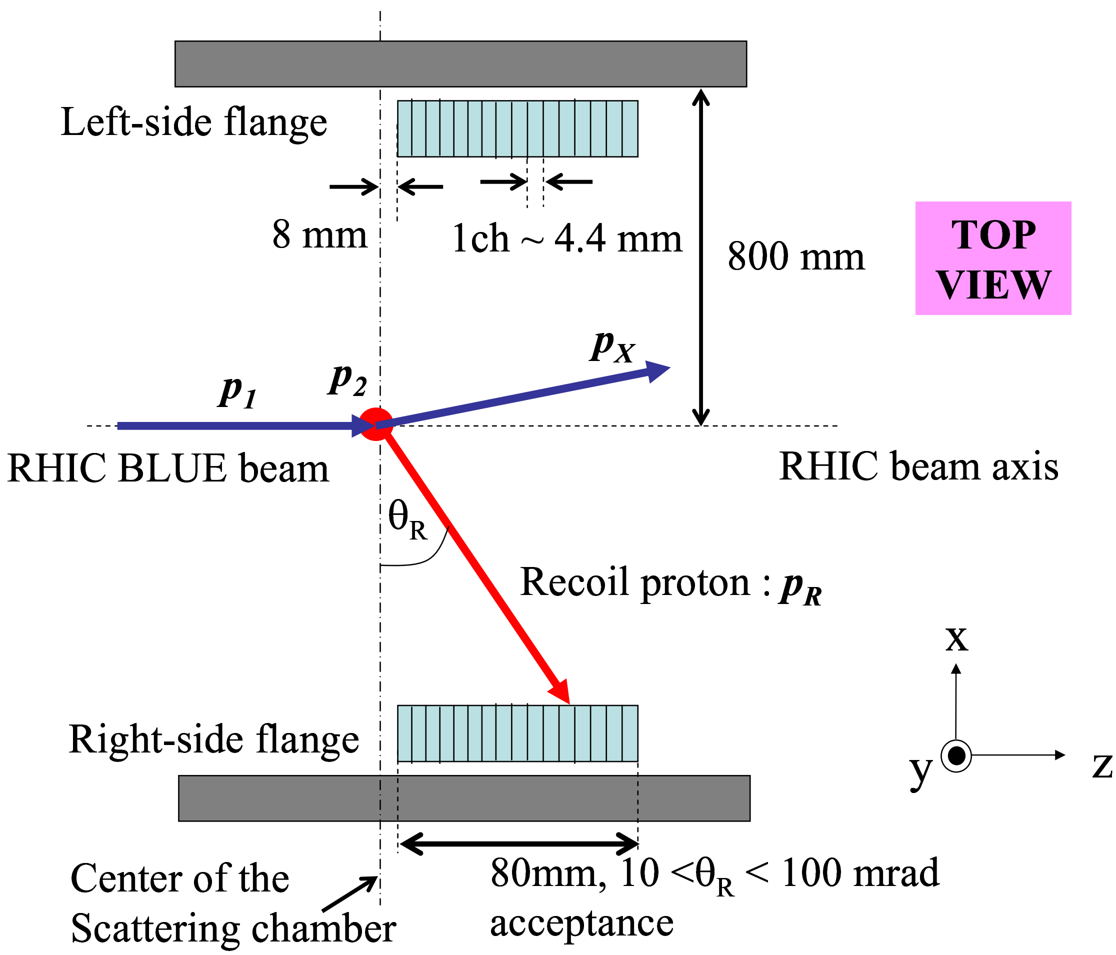

Figure 2.17: Schematic of scattering chamber from TOP VIEW

Actually the measured angle θ_R has some offset value because of the mis-alignment of the target chamber by θ_{align}. In addition to θ_R for low energy recoil proton is deflected the Holding-Magnet field, θ_{Mgnt}. Therefore, the *correct* recoil angle should be:

$$\theta_R = \frac{Z}{L} + \theta_{align} + \theta_{Mgnt} \tag{2.13}$$

The size of θ_{align} and θ_{Mgnt} are less than 5 mrad, respectively. The details are discussed in Appendix A.8. In practice we do not need to use θ_R for the missing particle identification and the hit position (channel number) data are enough. These discussions are mentioned in Subsection 3.5.2.

Silicon detector performance

As we have mentioned in Figure 2.16, two out of three pairs of silicon detectors (Si #1-4, 3-6) were fabricated by the Hamamatsu Photonics, K. K. The other pair of silicon detectors (Si #2-5) were fabricated by the BNL Instrumentation Division. We will discuss about the silicon properties Main characteristic are summarized in Table 2.2. The surface area were almost same but the strip size and detector thickness were different between Hamamatsu-type and BNL-type. The biggest difference was the thickness of the entrance window, which is the non-active volume on the surface of the silicon. This is the surface structure of the silicon detector which consists of read-out aluminum-pads , SiO_2 and Si.

Figure 2.18 depicts the cross-section of Hamamatsu-type.

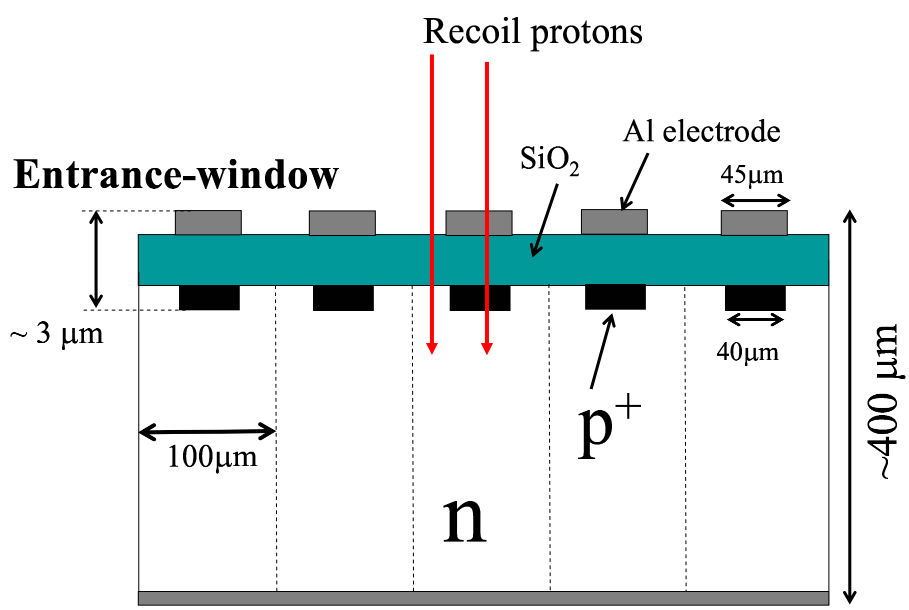

Figure 2.18: Cross section of Hamamatsu-type silicon. The entrance-window is the non-active volume on the surface of the silicon and consists from SiO_2, Al electrode and p^+.

	BNL (Si $\#2$ and 5)	Hamamatsu (Si $\#1, 3, 4$ and 6)
strip size (width $\times$ length)	1.09 mm $\times$64 mm	100 μm $\times$50 mm
Number of strip	64 strips	720 strips
effective detector size	70 mm $\times$ 64 mm	72 mm $\times$ 50 mm
Mechanical thickness	$\sim$ 450 μm	$\sim$ 400 μm
Entrance window thickness	(p^+ implant + SiO_2) ~ 0.15 μm	p^+ implant $\sim$ 1 μm SiO_2 $\sim$ 1 μm, Al $\sim$ 1 μm
Depletion voltage	$\sim$ 160 V (measured)	$\sim$ 90 V (given)
Operating voltage	180 V	200 V
Connection type with Pre-amplifier	DC coupled	AC coupled
Number of read-out channel (ch.)	16 ch. (4 strips / 1 ch.)	16 ch. (40 strips / 1ch.)
Width of single read-out channel	4.38 mm	4.44 mm
Capacitance /1channel	80 $\sim$ 100 pF (measured)	$\sim$ 60 pF (given)
Leak current /1channel	$\sim$ 10 nA at 180 V	$\sim$ 10 nA at 200 V
Yield rate	25% (Only 2 of 8 wafers are acceptable quality)	100%

Table 2.2: Characteristics of BNL-Type and Hamamatsu-Type silicon detectors

Because the deposit energy in the entrance-window can not be measured, the thinner entrance-window type is preferred. BNL-type has quite thin entrance-window and ideal to detect low energy particles of order of few MeV. This is a quite unique technology for over the world. At the beginning, we planed to use the BNL-type silicon detectors only. Although the thin entrance window with small size (10 mm $\times$24 mm) was produced and worked very well, it was difficult to make a bigger surface detector keeping the uniformity of each layers. Because of the thickness of the entrance window, the dedicated treatments for energy calibration were needed for Hamamatsu-type detectors. The details of discussion will be presented in Subsection 3.3.1.

Summary for Recoil Spectrometer Setup

The spectrometer employed for the experiment was silicon detector to measure the kinetic energy of recoil proton precisely. We have discussed the required and achieved acceptances. The range of covered recoil angle were $10 < \theta_R < 100$ mrad for two pairs (Hamamatsu-type) and $10 < \theta_R < 87.5$ mrad for one pair (BNL-type) for one-side. The acceptance of azimuthal angle was 210 mrad for one-side. Although we used two different types of silicon detector, the resolution of read-out channel of recoil angle were same: 5mrad.

2.2.4 Read-out Electronics

This section describes the overview of read-out electronics and the detailed silicon signal performance by single read-out channel. Although we were forced to employ two different types of silicon detector, we managed to make their performances similar. Specifically, it is preferable that the raw-signals of two different detectors are similar in terms of voltage and waveform in order to avoid the complications in the read-out electronics chain. The basic characteristics of silicon detectors, like depletion voltage, capacitance, etc., are mentioned in Appendix A.4.

Read-out Signal Flow

Figure 2.19 displays the outline of read-out signal processes.

Inside the RHIC Tunnel recoil protons were detected by the silicon detector at IP12. The deposit energy was converted to the electric charge in the silicon detectors. And the electric charge was converted to the voltage in the preamplifier. The preamplifier was mounted on the Front-End-Electronics Board which located outside of the scattering chamber.

Counting-house (Outside of the RHIC Tunnel) The signal output from preamplifier was transferred to the counting-house through twisted cables. The counting-house was apart from the H-Jet target location, $\sim$ 50 m. By use of twisted cables, the ground was isolated between inside and outside of the RHIC tunnel. The signal was shaped by the shaping-amplifier and processed by the Wave Form Digitizer (WFD). Inside of the WFD, the waveform analysis was done by the on-board Field Programmable Gate Array (FPGA) chip. These results were used for on-line analysis. The event-by-event waveform was recorded in the DAQ-PC for off-line analysis.

The signal processing is described step-by-step in the following subsections.

Front End Electronics in RHIC Tunnel Six silicon detectors were mounted on the left-right sides flanges of scattering chamber. Each detector had 16 read-out channels and there were 96 channels in total. Each output signal from silicon was pre-amplified at the Front-End-Electronics (FEE) Board. Sixteen preamplifier chips were mounted on one FEE. All 16 read-out signals from one silicon detector were processed by one FEE. Figure 2.20 displays the picture of FEEs.

Figure 2.21 display the read-out schematic diagram of silicon detectors. We employed two different types of silicon detectors (BNL-type and Hamamatsu-type) which we did not plan in the first design. Because the size and thickness of two silicon detectors were not same, so that the capacitances per single read-out channel were different. The diagram were also bit different; The connection between silicon detector and preamplifier was DC-coupled for BNL-type and AC-coupled for Hamamatsu-type. Because the silicon signal was amplified by charge-sensitive preamplifier, the output voltage and signal decay-time did not depend on the detector capacitance but the characteristics of preamplifier essentially and measured to be 3 μs. The preamplifier was needed to be discharged completely before the next signal comes. The overall event rate was estimated to be $\sim$ 30 kHz, that is, the event comes every 30 μs. Thus we confirmed that the preamplifier is discharged fast enough.

On the other hand, the signal rise-time would change depending on the capacitance of read-out channel. The larger capacitance read-out channel tends to result in a long rise-time in general. But we verified that the preamplifier does not change the output waveform much, even from the

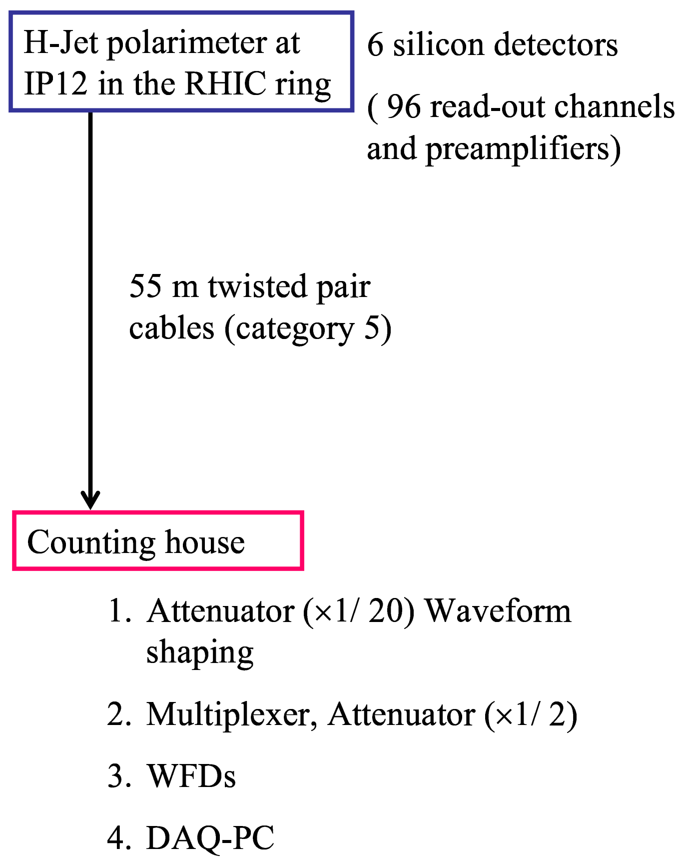

Figure 2.19: Read-out electronics outline

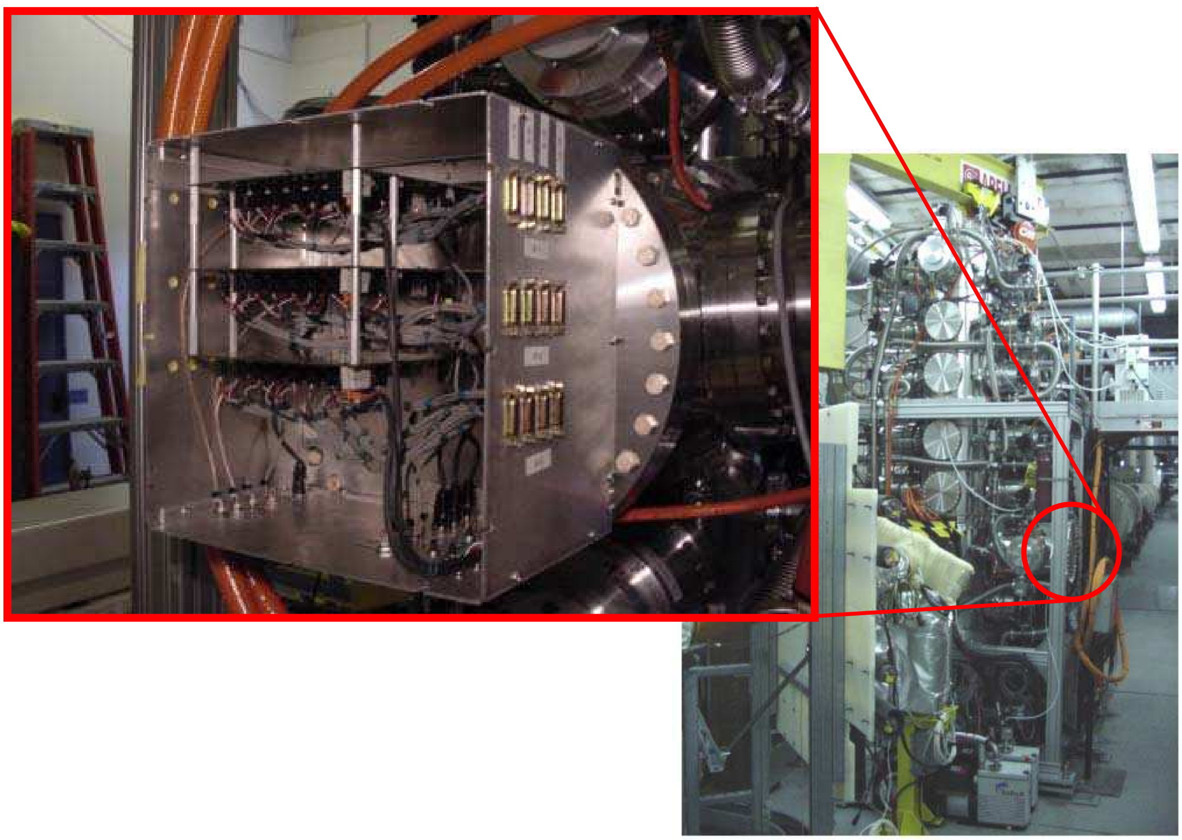

Figure 2.20: Picture of FEE Board including preamplifier chips.

different read-out capacitances . This fact was very fortunate for us because we do not need to care about the capacitance dependence for output signals.

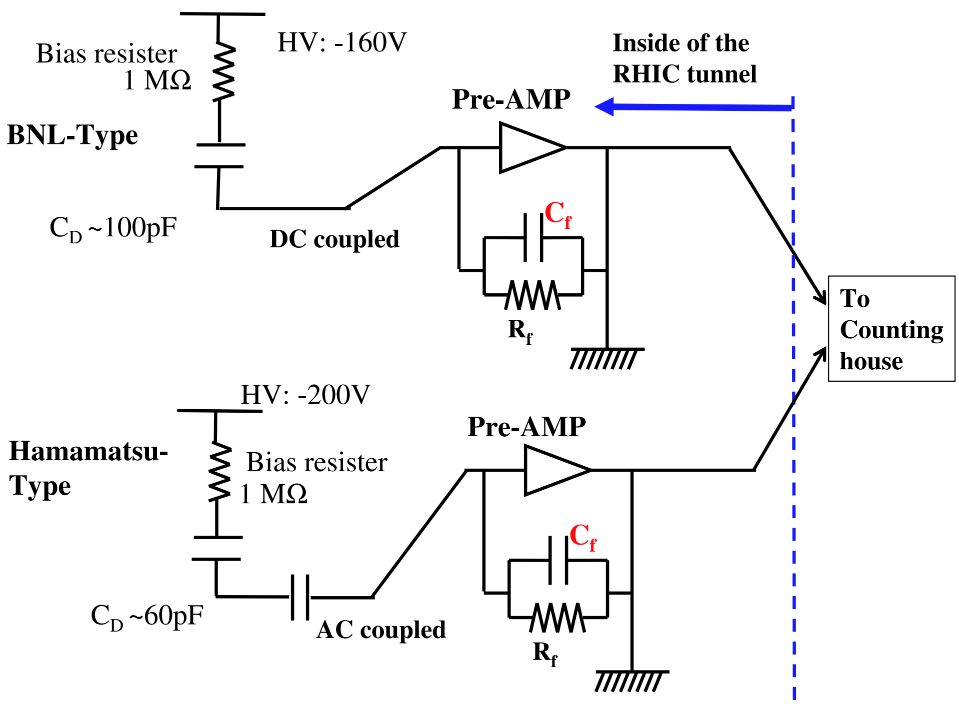

Figure 2.21: Schematic of the silicon detectors and the preamplifier

Figure 2.22 displays the comparison of the output signals from preamplifier between BNL-type and Hamamatsu-type. Although the detector characteristics between two different types were not completely same, the rise-time of them are similar $\sim$ 27.5 nsec for both cases fortunately.

Signal Shaping in the Counting House The output signal from preamplifier was transported to the counting-house through the twisted pair cables. The counting-house was apart from IP12 $\sim$ 50 m. The ground line was isolated between inside and outside of the RHIC tunnel. The signal was shaped and attenuated in order to adjust to the input requirements of the WFD.

One factor in the choice for time constant of shaping circuit is the charge collection time in the detector being used. To reduce pile-up events, it is important to keep these time constants short so that the shaped waveform can return to the baseline as quickly as possible. On the other hand, once the shaping time constants become comparable with rise-time of the pulse form the preamplifier, the input network no longer appears as step voltage and some of its amplitude is lost. This loss is called the ballistic deficit and can be avoided only by keeping the time constants long compared with the charge collection time in the detector.

Figure 2.23 displays the equivalent circuit of the shaping amplifier of FWHM 12 nsec. This shaper was used in 2004 run.

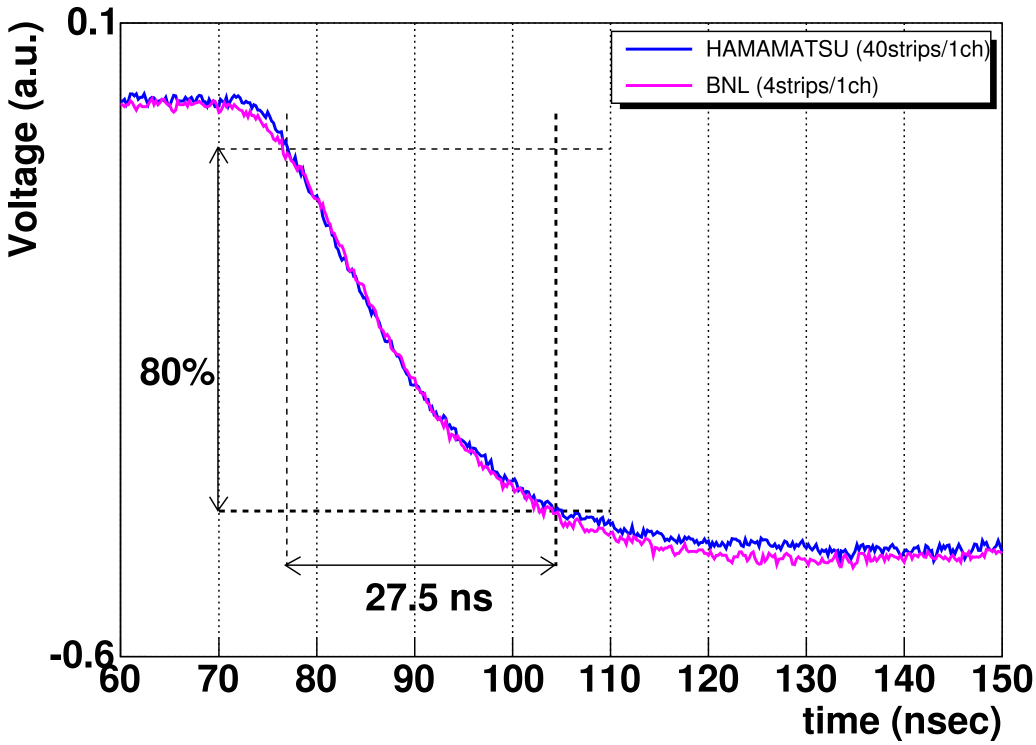

Figure 2.22: Rise-time comparison between BNL-type and HAMAMATSU-typ2

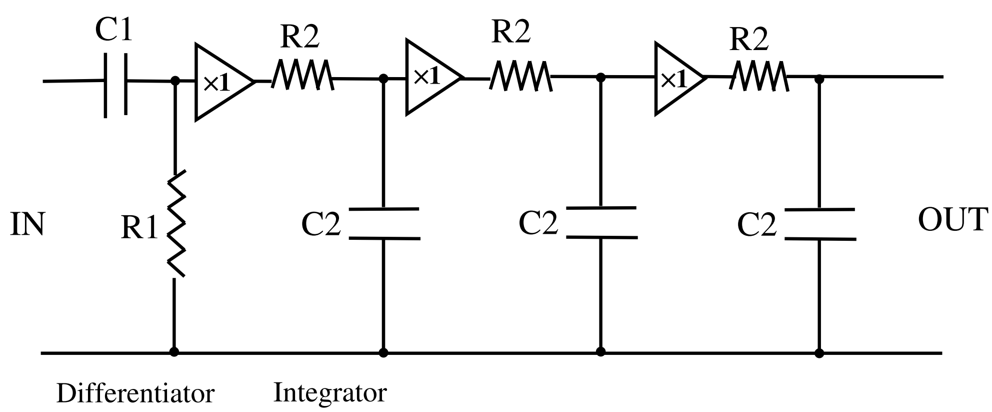

Shaper $\tau_s = C1 \times R1 = C2 \times R2 = [12ns]$

$E(t) = E0 \times (t/\tau_s)^n \times \exp(-t/\tau_s) \quad n=3$

(Unipolar type)

Figure 2.23: Equivalent circuit of the shaper : CR-(RC)^3

If we input step function into this shaper, the output shape can be express as below:

$$V_{out}(t) = V_{peak} \cdot \frac{t}{\tau_s}^3 \cdot \exp(\frac{-t}{\tau_s}) \tag{2.14}$$

$$\tau_s = C_1 \cdot R_1 = C_2 \cdot R_2 \tag{2.15}$$

The typical signal samples of *before* and *after* shaping are shown in Figure 2.24. The red waveform is *after* shaping.

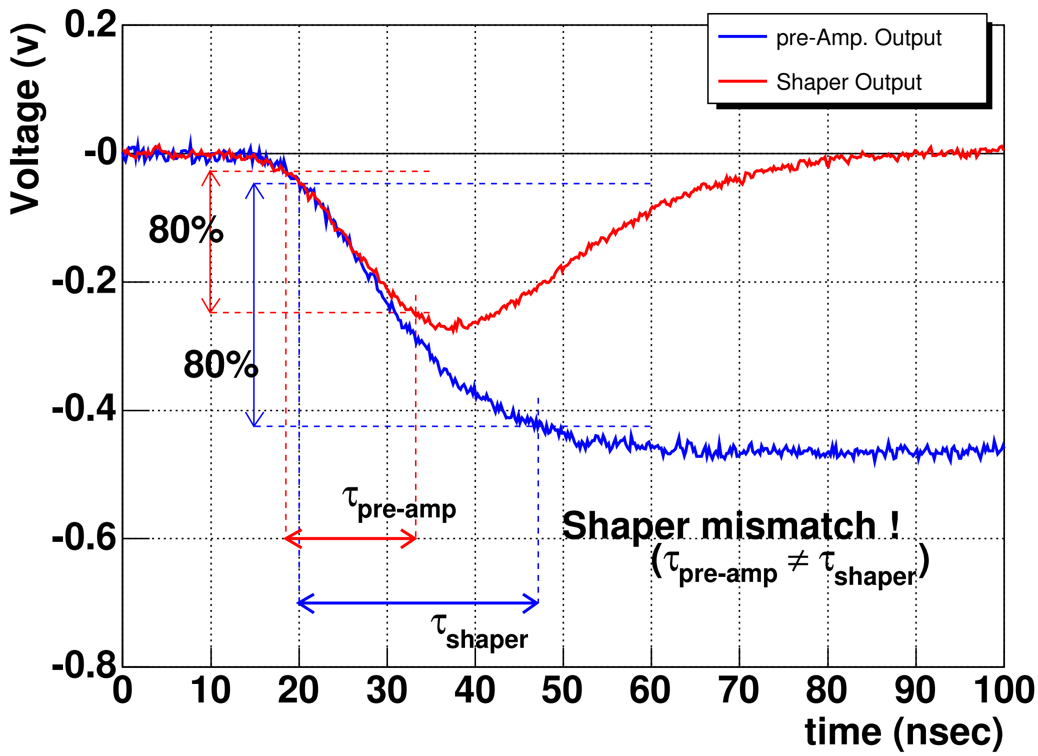

Figure 2.24: Explanation for shaper mismatching

Actually, this pulse shaping amplifier was not suitable for the output signal from preamplifier. The rise-time comparison between *before* and *after* pulse-shaping amplifier is also shown in the figure. This mismatch might cause the deterioration of energy resolution. Unfortunately, the suitable one was not ready for the 2004run, then the dedicated waveform study was needed to evaluate the waveform quality by off-line analysis (see Subsection 3.2.1) [2].

Data Acquisition System

The WFD modules recently developed as a deadtime-less DAQ system for the *p*C polarimeter at Yale University. Because of the limited number of the WFD, data-taking for this experiment was done alternatively with the *p*C polarimeter. The pulse shapes are digitized at the equivalent

[2]Basing on these studies, we have already replaced the shaping amplifier to suitable one from 2005run.

Data source	Contents
Silicon detector	channel ID#, Waveform data
FPGA outputs	maximum amplitude, integral for whole gate width, time at maximum
Beam (CDEV)	bunch ID#, bunch fill-pattern, bunch pol.-pattern (up/down/"0") Revolution number, Wall current monitor (WCM) [53]
H-Jet Target	polarization state (up/down/"0")

Table 2.3: Summary of the storage contents into the DAQ-PC

frequency of 420 MHz and analyzed inside the modules, providing the recoil proton deposit energy and time of flight as on-line results.

The WFD is a CAMAC module hosting 4 independent channels with common storage SDRAM (64 MByte) and CAMAC control circuitry as shown in Figure 2.25. In each channel the input signal is split into three, two of which are delayed by $\frac{1}{3}$ and $\frac{2}{3}$ of the ADC digitization period. We call them RGB. Three 8-bit ADCs (AD9483[3]) synchronously start conversions at 140 MHz resulting in triple equivalent digitization frequency. All waveform analysis is done inside the Virtex-E Xilinx FPGA chip at 70 MHz clock frequency.

The block diagram of analyzing circuits in the FPGA is shown in Figure 2.26. The input signal passes through a digital filter for noise reduction and partial compensation for different amplification of delayed sub-channels. A level trigger is used to determine the presence of a significant signal in a particular bunch crossing period, and if the signal is not detected, the ADC values are used for baseline calculations. The baseline is determined individually for all three sub-channels to compensate for different amplifier offsets and is averaged over 16 latest bunch crossing periods with no significant signal. The baseline is then subtracted and the signal is stored in a first-in first-out (FIFO) memory, from which it can be directly read out as a waveform or taken for further analysis. The analysis is of the conveyor type and takes up to 5 stages, each stage corresponding to a sequential bunch crossing. On the first stage the whole waveform is used to define the signal amplitude (maximum), integral and time at maximum. The second stage implements $\frac{1}{4}$ constant fraction discriminator (CFD) based on the amplitude value defined at the first stage. These analyzed values in the FPGA were used as on-line results. Waveform data was used for off-line analysis which is discussed in chapter: analysis. The FPGA keeps track of the bunch and revolution numbers, as well as of bunch polarization pattern. In addition to these contents, the H-Jet target polarization status was also tracked by the FPGA. The contents were read out and stored to the computer synchronized with H-Jet polarization status (+/0/-). The limiting the maximum event rate to $3 \cdot 10^6$ s^{-1} per channel was come from the speed of transfer to on-board storage memory by FIFO memory.

Record Data The storage contents are shown in Table 2.3. The recorded data size were about 250 MByte per 1 hour data-taking.

The on-line data from silicon detectors were used for keeping track data quality. Waveform data for event-by-event were used for further detailed analysis which is discussed in section 3.2.1.

[3]The specification is found at $<$ http://www.analog.com$>$

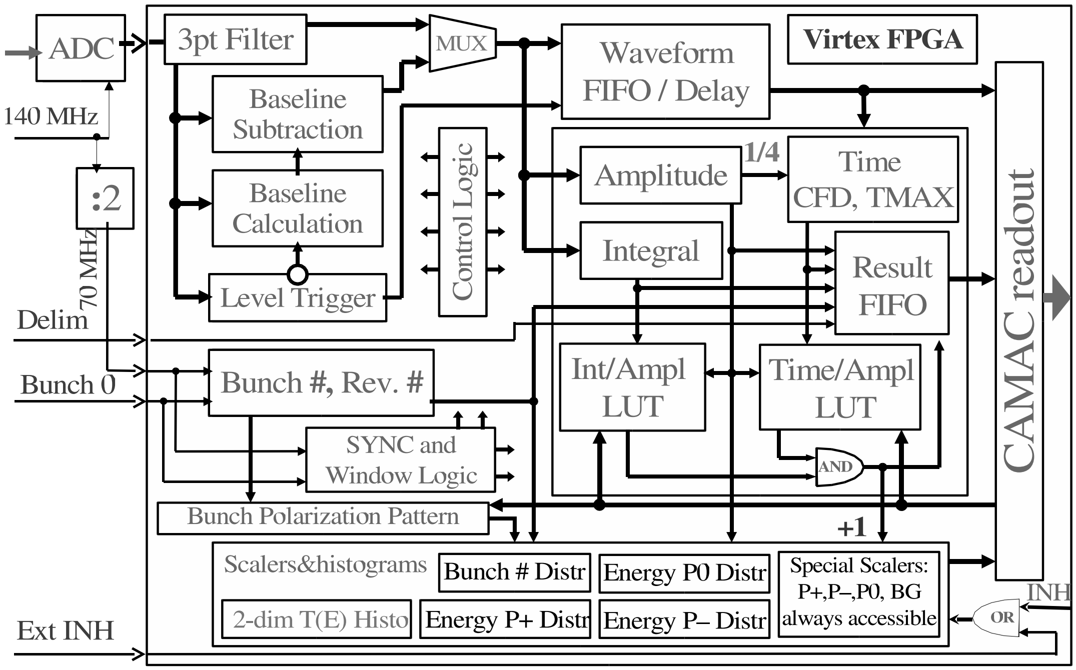

Figure 2.25: Block diagram of the WFD modules

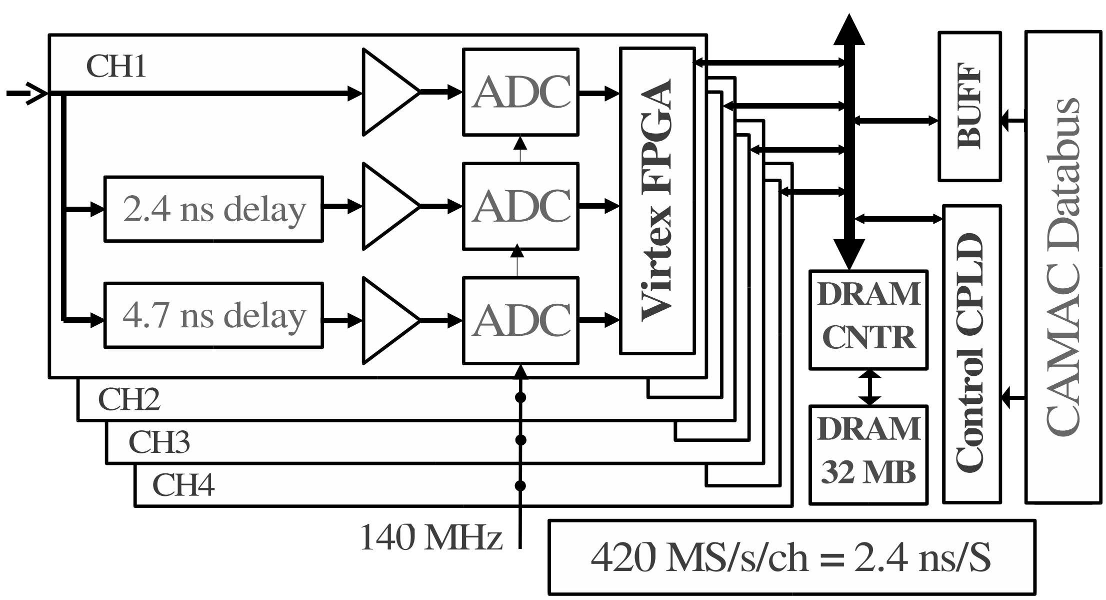

Figure 2.26: Simplified block diagram of one WFD channel

2.3 High-energy Polarized Proton Beam

The Relativistic Heavy Ion Collider (RHIC) storage rings are 3.83 km in circumference and are designed with six interaction points (IP's), where beam collisions are possible. The two independent storage rings are referred to the blue-ring and the yellow-ring respectively. In addition to heavy ion collisions, the RHIC also collide intense beams of polarized protons. The RHIC is the first and only polarized proton-proton collider in the world.

2.3.1 RHIC-AGS Complex as a Polarized $p+p$ Collider

The study of high energy polarized protons beams has been a long term program at BNL with the development of polarized beams in the Booster and the Alternating Gradient Synchrotron (AGS) rings for fixed target experiments. The capability of polarized proton beams have been extended to the RHIC machine. The RHIC was designed to provide collisions of polarized protons at a maximum beam energy of 250 GeV to study the proton spin structure. The first collision was made in 2000 and the performance has been improved every year in its luminosity and polarization.

A number of technological developments and advances have made the RHIC possible to create a high-current polarized sources, maintain the beam, polarization throughout acceleration and storage, and obtain accurate beam polarizations at several stages from the source to full-energy beams. The major components used for the acceleration of proton beams at RHIC are diagrammed in Figure 2.27. We will describe the overview of the RHIC as a polarized-proton collider. The more details are found in the reference [54, 55].

Polarized proton injection uses an optically-pumped polarized H^- ion source. The polarized H^- source produces 500 μA in a single 300 μs pulse, which corresponds to 9×10^{11} polarized H^-. The polarization of more than 80% has been reached at the source. There are several steps from polarized H^- pulse to a bunched polarized proton beam; the LINAC, the Booster, the AGS then the RHIC.

A pulse of polarized H^- ions are accelerated to 200 MeV kinetic energy in the 200 MHz LINAC. The pulse of H^- ions is strip-injected and captured into a single bunch in the AGS Booster. The single bunch of polarized proton is accelerated in the Booster to 1.5 GeV kinetic energy and then transfered to the AGS, where it is accelerated to 24.3 GeV (RHIC 100 GeV run parameter). Then, the polarized protons are transfered to the RHIC.

The AGS to RHIC transfer line has been designed to transport proton beams in the energy range, from 20.6 GeV to a maximum injection energy of 28.3 MeV. Each of the RHIC rings can be filled with up to 120 polarized proton bunches from the AGS, in which case the time between bunch crossing at IP's is 106 nsec. Since the high precision asymmetry measurements are required by the experiments, a frequent polarization sign reversal for single bunch is imperative in order to avoid systematic errors from any correlations that may exist between a bunch and its spin direction. The polarization sign of every single bunch is assigned at the source. It takes about 5 seconds from the ion source to the RHIC ring including acceleration in the AGS ring.

After filling of both rings is complete, the beams are accelerated to flat-top energy. During acceleration, polarized proton beams encounter two types of depolarizing resonances as discussed later. In order to maintain the polarization, six "Siberian snakes" are installed in the AGS ring and in the RHIC rings.

The brief history of the RHIC facility, which is focused on the polarized proton beam acceleration, is summarized below.

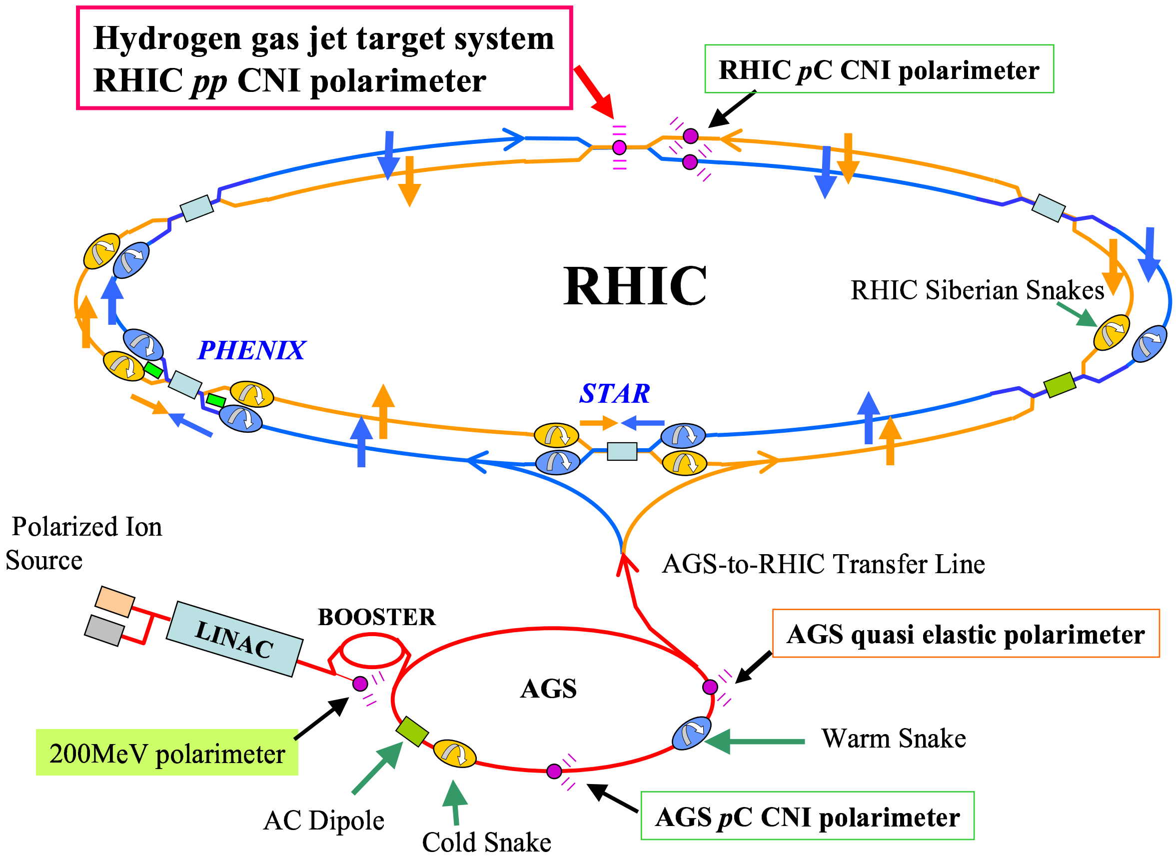

Figure 2.27: Layout of the RHIC facility. Polarized protons are accelerated from the source through a LINAC, a Booster synchrotron, and the AGS before being injected to the RHIC rings. Several of the components used to maintain polarization throughout the acceleration stages are shown. Locations of polarimeters are also noted.

- Fiscal-year 2000: Single Siberian snake and *p*C polarimeter were installed in the blue-ring.
- Fiscal-year 2001: 3 Siberian snakes were installed (not operational) and other 1 *p*C polarimeter was installed.
- Fiscal-year 2002: Commissioning of 2 Siberian snakes/ring and 8 spin rotators were installed around the STAR and the PHENIX. (Spin rotator rotates transverse spin to any direction.)
- Fiscal-year 2003: Commissioning of 8 spin rotators. Bunch-by-bunch polarimeter information were available.
- Fiscal-year 2004: Installation and the first operation of the hydrogen gas jet target and the absolute polarimeter. The first calibration for *p*C polarimeter (blue-ring) was completed by using the absolute beam polarization from the absolute polarimeter. The warm snake was installed in the AGS ring.
- Fiscal-year 2005: The calibration for *p*C polarimeters (in the blue-ring and yellow-ring) were completed. The cold snake was installed in the AGS ring.
- Fiscal-year 2006: Commissioning for the cold snake at the AGS ring.

To date, polarized proton beams have been accelerated, stored and collided in the RHIC rings at center-of-mass energies of $62.4, 200$ and 410 GeV. The acceleration of polarized beam in circular acceleration is complicated by the presence of numerous depolarization resonance. During acceleration, the polarization may be lost when the spin precession frequency passes through a depolarizing resonances. Therefore the polarization is maintained by the use of two partial Siberian snakes in the AGS and two full Siberian snakes in each RHIC ring. The average store polarization reached 40% and the average store intensity reached 10^{11} protons/bunch in 2004. Besides constant polarized beam deliveries to the experiments (the RHIC, the STAR, et cetera), the beam-development has also been continued. Polarized protons were first accelerated to the record beam energy of 205 GeV in the RHIC with a significant polarization measured at top energy in 2005 [56] and further high-energy beam commissioning has been continued in 2006 towards the maximum beam energy of 250 GeV.

2.3.2 Depolarizing Resonance and Siberian Snakes

To accelerate polarized proton beams, the understanding of the evolution of spin during acceleration and the tools to control it are needed. Beam polarization during acceleration can be compromised by depolarization mechanisms driven by magnetic fields which perturb the spin motion away from its precession around the guiding dipole field. The motion of the spin direction vector, $\overrightarrow{S}$, of a proton under the influence of external field is described by the Thomas-BMT equation.

$$\frac{d\vec{S}}{dt} = \frac{e}{\gamma m}\vec{S} \times [(1+G\gamma)\vec{B_\perp} + (1+G)\vec{B}_{||}] \tag{2.16}$$

Here γ is the Lorenz factor and *G* = 1.793 is the proton anomalous g-factor. $\vec{B_\perp}$ and $\vec{B}_{||}$ are magnetic fields perpendicular and parallel to the beam direction, respectively. Equation (2.16) also shows that in a perfect accelerator with only guiding dipole field, the spin direction vector precesses $G\gamma$ times per orbital revolution. Horizontal magnetic fields from misaligned dipole magnetic and focusing quadrupole magnets can perturb the spin direction away from the stable vertical direction.

During acceleration, the depolarizing spin resonances occur if the spin precession frequency, ν_{sp}, is equal to the frequency of the encountered spin-perturbing magnetic fields. There are two main types of depolarizing resonances which are corresponding to the possible sources of such fields: *imperfection resonances*, which are driven by magnet error and misalignments, and *intrinsic resonances*, driven by the focusing fields.

The resonance conditions are usually expressed in term of ν_{sp}. For ideal planar accelerator, where orbiting particles experiences only the vertical guide field, the spin tune is equal to $G\gamma$. Imperfection resonance arises when

$$\nu_{sp} = G\gamma = k \tag{2.17}$$

is an integer. Because if the condition of Equation (2.17) is satisfied, the spin vector is at the same phase in its precession every time. And it encounters imperfect fields which exist with a more or less random distribution around a ring.

Intrinsic resonances arises when

$$\nu_{sp} = G\gamma = kP \pm Q_y, \tag{2.18}$$

where P is the superperiodicity of the machine and Q_y is the vertical betatron tune. For example, $P = 12$ and $Q_y \approx 8.70$ at the Brookhaven AGS. A superperiodicity is a repeated section of bending and focusing magnets. The betatron tune is the number of oscillations around the stable beam orbit per beam revolution, in the vertical plane (the y-z plane). The z-axis is taken to be in direction of proton motion. Depending on the strength of the resonance and resonance crossing rate, the amount of depolarization can vary. For the most of the time during the acceleration cycle, the precession axis, or stable spin direction, coincides with the main vertical magnetic field. Close to a resonance, the vertical direction by the resonance driving fields. When a polarized beam is accelerated through an isolated resonance the polarization loss can be calculated using the Froissart-Stora equation [57]

$$P_f = (2e^{-\pi|\varepsilon|^2/2\alpha} - 1)P_i, \tag{2.19}$$

where P_i and P_f are the polarization before and after crossing the resonance. ε is the resonance strength, defined as the Fourier amplitude of spin perturbing fields. $\alpha = \frac{dG\gamma}{d\theta}$ is the resonance crossing rate, θ is the azimuthal angle around the acceleration. When the beam is slowly ($\alpha \ll |\varepsilon|^2$) accelerated through the resonance, the spin vector will adiabatically follow the stable spin direction resulting in spin flip. However, for a faster acceleration rate partial depolarization or partial spin flip will occur. Traditionally, the intrinsic resonances are overcome by using a betatron tune jump, which is effectively makes α large, and the imperfection resonances are overcome with harmonic corrections of the vertical orbit to reduce the resonance strength ε. At high energy, these traditional methods become difficult and tedious because the strength of imperfection resonances generally increase linearly with the beam energy.

By introducing a **Siberian Snake** [58], which generates a 180 degrees spin rotation about a horizontal axis, the stable spin direction remains unperturbed at all times as long as the spin rotation from the Siberian Snake is much larger than the spin rotation due to the resonance driving fields. Therefore the beam polarization is preserved during acceleration. An alternative way to describe the effort of the Siberian Snake comes from the observation that the spin tune with the

Snake is a half-integer and energy independent. That is, the spin tune:

$$\nu_{sp} = G\gamma$$

is changed to

$$\nu_{sp} = G\gamma \pm \frac{1}{2}.$$

Therefore, neither imperfection nor intrinsic resonance conditions can ever be met as long as the betatron tune is different from a half-integer. Since the orbit distortion is inversely proportional to the momentum of the particle, a dipole magnet snake is particularly effective for high-energy accelerators, e.g. energies above about 30 GeV. Figure 2.28 displays a spin motion image through one Siberian snake. This device was named because of the beam trajectory through the magnet and in honor of Siberian-based inventors.

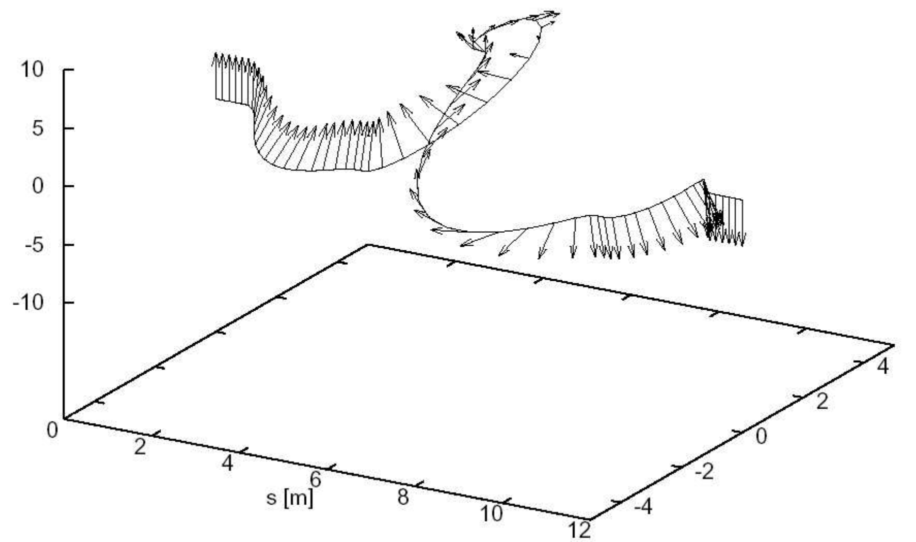

Figure 2.28: Spin motion image through one Siberian snake. Siberian snake, which is a series of spin-rotating dipoles, was named because of the beam trajectory through the magnet and in honor of Siberian-based inventors.

For lower-energy synchrotron, such as the Brookhaven AGS, a partial snake, which rotates the spin by less than 180 degrees, is sufficient to keep the stable spin direction unperturbed at the imperfection resonances.

Polarized Proton Beam Acceleration in the AGS Ring

Over 40 imperfection resonance conditions are crossed in the AGS as the beam is accelerated from energy of 2.4 GeV ($G\gamma = 4.6$) up to 24.3 GeV ($G\gamma = 46.5$).

To overcome imperfection resonances in the AGS, a normal conducting helical dipole magnet (warm snake) has been used as a 5% partial Siberian snake. (Since there is not enough space to permit a full snake in the AGS, only a partial snake is possible.) The 5% partial Siberian snake (snake strength $s = 0.05$) generates a 9 degrees spin rotation about a horizontal axis. The spin tune becomes:

$$\nu_{sp} = G\gamma \pm \frac{s}{2},$$

which does not satisfy the imperfection resonance condition.

However, the strength of the partial snake is insufficient to overcome the effects of intrinsic resonance. There are seven intrinsic resonances that are crossed during acceleration in the AGS. With the typically fast acceleration rate in the AGS, there are only four strong intrinsic resonances at $0 + Q_y$, $12 + Q_y$, $36 - Q_y$ and $36 + Q_y$ that cause significant polarization loss. Figure 2.29 displays the AGS intrinsic spin resonance strength as a function of $G\gamma$.

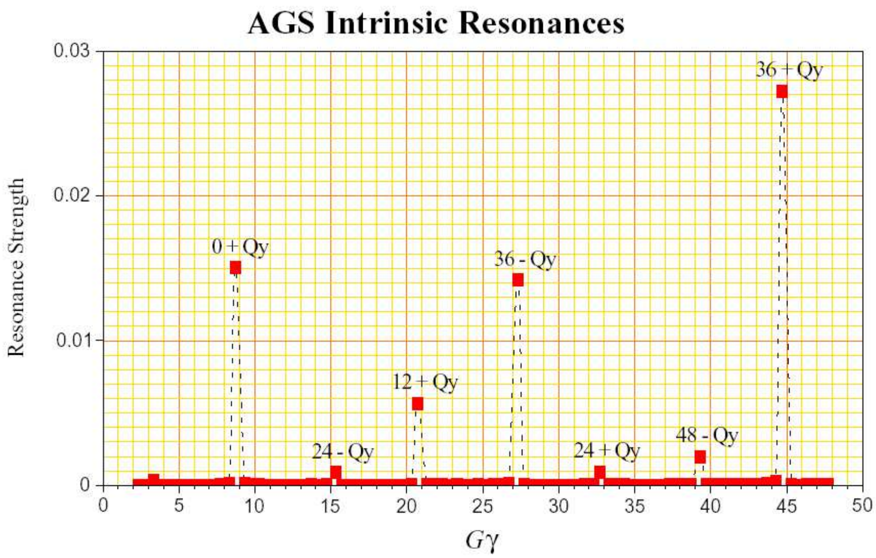

Figure 2.29: The calculated AGS intrinsic spin resonance strength as a function of $G\gamma$. ($G\gamma \approx 1.9\times$ beam energy in GeV.)

In order to handle intrinsic resonances, the technique used was to artificially enhance the resonances such that they were tuned to produce a complete spin flip each time one is encountered, rather than depolarization. A pulsed AC dipole magnet is used to induce a full spin flip for all particles as these resonance are crossed. The AC dipole is pulsed in such a way that the vertical betatron oscillation amplitude is increased for all beam particles.

The use of the 5% partial Siberian snake and the pulsed AC dipole in the AGS significantly reduce the depolarization effects from imperfection and strong intrinsic resonances. Consequently, the maximum beam polarization at extraction from AGS was increased to 50% approximately.

The *p*C-CNI polarimeter, which is installed in AGS and is introduced later, measures the effects of depolarizing resonances at a number of different beam momenta ($P_{beam} = 2.4$ – 24.3 GeV/c). Figure 2.30 shows the measured asymmetry versus the parameter $G\gamma$ ($G\gamma \approx 1.9\times$ beam energy in GeV) by use of this polarimeter [59]. The decreasing of the measured asymmetry as the beam energy increase is come from two reasons; the beam depolarization and the decreasing of the analyzing power itself as the beam energy increase (See Figure A.7 in Appendix A.5).

The ramp-up takes about 0.5 sec. The ramp was repeated hundreds times to collect these data. The data are binned by the beam momentum. Each point corresponds to a bin width of 50 MeV/c, which is about 1 msec. The sign of asymmetry changes when resonance conditions are crossed. The solid line is a predicted spin direction due to resonances based on magnet strengths in the machine. The amplitude of the line is adjusted to fit the data. The error bars are statistical only.

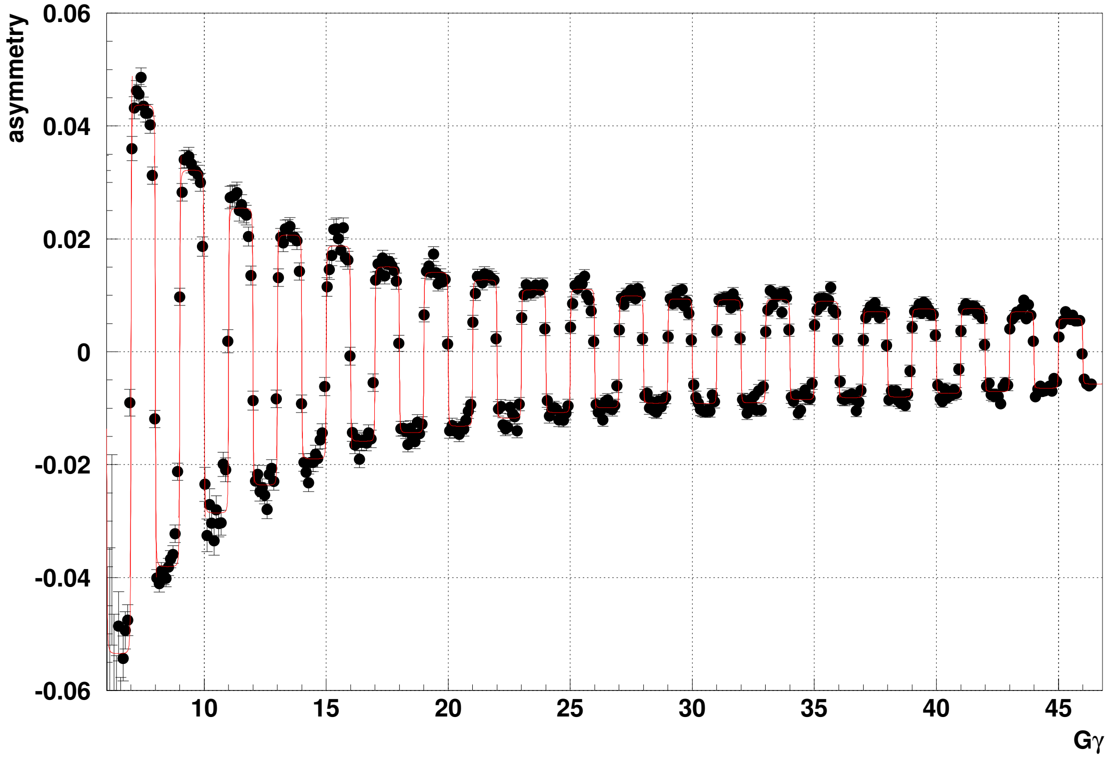

Figure 2.30: Measured analyzing power versus $G\gamma$ for the ramp-up. The data were taken in 2005. The ramp-up takes about 0.5 sec. The ramp was repeated hundreds on times to collect this data. The data are binned by the beam momentum. Each point corresponds to a bin width of 50 MeV/c, which is about 1 msec. The sign of asymmetry changes when resonance conditions are crossed. The solid line is a predicted spin direction due to resonances based on magnet strengths in the machine. The amplitude is adjusted to fit the data. The error bars are statistical only. The data were taken in 2005.

A study has shown that a stronger Siberian snake could also be effective in overcoming the strong intrinsic resonance in the AGS. A super-conduction helical dipole magnet as a 20% partial Siberian snake in the AGS is currently being developed.

Polarized Proton Beam Acceleration in the RHIC Rings

Without Siberian Snake there are numerous depolarizing resonances in RHIC, both intrinsic and imperfection resonances.

Figure 2.31 displays the RHIC intrinsic spin resonance strength as a function of beam energy. The strong intrinsic spin resonances at higher energy are expected to be over a factor of two stronger than those below 100 GeV.

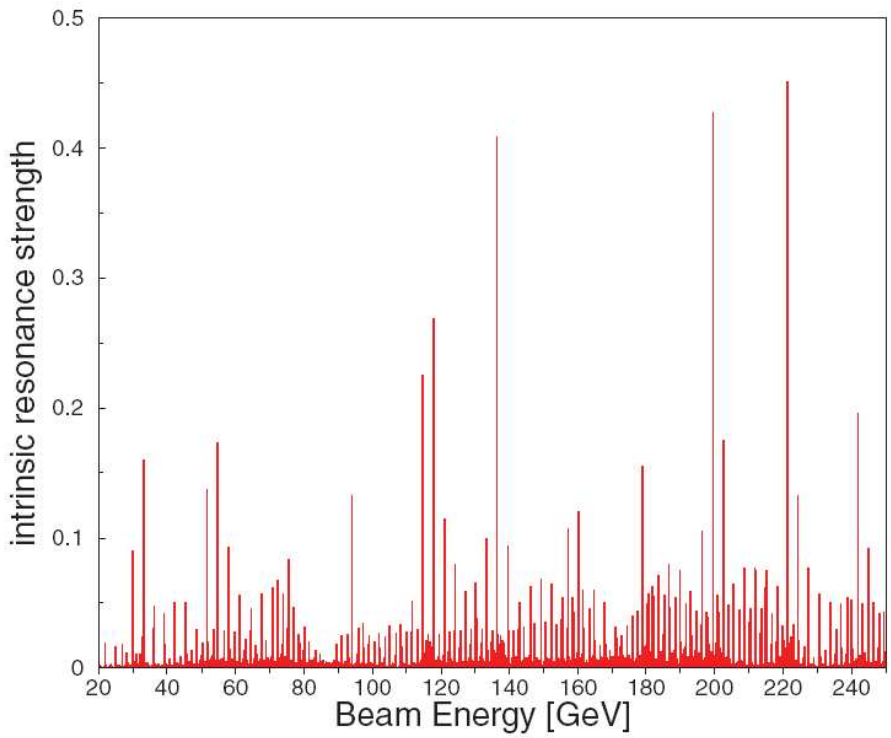

Figure 2.31: The calculated RHIC intrinsic spin resonance strength as a function of beam energy.

Full Siberian snakes are used to overcome both imperfection and intrinsic resonances in the RHIC. But even in a perfect accelerator, which has no magnetic field errors, with snakes, the spin perturbations can still add coherently and result in significant polarization loss at certain tune values. For a single snake case, the accumulated spin perturbations can't perfectly canceled out if

$$mQ_y = \nu_{sp} + k,$$

where m and k are integers. These are called snake resonances and m is the order of the snake resonance. Adding the second snake at the opposite side of the ring to the first snake provides additional cancellation when m is an even number.

A configuration of two Siberian snakes in each ring was chosen to overcome both imperfection and intrinsic resonances. As displayed in Figure 2.32, the two snakes are places on opposite sides of the ring with their spin precession axes perpendicular to yield an energy independent spin tune. Hence, with two snakes, all the even order snake resonances disappear.

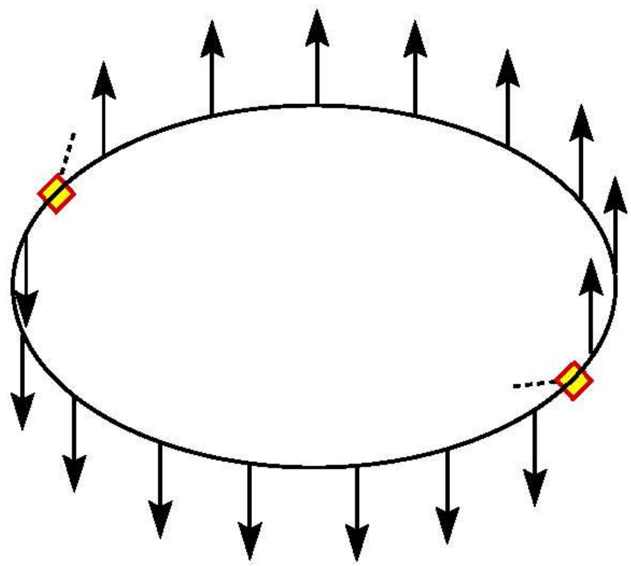

Figure 2.32: Two snakes are placed on opposite sides of the ring with their spin precession axes perpendicular to yield an energy independent spin tune.

However, the even order snake resonances reappear if the intrinsic resonance overlaps an imperfection resonance. The overlap of an intrinsic resonance with an imperfection resonance also splits the existing odd order resonances. All of this greatly reduces the available betatron tune space to avoid polarization loss. Hence, careful control of tunes and vertical closed orbit is necessary for any high energy accelerator. And the beam polarization measurements at various stage of acceleration in order to identify and address possible origins of depolarization at each step are needed to provide feedback for accelerator developments.

Currently, polarized protons have been successfully accelerated up to 100 GeV with minimum or no polarization loss with Siberian snakes and proper control of betatron tunes and the vertical orbit distortions. The polarized proton beams have been achieved an average beam polarization in RHIC of $45 \sim 50\%$ and delivered to the experiments in 2005 and 2006.

Even with the success of accelerating polarized protons to 100 GeV, as Figure 2.31 displays, the strong intrinsic spin resonances at higher energy are expected to be over a factor of two stronger than those below 100 GeV. During polarized proton run-05, polarized protons were accelerated to a new record energy of 205 GeV. Significant beam polarization was measured at the top energy, after successfully crossing through strong spin resonances between 100 GeV and 205 GeV [56].

2.3.3 *p*C Polarimeter

The proton-carbon (*p*C)-CNI polarimeter, which takes advantage of an analyzing power, $A_N^{pC} \approx 0.01$, in the elastic scattering of polarized protons with carbon atoms, serves as a fast feedback tool to tune up the beam acceleration. A_N^{pC} originates from interference between electromagnetic force and hadronic force was initially measured by AGS experiment E950 [6].

The pC-CNI polarimeters are installed in the AGS, the blue-ring and the yellow ring respectively. They employed ultra-thin carbon ribbon target (3.5μg/cm^2 thick and 5μm wide typically), which have been developed at IUCF, and collected 20 million events of recoil carbons of the elastic scattering process within 20 seconds. The pC polarimeter measures beam polarization several times in a store and also measures bunch-by-bunch polarization.

The accuracy of the pC-CNI polarimeter was limited by the uncertainty of A_N of pC elastic scattering. The A_N data of proton-carbon elastic scattering was measured at $P_{beam} = 22$ GeV/c [6] and we need to extrapolate to get A_N at $P_{beam} = 100$ GeV/c using a theoretical calculation [11]. The uncertainty of A_N would cause a wrong scale of the measured beam polarization. Once we know the exact A_N at $P_{beam} = 100$ GeV/c, we can correct a wrong scale and calibrate the measured beam polarizations.

Calibration of pC polarimeter to achieve $\Delta P_b/P_b \sim 0.05$ was provided by a polarized hydrogen-jet-target polarimeter in 2004. Taking advantage of the pp elastic scattering process, which is 2-body exclusive scattering with identical particles, we can change the role of which is polarized between the target proton and the beam proton. Thus the beam polarization is measured utilizing the A_N which is measured by a well calibrated polarized proton target. Requiring a new measurement of A_N is better than $\Delta A_N/A_N \sim 0.05$, the accuracy of absolute beam polarization can be achieved $\Delta P_b/P_b \sim 0.05$.

2.4 Brief History of Run-4 and Experimental Setup Parameters

- Installation
  - April 5th-7th: Installation of H-Jet target system into the RHIC ring at IP12.
  - 6th-7th: H-Jet target system was set up. We started vacuuming.
  - 7th: We installed FEE boards. We checked test-pulse signals, calibration α source signals at IP12.
- The H-Jet target and the recoil detector setup (April 7th – 25th) We applied bias voltage to the silicon detector and adjusted the shapers using α source signals. We also took the energy calibration data using alpha particles ($^{148}\mathrm{Gd}$ and $^{241}\mathrm{Am}$). Then we adjust the timing window with the RHIC clock and tried to find the H-Jet target center position by use of the RHIC-blue beam (the first target profile measurement data on April 15th).
- Physics data taking (April 26 th $\sim$ May 14 th. H-Jet target polarization = 0.924 ± 0.018)
  - Normal physics run with 100GeV/c proton beam $\sim$ 90 hours
  - Accumulated 3 million elastic events in the 4-momentum transfer squared $|t|$ range $0.001 < |t| < 0.032$ (GeV/c)^2.
  - Normal physics run with 24GeV/c proton beam (injection energy) $\sim$ 14 hours.
  - Data for systematic error study
    - Background study (See Section 3.6)
      - Empty-target runs; 6.5 hours
      - No-beam runs; 8 hours
      - Empty-target, No-beam runs; 3hours
    - Holding magnet study (See Appendix A.8)

	Planed, designed values	Achieved values in 2004
Thickness (atoms/cm^2)	$5 \cdot 10^{11}$	$(1.3 \pm 0.2) \cdot 10^{12}$
FWHM size (mm)	5.5	6.5
Polarization	0.9	0.924 ± 0.018

Table 2.4: H-Jet target

	Planed, designed values	Achieved values
$-t$ range (GeV/c)^2	0.001 – 0.02	0.001 – 0.032
recoil angle range (mrad)	10– 90	10 – 100
recoil angle resolution (mrad)	< 8	5
Azimuthal angle range (mrad)	262×2	205×2
Depletion thickness μm	800	~ 420 (BNL), ~ 400 (Hama.)
Entrance window thickness	~ 150 nm	~ 150 nm (BNL), $1 \sim 2\mu$m (Hama.)

Table 2.5: Recoil spectrometer. (BNL) and (Hama.) denote silicon types.

- · Non-magnetic field; 1.7 hours
- · Reversed-magnetic field; 1.5 hours

$*$ Target profile measurement (the second trial on May 5th).

We summarized the parameters of H-Jet-target system, recoil spectrometer in Table 2.4 and 2.5.

The RHIC-beam intensity (proton/bunch) was $1 \cdot 10^{11}$ with 55 bunch mode. The revolution frequency was 78 kHz. β^* at IP12 was 10m. The RHIC-beam diameter is $\sigma \sim 1$ mm and smaller than The H-jet-target size. The beam position at IP12 was always fixed and monitored by Beam Positioning Monitor (BPM) [52]. The achieved luminosity was 4.7×10^{29} cm^{-2} sec^{-1}.

Chapter 3

Data Analysis

3.1 Analysis Outline

Off-line analysis was performed to determine A_N and A_{NN} for the *pp* elastic scattering in the CNI region as a function of four-momentum transfer squared $-t$. The experimental data taken with the setup are summarized in Table 2.3. The main two parts of the analysis are determination of $-t$ and the elastic event selection.

Firstly, we will discuss about the waveform analysis as groundwork in Section 3.2. The kinetic energy T_R and the arrival time of the recoil particles are obtained from waveform, which is taken with silicon detector, event-by-event. We will also describe how to perform a quality assurance for raw data.

In Section 3.3, we will describe the conversion from waveform data to T_R. Obtained T_R is connected to $-t$ via Equation (2.2). T_R was obtained from the energy deposit in the silicon detector, E_R, by correcting the energy loss due to the entrance-window of the silicon detector and/or unmeasured energy due to the punch-through of the proton. In order to estimate the energy loss, we need to estimate the entrance-window thickness and the fiducial volume of the silicon detector.

In Section 3.4, we will discuss the ToF resolution prior to the event selection. ToF from the collision point to the silicon detector was obtained from the arrival time of the recoil particle. In order to distinguish recoil protons from the huge amount of *prompt* particles, we utilize ToF separation.

The essentials for the elastic event selection are the recoil particle identification and the mass measurement of all the rest particles, which we do not detect. The recoil particle is identified as the proton by use of T_R and ToF correlation. Then we apply further selection using T_R and hit-channel$\#$ correlation to select the elastic event. The T_R and hit-channel$\#$ correlation confirms the forward scattered particle is proton. This process is described in detail in Section 3.5.

In Section 3.6, we will describe the background estimation, which is also important. We itemized the background sources and confirmed that they are unpolarized. Based on these studies, A_N and A_{NN} were corrected to avoid a dilution by background events.

3.2 Waveform Analysis

Off-line analysis starts from waveform analysis. T_R and the arrival time of recoil particle are obtained from waveform event-by-event. Waveforms are shaped by the shaping amplifier (12 nsec

FWHM). At the Waveform Digitizer (WFD), the offset voltage of every single waveform data has been subtracted and digitized by 8bit ADC at the equivalent frequency of 420 MHz. The detailed process in WFD modules has been discussed in Subsection 2.2.4. WFD samples waveform every 2.38 nsec and records all waveforms above threshold (500 keV). Every waveform is recorded with 90 points. The acquisition timing gate signal is synchronized with the RHIC-rf clock. We applied quality assurance check for all recorded waveforms because the uniformity of waveform data have a direct bearing on T_R and ToF resolutions.

3.2.1 Introduction of Waveform Data

Energy and Arrival Time from Waveform Figure 3.1 and 3.2 display the sample waveform data and AMP,T_{meas}, $TMAX$ and $INTG$. We refer to maximum pulse height and its timing as AMP and $TMAX$. We define the arrival time, T_{meas}, which is two times the average of the nearest two $1/4$ maximum pulse height timings T_a and T_b (constant fraction triggering). Therefore one digit size of T_{meas} is equivalent to a half of internal WFD sampling time cycle, 1.19nsec.

$INTG$ is one forth of the sum of waveform data for 31 points. Filled gray region in Figure 3.2 corresponds to $INTG$. G is the center of gravity,

$$G = \sum_{i=1}^{90} i \times ph(i) / \sum_{i=1}^{90} ph(i),$$

where $ph(i)$ is the pulse height of each waveform data point as displayed in Figure 3.1.

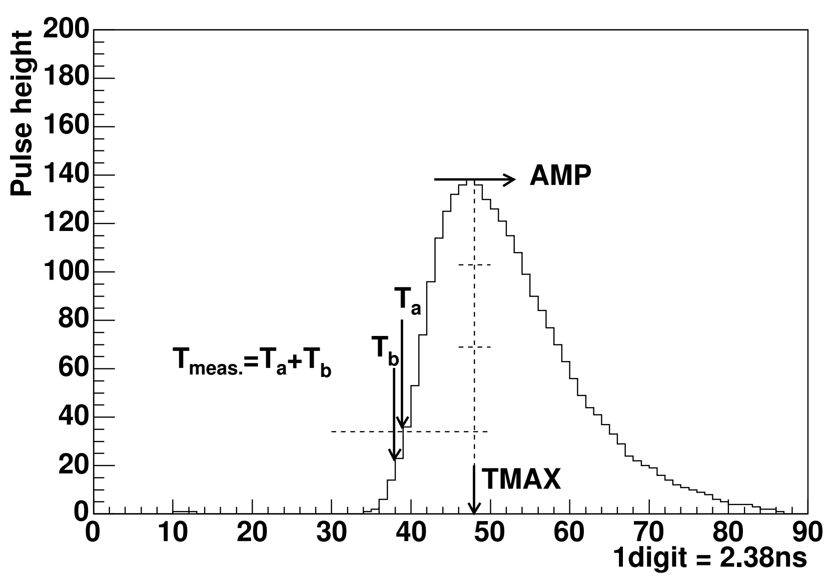

Figure 3.1: Waveform data sample and explanation of AMP, T_{meas} and $TMAX$.

AMP and $INTG$ are related to the deposit energy in the silicon detector. T_{meas} is related to the arrival time comparing with RHIC rf-clock. Figure 3.3 displays the correlation of $INTG$ and T_{meas} of one of the read-out channels. We can see the signals of the recoil proton clearly.

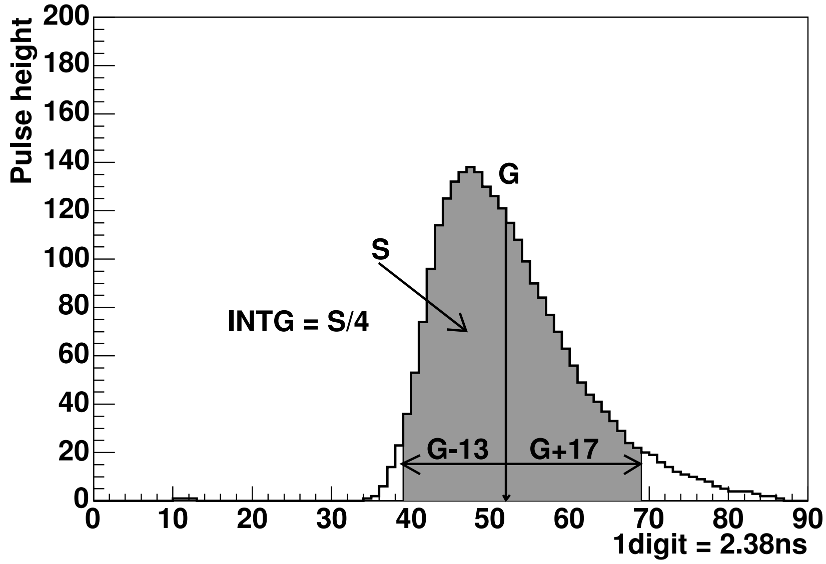

Figure 3.2: Explanation of $INTG$

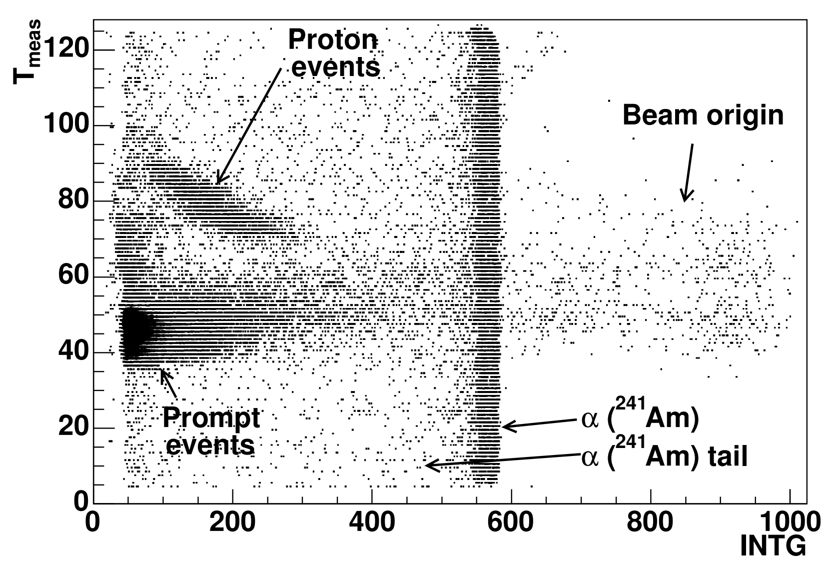

Figure 3.3: $INTG$ vs. T_{meas} from channel $\#3$

The events which is vertically distributed around $INTG = 550$ in $INTG$ are calibration α source (^{241}Am) events. We equipped the left arm with the ^{241}Am source and the right arm with ^{241}Am and ^{148}Gd sources, respectively. Since we could not prepare a shutter from calibration source, α particles were always detected by the detectors during RUN-4 period. We cut out these region from the asymmetry calculation. The significant energies for calibration sources are 5.486 MeV for ^{241}Am and 3.183 MeV for ^{148}Gd. The width of spectrum in terms of FWHM are less than few keV [60]. There is some tail towards less energy than $INTG = 550$. These are calibration α events and randomly scattered in time. Although the energy spectrum of calibration α is quite sharp but the deposit energy distribution in the silicon detector fluctuates statistically and has a tail shape. However the events from α source are lower than protons and should not have any correlation with spin states. The ratio of tail events is estimated using special data for background study as discussed in Subsection 3.6.3. as displayed in Figure A.12.

In Figure 3.3, there are the huge amount of events around $T_{meas} = 45$ and $INTG = 75$ are *prompt* particles, which are possibly pions from the beam-related interaction upstream. They are synchronized with RHIC beam bunches and comprise one of the background sources. The events in the region $40 < T_{meas} < 80$ and $INTG > 600$ are also synchronized with RHIC beam bunches. The ratio of background regarding the RHIC-beam is discussed in Subsection 3.6.3.

3.2.2 Waveform Quality Assurance

Average Waveform and Characteristics

A uniformity of waveforms is important to obtain good T_R and ToF resolutions. To evaluate a uniformity, we made *average* waveform by gathering a few thousands of waveforms from α source events per read-out channel. Here we applied rough eye selection to gather waveforms in order to reject bad waveforms. Figure 3.4 displays the accumulated 1725 waveforms in 2-D plot. As a result of smoothing, we have obtained 10 times finer time binning as displayed in Figure 3.4. They are normalized by the area. Then normalized waveforms are shifted along horizontal-axis in order to keep their center of gravity, G, at 450. To obtain the mean envelope of accumulated waveforms, we sliced the 2-D plot along the horizontal-axis and apply the Gaussian fitting. The red data points are the mean envelope and we refer to them as *average* waveform. The dispersion band along the red points correspond to the error of *average* waveform. A *rise-time* from 10% to 90% of the maximum amplitude is 14.6 nsec.

The enlargement accumulated waveforms around the maximum pulse height is displayed in the left side of Figure 3.5. The projection along the vertical-axis of the red dashed box is displayed in the right side plot. The mean peak pulse height value of the accumulated waveforms is $AMP = 127$ and $\sigma \sim 2$ counts.

The detailed procedure of making the *average* waveform is described in Appendix A.6.

The ratio $INTG/AMP$ is a one of parameters to confirm waveform uniformity. It should be constant value as long as waveforms are uniform at any energies. The ratio for the *average* waveform is obtained to be 3.9 using *average* waveform, $INTG = 500$ and $AMP = 127$.

We utilized *average* waveform as a reference in order to categorize waveforms into ”good” and ”bad” groups.

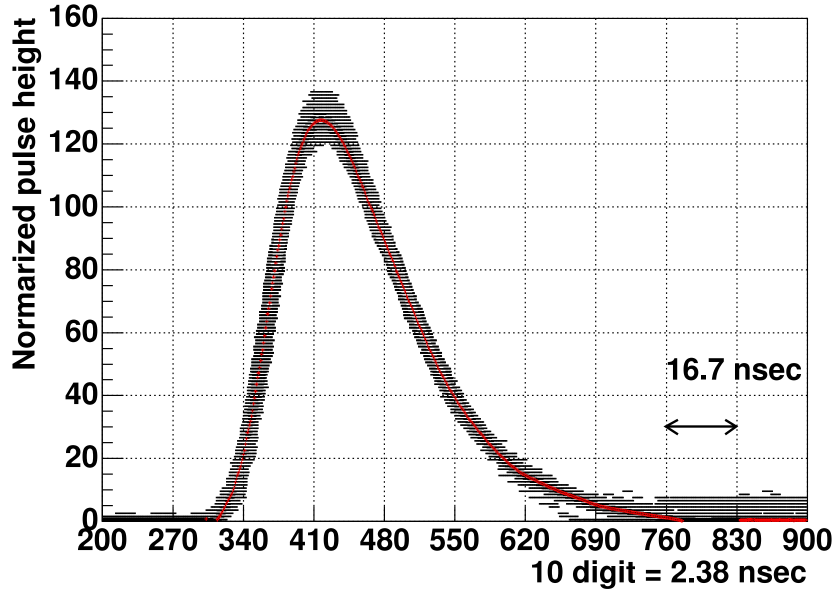

Figure 3.4: Accumulated Waveforms 1725 samples. They are normalized to have constant $INTG$ value.

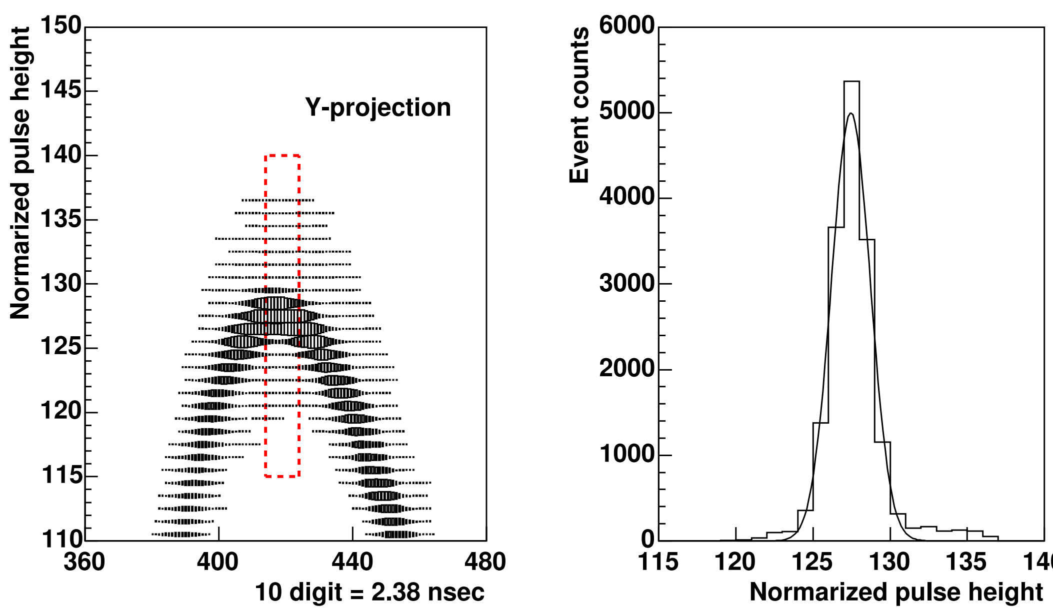

Figure 3.5: The enlargement of accumulated waveforms around the maximum pulse height.

”Good” Waveform Selection

In order to categorize every waveform, the χ^2 fit was done by scaling the reference-waveform. ”Prompt” region events, which are in the region of $T_{meas} < 60$ and $INTG < 200$, are removed in the following discussions. We leave the center of gravity timing, G, and the maximum pulse height, AMP as fit parameters. The error of every waveform data point is set to 2 counts in terms of pulse height. This value corresponds to the width of energy spectrum for the calibration source (we will discuss in Subsection 3.3.1). Thirty-one data points of every waveform are used for fit with the reference-waveform. This is same as the integral region for $INTG$ as shown in Figure 3.2.

The reduced chi-square (χ^2/ndf) is used as a measure to categorize waveforms into ”good” and ”bad” groups. Basing on the distribution of χ^2/ndf as displayed in Figure 3.6, we set the criteria χ^2/ndf ≥ 5 for bad in order to distinguish waveforms are ”good” or ”not-good”.

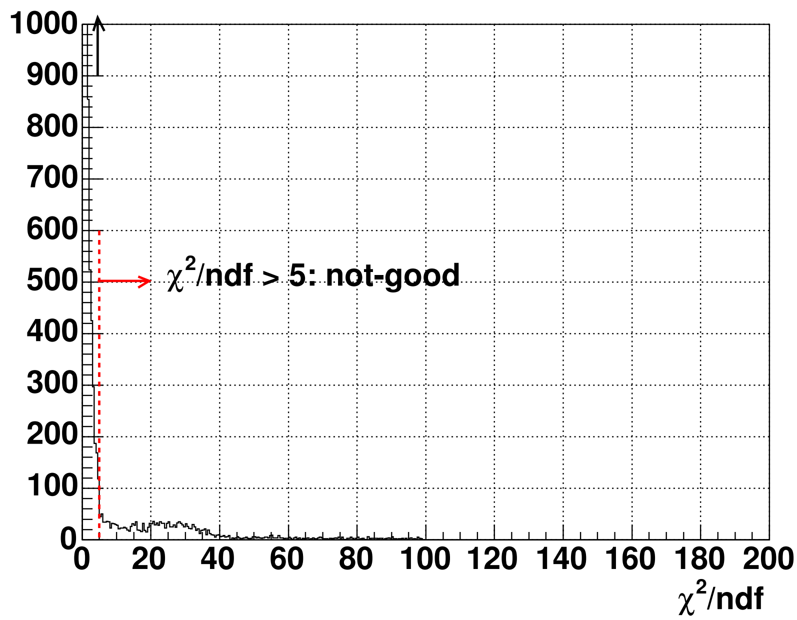

Figure 3.6: χ^2/ndf distribution

The distribution of χ^2/ndf is obtained from the data set which is displayed as the correlation between $INTG$ and T_{meas} in Figure 3.7.

Figure 3.8 displays the samples of ”good” and ”not-good” waveform.

Figure 3.9 displays the $INTG$-T_{meas} correlation for categorized as ”good” waveform events from the total events (Figure 3.7). Figure 3.10 displays ”not-good” waveforms. From this figure, ”not-good” waveforms occur randomly in time. The ratio of ”not-good” event to the total events are $\sim 10\%$.

Figure 3.11 suggests the correlation between χ^2/ndf and $INTG$. Considering Figure 3.10 and 3.11, most of ”not-good” waveforms are related to calibration α ”tail” events and the rate of occurrence depends on $INTG$.

We think ”not-good” waveforms are due to the mismatch between shaper and preamplifier.

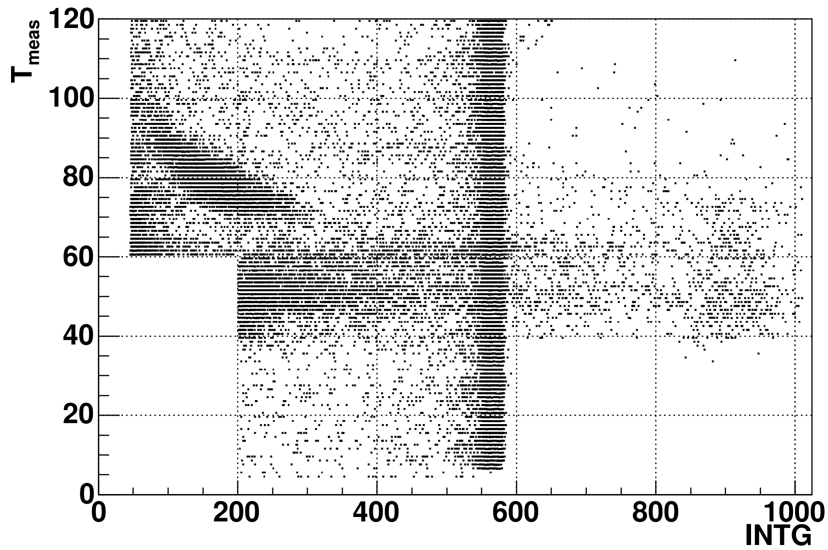

Figure 3.7: $INTG$ vs. T_{meas} correlation for all except "prompt" events.

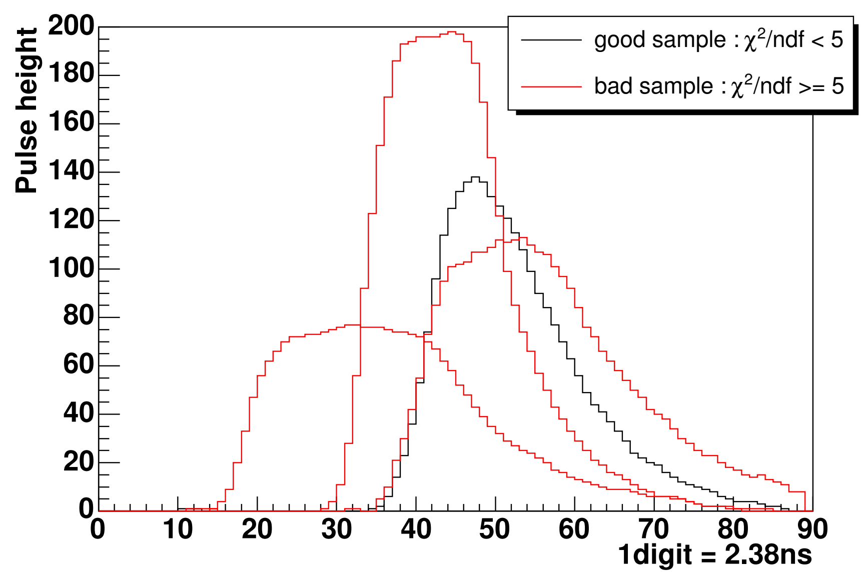

Figure 3.8: Sample waveforms of "good" and "not-good".

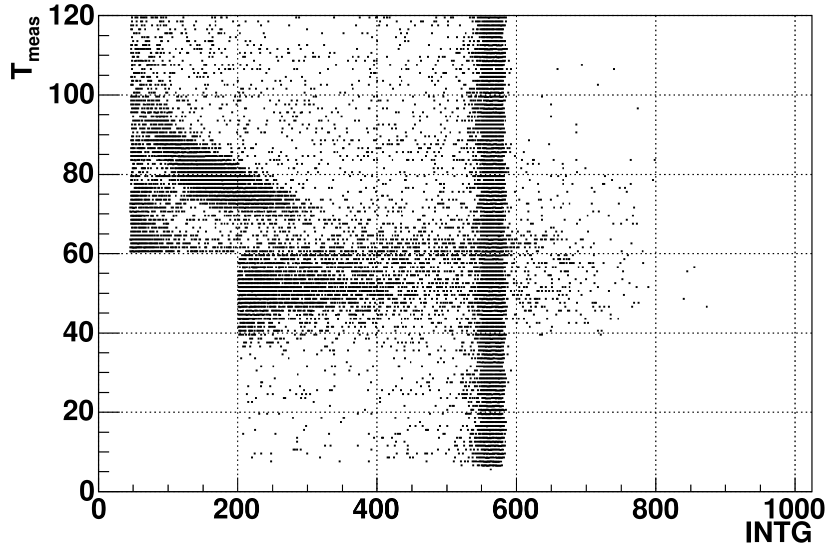

Figure 3.9: $INTG$ vs. T_{meas} correlation for "good" waveforms only

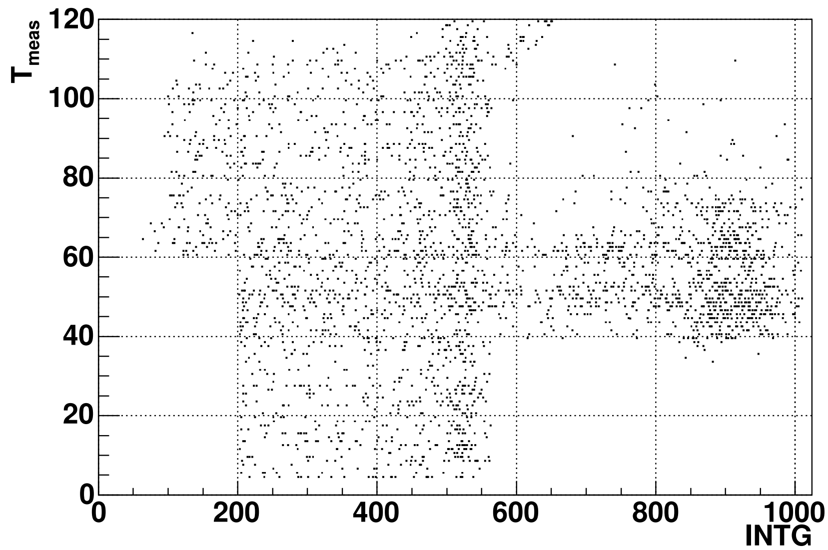

Figure 3.10: $INTG$ vs. T_{meas} correlation for "not-good" waveforms only.

The shaping amplifier did not match with the output of preamplifier signal as we have discussed in Subsection 2.2.4. Actually some irregular waveform are found and these should be discarded by off-line analysis.

As long as the reason of strange waveform is the mismatch between the preamplifier and the shaper, the discard ratio should be independent of the polarization states but depend on the energy. We can't measure $INTG$ nor T_{meas} data correctly from these kinds of "not-good" waveform.

From these studies, the most of "not-good" waveforms are regarded as the tail events of α particles from the calibration sources. Therefore, we can discard these events. In practice, we need to concentrate on the events which pass the elastic event selection which will be discussed in Section 3.5. The discard ratio in the elastic event selection are only few$\%$ and the values are summarized in Subsection 3.5.2 as a function of energy bins.

Uniformity Evaluation of "Good" Waveforms

$INTG/AMP$ uniformity Figure 3.12 displays the correlation of AMP and $INTG$ of the same data set as Figure 3.7. The black points and red points are corresponds to χ^2/ndf < 5 and χ^2/ndf ≥ 5, respectively. From this figure, the criteria to distinguish "good" and "not-good" waveforms are thought to be reasonable.

Seeing Figure 3.13, most of waveforms are independent of the energy-range.

Figure 3.13 displays the distribution of $INTG/ADC$. Black line and red line correspond to χ^2/ndf < 5 and χ^2/ndf ≥ 5, respectively. The mean value is 3.9 and agree with that of *reference* waveform (~ 4).

Good agreement between the mean values of $INTG/ADC$ between *reference* waveform and "good" waveforms means that there is no obvious energy dependence among "good" waveforms in the whole energies. We conclude that the criteria for "good" waveform selection ($\chi^2/ndf < 5$) is reasonable. Thus, applying the pattern matching selection for every waveform, "good" waveform selection works for the whole energy range.

T_{meas} resolution and *rise-time* uniformity As long as waveform does not change, in principle, a *rise-time* from 10% to 90% of the full amplitude should be stable. Figure 3.14 displays the distribution of *rise-time* for one of the silicon detector. The mean value is 14.9 nsec and agree with that of *reference* waveform. σ is ~ 0.7 nsec and then uniformity of *rise-time* is better than one digit size of T_{meas}(1.19 nsec). Black and red points are corresponds to χ^2/ndf < 5 and χ^2/ndf ≥ 5, respectively. Since every waveform is shaped by the shaping amplifier, the difference of *rise-time* between "good" and "non-good" waveforms is not so clear.

Seeing Figure 3.13 and 3.14, most of waveforms are "good" and same as the *reference* waveform for all energies. Thus, we confirmed the uniformity of waveform for event-by-event.

So far we have discussed the waveform uniformity limited in single read-out channel. We have 96 independent read-out channels and each of *reference* waveform should be same if the read-out electronics are adjustment ideally. However, in practice, the mean values of factor K and *rise-time* are not completely same over all read-out channels. Therefore we prepared the proper evaluation-waveform of all 96 read-out channels.

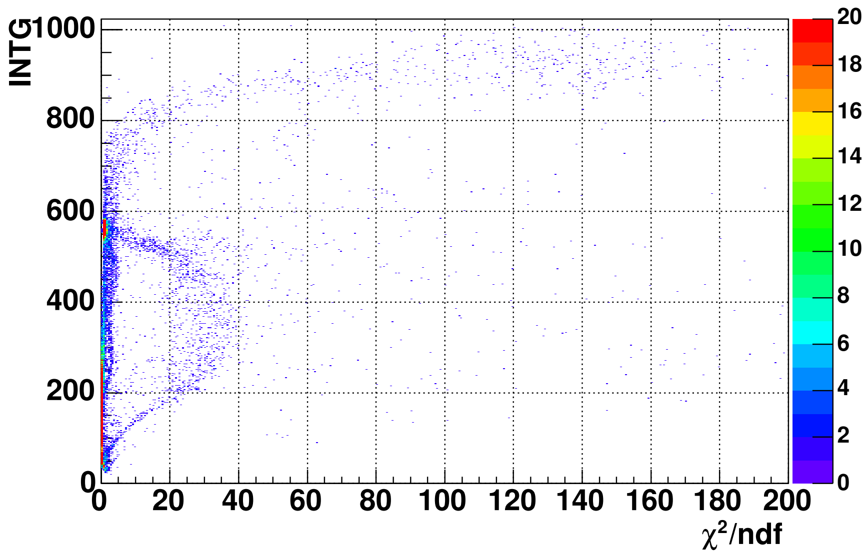

Figure 3.11: χ^2/ndf vs. $INTG$

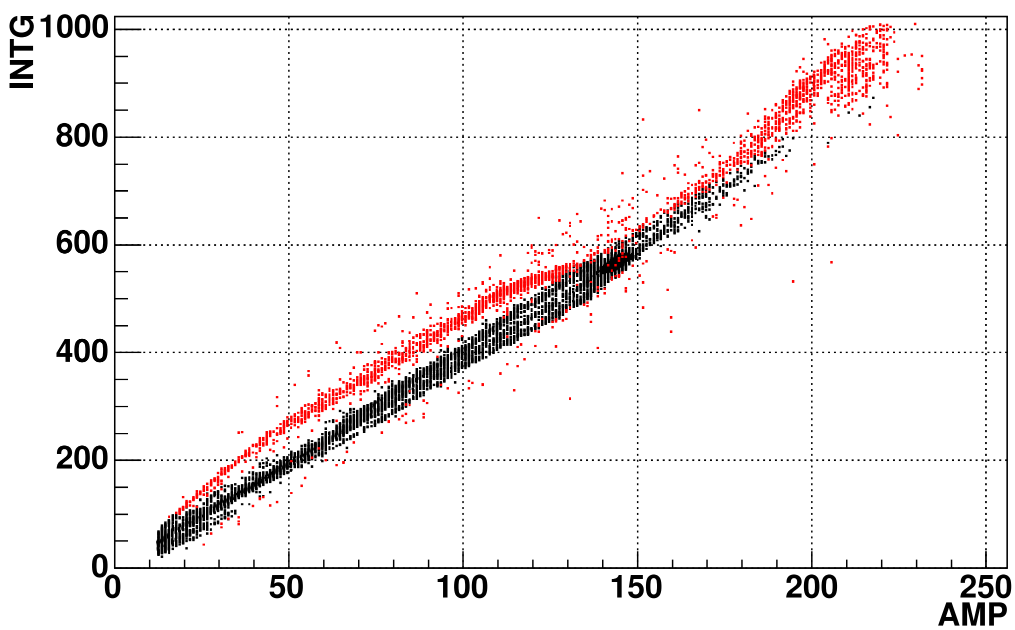

Figure 3.12: The correlation of AMP and $INTG$ for one of the read-out channel. The black points and red points are corresponds to χ^2/ndf < 5 and χ^2/ndf ≥ 5, respectively. The ratio of "not-good" events to the total events are $\sim 10\%$.

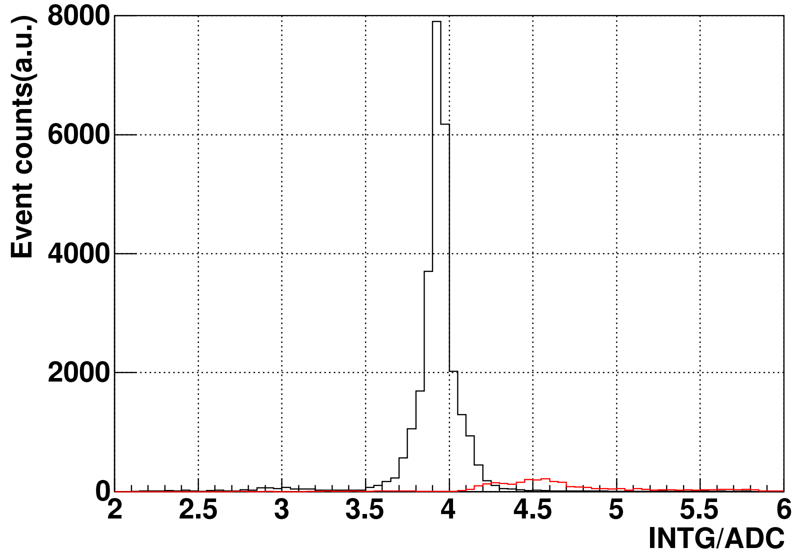

Figure 3.13: $INTG/AMP$ as a function of $INTG$ for one of the read-out channel. The mean value is 3.9 and agree with that of *reference* waveform (~ 4).

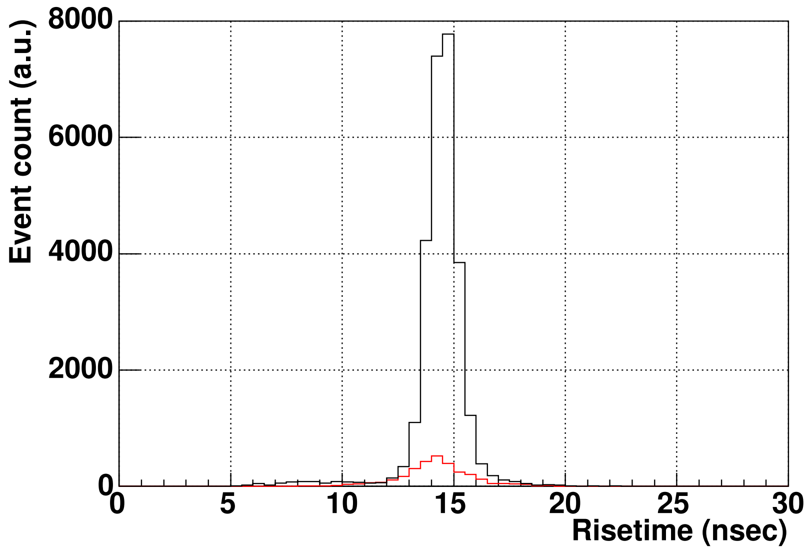

Figure 3.14: *Rise-time* distribution for one of the read-out channel. The mean value is 14.9 nsec and agree with that of *reference* waveform. σ is ~ 0.7 nsec and then uniformity of *rise-time* is better than one digit size of T_{meas}(1.19 nsec).

3.3 Kinetic Energy of Recoil Protons

In this section, we will discuss about the energy conversion from $INTG$ to the incident kinetic energy, T_R (MeV). As we have described in Subsection 2.2.3, two out of three pairs of silicon detectors were fabricated by the Hamamatsu Photonics, K. K. The other pair of silicon detectors were fabricated by the BNL Instrumentation Division. The entrance-window thickness and the detector thickness were different between Hamamatsu-type and BNL-type, In order to achieve the energy resolution better than 0.1 MeV, we need to correct the energy loss appropriately.

The detection energy range for the recoil proton is $0.6 - 17$ MeV. As described in Equation (3.1), T_R is obtained as a sum of the deposit energy in the silicon detector, E_R and the energy loss, ΔE_R. E_R is obtained as a product of $INTG$ and the energy calibration scale constant C_E (MeV/INTG). C_E differs slightly among read-out channels because the read-out electronics chains are individual.

$$
\begin{aligned}
T_R &= E_R + \Delta E_R \\
&= C_E \times INTG + \Delta E_R, \qquad (3.1)
\end{aligned}
$$

where ΔE_R includes the energy pedestal, energy loss due to the entrance-window of the silicon detector and/or unmeasured energy due to the punch-through of the proton. Since the energy baseline properly estimated and subtracted in the WFD modules (See Subsection 2.2.4), the energy pedestal is estimated to be small compared to other components.

The recoil protons, in the energy of $T_R > 7$ MeV, are not fully absorbed in fiducial volume in the detectors. In this case, T_R is reconstructed using the entrance-window thickness, the fiducial volume thickness.

3.3.1 Energy Calibration

The energy calibration was performed using α particle. At first, we will describe the how we estimate the entrance-window thickness using the calibration α sources, in order to perform the energy loss correction in the entrance-window. Then the achieved energy resolution will be discussed comparing to the required energy resolution. We also discuss about the stability of C_E during whole RUN-4 period.

Energy Loss Correction in the Entrance-window

In order to convert $INTG$ into the deposit energy in MeV, we used two calibration α sources. During RUN-4 period in 2004, we equipped the left arm with the ^{241}Am source and the right arm with ^{241}Am and ^{148}Gd sources respectively. Their significant energies are 5.486 MeV for ^{241}Am and 3.183 MeV for ^{148}Gd, and FWHM are less than few keV [60].

Figure 3.15 displays the $INTG$ spectrum of single read-out channels for BNL-type. Two peaks, which we call $Gd0$ and $Am0$ of $INTG$ readings, correspond to the α spectrum of ^{148}Gd and ^{241}Am, respectively. The energy resolution is estimated to be ~ 70 keV from the width of spectra.

Figure 3.16 displays the $INTG$ spectrum of single read-out channels for Hamamatsu-type. Although the significant energy spectra of the two types of calibration sources are quite narrow in order of few keV, the $INTG$ spectrum of Hamamatsu-type have two sets of double peaks.

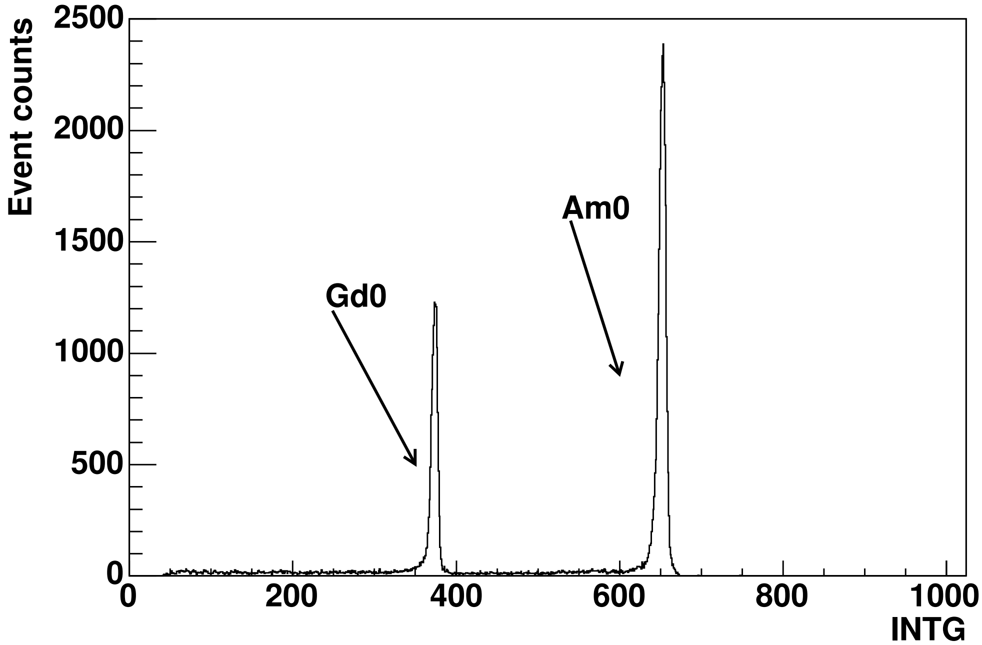

Figure 3.15: $INTG$ spectrum for one of read-out channels of BNL-type detector.

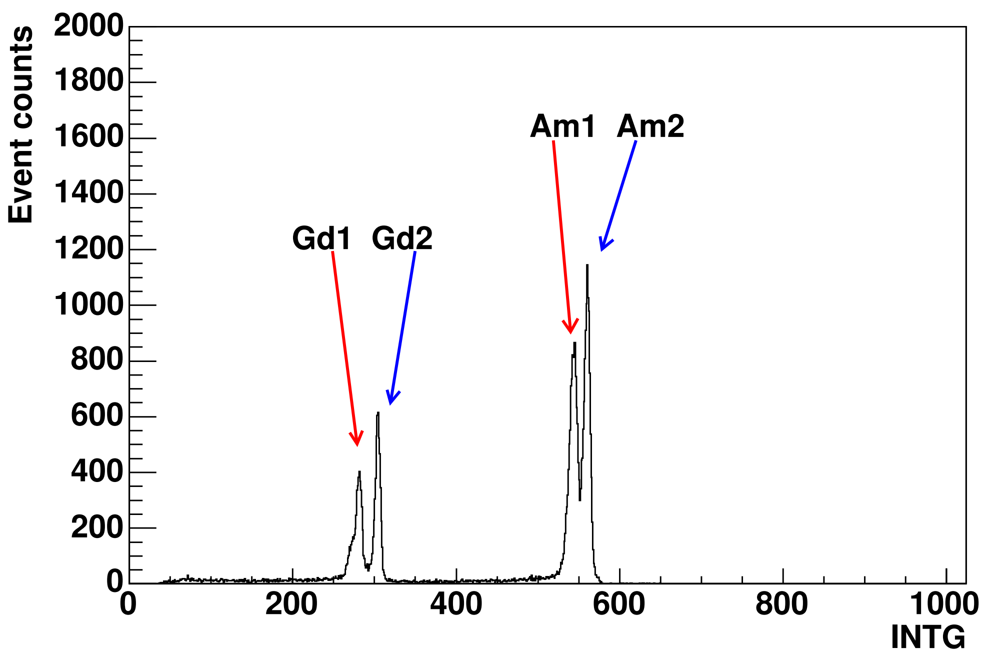

Figure 3.16: $INTG$ spectrum for one of read-out channels of Hamamatsu-type detector.

Double peaks to the left correspond to α particles of ^{148}Gd and double peaks to the right correspond to that of ^{241}Am. We refer to left two peaks as $Gd1$, $Gd2$ and refer to right two peaks as $Am1$, $Am2$, respectively.

Double peaks implies the double structure of the entrance-window. Seeing the width of each spectrum, the energy resolution is estimated to be ~ 70 keV. However we need to estimate how much α particle loses its energy in the entrance-window in order to convert $INTG$ into the absolute energy.

By use of two α calibration sources, we evaluated the thickness of the entrance window. We refer the incident energies of ^{241}Am source and ^{148}Gd source to E_{Am} and E_{Gd}, respectively. The deposit energies in the fiducial volume are referred to E^i_{Am} and E^i_{Gd}. Here i denotes the type of entrance-windows. $i = 0$ is BNL-type and $i = 1, 2$ Hamamatsu-type.

Then we have :

$$E_{Am} = E^i_{Am} + \Delta E^i_{Am}, \tag{3.2}$$
$$E_{Gd} = E^i_{Gd} + \Delta E^i_{Gd}, \tag{3.3}$$

where ΔE^i_{Am} and ΔE^i_{Gd} include the energy loss in the entrance-window and the energy pedestal.

The deposit energy (E^i_{Am} and E^i_{Gd}) are connected with the $INTG$ readings (Ami and Gdi) via C_E.

$$E^i_{Am} = C_E \times Ami, \tag{3.4}$$
$$E^i_{Gd} = C_E \times Gdi. \tag{3.5}$$

BNL-type Figure 3.17 displays the ratios of $Am0$ and $Gd0$ for all 16 channels (ch #64 – ch #80) of Si #5. As we described in Subsection 2.2.3, Si #2 and Si #5 are BNL-type. Since only Si #5 in the left-side is calibrated by two sources, we presume Si #2 is comparable level in the entrance-window thickness to Si #5 by comparing the width of $INTG$ for ^{241}Am source spectra. We set the error of $INTG$ readings of peak on the $Am0$ and $Gd0$ are 1.5 digits. Thus the mean ratio $Gd0/Am0$ for the first 10 channels is estimated to be 0.575 ± 0.001. The ratio of calibration source energy is obtained as $E_{Gd}/E_{Am} = 0.580 \pm 0.001$. Here we set the width of significant energy spectra for calibration sources are 1 keV. (We did not use the channels of ch #75–ch #80 with empty circles for the asymmetry calculations. Because the waveforms are not uniform compare to other channels.

Comparing these ratios, we can assume that the energy loss in the entrance window is quite small and can assume that the energy pedestal would dominate ΔE^0_{Am} and ΔE^0_{Gd}. If we refer to the energy pedestal as δ^0, Equations (3.2), (3.3) are rewritten as

$$E_{Am} = E^0_{Am} + \delta^0, \tag{3.6}$$
$$E_{Gd} = E^0_{Gd} + \delta^0. \tag{3.7}$$

Figure 3.18 displays δ^0 for 16 channels of Si #5. The estimated δ^0 is 50 ± 30 keV. This value is smaller than the intrinsic pulse-height digitize resolution inside of WFD modules. Thus, we treat the incident energy is same as the deposit energy for BNL-type detector, $T_R = E_R$. Just for the reference, the energy loss of 50 ± 30 keV corresponds to 0.3 ± 0.2 μm in terms of the entrance-window thickness.

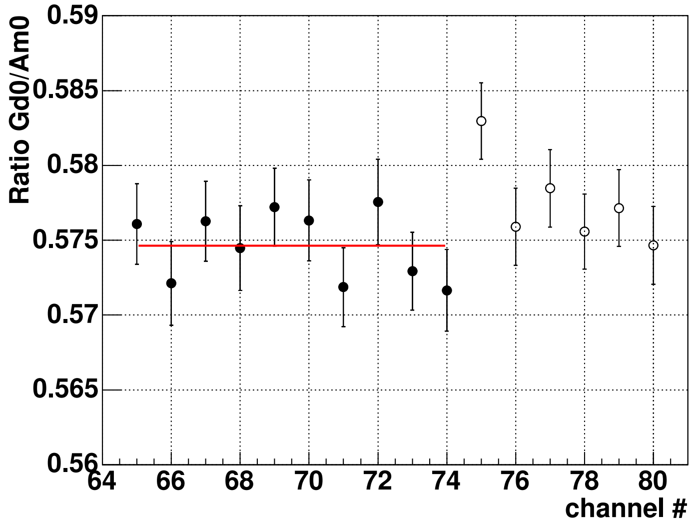

Figure 3.17: The ratio of $INTG$ peak position $Gd0$ and $Am0$ (We used the channels with filled circle only)

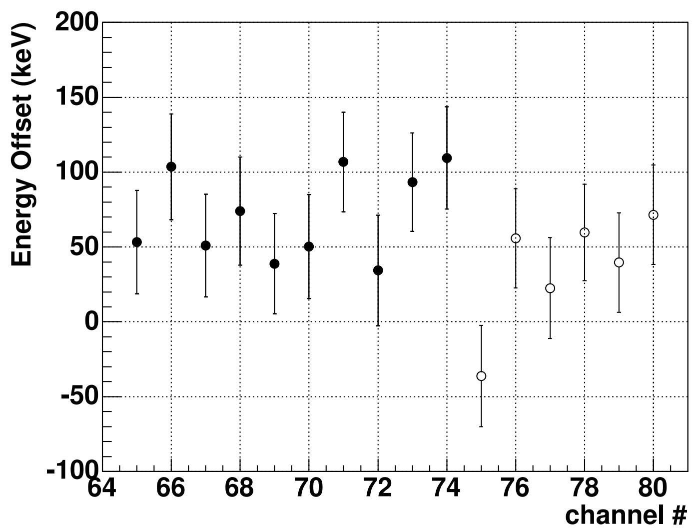

Figure 3.18: The energy offset for BNL detector. (We used the channels with filled circle only)

Hamamatsu-type Double peaks of $INTG$ spectrum in Figure 3.16 implies the double structures of the entrance-window. Although we do not have accurate design values of the entrance-window, two types of the entrance-window are possible as displayed in Figure 3.19.

Figure 3.19 depicts the cross-section of Hamamatsu-type.

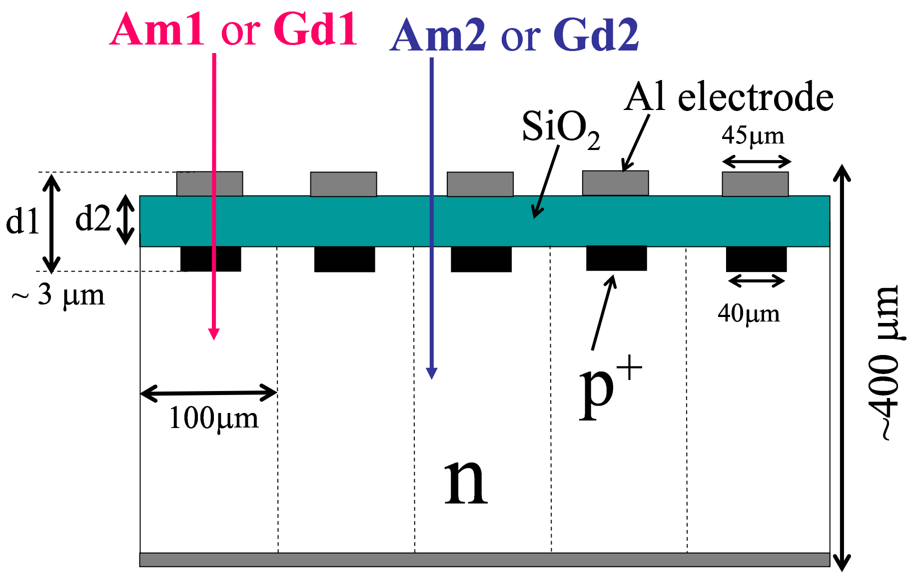

Figure 3.19: Cross section of Hamamatsu-type silicon. $d1$ and $d2$ are the thickness of 2 different types of entrance window.

Here we refer to the thickness of two types of entrance-windows as $d1$ and $d2$, respectively. $d1$ is expected to be around $2 \sim 3$ μm from designed values. In the case that the calibration α particles penetrate the thickness $d1$, the spectra will be $Am1$ and $Gd1$. The energy loss in the silicon material is evaluated by use of the stopping-power data as displayed in Figure 3.20 [61]. For example, if 5.486 MeV α particle penetrates the 3 μm thickness silicon, a deposit energy would be amounted to $\sim$ 0.6 MeV. The deposit energy in the silicon detector is not same as the incident kinetic energy but is small. Therefore we can not neglect the energy loss in the entrance-window in order to satisfy the required energy resolution (better than ~ 0.1 MeV). And the estimation of the entrance-window thickness in the order of sub-μm is required.

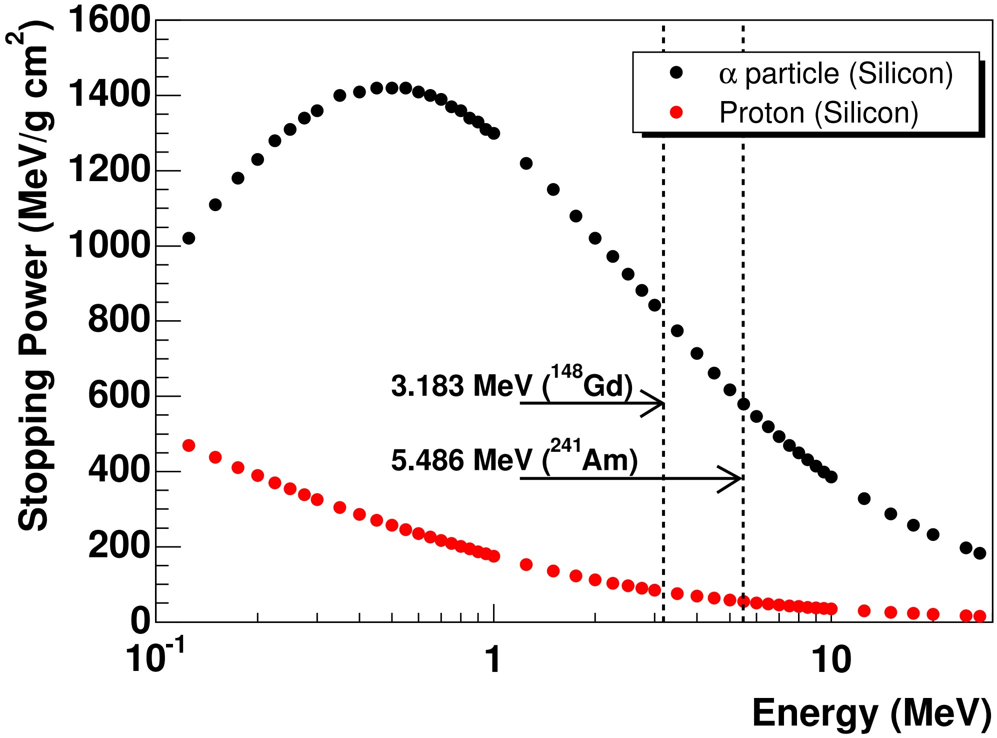

Figure 3.20: Stopping Power in the silicon material for α particle and proton as a function of the injection energy of each particle [61]

i	Entrance Window Thickness in μm	^{148}Gd ($E_{Gd} = 3.183$ MeV)		^{241}Am ($E_{Am} = 5.486$ MeV)	
		ΔE^i_{Gd} (MeV)	E^i_{Gd} (MeV)	ΔE^i_{Am} (MeV)	E^i_{Am} (MeV)
1	d1 = 2.69 ± 0.06 μm	0.55 ± 0.02	2.63 ± 0.02	0.39 ± 0.01	5.10 ± 0.01
2	d2 = 1.79 ± 0.06 μm	0.34 ± 0.02	2.84 ± 0.02	0.24 ± 0.01	5.24 ± 0.01

Table 3.1: The energy loss in the entrance-window and deposit energy in the fiducial volume for Hamamatsu-type detector.

Assigning $i = 1, 2$ to Equation (3.2) and (3.3), we have the four ratios:

$$\frac{Gd1}{Am1} = \frac{E^1_{Gd}}{E^1_{Am}} = \frac{E_{Gd} - \Delta E^1_{Gd}}{E_{Am} - \Delta E^1_{Am}}, \tag{3.8}$$

$$\frac{Gd2}{Am2} = \frac{E^2_{Gd}}{E^2_{Am}} = \frac{E_{Gd} - \Delta E^2_{Gd}}{E_{Am} - \Delta E^2_{Am}}, \tag{3.9}$$

and,

$$\frac{Gd1}{Gd2} = \frac{E^1_{Gd}}{E^2_{Gd}} = \frac{E_{Gd} - \Delta E^1_{Gd}}{E_{Gd} - \Delta E^2_{Gd}}, \tag{3.10}$$

$$\frac{Am1}{Am2} = \frac{E^1_{Am}}{E^2_{Am}} = \frac{E_{Am} - \Delta E^1_{Am}}{E_{Am} - \Delta E^2_{Am}}, \tag{3.11}$$

where ΔE^i_{Am} and ΔE^i_{Am} $(i = 1, 2)$ are dominated by the energy loss in the entrance-window. The energy loss in the entrance-window is estimated to be several hundred of keV assuming the thickness is order of few μm and on the other hand, the energy pedestal is estimated to be only several tens of keV as we discussed in the previous section.

Figure 3.3.1 displays the ratios of Equation (3.8) and (3.9). $d1$ and $d2$ are estimated using Equation (3.8), (3.9) and the stopping power in Figure 3.20. Firstly we set some initial value for the entrance-window thickness, and we repeat the iteration with changing the entrance-window thickness, then we find the convergence values. Here, Si $\#1$ and Si $\#3$ are also Hamamatsu-type detectors but they are not calibrated by ^{148}Gd source. Therefore we presume Si $\#1$ and Si $\#3$ are comparable level in the entrance-window thickness to Si $\#4$ and Si $\#6$.

Figure 3.22 displays these ratios of Equation (3.10) and (3.11). The difference of thickness between $d1$ and $d2$ is estimated independently by use of Equation (3.10) and (3.11). This result is useful for a redundant check. Particularly, Equation (3.11) is applicable for all 4 Hamamatsu-type detectors.

In a strict sense, the silicon detector is made of silicon, aluminum and SiO_2 mainly. Because the deference for the correction of the incident proton energy between three materials are known to be small, We estimated the entrance-window thickness in terms of silicon material.

The two types of entrance-window thicknesses $d1$ and $d2$ are estimated to be 2.69 ± 0.06 μm and 1.69 ± 0.06 μm, respectively. The difference between $d1$ and $d2$ is estimated to be ~ 1 μm. Therefore we have consistent results for $d1$ and $d2$ from Equation (3.8) – (3.9), Figure 3.3.1 and 3.22.
The energy loss in the entrance-window (ΔE^i_{Gd}, ΔE^i_{Am}) and the deposit energy in the fiducial volume (E^i_{Gd} and E^i_{Am}) are listed in Table 3.1.

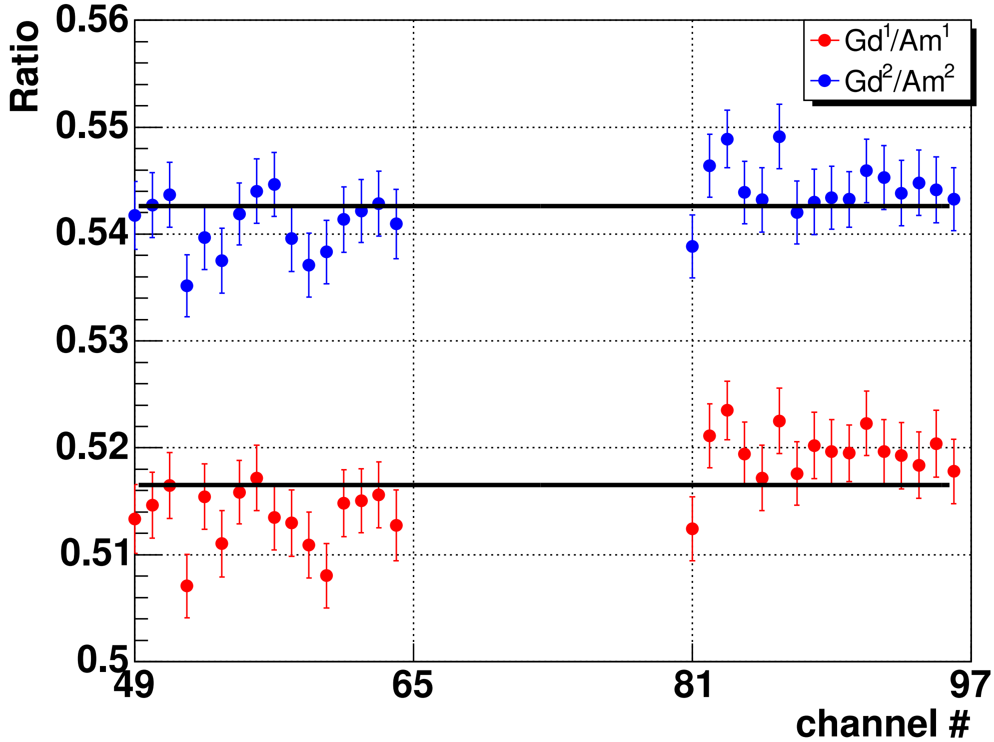

Figure 3.21: The ratios of $Gd1/Am1$ and $Gd2/Am2$ for Si$\#4$ and $\#6$ in Equation (3.8) and (3.9). $d1$ and $d2$ are estimated by use of these ratios to 2.69 ± 0.06 μm and 1.69 ± 0.06 μm.

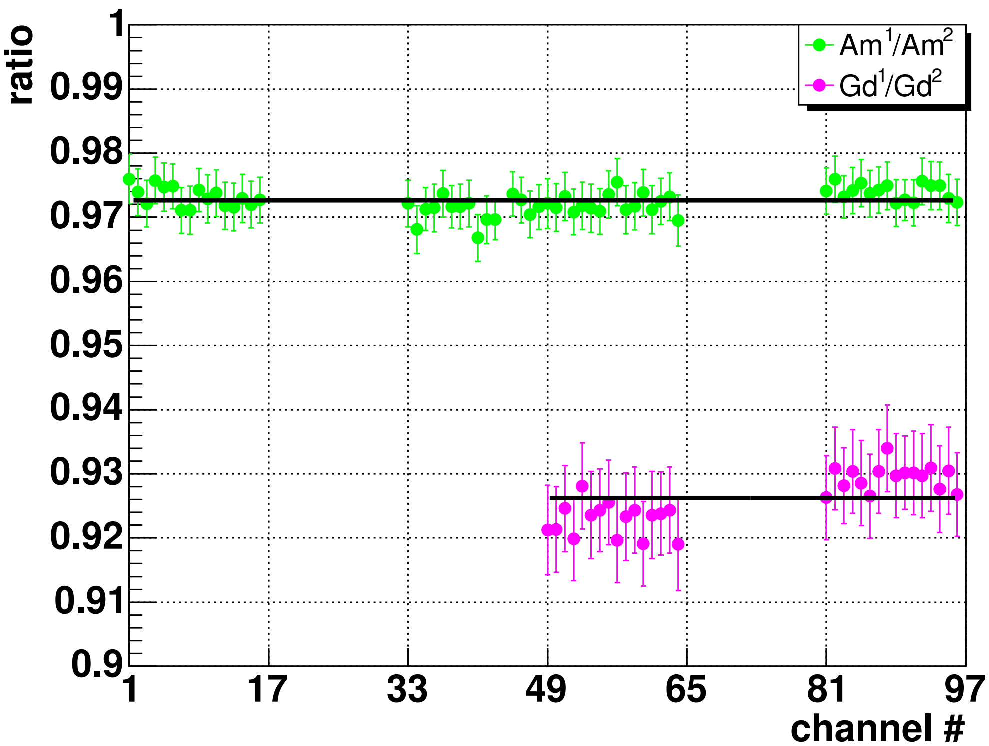

Figure 3.22: The ratios of $Gd1/Gd2$ and $Am1/Am2$ for Si $\#1, 3, 4$ and $\#6$. We confirmed the difference between $d1$ and $d2$ is 1 ± 0.06 μm.

Stability of C_E

We can obtain C_E by use of Equation (3.4) for all read-out channels. Figure 3.23 displays the stabilities for C_E of 16 read-out channels of Si $\#1$.

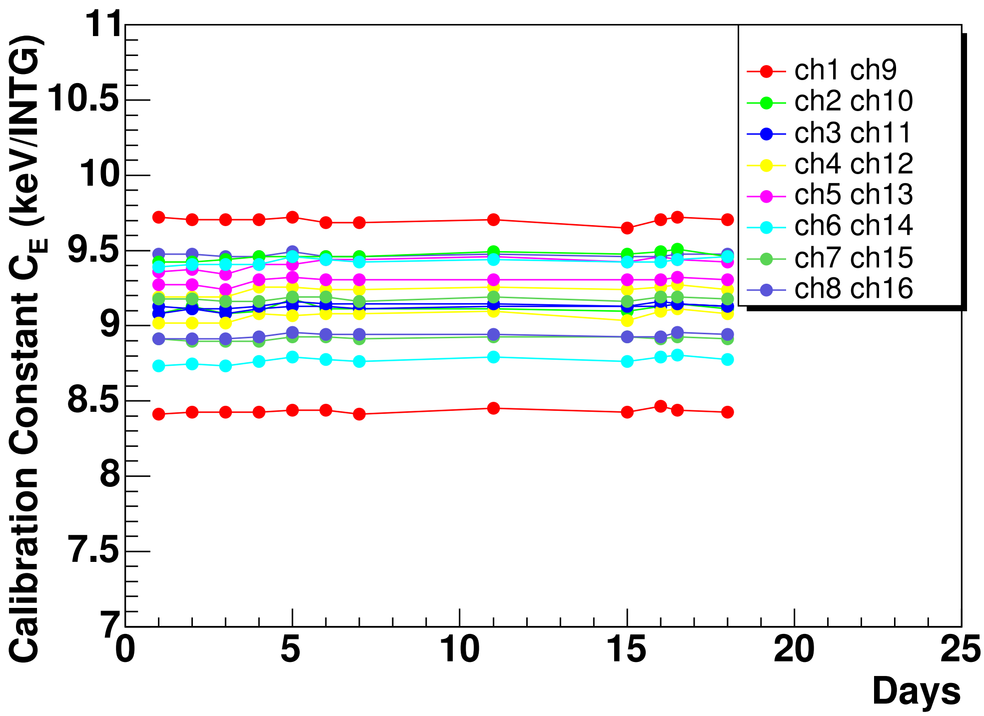

Figure 3.23: The stability of C_E of Si $\#1$during RUN-4 period.

C_E for all 96 read-out channels are stable: $\Delta C_E \leq 1$ (keV/INTG) during run period.

3.3.2 Energy Loss Correction

$T_R < 5$ MeV region

Taking into account for the entrance-window thickness, the kinetic energy of recoil proton (T_R) is reconstructed. As displayed in Figure 3.20, the energy loss of the proton in the entrance-window is less than one sixth that of α particles at the same energy. Since the entrance-window thickness of BNL-type silicon is quite thin, 200 ± 100 nm and the energy loss of the recoil proton is below the intrinsic energy resolution, we do not need to correct the energy loss in the entrance-window of BNL-type. Therefore the kinetic energy of recoil proton is obtained as:

$$T_R = E_R = C_E \times INTG. \tag{3.12}$$

On the other hand we need to correct the energy loss in the entrance-windows for Hamamatsu-type. We calculate the energy loss in the entrance-window for three different incident proton energies, 0.5, 0.75 and 1 MeV using Figure 3.20. The results are summarized in Table 3.2. The first

T_R (MeV)	ΔE_p^1 (MeV)	ΔE_p^2 (MeV)	ΔE_p^2-ΔE_p^1 (MeV)
0.5	0.16 ± 0.02	0.11 ± 0.01	0.05
0.75	0.14 ± 0.01	0.09 ± 0.01	0.05
1.0	0.11 ± 0.01	0.07 ± 0.01	0.04

Table 3.2: The energy loss comparison between two different entrance-windows with several incident energies. The first column is the incident kinetic energies T_R, the second and third column are the energy losses, ΔE_p^1 and ΔE_p^2, in the entrance-windows $d1$ and $d2$. The forth column is a difference of the energy losses between two entrance-windows.

column is the incident kinetic energies T_R, the second and third column are the energy losses, ΔE_p^1 and ΔE_p^2 in the entrance-windows $d1$ and $d2$. The forth column is difference of the energy losses between two entrance-windows.

As T_R increases, ΔE_p^1 and ΔE_p^2 decreases and the energy loss become negligible in the $T_R > 1$ MeV region.

The difference of energy losses between $d1$ and $d2$ ($\Delta E_p^2 - \Delta E_p^1$) is smaller than the energy resolution ($\sim$ 0.07 MeV). Actually, we can not distinguish which entrance-window the recoil proton penetrates. The recoil proton is expected to penetrate the two of entrance-windows equally from the rough schematic as displayed Figure 3.19 and the $INTG$ spectrum as displayed in Figure 3.16. In this way, we conclude that we take the average of $d1$ and $d2$ and use as an "effective" entrance-window thickness (2.24 ± 0.1 μm). And the conversion function from E_R to T_R is obtained as:

$$T_R = -0.0045 \times E_R^3 + 0.0378 E_R^2 + 0.8836 E_R + 0.1756. \quad (3.13)$$

The calibration energy uncertainty from dead layer thickness uncertainty (± 5 μm) is quite small ~ 0.01 MeV.

$T_R \geq 8$ MeV Region

Figure 3.24 displays the correlation of the channel number and the deposit energy (E_R) of roughly ToF-selected events. The locus on the left in Figure 3.24 is generated by fully absorbed protons, while the locus on the right is due to punched-through protons. The red arrow in Figure 3.24 indicates the channel which is measured the maximum deposit energy, for example, ch $\#8$ of Si $\#1$. We refer it to a *critical* channel.

We estimate the fiducial volume thickness by use of the *maximum* deposit energies. We call this procedure, (A).

In order to evaluate uniformity of the fiducial thickness among whole detector, we utilized several channels displayed with blue arrow in Figure 3.24 and rough angle data. We call this procedure, (B), and refer these channels to *punched-through* channels. In both procedures, the fiducial detector thickness is estimated in terms of silicon material using the stopping-power in Figure 3.20.

We will describe the procedure (A) in the text. The details of procedure (B) are described in Appendix A.10. As a redundant check for (A), we use the parameterized formula, called (C). The results of the procedure (A), (B) and (C) agree very well, as we discuss later.

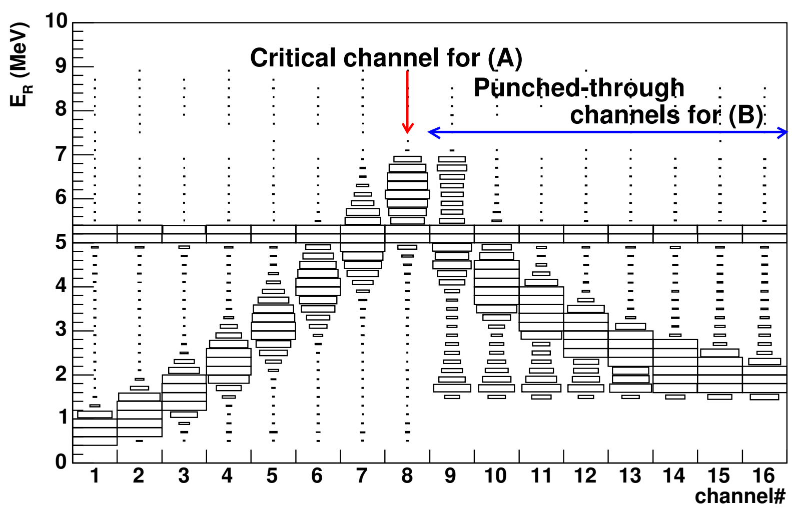

Figure 3.24: E_R and channel number correlation and the explanation of procedure A,B

The Procedure Using the *Maximum* Deposit Energy ; (A)

Figure 3.25 and -3.26 display the energy spectrum of the *critical* channels of Hamamatsu-type (Si$\#1$, $\#3$, $\#4$ and $\#6$) and BNL-type (Si4$\#2$ and $\#5$) silicon detectors. The spectrum have the steep shoulder at the maximum deposit energy. Actually, the *critical* channel detects fully deposit protons and punched through protons simultaneously. But we can not distinguish them in *ToF* as we discuss later in Subsection 3.3.2.

Figure 3.27 is the energy spectrum of selected *critical* channels of Si $\#1$ for the whole run4 period. This figure tells us the stability of the maximum deposit energy during run period and confirms that the fiducial detector thickness is stable.

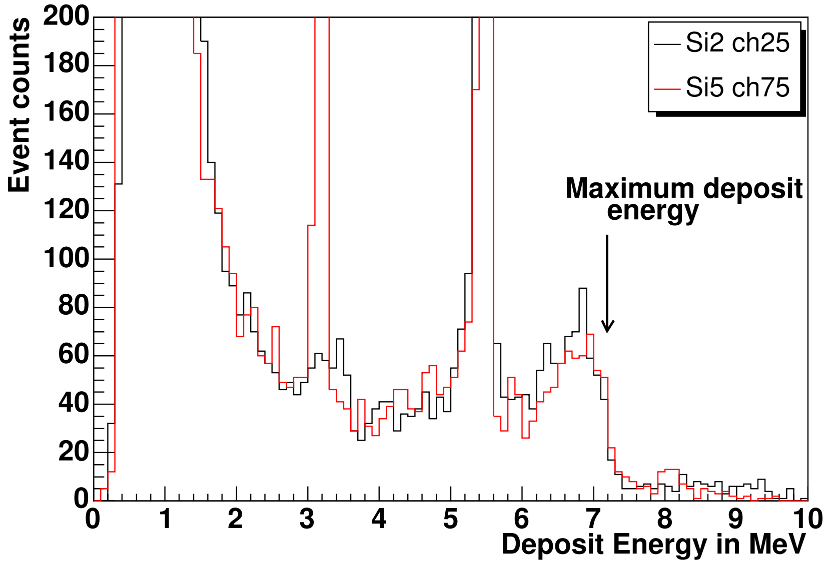

Figure 3.25: Energy spectrum of *critical* channels of BNL detector (ch#25 and #75)

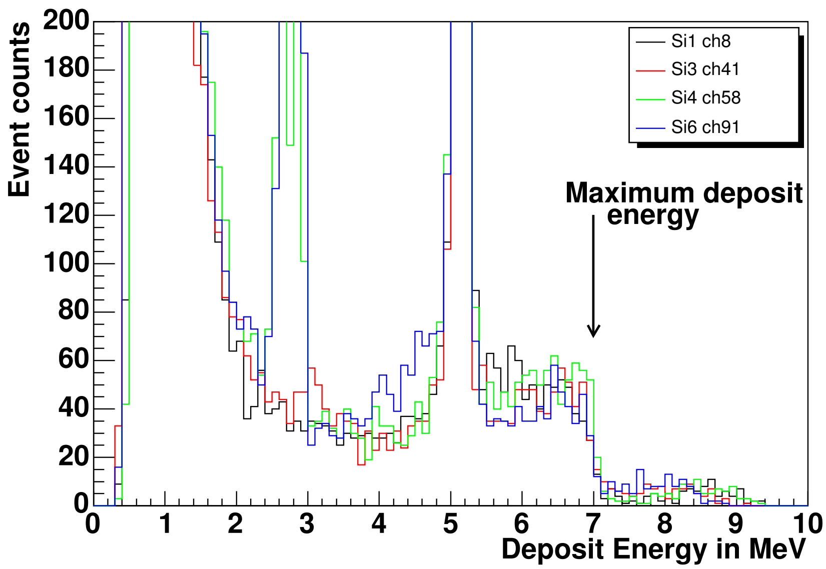

Figure 3.26: Energy spectrum of *critical* channels of Hamamatsu-type detector (ch #9, #41, #58 and #91)

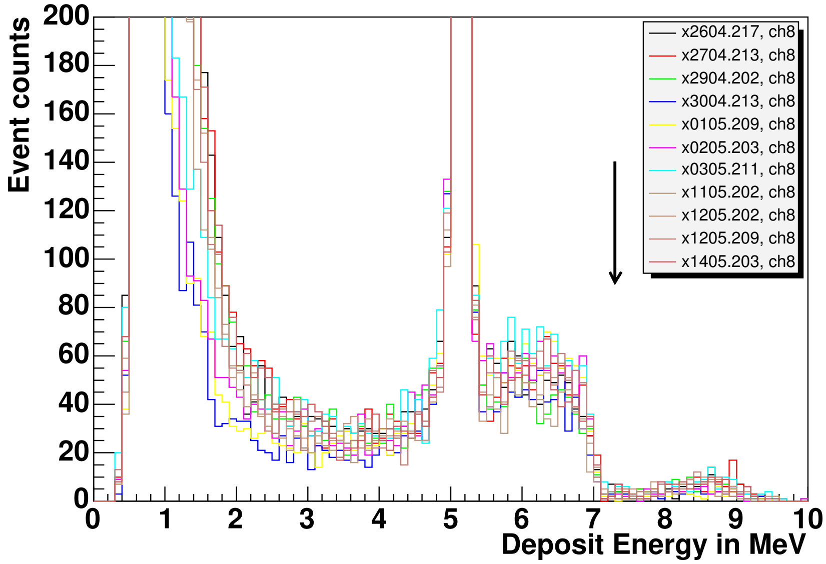

Figure 3.27: Maximum deposit energy stability of ch #8 (Hamamatsu-type) for RUN4 period

From these results, the maximum deposit energies are same between the same manufactured detectors. The maximum deposit energies are 7.0 ± 0.1 MeV for Hamamatsu-type and 7.3 ± 0.1 MeV for BNL-type, respectively. Then we can estimate effective thickness as below.

By use of the stopping-power in Figure 3.20, the estimated results of procedure (A) are 385 ± 5 μm for Hamamatsu and 414 ± 5 μm for BNL, respectively. The resolution ± 5 μm is come from the sharpness of the spectrum.

Comparison of the Estimated Thickness Among (A), (B) and (C)

In addition to the results from (A) and (B), we also used parameterized formula [62] to estimate the fiducial thickness of silicon with proton deposit energy with good accuracy over the range of energies E (MeV). We call this procedure (C) and the formula is:

$$R(mm) = 0.004 + 0.01333 \cdot E^{1.73}. \tag{3.14}$$

$E = 7 \pm 0.1$ MeV corresponds to $R = 389 \pm 10\mu$m (Hamamatsu-type), $E = 7.3 \pm 0.1$ MeV corresponds to $R = 418 \pm 10\mu$m (BNL-type).

Table 3.3 summarized the estimated fiducial thicknesses by different procedures (A), (B) and (C).

The results from procedure (A), (B) and (C) agree within the errors. In summary, we fixed the actual detector thicknesses are 414 μm for Hamamatsu and 385 μm for BNL. Uniformity of the fiducial volume thickness of whole detector is estimated to be ± 10 μm from the results of procedure (B). The corresponding energy uncertainty differs depend on T_R, for example, ± 90 keV for $T_R = 10$ MeV and ± 200 keV for $T_R = 16$ MeV, respectively.

Actually, the energy resolution for punched-through region is worse than the required energy resolution. But these energies beyond the expected region of the CNI peak (1 – 5 MeV). Therefore we do not need to set narrow energy bins and the energy resolution is allowable.

Procedure type	BNL-type (μm)	Hamamatsu-type (μm)
(A)	414 ± 5	385 ± 5
(B)	420 ± 10	380 ± 10
(C)	418 ± 10	389 ± 10

Table 3.3: Comparison of the fiducial thickness of silicon detector for Hamamatsu-type and BNL-type.They agree within the errors

T_R reconstruction in Critical Channels

By use of estimated detector thickness, we have an itemized the conversion table between deposit energy and incident energy. Fitting the correspondence with polynomial function, we got the functions to convert E_R into T_R for the punched-through protons. The details are described in Appendix A.9.

Here we discuss about the treatment of the *transition* region of "punched-through" and "full deposit" events. We set *punched-through* channels using Figure 3.24. However, we can not distinguish the punched-through protons from fully absorbed protons if they are detected in the "critical" channels. For example, if we apply punch through correction to the proton, whose deposit energy is $E_R = 6.0$ MeV, the reconstructed incident energy is estimated to be $T_R = 7.2$ MeV. The calculated *ToF* from the kinetic energy is 23.6 nsec for $T_R = 6.0$ MeV and 21.5 nsec for $T_R = 7.2$ MeV. Since the intrinsic time resolution is 1.19 nsec, it is hard to distinguish between fully absorbed proton and punched-through proton by ToF in the *transition* energy region of energy. Therefore, we do not apply the punched-through correction for the events of the *critical* channels but apply for the events of the beyond *critical* channels. This made the in-continuity of the T_R spectrum around 7.5 MeV.

Figure 3.28 displays energy conversion function from $INTG$ to T_R (MeV) for the entire T_R range of one of read-out channel of Hamamatsu-type silicon detector considering the loss energy in the entrance-window thickness. Black solid line corresponds T_R reconstruction for full-absorbed protons. Red solid line corresponds T_R reconstruction for punched-through protons. Black and red dashed lines correspond to the *transition* energy protons.

3.3.3 Resolution and Binning

The resolution of the deposit energy is estimated ~ 0.07 MeV from the calibration source spectra. We applied two different types of energy corrections regarding the incident energies. One is the entrance-window energy corrections and the other is the punched-through energy correction. Therefore, we need to estimate the systematic errors regarding the incident energies.

Systematic Errors in Energy Calibration

***Lower* energy region ($<$ 1 MeV) for Hamamatsu-type silicon detectors** To reconstruct the incident kinetic energy in the *lower* region of less than ~ 1 MeV, we need to add the lost energy in the entrance window. We estimated *averaged* entrance window thickness is 2.24 ± 0.10 μm. The possible source for the systematic error in this energy region is the error of entrance window thickness. And then, the systematic errors is estimated quite small in the order of 0.05 MeV. It is negligible small value.

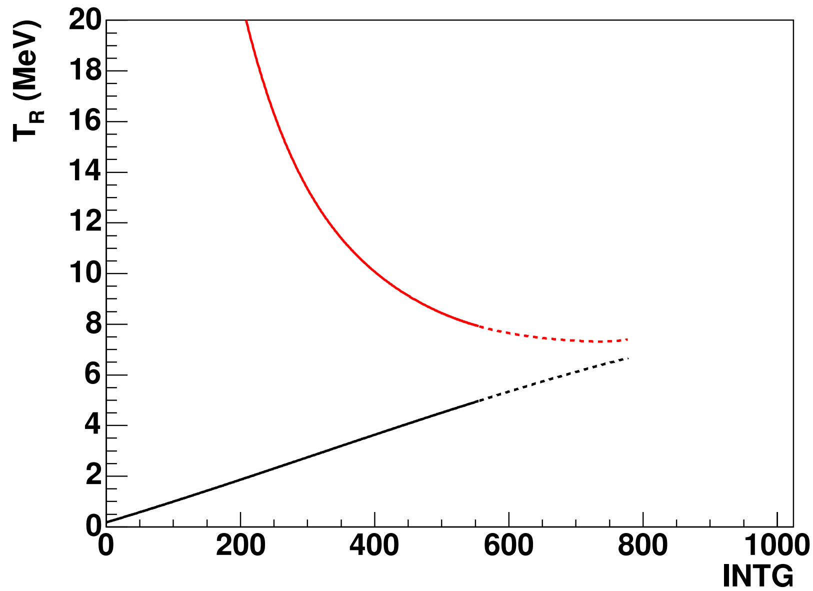

Figure 3.28: Energy conversion from $INTG$ to T_R (MeV) for one of read-out channel of Hamamatsu-type silicon detector considering the loss energy in the entrance-window thickness. Black solid line corresponds T_R reconstruction for full-absorbed protons. Red solid line corresponds T_R reconstruction for punched-through protons. Black and red dashed lines correspond to the *transition* energy protons.

***Higher* energy region (> 8 MeV)** For the *higher* energy resolution more than 8 MeV, we need to care about punched-through corrections. The silicon detector can not stop completely the protons more than 7 MeV for BNL-type and 7.3 MeV for Hamamatsu-type. To reconstruct the incident kinetic energy correctly, we need to add the outgoing energy to the measured deposit energy. The possible source for the systematic error in this *higher* energy region is the error of the depleted thickness. We estimated the depleted thicknesses are 385 ± 10 μm and 414 ± 10 μm for Hamamatsu-type detectors and BNL-type detectors, respectively. The systematic errors in the higher energy region is estimated to be ± 0.1 MeV for $T_R < 10.6$ MeV and ± 0.2 MeV for $T_R > 10.6$ MeV.

Between 5 – 8 MeV region It is quite difficult to distinguish the proton is full absorbed or not in this energy region by use of *ToF* nor angle information. In actual analysis, I do punched-through correction for the event beyond ”critical channel”. This procedure can make wrong energy correction in case of wrong event type assignment. For example the proton of 6.5 MeV in terms of deposit energy, is 7.5 MeV in terms of punched-through corrected energy. The miss event assignment whether the event was full deposit or not can be a systematic error source. To reduce this affection, we putted together these energy region events into one binning (5.7 – 7.2 MeV) . And we set the systematic error is ± 0.2 MeV

The other region ($1 \leq T_R \leq 5$ MeV) In this energy region, the recoil proton is fully absorbed in the silicon detector and its energy loss in the entrance-window is negligible. Therefore the incident kinetic energy is obtained from $INTG$ directly:

$$T_R = C_E \times INTG,$$

and there is no systematic uncertainty.

Energy Binning

Our energy bin for asymmetry calculation is below table. The energy gaps between bin5 and 6, bin12 and 13 are to avoid calibration α particles from ^{148}Gd source. The energy gaps between bin8 and 9, bin9 and 10 are to avoid calibration α particles from ^{241}Am source. The mixture of full deposit and punched through energy region is bin9.

	Incident Energy T_R (MeV)		
BIN#	minimum	maximum	Systematic Error
1	0.6	1.0	0.05
2	1.0	1.4	-
3	1.4	1.8	-
4	1.8	2.2	-
5	2.2	2.5	-
–	^{148}Gd α source energy region		
6	3.0 (3.2 for BNL- type)	3.5	-
7	3.5	4.2	-
8	4.2	4.7	-
–	^{241}Am α source energy region		
9	5.7	7.2	$\pm$ 0.2
–	^{241}Am α source energy region (punched-through treatment)		
10	8	9.3	$\pm$ 0.1
11	9.3	10.6	$\pm$ 0.1
12	10.6	12	$\pm$ 0.2
–	^{148}Gd α source energy region (punched-through treatment)		
13	14.5	16	$\pm$ 0.2
14	16	17	$\pm$ 0.2

Table 3.4: T_R binning

3.4 ToF of Recoil Protons

In this section, we will discuss how we get ToF of the recoil protons as well as the resolution.

3.4.1 Conversion from T_{meas} to ToF

Silicon detectors measure the arrival time of the recoil proton, T_{meas} :

$$T_{arrival} = T_{meas} \times C_{ToF} \text{ (nsec/digit)}.$$

where $C_{ToF} = 1.19$ (nsec/digit) is the time scale constant, which is determined by the intrinsic time resolution of DAQ. The trigger of T_{meas} coincides with internal clock of our DAQ system at the equivalent frequency of 420 MHz. $T_{arrival}$ is a sum of the collision time between the H-Jet target proton and RHIC-beam proton ($T_{collision}$), signal process time ($T_{process}$) and *ToF* of the recoil proton.

ToF is written as:

$$ToF = T_{arrival} - (T_{collision} + T_{process}), \tag{3.15}$$

and the resolution of *ToF* is obtained by quadratic sum of possible three possible components (ΔT_{event}, $\Delta T_{process}$ and $\Delta T_{arrival}$):

$$\Delta ToF = \Delta T_{collision} \oplus \Delta T_{process} \oplus \Delta T_{arrival}. \tag{3.16}$$

It is important to fully understand of these components in order to evaluate ΔToF.

3.4.2 ToF resolution

Expected Resolution

$T_{collision}$ would fluctuate because of:

- RHIC rf-clock might fluctuate < 0.5 nsec.
- RHIC beam bunch size, which measured by WCM $\sigma \sim 2.2$ nsec as displayed in Figure 3.29.
- H-Jet target size ~ 0.021 nsec (FWHM = 6.5 mm).

Therefore $\Delta T_{collision} \simeq 2.2$ nsec.

$T_{process}$ consists of:

- Charge correction time in the silicon detector.
- Signal process time at several electric process stages: charge-sensitive preamplifier, shaping-amplifier and attenuator etc.
- The signal transfer time from the RHIC-ring tunnel to the counting house via twisted pair cables (~ 55m).

Thus $T_{process}$ is independent and is slightly different among read-out channels. But it is expected to be quite stable during data taking period. Therefore $\Delta T_{process}$ is negligible.

$T_{arrival}$ would fluctuate because of:

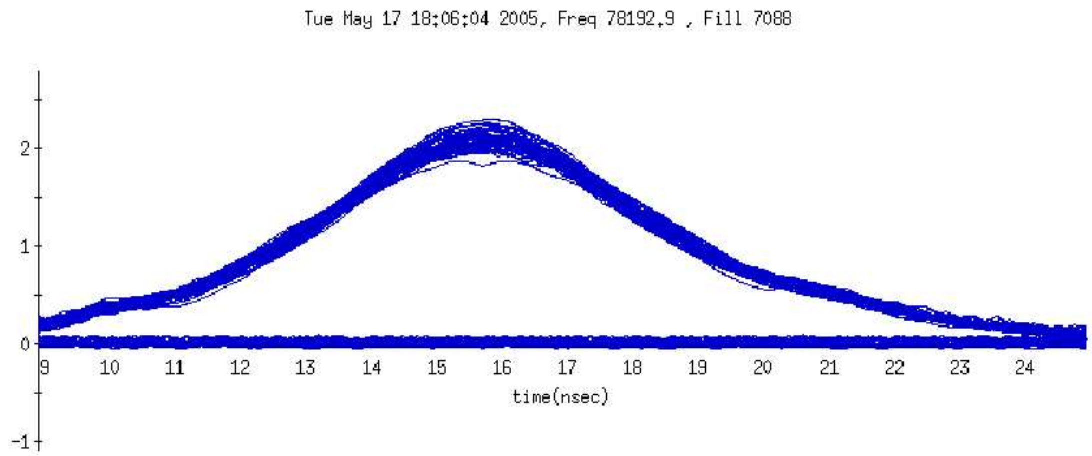

Figure 3.29: Typical beam bunch profiles measured Wall Current Monitor (WCM) [53]. Data of 112 bunches and abort gap are superimposed.

- Trigger start timing might fluctuate 2.4 nsec (Internal DAQ clock has the equivalent frequency of 420 MHz). This is common to all read-out channels.
- The intrinsic time resolution of DAQ (1.19 nsec).
- *Rise-Time* stability of waveforms ~ 0.7 nsec as discussed in Subsection 3.2.2.

Therefore, $\Delta T_{arrival} \simeq 2.8$ nsec.

Substituting $\Delta T_{collision}$, $\Delta T_{process}$ and $T_{arrival}$ into Equation (3.16),

$$\Delta ToF \sim 3.6 \text{ nsec}. \tag{3.17}$$

Considering these possible components, $T_{collision}$, $T_{process}$ and their resolutions are stable whole run period. $\Delta T_{arrival}$ is also expected to be stable. Therefore we expect that ΔToF is also stable whole run period.

Comparison between "Expected" and "Achieved" Resolutions

By use of the kinetic energy T_R of recoil proton, the flight path length L and the mass of proton m_p, we calculate "expected" the time of flight of recoil proton, ToF_{calc}.

$$ToF_{calc} = L \cdot \sqrt{\frac{m_p}{2 \cdot T_R}}, \tag{3.18}$$

In principle, we obtained the sum of $T_{collision}$ and $T_{process}$ instead we estimate each of them. Because both of them are stable, we can treat the sum of them as mere offset value. We refer this offset value to $t0$.

We take a difference between $T_{arrival}$ and ToF_{calc} for event-by-event and have a distribution of $t0$ as displayed in Figure 3.30.

The events around 55 nsec are regard as possible candidates for recoil protons. This figure is the for one of read-out channels.

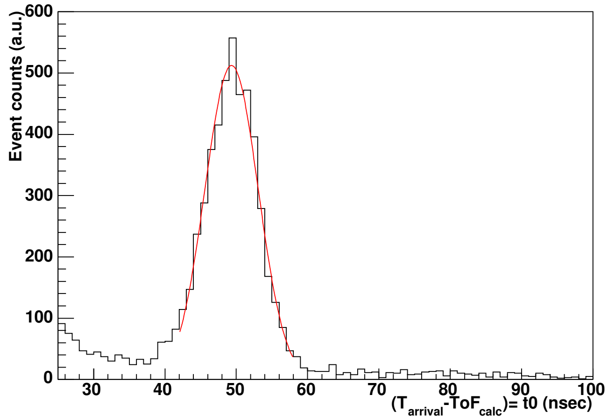

Figure 3.30: $t0$ distribution for one of read-out channels. The mean value of Gauss fit corresponds to the offset value (= $T_{collision} + T_{process}$).

We applied Gaussian fitting and take mean value of $t0$, we call $\bar{t0}$. $\bar{t0}$ corresponds to the offset value (= $T_{collision} + T_{process}$). Then we can estimate ToF of each events as Equation (3.19).

$$ToF = T_{arrival} - \bar{t0} \tag{3.19}$$

The width of $t0$ distribution is estimated to be $\sigma_{t0} \sim 3.9$ nsec and is regarded as ToF resolution, σ_{ToF}. Thus, the good agreement between the expected ToF resolution using specifications ($\Delta ToF \simeq 3.6$ nsec) and the measured ToF resolution ($\sigma_{ToF} \simeq 3.9$ nsec) confirms that we fully understand for the ToF properties.

3.5 Elastic Event Selection

As we have discussed in Section 2.1, the recoil particle identification and the mass measurement of all the rest particles, which we do not detect, are the essentials for the elastic event selection. In this section, we will describe the specific procedures of particle identifications using T_R, ToF and θ_R. Firstly we select the events which recoil particles are identified as the proton by use of T_R and ToF correlation. Then we apply further selection using the missing mass squared spectra and finally we can collect the elastic events.

3.5.1 Recoil Particle Identification

Figure 3.31 displays the correlation of T_R and *ToF*. The dotted curve is calculated by the kinematic function of Equation (3.18).

The locus of the recoil proton events is quite clear and agree with the kinematic function very well. The dotted line shows the results of kinematical function of Equation (3.18). There are four lines which are shifted $\pm 4, 8$ and 12 nsec with respect to the kinematical function.

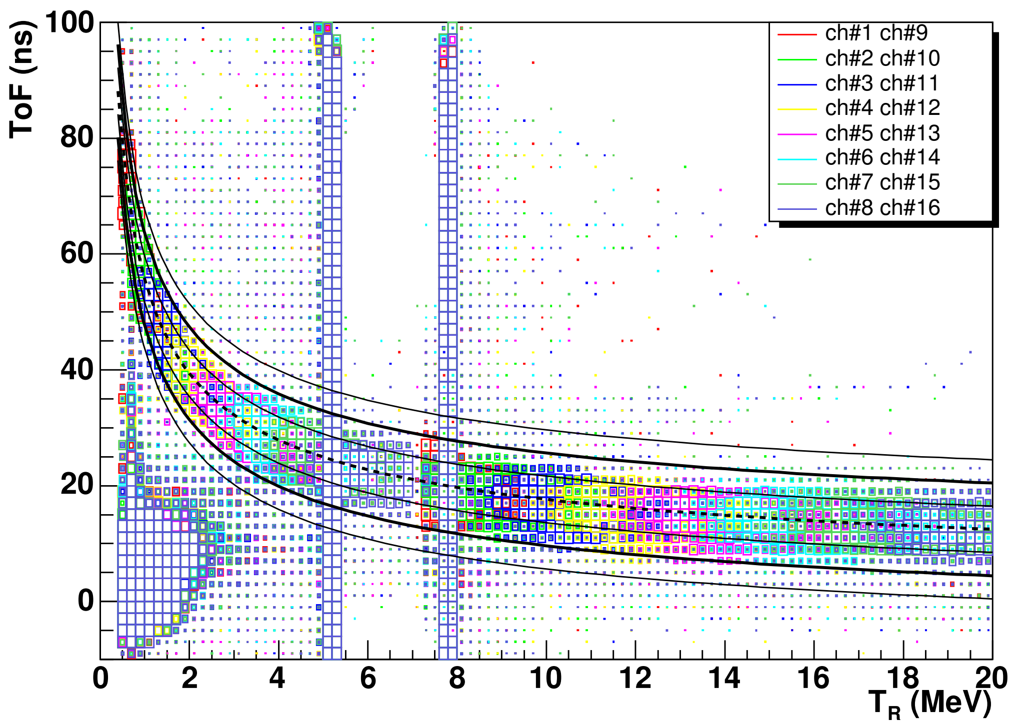

Figure 3.31: The correlation between ToF and the incident energy, T_R, in one of the silicon detectors. The dotted curve shows the kinematic function of Equation (3.18). The four lines corresponds to $\pm 4, \pm 8$ and ± 12 nsec shifted with respect to the dotted line.

The broadening of *ToF* was estimated as $\sigma_{ToF} \sim 3.9$ nsec. This width is well understood from bunch size of the RHIC-beam and specifications of the read-out electronics. The details have been discussed in Section 3.4.

Figure 3.32 displays the m_R spectrum in one of the silicon detectors with the energies $(0.6-1.4)$ MeV, (1.4-2.5) MeV, (3.0-4.7) MeV, (5.7-7.2) MeV, (8.0-12.0) MeV and (14.5-17.0) MeV. The recoil particles in the blue area are passed $(ToF_{calc} \pm 8)$ nsec cut as displayed in Figure 3.31. We regard these particles are the recoil protons. The width of m_R spectrum increases as T_R increases.

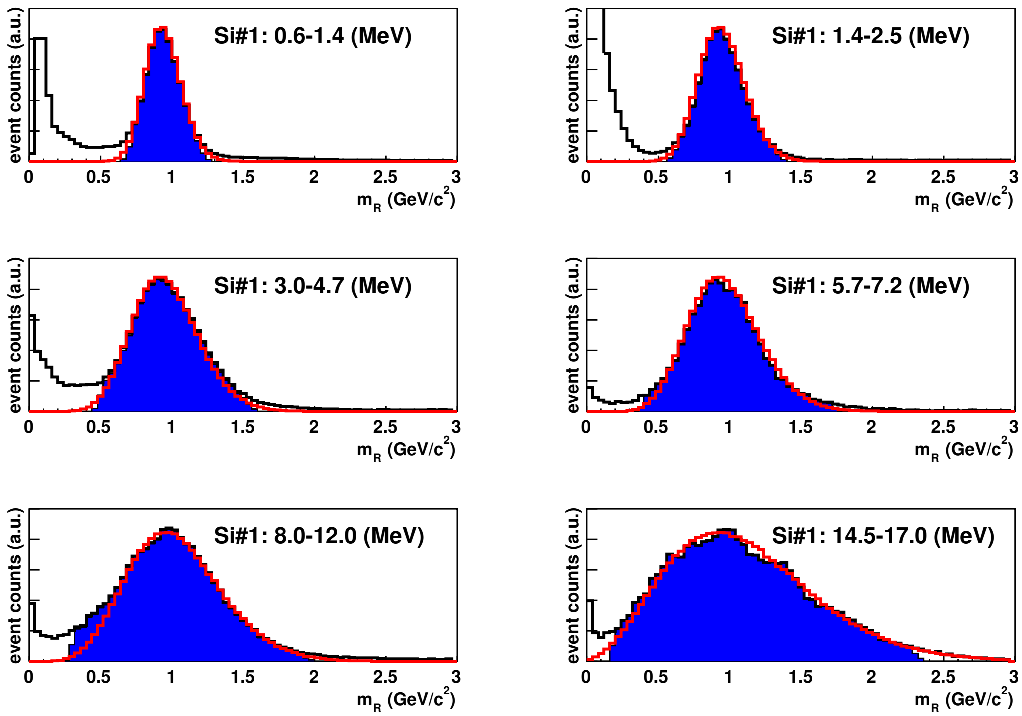

Figure 3.32: m_R spectrum of Si#1 for several energies

In order to understand the growth of blue area as T_R increases, we estimate the expected mass spectra for each energies regions with following conditions in Equation (2.3):

- T_R and ToF fluctuate as Gaussian shape with σ_{T_R} and σ_{ToF}.
- $\sigma_{ToF} = 4$ nsec. It is independent over all T_R.
- $\sigma_{T_R} =$ 0.07 MeV for $T_R < 5$ MeV and
- $\sigma_{T_R} =$ 0.20 MeV for $T_R > 10$ MeV.
- Vertical axis is normalized by peak value of the spectrum.

Red lines, which are superimposed onto the spectra, are the results of this simple estimation. They agree very well. Using Equation (3.20), we would understand the behavior of the width of blue areas (Δm_R) intuitively.

$$\frac{\Delta m_R}{m_p} = \frac{\Delta T_R}{T_R} \oplus 2\frac{\Delta ToF}{ToF} \tag{3.20}$$

The dominance of Δm_R by the first and second terms of Equation (3.20) are comparable in size at $T_R \sim 1$ MeV. For example, in case of $T_R \sim 0.6$ MeV, *ToF* is ~ 80 nsec and the size of two terms are ~ 0.1. On the other hand, the second term becomes dominant in accordance with T_R increases. In case of $T_R \sim 17$ MeV, ToF is ~ 16 nsec and the size of the first term is fifty times smaller than the second term.

The good agreement between the data and the simple simulation confirms that the blue areas in m_R spectra are reasonable and well understood. The events in blue areas in Figure 3.32 are satisfied with $|ToF - ToF_{calc}| < 8(\sim 2\sigma_{ToF})$ nsec. We regard recoil particles in blue areas as protons. ToF cut width dependence on the raw-asymmetry is included as the systematic errors.

3.5.2 M_X^2 measurement

We applied the following event selection for all events which are passed the recoil proton selection. As we have discussed in Section 2.1, M_X^2 is obtained using Equation (3.21):

$$M_X^2 = m_p^2 - 2T_R(m_p + E_1) + 2|\vec{p}_1|\sqrt{2m_pT_R}\theta_R \tag{3.21}$$

where this equation is same as Equation (2.4) but we substituted $|\vec{p}_R| = \sqrt{2m_pT_R}$, $-t = 2m_pT_R$ and $\sin\theta_R \approx \theta_R$. In case that the forward-scattered particle is proton, $M_X = m_p$, Equation (3.21) becomes:

$$T_R \simeq 2m_p\theta_R^2 \tag{3.22}$$

Thus, the correlation between T_R and θ_R comes as a consequence of a forward-scattered proton. In principle we can obtain the correct θ_R from channel number and applying the bend angle correction. The bend angle is smaller than a few mrad but it varies according to T_R because of the holding-magnetic-field in the scattering chamber (See Section 2.7). However, because of geometrical miss-alignment, the bend angle correction were not common among the silicon detectors. (The details are described in Appendix A.8.)

Although the correction of bend angle is not perfect, it does not affect the purity for the elastic event selection. Whether a scattering process is elastic or inelastic, recoil particle is always proton for either case. And recoil proton is bent in the same way as long as T_R is same.

Figure 3.33 displays the correlation between the channel number and T_R in one of silicon detectors (Si #1). Horizontal-axis is the channel number. In Si #1 case, the events less than ch #9 are thought to be fully absorbed in the detector and the events above and beyond ch #9 punched-through the detector. Then we reconstructed T_R from E_R event-by-event and applied $|ToF - ToF_{calc}| < 8$ nsec cut. These events are color-coded with 8 colors except for grays. For example, ch #1 and ch #8 are shown in red. Color-code for 16 channels are same as Figure 3.31. The solid line shows the kinematic function of Equation (3.22), (3.23) and (3.24). The line is not applied the holding-magnetic field correction to convert θ_R to channel number.

As we have displayed in Figure 2.17 and mentioned in Subsection 2.2.3, the silicon strip runs along the z-axis (RHIC-beam direction). Therefore, the hit position, Z, is obtained from the channel number.

$$Z = Z_0 + \text{ch\#} \times dZ \tag{3.23}$$

where, $Z_0 = 8$mm, $dZ = 4.4$mm (See Figure 2.17). In addition to the alignment offset, the angle data especially for low energy recoiled proton is bent by the Holding-Magnet field, θ_{Mgnt}. Therefore, the recoil angle is obtained as:

$$\theta_R = \frac{Z}{L} + \theta_{align} + \theta_{Mgnt} \tag{3.24}$$

where, $L \sim 800$mm (See Figure 2.17).

We selected "proper" channels for selecting the forward-scattered protons for 14 T_R bins.

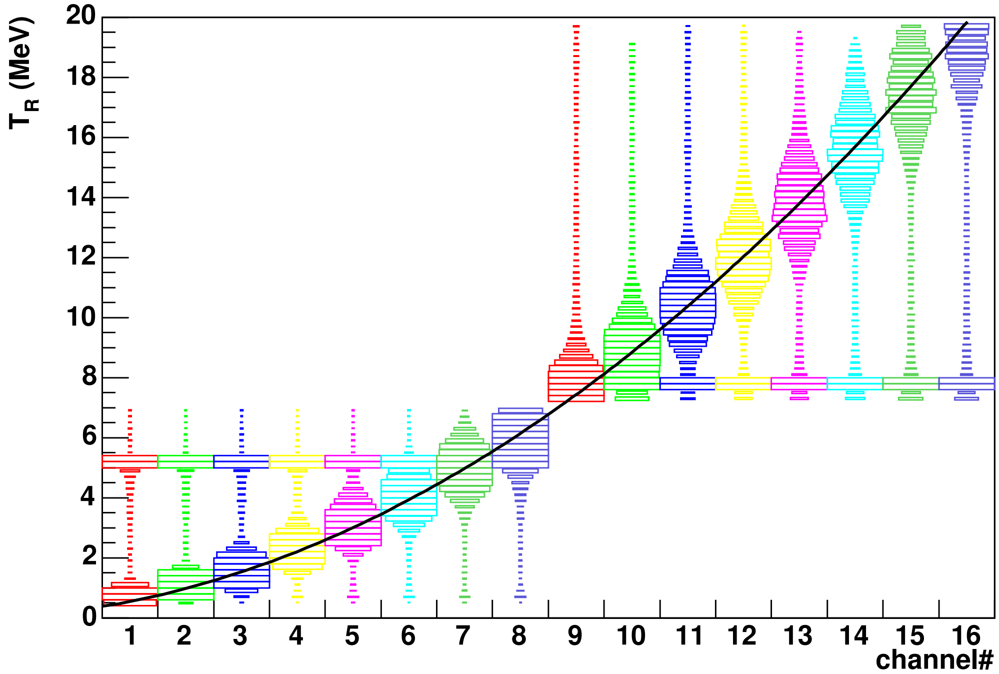

Figure 3.33: T_R and channel number correlation in one of the silicon detectors (Si #1). The events are already selected recoil protons applying $|ToF - ToF_{calc.}| < 8$ nsec cut. The solid line is kinetics function in Equation (3.22), (3.23) and (3.24). The line is not applied the holding-magnetic filed correction to convert θ_R to channel number ($\theta_{Mgnt} = 0$). The clear correlation suggests that these are the elastic *pp* scattering events.

In order to confirm whether the channel selection is reasonable, we checked the width of missing mass squared (M_X^2) spectra. Figure 3.34 displays M_X^2 spectra in one of the silicon detectors with the energies $(0.6 - 1.4)$ MeV, (1.4-2.5) MeV, (3.0-4.7) MeV, (5.7-7.2) MeV, (8.0-12.0) MeV and (14.5-17.0) MeV. Blue areas correspond to the events from selected channels. θ_{align}(=1.5 mrad) is added that the means value of blue areas in M_X^2 spectra agree with m_p^2. The width of missing mass squared (ΔM_X^2) increases as the kinetic energy increases. The remaining tails are regarded as backgrounds. They are asymmetric between left-side and right-side because we used the data from ch #1 – ch #8 for $T_R < 5$ MeV region and we used the data from ch #9 – ch #16 for $T_R > 8$ MeV region. We will mention about backgrounds in the next section.

In order to understand the growth of ΔM_X^2, we estimate the expected missing mass-squared spectra for each energy region with following conditions in Equation (3.21):

- θ_R and T_R fluctuate as Gaussian shape with σ_{θ_R} and σ_{T_R}
- $\sigma_{\theta_R} = 4.2$ mrad and independent of over all T_R (See Appendix A.8).
- $\sigma_{T_R} = 0.07$ MeV for $T_R < 5$ MeV and

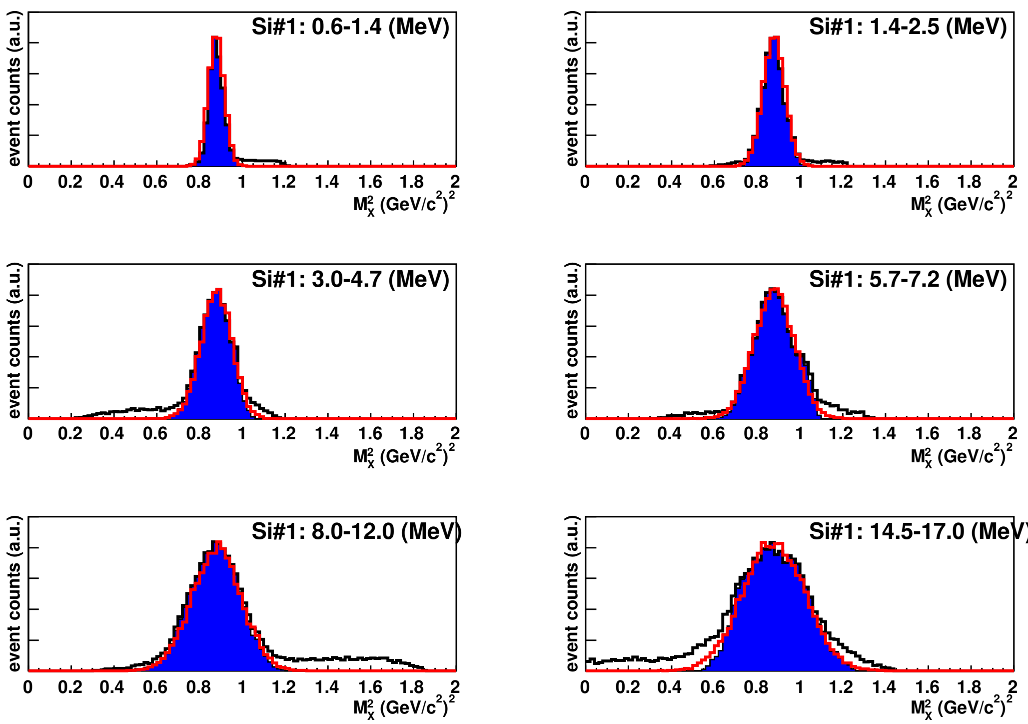

Figure 3.34: M_X^2 spectrum in one of the silicon detectors with the energies $(0.6-1.4)$ MeV, (1.4-2.5) MeV, (3.0-4.7) MeV, (5.7-7.2) MeV, (8.0-12.0) MeV and (14.5-17.0) MeV. We corrected θ_{align}(=1.5 mrad) but did not correct holding magnetic field effect (θ_{Mgnt}=0). The white areas are regarded as background tails and asymmetric between left-side and right-side. The reason is that we used the left half side of detector for $T_R < 5$ MeV regions and we used the right half side of detector for $T_R > 8$ MeV regions.

BIN#	T_R (MeV)	Event count	Ratio of ”good” waveforms
1	0.6 – 1.0	$450,112$	0.982
2	1.0 – 1.4	$309,650$	0.989
3	1.4 – 1.8	$258,166$	0.977
4	1.8 – 2.2	$229,871$	0.964
5	2.2 – 2.5	$172,815$	0.954
6	3.0 – 3.5	$194,095$	0.951
7	3.5 – 4.2	$270,279$	0.933
8	4.2 – 4.7	$305,383$	0.900
9	5.7 – 7.2	$449,352$	0.843
10	8.0 – 9.3	$217,921$	0.860
11	9.3 – 10.6	$297,811$	0.955
12	10.6 – 12.0	$304,399$	0.961
13	14.5 – 16.0	$283,075$	0.975
14	16.0 – 17.0	$171,338$	0.980

Table 3.5: The selected event counts and the ratio as a function of T_R

- $\sigma_{T_R} = 0.21$ MeV for $T_R > 10$ MeV.
- Vertical-axis is normalized by peak value of the spectrum.

Red lines, which are superimposed on the spectra, are the results of this simple estimation. The good agreement between the data and the simple simulation confirms that the M_X^2 spectra are understood and selected channels are reasonable.

We would understand the behavior of ΔM_X^2 intuitively. The deviation of M_X^2 from m_p^2 is obtained as $\Delta(M_X^2) = M_X^2 - m_p^2$. Substituting Equation (2.5) into Equation (3.21), we have the equation below:

$$\Delta(M_X^2) \cong 2|\vec{p}_1|\sqrt{2m_pT_R}\Delta\theta_R \tag{3.25}$$

Table 3.5 shows the selected events count. These events do not include ”bad” waveform events. The ratio of ”good” waveform events to the total events are also listed in the table.

3.6 Background Estimation

The elastic *pp* event selection is carried out confirming that both the recoil particle and the forward scattered particles are proton. However, there might remain some background events which sneak through recoil proton selection and forward-scattered proton selection. The possible background sources are:

- Inelastic processes,
- α particles from calibration sources and
- *Prompt* particles.

In principle, the inelastic scattering process can be discarded by forward-scattered proton selection. But at the higher T_R bins, the width of M_X^2 spectrum grows and its tail incursions into the $(m_\pi + m_p)^2 = 1.16$ (GeV/c^2)^2 threshold. Therefore, we studied the tail shape of M_X^2 spectrum carefully to estimate the inelastic processes contribution.

We can estimate the level of α particles in absence of the RHIC-beam and the H-Jet target condition. Because the calibration α particles are assumed to be emitted randomly, independent of *ToF* and stable rate whole run-period.

Prompt particles are possibly pions from the beam-related interaction upstream (beam-origins). We can assume that they are evenly distributed among the read-out channels and they does not change dramatically whole run period. But they coincide with RHIC-clock. It is difficult to distinguish between higher T_R recoil protons and"prompt" particles. The background from "prompt" particles would increase as T_R increases in the energy of $T_R > 8$ MeV.

In addition to above sources, we would mention about the contribution which comes from the H-Jet-target tail-part. In the beginning of RUN4, we had scanned the H-Jet target by RHIC-beam to fined the H-Jet center position. Once we find the best position, we fixed the positions of H-Jet target and RHIC-beam. Because the density of H-Jet target is 3-dimensional distribution, The RHIC-beam would hit the H-Jet target tail as well as the center part as displayed in Figure 3.35. Thus the recoil protons which come from the target-tail would broaden whole channels. The contribution from the H-Jet target tail-part was studied by scanning the H-Jet target with the RHIC-beam every 1.5 mm step as displayed in Figure 3.36.

In this section, we will describe the contribution from the inelastic process, firstly. Secondly, we will estimate the event count of "side" channels and compare with the H-Jet tail contribution. Thirdly, we will mention the contribution from the calibration α particles and the RHIC-beam-gas, respectively.

3.6.1 Inelastic Event Estimation

The inelastic background to *pp* elastic scattering comes from the diffractive dissociation *pp* $\rightarrow$ *Xp* of the forward going proton to a state of invariant mass M_X^2 ($> m_p^2$). It is sufficient to discuss how to distinguish the reactions between *pp* $\rightarrow$ *pp* and *pp* $\rightarrow$ (*p*+π)*p* as displayed in Figure 3.37.

In this figure, the kinematically accessible region for the event: *pp* $\rightarrow$ (*p*+π)*p* is shown as red area. There is no inelastic events $\theta_R < 55$ mrad. The *pp* elastic events are isolated from the inelastic processes on the basis of T_R and θ_R correlation.

For the region $\theta_R \geq 55$ mrad, the recoil protons from inelastic processes start to be possible. By comparing the event counts of "inside" and "outside" of kinematical boundary of inelastic region, we can estimate how much we detect inelastic process in energy 4-4.7 MeV and 5.7-7

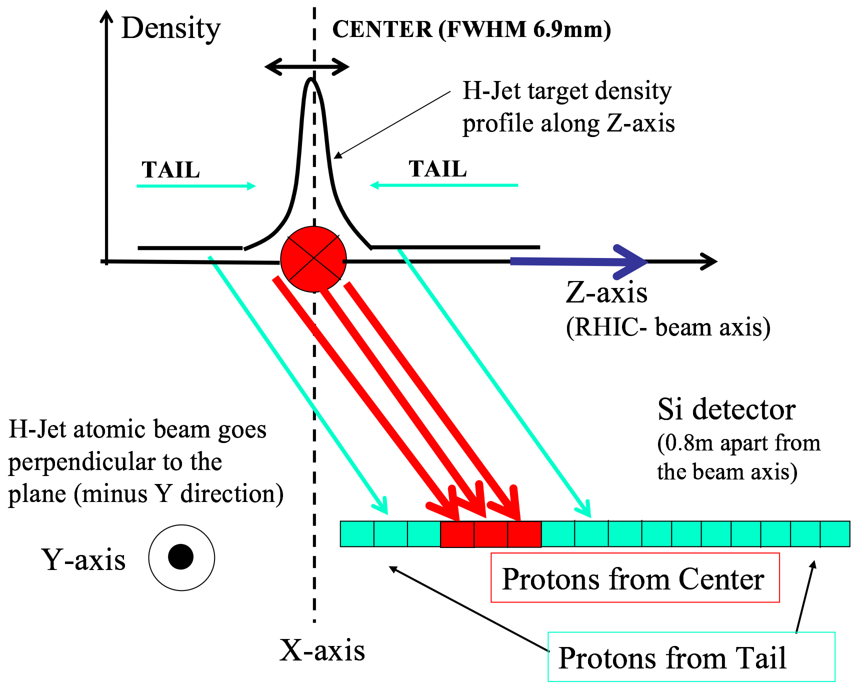

Figure 3.35: Explanation of the recoil protons from the H-Jet target-tail

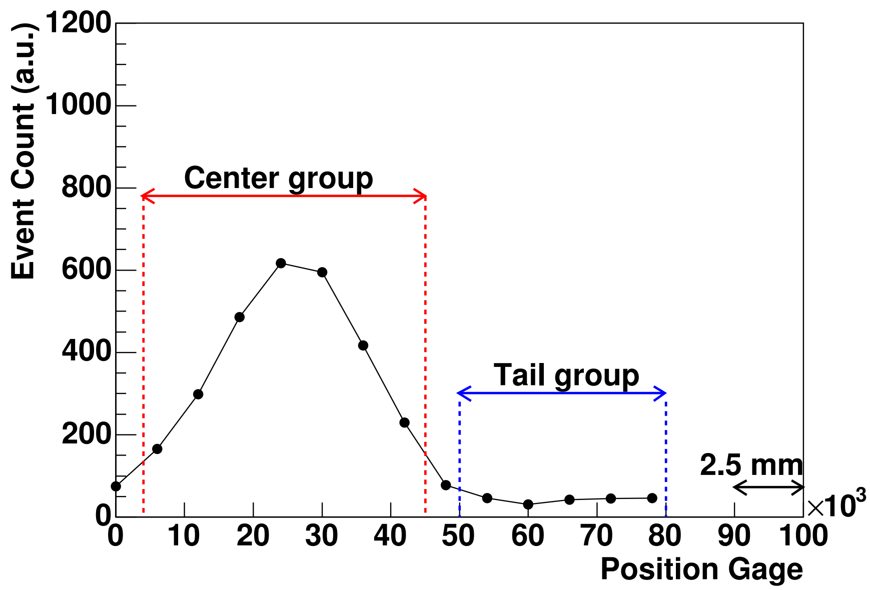

Figure 3.36: Target profile measurement with the RHIC-beam. We moved H-Jet target every 1.5 mm fixing the RHIC-beam position. The size of RHIC-beam is $\sigma \sim 1$ mm. Once we found the best condition, we fixed the positions of H-Jet target and RHIC-beam during data taking period.

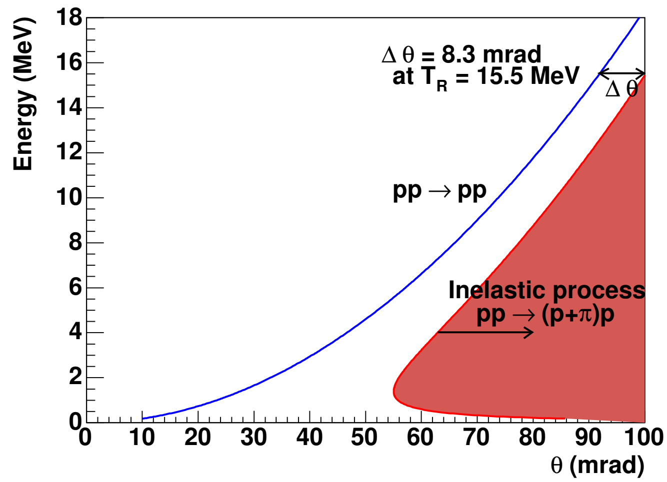

Figure 3.37: recoil proton energy vs. θ_R of $pp \rightarrow pp$ and $(\pi{+}p)p$

MeV as shown in Figure 3.38. Events in the blue area are come from ”selected channels”. The red broken line shows the background level of inside/outside of inelastic boundary. This figure confirms that the events counts of ”inside” and ”outside” of kinematical boundary are same. Then we can say the contribution from inelastic background is very small and negligible.

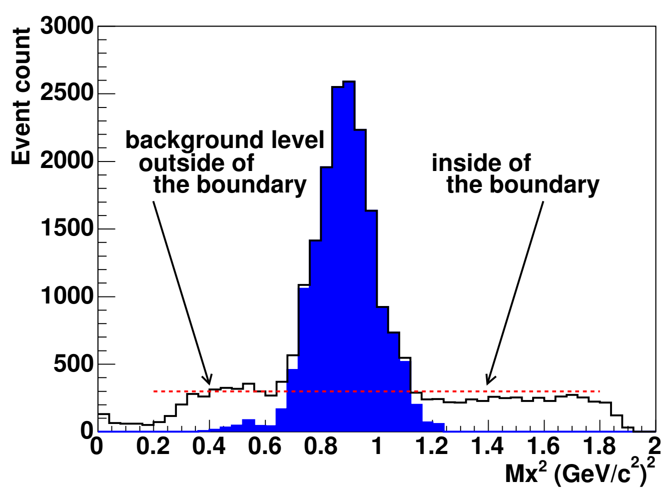

Figure 3.38: Missing mass spectrum ”inside” and ”outside” of kinematical boundary of inelastic region for the kinetic energy $4.7 < T_R < 4.7$ MeV and $5.7 < T_R < 7.0$ MeV.

3.6.2 Elastic Event from H-jet-target Tail

Figure 3.39 and 3.40 display the event distribution for certain T_R ranges from 1.8 to 2.2 MeV and from 16 to 17 MeV. These events have been applied $\Delta ToF < 8$ nsec cut. In these cases, we selected "proper" channels $\#3, 4$ and 5 for Figure 3.39 and $\#13, 14, 15$ and 16 for Figure 3.40, respectively.

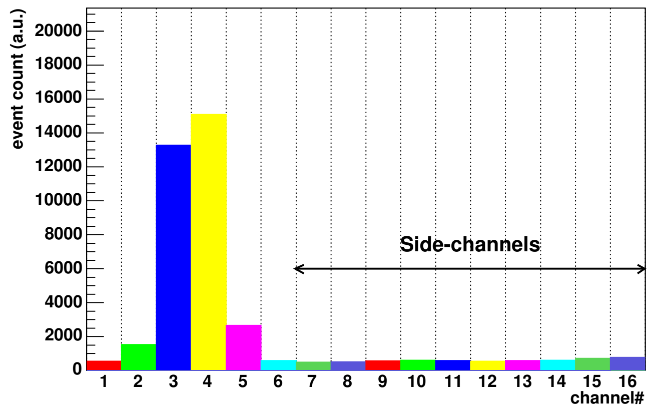

Figure 3.39: Channel distribution for T_R bin$\#4$

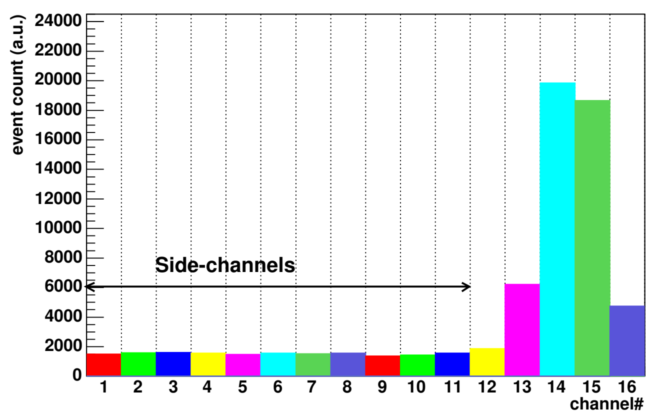

Figure 3.40: Channel distribution for T_R bin$\#14$

We call "side" channels are the whole channels except for the "proper" and their neighbors (both sides). To gain the statistics of backgrounds of the side-channels, we used them maximally as displayed in arrows in Figure 3.39 and -3.40. In order to estimate the "base-level" of the full-deposit energies, we do not apply the punched-through correction for all read-out channels even beyond the critical channel. Then we took the average among "side-channels" and regarded as "base-level".

On the other hand, to estimate the "base-level" of the punched-through energy, we do apply the punched-through correction for read-out channels. Then we took the average among "side-channels" and regarded as "base-level" assuming that the "base-level" is flat distribution for one detector. We call the averaged "base-level" by use of "side" channels $< side >$.

We considered that the "proper" channels also include "base-level" as well as "side" channels. In order to understand the "base-level" of "proper" channels, we took the ratio of event counts between "proper" channels, we call N, and the expected $< side >$. Blue data points in Figure 3.41 are the ratios between $< side >$ and N as a function of 14-bins (represented as $< side > /N$).

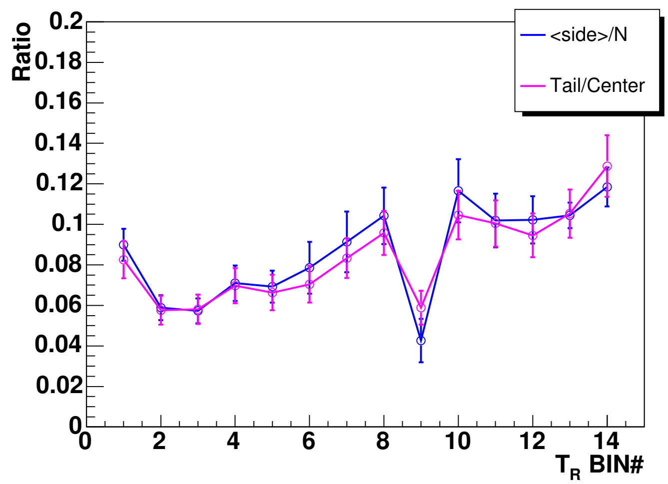

Figure 3.41: R_{side} as a function of T_R-bin

As we have mentioned previously, we studied the contribution from the H-Jet target "tail-part" compare to the "center-part" as displayed in Figure 3.36. In practice, we studied these comparison as a function of 14 T_R bins. Figure 3.42 and -3.43 display the event distribution profiles of the H-Jet target. H-Jet target was scanned by the RHIC-beam every 1.5mm step. The colors correspond to each T_R bin.

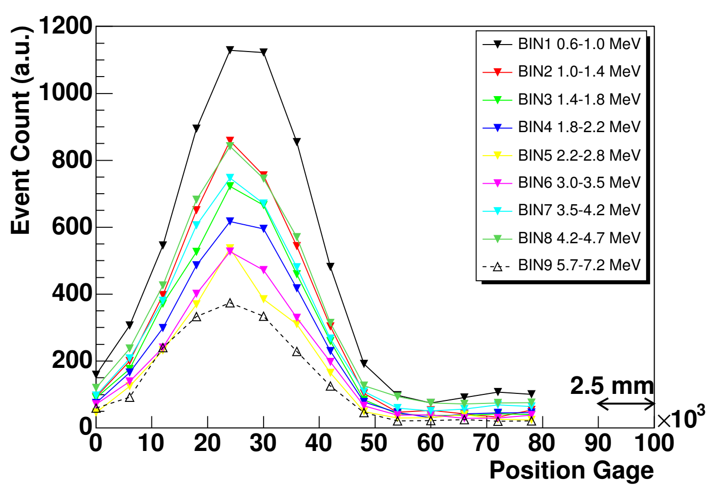

Figure 3.42: Target Profile BIN$\#1-9$

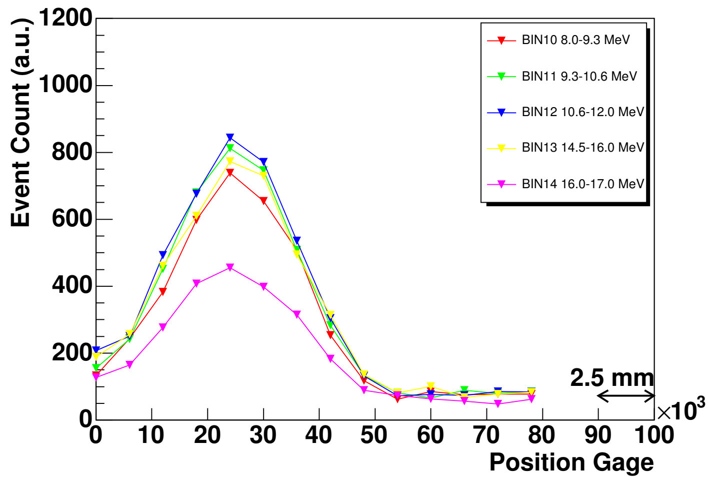

Figure 3.43: Target Profile BIN#10 - 14

We summed 7 "center-part" data and 5 "tail-part" data and normalized by data-taking time.then took the ratios, $Tail/Center$. The pink data points in Figure 3.41 are the normalized event counts ratios between "tail-part" and "center-part" as a function of 14-bins (represented as $Tail/Center$). The blue and pink data points agree within the errors. Therefore, we confirmed that $< side >$ can be considered as the sum of these three contributions:

- the H-Jet target "tail",
- α particles and
- Beam-origins.

where, we assumed that there is no event from the inelastic process in the target tail-part.

3.6.3 Beam-origins and Calibration α Particles

To estimate these items independently, we took two type of data sets in addition to ordinal physics run data:

- (A) H-Jet target OFF and RHIC-beam ON condition.
  This data tells us the summed contribution of the calibration α particles and "beam-origins".
- (B) RHIC-beam OFF condition and H-Jet target ON
  This data tell us the contribution of the calibration α particles.

We took the data of set up (A) and (B) for 5 hours and 8 hours, respectively. The ratio of the calibration $\alpha+$"beam-origins" to the total event counts, we call $R_{\alpha+beam}$, and the ratio of α, R_α, to the total event counts are displayed in figure 3.44 as a function of 14-bins. The black data points are R_α and the red points are $R_{\alpha+beam}$.

From this figure, the component of α particles, R_α, is $\sim 2\%$ for T_R-bin$\#1 - 8$. It is almost zero at T_R-bin$\#9$, because the bin#9th covers the energy region higher than α particles. For the

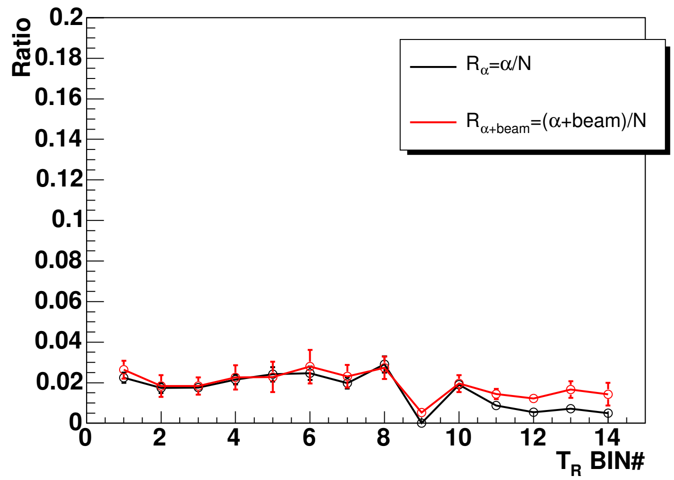

Figure 3.44: The ratios of ("beam-origin"+α) background and total events. (red line)

energy bin$\#11$– 14, the ratio is $\sim 1\%$ and smaller than that of the lower T_R-bins. The reason of this behavior is thought as this way. The reconstructed kinetic energy is not linear to the deposit energy but shrink as Figure A.17 in Appendix A.9. That is, the energy range Δ1MeV in terms of incident kinetic energy is less than Δ1 MeV in terms of the deposit energy. Therefore, R_α become small compare to *full-deposit* T_R-bin region. The component of "beam-origin" background is zero-consistent in lower bin$\#1$–10 and about 1% for bin$\#11$–14. The higher the incident proton energy increase, the smaller *ToF* become. Thus the beam origin background increase.

The errors of R_α and $R_{\alpha+beam}$ are included in the systematic errors on A_N.

Chapter 4

A_N, A_{NN} and the Observables

In this chapter, we will describ how to obtain A_N and A_{NN} from the spin-dependent elastic event count. Derivation of Equation (4.29) and (4.42), and the systematic error estimation for A_N and A_{NN} are the main goals of this chapter.

At first, we will discuss the definitions of A_N and A_{NN}. Originally, A_N and A_{NN} are defined by the asymmetry of cross-sections with up-down polarization for one or two of the protons as Equation (1.1) and (1.2) in Section 1.1. We will show the detailed derivation for these equations in Subsection 4.1.1.

Usually, however, cross-sections are not obtained simply. Since we need to normalize the event count by the detector acceptance, the luminosity. Instead of using the spin-dependent cross-sections, we calculated A_N and A_{NN} from the the spin-dependent elastic event count directly. The relationship between spin-dependent cross-section and event count are discussed in Subsection 4.2.1. And the details of the procedure will be discussed in Subsection 4.2.2 for A_N and Subsection 4.2.3 for A_{NN}. We will also discuss the systematic errors.

4.1 Spin-dependent Cross-sections

The relationship between the spin-dependent cross-section of elastic *pp* scattering and the asymmetries is:

$$\frac{\mathrm{d}^2\sigma}{\mathrm{d}t\mathrm{d}\varphi} = \frac{1}{2\pi}\frac{\mathrm{d}\sigma}{\mathrm{d}t}[1 + A_N\cos\varphi(P_b + P_t) + A_{SS}\sin^2\varphi P_b P_t + A_{NN}\cos^2\varphi P_b P_t] \tag{4.1}$$

P_t and P_b are the polarization of the H-Jet target and the RHIC-beam, respectively. φ denotes the azimuthal angle for the **forward-scattered** proton on the x-y plane as defined in Figure 4.1. We consider only initial state transverse polarization measurements. In the case that the polarization axis is the y-axis, the proton is polarized transversely. In the case that the absolute polarization values for up-state and down-state are same, the beam (target) polarizations are $P_{b(t)} = +\bar{P}_{b(t)}$ for up-state and $P_{b(t)} = -\bar{P}_{b(t)}$ for down-state. (Here $\bar{P}_{b(t)}$ is the average value of the absolute polarization values for up-state and down-state.) A_N is a single spin asymmetry with reference to the y-axis. A_{SS} and A_{NN} are double spin asymmetries with reference to the x-axis and the y-axis, respectively. It must be noted that σ in this section is not "invariant" cross-section strictly but the variable which is proportional to the yield for the collision of the beam with polarization= P_b and the target with polarization= P_t. The spin-dependent "invariant" corss-section is obtained by substituting $P_{b(t)} = 1,\ -1$.

In the case that the forward-scattered proton goes to the left direction; $\varphi = 0$ (or right direction; $\varphi = \pi$), this process is defined as the left-reaction (right-reaction). We consider the reactions on the x-z reaction plane only ($\varphi = 0$ or $\varphi = \pi$).

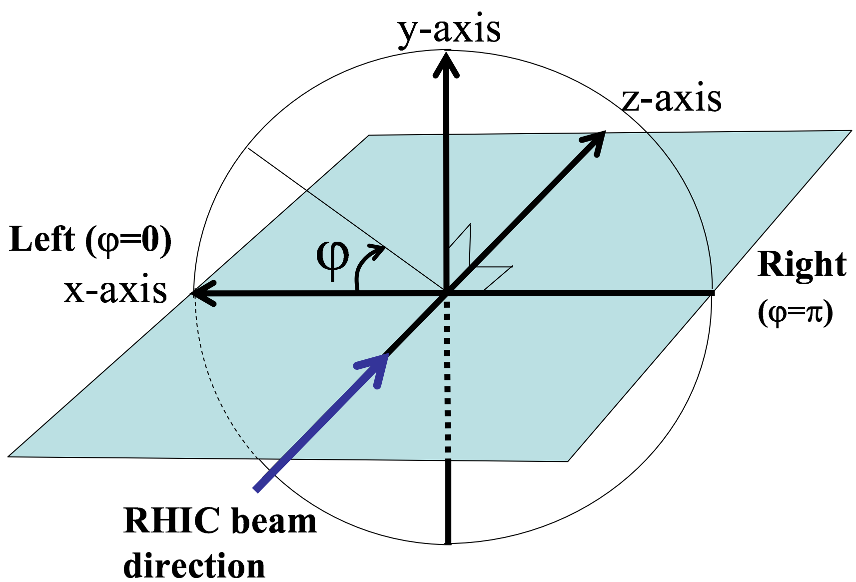

Figure 4.1: The x-y-z-axis definition. RHIC-beam moves along the z-axis. The transverse polarization axis is along the y-axis.

Equation (4.1) is rewritten as follows in accordance with the beam and target polarization states:

$$\sigma^L_{\uparrow\uparrow} = \frac{1}{2\pi}\frac{\mathrm{d}\sigma}{\mathrm{d}t}[1 + A_N(\bar{P}_b + \bar{P}_t) + A_{NN}\bar{P}_b\bar{P}_t], \quad (4.2)$$

$$\sigma^L_{\uparrow\downarrow} = \frac{1}{2\pi}\frac{\mathrm{d}\sigma}{\mathrm{d}t}[1 + A_N(\bar{P}_b - \bar{P}_t) - A_{NN}\bar{P}_b\bar{P}_t], \quad (4.3)$$

$$\sigma^L_{\downarrow\uparrow} = \frac{1}{2\pi}\frac{\mathrm{d}\sigma}{\mathrm{d}t}[1 + A_N(-\bar{P}_b + \bar{P}_t) - A_{NN}\bar{P}_b\bar{P}_t], \quad (4.4)$$

$$\sigma^L_{\downarrow\downarrow} = \frac{1}{2\pi}\frac{\mathrm{d}\sigma}{\mathrm{d}t}[1 + A_N(-\bar{P}_b - \bar{P}_t) + A_{NN}\bar{P}_b\bar{P}_t], \quad (4.5)$$

for the left-reactions.

$$\sigma^R_{\uparrow\uparrow} = \frac{1}{2\pi}\frac{\mathrm{d}\sigma}{\mathrm{d}t}[1 - A_N(\bar{P}_b + \bar{P}_t) + A_{NN}\bar{P}_b\bar{P}_t], \quad (4.6)$$

$$\sigma^R_{\uparrow\downarrow} = \frac{1}{2\pi}\frac{\mathrm{d}\sigma}{\mathrm{d}t}[1 - A_N(\bar{P}_b - \bar{P}_t) - A_{NN}\bar{P}_b\bar{P}_t], \quad (4.7)$$

$$\sigma^R_{\downarrow\uparrow} = \frac{1}{2\pi}\frac{\mathrm{d}\sigma}{\mathrm{d}t}[1 - A_N(-\bar{P}_b + \bar{P}_t) - A_{NN}\bar{P}_b\bar{P}_t], \quad (4.8)$$

$$\sigma^R_{\downarrow\downarrow} = \frac{1}{2\pi}\frac{\mathrm{d}\sigma}{\mathrm{d}t}[1 - A_N(-\bar{P}_b - \bar{P}_t) + A_{NN}\bar{P}_b\bar{P}_t], \quad (4.9)$$

for the right-reactions. Two arrows in the subscript of σ denote the RHIC-beam polarization state (left) and the H-Jet polarization state (right), respectively. $\uparrow$ ($\downarrow$) denotes the proton is polarized *plus* (*minus*) direction along the y-axis. L (R) in the superscript of σ denotes the left-reaction (the right-reaction).

Figure 4.2 and 4.3 depict the reactions for Equation (4.2) and (4.3), respectively.

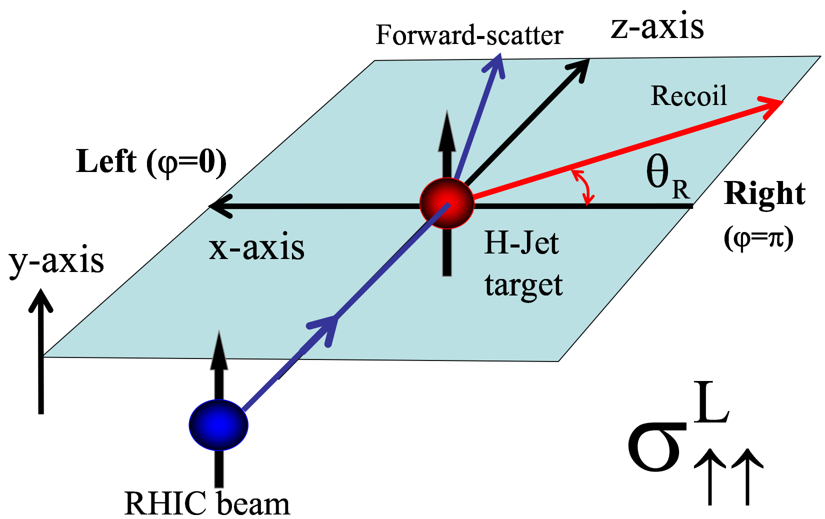

Figure 4.2: Definition of the left-reaction with the target and beam protons polarized in the plus direction ($\sigma^L_{\uparrow\uparrow}$).

4.1.1 A_N and A_{NN} from Spin-dependent Cross-sections

A_N and A_{NN} are obtained using 8 equations: Equation (4.2) – (4.9).

A_N is obtained with the polarized H-Jet target and the unpolarized RHIC-beam. Substituting $\bar{P}_b = 0$ and $\varphi = 0$ or $\varphi = \pi$ into Equation (4.2) – (4.5), we have 4 spin-dependent cross-sections:

$$\sigma^L_{\uparrow\uparrow} + \sigma^L_{\downarrow\uparrow} = \sigma^L_{0\uparrow} = \frac{1}{\pi}\frac{\mathrm{d}\sigma}{\mathrm{d}t}(1 + A_N\bar{P}_t), \tag{4.10}$$

$$\sigma^L_{\uparrow\downarrow} + \sigma^L_{\downarrow\downarrow} = \sigma^L_{0\downarrow} = \frac{1}{\pi}\frac{\mathrm{d}\sigma}{\mathrm{d}t}(1 - A_N\bar{P}_t), \tag{4.11}$$

$$\sigma^R_{\uparrow\uparrow} + \sigma^R_{\downarrow\uparrow} = \sigma^R_{0\uparrow} = \frac{1}{\pi}\frac{\mathrm{d}\sigma}{\mathrm{d}t}(1 - A_N\bar{P}_t). \tag{4.12}$$

$$\sigma^R_{\uparrow\downarrow} + \sigma^R_{\downarrow\downarrow} = \sigma^R_{0\downarrow} = \frac{1}{\pi}\frac{\mathrm{d}\sigma}{\mathrm{d}t}(1 + A_N\bar{P}_t). \tag{4.13}$$

Figure 4.4 and 4.5 depict the reaction of Equation (4.10) and (4.12), respectively.

We would define an asymmetry, ϵ, between A and B as:

$$\epsilon = \frac{A - B}{A + B}. \tag{4.14}$$

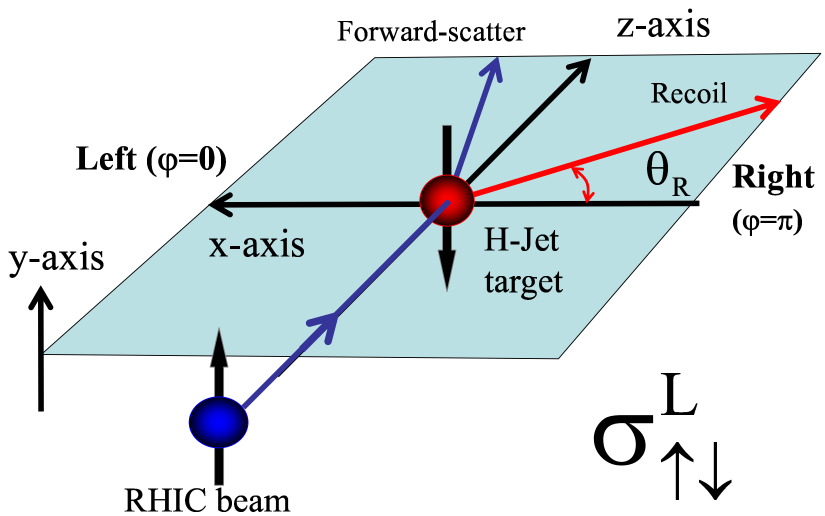

Figure 4.3: Definition of the left-reaction with the target and beam protons polarized in the plus direction and in the down direction ($\sigma^{L}_{\uparrow\downarrow}$).

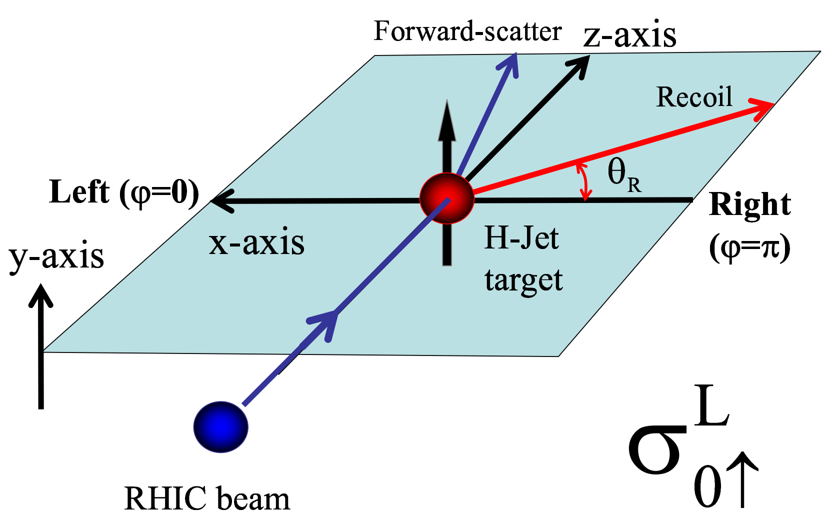

Figure 4.4: Definition of the left-reaction with the target proton polarized in the plus direction ($\sigma^{L}_{0\uparrow}$).

We often call this the ”raw asymmetry” or the ”unnormalized asymmetry”.

Thus A_N is obtained by taking asymmetry of the proper combination of spin-dependent cross-sections:

$$A_N = \frac{1}{\bar{P}_t}\frac{\sigma^L_{0\uparrow} - \sigma^R_{0\uparrow}}{\sigma^L_{0\uparrow} + \sigma^R_{0\uparrow}} = \frac{1}{\bar{P}_t}\frac{\sigma^R_{0\downarrow} - \sigma^L_{0\downarrow}}{\sigma^R_{0\downarrow} + \sigma^L_{0\downarrow}} = \frac{\epsilon_N}{\bar{P}_t}, \tag{4.15}$$

where ϵ_N is a *raw* asymmetry for the target polarization.

Alternatively A_N can be obtained from the left-reactions or the right-reactions changing the H-Jet target polarization state periodically.

$$A_N = \frac{1}{\bar{P}_t}\frac{\sigma^L_{0\uparrow} - \sigma^L_{0\downarrow}}{\sigma^L_{0\uparrow} + \sigma^L_{0\downarrow}} = \frac{1}{\bar{P}_t}\frac{\sigma^R_{0\downarrow} - \sigma^R_{0\uparrow}}{\sigma^R_{0\downarrow} + \sigma^R_{0\uparrow}} = \frac{\epsilon_N}{\bar{P}_t}. \tag{4.16}$$

Note that Equation (4.29) is reproduced by substituting $\bar{P}_t = 1$.

In the case that the beam proton is polarized and the target proton is unpolarized ($\bar{P}_t = 0$), we can obtain *raw* asymmetry for the beam polarization, ϵ_b. Since we utilize the *pp* elastic scattering process, A_N does not depend on either the target nor beam polarizations:

$$A_N = \frac{\epsilon_N}{\bar{P}_t} = \frac{\epsilon_b}{\bar{P}_b}. \tag{4.17}$$

Therefore, we can transfer the target polarization $\bar{P}_t$ to the beam polarization $\bar{P}_b$ by measuring a ratio of spin-dependent *raw* asymmetries:

$$\bar{P}_b = \frac{\epsilon_b}{\epsilon_N}\bar{P}_t. \tag{4.18}$$

A_{NN} is obtained in the case that the beam and target protons are polarized transversely. In the case that the absolute polarization values for the beam (target) for the up-state and down-state are the same except for the sign, they are expressed as $P_{b(t)} = +\bar{P}_{b(t)}$ for up-state and $P_{b(t)} = -\bar{P}_{b(t)}$ for down-state.

For the cross-section for which the polarization states for beam and target are parallel:

$$\sigma^{L(R)}_{\uparrow\uparrow} + \sigma^{L(R)}_{\downarrow\downarrow} = \frac{1}{\pi}\frac{\mathrm{d}\sigma}{\mathrm{d}t}(1 + A_{NN}\bar{P}_b\bar{P}_t). \tag{4.19}$$

For the cross-section which the polarization states for beam and target are anti-parallel:

$$\sigma^{L(R)}_{\uparrow\downarrow} + \sigma^{L(R)}_{\downarrow\uparrow} = \frac{1}{\pi}\frac{\mathrm{d}\sigma}{\mathrm{d}t}(1 - A_{NN}\bar{P}_b\bar{P}_t). \tag{4.20}$$

Thus, A_{NN} is obtained as:

$$A_{NN} = \frac{1}{\bar{P}_b\bar{P}_t}\frac{(\sigma^{L(R)}_{\uparrow\uparrow} + \sigma^{L(R)}_{\downarrow\downarrow}) - (\sigma^{L(R)}_{\uparrow\downarrow} + \sigma^{L(R)}_{\downarrow\uparrow})}{(\sigma^{L(R)}_{\uparrow\uparrow} + \sigma^{L(R)}_{\downarrow\downarrow}) + (\sigma^{L(R)}_{\uparrow\downarrow} + \sigma^{L(R)}_{\downarrow\uparrow})}. \tag{4.21}$$

Note that Equation (4.21) is reproduced by substituting $\bar{P}_t = 1$ and $\bar{P}_b = 1$

4.2 A_N and A_{NN} Calculations from the Measured Spin-dependent Yield

4.2.1 Spin-dependent Yield

In the former discussions, we assumed that $\mathrm{d}\sigma/\mathrm{d}t$ is well known and the absolute polarization values for the up-state and the down-state are same.

In practice, it is not easy to measure $\mathrm{d}\sigma/\mathrm{d}t$ accurately. One of the reasons is the luminosity, which might be different among the different polarization-state combinations. The acceptance between the left-side and right-side detectors is also different. If we write the event yields instead of the spin-dependent cross-sections, Equation (4.2) – (4.9) are modified as:

For the left side:

$$\begin{aligned} N^L_{\uparrow\uparrow} &= N_0 d\Omega_L[L_{\uparrow\uparrow}\{1 + A_N(P^\uparrow_b + P^\uparrow_t) + A_{NN}P^\uparrow_b P^\uparrow_t\} + B/4] \\ N^L_{\uparrow\downarrow} &= N_0 d\Omega_L[L_{\uparrow\downarrow}\{1 + A_N(P^\uparrow_b - P^\downarrow_t) - A_{NN}P^\uparrow_b P^\downarrow_t\} + B/4] \\ N^L_{\downarrow\uparrow} &= N_0 d\Omega_L[L_{\downarrow\uparrow}\{1 + A_N(-P^\downarrow_b + P^\uparrow_t) - A_{NN}P^\downarrow_b P^\uparrow_t\} + B/4] \\ N^L_{\downarrow\downarrow} &= N_0 d\Omega_L[L_{\downarrow\downarrow}\{1 + A_N(-P^\downarrow_b - P^\downarrow_t) + A_{NN}P^\downarrow_b P^\downarrow_t\} + B/4] \end{aligned} \quad (4.22)$$

For the right side:

$$\begin{aligned} N^R_{\uparrow\uparrow} &= N_0 d\Omega_R[L_{\uparrow\uparrow}\{1 - A_N(P^\uparrow_b + P^\uparrow_t) + A_{NN}P^\uparrow_b P^\uparrow_t\} + B/4] \\ N^R_{\uparrow\downarrow} &= N_0 d\Omega_R[L_{\uparrow\downarrow}\{1 - A_N(P^\uparrow_b - P^\downarrow_t) - A_{NN}P^\uparrow_b P^\downarrow_t\} + B/4] \\ N^R_{\downarrow\uparrow} &= N_0 d\Omega_R[L_{\downarrow\uparrow}\{1 - A_N(-P^\downarrow_b + P^\uparrow_t) - A_{NN}P^\downarrow_b P^\uparrow_t\} + B/4] \\ N^R_{\downarrow\downarrow} &= N_0 d\Omega_R[L_{\downarrow\downarrow}\{1 - A_N(-P^\downarrow_b - P^\downarrow_t) + A_{NN}P^\downarrow_b P^\downarrow_t\} + B/4] \end{aligned} \quad (4.23)$$

As we have discussed in Section 3.6, measured event yields include the calibration α particles and beam-related backgrounds. These backgrounds are independent of beam and target polarization states. We call the sum of them BG.

The components of right-hand side of Equation (4.22) and (4.23) are:

- N_0 is numerical constant value.
- $d\Omega_L$ and $d\Omega_R$ are left and right acceptances.
- $L_{\uparrow\uparrow}$ is spin-dependent luminosity for both polarizations are the up-states; similarly for $L_{\uparrow\downarrow}, L_{\downarrow\uparrow}$ and $L_{\downarrow\downarrow}$.
- $P^\uparrow_{b(t)}$ denotes the polarization of the RHIC-beam (the H-Jet target) for the up-state.
- $-P^\downarrow_{b(t)}$ denotes the polarization of the RHIC-beam (the H-Jet target) for the down-state.
- B is the background luminosity, which is, in principle, independent of the RHIC-beam nor the H-Jet target polarizations. (Actually B has statistical fluctuations, so it is not the same for each spin combination.)

We would introduce these event yields:

- Total event yield $(N^L_{\uparrow\uparrow} + N^L_{\uparrow\downarrow} + N^L_{\downarrow\uparrow} + N^L_{\downarrow\downarrow} + N^R_{\uparrow\uparrow} + N^R_{\uparrow\downarrow} + N^R_{\downarrow\uparrow} + N^R_{\downarrow\downarrow})$ is referred to as N.

- Total "background" yield is related to the background luminosity (B); $BG = N_0(d\Omega_L + d\Omega_R)B$.
- The total "elastic *pp*" event yield is referred to as ($N - BG$).

The numerical values of these yields ($N^L_{\uparrow\uparrow}, N^L_{\uparrow\downarrow}, N^L_{\downarrow\uparrow}, N^L_{\downarrow\downarrow}, N^R_{\uparrow\uparrow}, N^R_{\uparrow\downarrow}, N^R_{\downarrow\uparrow}, N^R_{\downarrow\downarrow}$) are summarized in Appendix A.11.

We define asymmetries between $P^{\uparrow}_{b(t)}$ and $P^{\downarrow}_{b(t)}$:

$$\epsilon_{P_b} = \frac{P_b^{\uparrow} - P_b^{\downarrow}}{P_b^{\uparrow} + P_b^{\downarrow}} = \frac{P_b^{\uparrow} - P_b^{\downarrow}}{2\bar{P}_b} \sim 0.001, \tag{4.24}$$

$$\epsilon_{P_t} = \frac{P_t^{\uparrow} - P_t^{\downarrow}}{P_t^{\uparrow} + P_t^{\downarrow}} = \frac{P_t^{\uparrow} - P_t^{\downarrow}}{2\bar{P}_t} \sim 0.001, \tag{4.25}$$

where we replace $(P_b^{\uparrow} + P_b^{\downarrow})$ by $2\bar{P}_b$, and $(P_t^{\uparrow} + P_t^{\downarrow})$ by $2\bar{P}_t$. Both ϵ_{P_b} and ϵ_{P_t} are estimated to be ~ 0.001. The asymmetry between up-down polarizations of RHIC-beam was obtained from the *p*C-polarimeter.

The H-Jet target up-down polarizations were measured to be $P_t^{\uparrow} = 0.923 \pm 0.018$ and $P_t^{\downarrow} = 0.925 \pm 0.018$ by the Breit-Rabi polarimeter (BRP, see Subsection 2.2.2). Thus the absolute polarization is $\bar{P}_t = 0.924 \pm 0.018$ and the target polarization asymmetry is $\epsilon_{P_t} \sim 0.001$.

4.2.2 A_N

In the following discussion, we will show the extract A_N from the measured spin-dependent event yields. The goal is Equation (4.29).

Substituting $P_t^{\uparrow} = \bar{P}_t(1 + \epsilon_{P_t})$ and $P_t^{\downarrow} = \bar{P}_t(1 - \epsilon_{P_t})$ into Equation (4.22) and (4.23), we have:

$$\begin{aligned}
N^L_{\uparrow\uparrow} + N^L_{\downarrow\uparrow} = N^L_{0\uparrow} &= N_0 d\Omega_L[L_{0\uparrow}\{1 + A_N\bar{P}_t(1 + \epsilon_{P_t})\} + B/2],\\
N^L_{\uparrow\downarrow} + N^L_{\downarrow\downarrow} = N^L_{0\downarrow} &= N_0 d\Omega_L[L_{0\downarrow}\{1 - A_N\bar{P}_t(1 - \epsilon_{P_t})\} + B/2],\\
N^R_{\uparrow\uparrow} + N^R_{\downarrow\uparrow} = N^R_{0\uparrow} &= N_0 d\Omega_R[L_{0\uparrow}\{1 - A_N\bar{P}_t(1 + \epsilon_{P_t})\} + B/2],\\
N^R_{\uparrow\downarrow} + N^R_{\downarrow\downarrow} = N^R_{0\downarrow} &= N_0 d\Omega_R[L_{0\downarrow}\{1 + A_N\bar{P}_t(1 - \epsilon_{P_t})\} + B/2].
\end{aligned} \tag{4.26}$$

where, $L_{0\uparrow} = (L_{\uparrow\uparrow} + L_{\downarrow\uparrow})$ and so on.

In order to extract A_N from Equation (4.26), we employed one of the outputs of the *so-called* **square-root formula**, which cancels out $L_{0\uparrow}$, $L_{0\downarrow}$ and $d\Omega_{L(R)}$. (The details of the square-root formula and these developments of formula are mentioned in Appendix B.)

$$\begin{aligned}
\epsilon_N^{meas} &= \frac{\sqrt{N^L_{0\uparrow}N^R_{0\downarrow}} - \sqrt{N^L_{0\downarrow}N^R_{0\uparrow}}}{\sqrt{N^L_{0\uparrow}N^R_{0\downarrow}} + \sqrt{N^L_{0\downarrow}N^R_{0\uparrow}}}\\
&\cong A_N\bar{P}_t\frac{N - BG}{N}.
\end{aligned} \tag{4.27}$$

The statistical error of ϵ_N^{meas} is:

$$\Delta\epsilon_N^{meas} \cong \frac{1}{\sqrt{N^L_{0\uparrow} + N^L_{0\downarrow} + N^R_{0\uparrow} + N^R_{0\downarrow}}}. \tag{4.28}$$

Figure 4.6 displays ϵ_N^{meas} as a function of $|t|$ together with other *raw* asymmetries which we will discuss later.

We have ignored contributions beyond the third order of the products $A_N \bar{P}_t$, ϵ_{P_t} and B/L, because those are smaller by 10^{-3}.

The final A_N values are corrected for α source background and beam-related background, determined from empty target runs as we have discussed in Section 3.6. The background originating from the unpolarized residual target gas and the target tail has been already accounted for a dilution of the target polarization.

Substituting $\frac{N-BG}{N} = (1 - R_{(\alpha+beam)})$, Equation (4.27) is rewritten as :

$$A_N \cong \frac{\epsilon_N^{meas}}{\bar{P}_t(1 - R_{(\alpha+beam)})}, \tag{4.29}$$

where $R_{(\alpha+beam)}$ is mentioned in Section 3.6. We use this expression for the final results.

The statistical error of A_N is:

$$\Delta A_N^{stat} = \frac{(\Delta\epsilon_N^{meas})^{stat}}{\bar{P}_t(1 - R_{(\alpha+beam)})} \cong \frac{1}{\bar{P}_t(1 - R_{\alpha+beam})} \frac{1}{\sqrt{N_{0\uparrow}^L + N_{0\downarrow}^L + N_{0\uparrow}^R + N_{0\downarrow}^R}}. \tag{4.30}$$

The final A_N values and the statistical errors as a function of $|t|$ are provided in Table 4.1.

There are two categories of the systematic uncertainties in the measurement: T_R bin-dependent and overall normalization. These are obtained from the derivation of the first term in Equation (4.29):

$$\Delta A_N^{sys} = A_N \left(\frac{(\Delta\epsilon_N^{meas})^{sys}}{\epsilon_N^{meas}} \oplus \frac{\Delta R_{(\alpha+beam)}}{1 - R_{(\alpha+beam)}} \oplus \frac{\Delta \bar{P}_t}{P_t} \right), \tag{4.31}$$

where $\oplus$ denotes the quadratic sum ($A \oplus B = \sqrt{A^2 + B^2}$).

The first and the second terms are T_R bin-dependent. The first term is related to the false, acceptance asymmetries (ΔA_N^{acc}) and the elastic event selection (ΔA_N^{sel}). The second term is related to the background corrections of α sources and beam gas scattering (ΔA_N^{BG}). The third term in Equation (4.31) is the uncertainty about the normalization ($\Delta A_N^{norm.}$).

⟨ Error from the acceptance and false asymmetries ⟩

ΔA_N^{acc} is estimated from:

$$\Delta A_N^{acc} = |A_N^{\uparrow} - A_N^{\downarrow}|,$$

where

$$A_N^{\uparrow} = \frac{1}{\bar{P}_t} \frac{N_{0\uparrow}^L - N_{0\uparrow}^R}{N_{0\uparrow}^L + N_{0\uparrow}^R}, \; A_N^{\downarrow} = -\frac{1}{\bar{P}_t} \frac{N_{0\downarrow}^L - N_{0\downarrow}^R}{N_{0\downarrow}^L + N_{0\downarrow}^R}.$$

ΔA_N^{acc} is related to the left-right unbalanced acceptance and is provided in Table 4.2. The 1st, 9th and 14th T_R bins of ΔA_N^{acc} are bigger than the other T_R bins. As long as the left-right acceptance asymmetry is less than 0.1, the square-root formula can cancel the acceptance unbalance. However, for example the 14th T_R bin, the event yield of the left-reaction is 1.9 times lager than that of right-reaction. The 1st and 14th bins correspond to the events from the detector edge and the acceptance balance is worse. The 9th T_R bin is affected by the uncertainty of the definition whether full-deposit and punched-through proton. This uncertainty is also related to the acceptance unbalance. The other T_R bins are about 10 times smaller than the statistical errors.

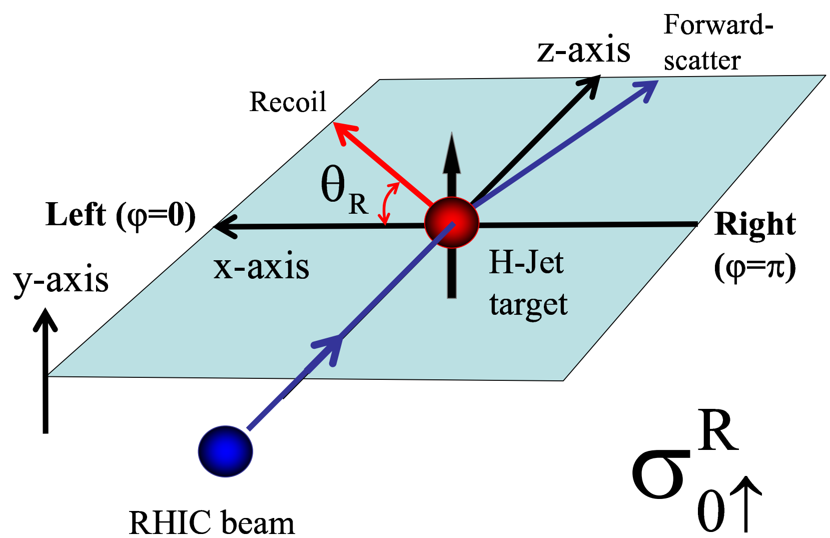

Figure 4.5: Definition of the right-reaction with the target proton polarized in the plus direction ($\sigma^R_{0\uparrow}$).

T_R MeV	$-\langle t \rangle$ (GeV/c)^2	A_N	ΔA_N^{stat} stat	ΔA_N^{norm} norm.
0.6 – 1.0	0.0015	0.0348	0.0017	0.0007
1.0 – 1.4	0.0022	0.0422	0.0020	0.0008
1.4 – 1.8	0.0030	0.0493	0.0022	0.0010
1.8 – 2.2	0.0037	0.0442	0.0023	0.0009
2.2 – 2.5	0.0044	0.0430	0.0027	0.0008
3.0 – 3.5	0.0061	0.0423	0.0025	0.0008
3.5 – 4.2	0.0071	0.0363	0.0021	0.0007
4.2 – 4.7	0.0084	0.0388	0.0020	0.0008
5.7 – 7.2	0.0118	0.0348	0.0015	0.0007
8.0 – 9.3	0.0165	0.0272	0.0023	0.0005
9.3 – 10.6	0.0187	0.0242	0.0020	0.0005
10.6 – 12.0	0.0212	0.0227	0.0020	0.0004
14.5 – 16.0	0.0287	0.0271	0.0021	0.0005
16.0 – 17.0	0.0309	0.0263	0.0027	0.0005

Table 4.1: A_N as a function of t in 14 T_R bins. The statistical errors and normalization errors of $\bar{P}_t$ are also listed.

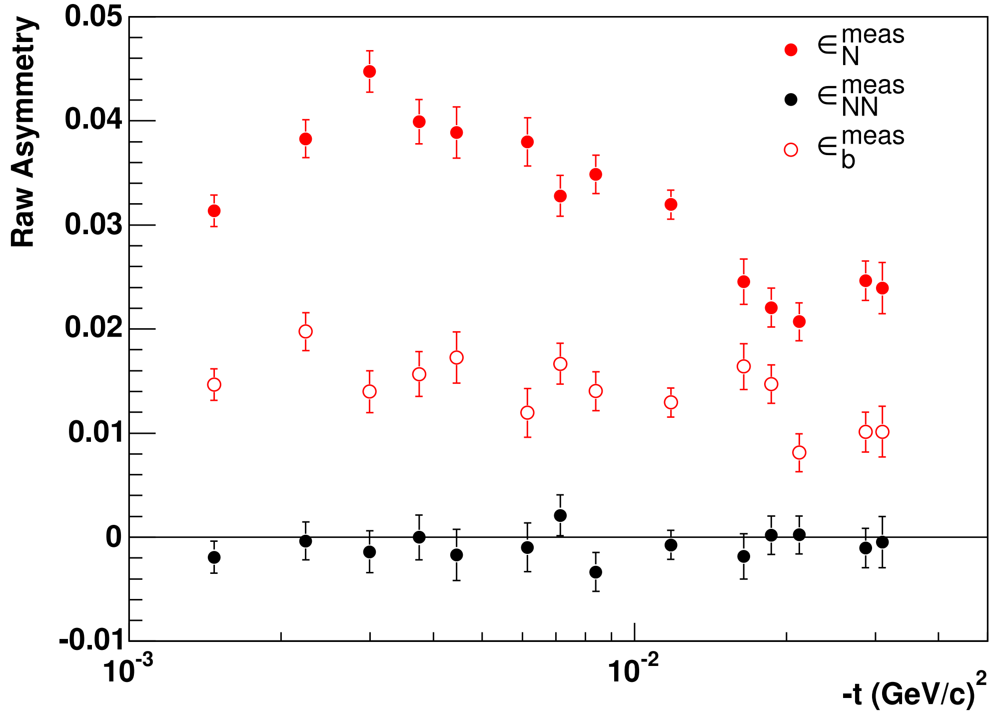

Figure 4.6: ϵ_N^{meas}, ϵ_b^{meas} and ϵ_{NN}^{meas} as a function of t. The errors on the data points are statistical.

T_R MeV	$-\langle t \rangle$ $(\text{GeV}/c)^2$	Systematic Error ΔA_N^{sys}	Components $(\Delta A_N^{acc} \pm \Delta A_N^{sel} \pm \Delta A_N^{BG})$
0.6 – 1.0	0.0015	0.0030	$0.0029 \pm 0.0006 \pm 0.0002$
1.0 – 1.4	0.0022	0.0007	$0.0006 \pm 0.0003 \pm 0.0002$
1.4 – 1.8	0.0030	0.0010	$0.0001 \pm 0.0010 \pm 0.0002$
1.8 – 2.2	0.0037	0.0006	$0.0002 \pm 0.0005 \pm 0.0003$
2.2 – 2.5	0.0044	0.0004	$0.0002 \pm 0.0002 \pm 0.0003$
3.0 – 3.5	0.0061	0.0017	$0.0001 \pm 0.0016 \pm 0.0003$
3.5 – 4.2	0.0071	0.0018	$0.0003 \pm 0.0017 \pm 0.0002$
4.2 – 4.7	0.0084	0.0023	$0.0015 \pm 0.0018 \pm 0.0002$
5.7 – 7.2	0.0118	0.0031	$0.0031 \pm 0.0003 \pm 0.0001$
8.0 – 9.3	0.0165	0.0016	$0.0016 \pm 0.0005 \pm 0.0001$
9.3 – 10.6	0.0187	0.0013	$0.0004 \pm 0.0012 \pm 0.0001$
10.6 – 12.0	0.0212	0.0008	$0.0005 \pm 0.0006 \pm 0.0002$
14.5 – 16.0	0.0287	0.0018	$0.0016 \pm 0.0007 \pm 0.0003$
16.0 – 17.0	0.0309	0.0065	$0.0064 \pm 0.0010 \pm 0.0003$

Table 4.2: The T_R-dependent systematic error in A_N. ΔA_N^{sys} and three systematic error components which are described in the text.

$\langle$ **Error from the elastic event selection** $\rangle$

ΔA_N^{sel} is originated in the criteria of the elastic event selection. In Section 3.5, we have discussed about the criteria for the recoil proton identification was $|ToF - ToF_{calc}| < 8$ nsec. We have also estimated A_N with narrow cut (${A_N}^{|ToF-ToF_{calc}|<6}$) and wide cut (${A_N}^{|ToF-ToF_{calc}|<10}$). The values of subtraction ${A_N}^{|ToF-ToF_{calc}|<6}$ from ${A_N}^{|ToF-ToF_{calc}|<10}$ for the $14 T_R$ bins are smaller than the statistical uncertainty but always positive. Therefore we consider the ToF-cut width dependence by comparing the results of $|ToF - ToF_{calc}| < 6$ nsec and $|ToF - ToF_{calc}| < 10$ nsec cases,

$$\Delta A_N^{sel} = ({A_N}^{|ToF-ToF_{calc}|<6} - {A_N}^{|ToF-ToF_{calc}|<10}),$$

conservatively. ΔA_N^{sel} is provided in Table 4.2 and is ranging between 0.0002 and 0.0018 for all T_R bins. They are small or comparable in size compared to the statistical errors.

$\langle$ **Error from the backgrounds correction** $\rangle$

ΔA_N^{BG} is originated in the backgrounds correction.

$$\Delta A_N^{BG} = A_N \cdot \sqrt{\Delta {R_\alpha}^2 + \Delta {R_{beam}}^2}$$

ΔA_N^{BG} is provided in Table 4.2 and is ranging between 0.0001 and 0.0003 for all T_R bins. They are less than tenth part of the statistical errors. The details of ΔR_α and ΔR_{beam} have been discussed in Section 3.6.

4.2.3 A_{NN}

In the following discussion, we will show the extract A_{NN} from the measured spin-dependent event yields. The goal is Equation (4.41). The event yields of parallel or anti-parallel polarization states are obtained from Equation (4.22) and (4.23) as:

$$\begin{aligned} N^L_{\uparrow\uparrow} + N^L_{\downarrow\downarrow} &= N_0 d\Omega_L\{(L_{\uparrow\uparrow} + L_{\downarrow\downarrow})(1 + A_{NN}\bar{P}_b\bar{P}_t) + (L_{\uparrow\uparrow} - L_{\downarrow\downarrow})A_N(\bar{P}_b + \bar{P}_t) + B/2\}, \\ N^L_{\uparrow\downarrow} + N^L_{\downarrow\uparrow} &= N_0 d\Omega_L\{(L_{\uparrow\downarrow} + L_{\downarrow\uparrow})(1 - A_{NN}\bar{P}_b\bar{P}_t) + (L_{\uparrow\downarrow} - L_{\downarrow\uparrow})A_N(\bar{P}_b - \bar{P}_t) + B/2\}, \end{aligned} \tag{4.32}$$

for the left-reactions and,

$$\begin{aligned} N^R_{\uparrow\uparrow} + N^R_{\downarrow\downarrow} &= N_0 d\Omega_R\{(L_{\uparrow\uparrow} + L_{\downarrow\downarrow})(1 + A_{NN}\bar{P}_b\bar{P}_t) - (L_{\uparrow\uparrow} - L_{\downarrow\downarrow})A_N(\bar{P}_b + \bar{P}_t) + B/2\}, \\ N^R_{\uparrow\downarrow} + N^R_{\downarrow\uparrow} &= N_0 d\Omega_R\{(L_{\uparrow\downarrow} + L_{\downarrow\uparrow})(1 - A_{NN}\bar{P}_b\bar{P}_t) - (L_{\uparrow\downarrow} - L_{\downarrow\uparrow})A_N(\bar{P}_b - \bar{P}_t) + B/2\}. \end{aligned} \tag{4.33}$$

for the right-reactions. The difference of the second equation and the first equation in (4.32):

$$(N^L_{\uparrow\uparrow} + N^L_{\downarrow\downarrow}) - (N^L_{\uparrow\downarrow} + N^L_{\downarrow\uparrow}) = N_0 d\Omega_L L\{(\epsilon_{L_t}A_N\bar{P}_b + \epsilon_{L_b}A_N\bar{P}_t + A_{NN}\bar{P}_b\bar{P}_t) + \epsilon_{L_b}\epsilon_{L_t}\}, \tag{4.34}$$

where $L = (L_{\uparrow\uparrow} + L_{\downarrow\downarrow} + L_{\uparrow\downarrow} + L_{\downarrow\uparrow})$, and ϵ_{L_b}, ϵ_{L_t} are defined as:

$$\epsilon_{L_b} = \frac{(L_{\uparrow\uparrow} + L_{\uparrow\downarrow}) - (L_{\downarrow\uparrow} + L_{\downarrow\downarrow})}{L}, \tag{4.35}$$

$$\epsilon_{L_t} = \frac{(L_{\uparrow\uparrow} + L_{\downarrow\uparrow}) - (L_{\uparrow\downarrow} + L_{\downarrow\downarrow})}{L}, \tag{4.36}$$

and

$$\epsilon_{L_b}\epsilon_{L_t} = \frac{L_{\uparrow\uparrow} + L_{\downarrow\downarrow} - L_{\uparrow\downarrow} - L_{\downarrow\uparrow}}{L}. \tag{4.37}$$

The sum of the first equation and the second equation (4.32)is:

$$(N^L_{\uparrow\uparrow} + N^L_{\downarrow\downarrow}) + (N^L_{\uparrow\downarrow} + N^L_{\downarrow\uparrow}) = N_0 d\Omega_L L\{1 + B/L + \epsilon_{L_t}A_N\bar{P}_b + \epsilon_{L_b}A_N\bar{P}_t\} \tag{4.38}$$

Because $\epsilon_{L_b} = 0.0001\pm < 0.0001$, which is measured by WCM, and $\epsilon_{L_t} = -0.0005\pm < 0.0001$, which is measured by BRP, are small, $\epsilon_{L_b}\epsilon_{L_t}$ is in the order of 10^{-8}, $(A_N\bar{P}_t\epsilon_{L_b}))$ and $(A_N\bar{P}_b\epsilon_{L_t})$ are in the order of 10^{-6}. And we can omit $\epsilon_{L_b}\epsilon_{L_t}$ in Equation (4.34), $\epsilon_{L_t}A_N\bar{P}_b$ and $\epsilon_{L_b}A_N\bar{P}_t$ in Equation (4.38).

Thus the ratio of Equation (4.34) and (4.38) is:

$$\frac{N^L_{\uparrow\uparrow} + N^L_{\downarrow\downarrow} - N^L_{\uparrow\downarrow} - N^L_{\downarrow\uparrow}}{N^L_{\uparrow\uparrow} + N^L_{\downarrow\downarrow} + N^L_{\uparrow\downarrow} + N^L_{\downarrow\uparrow}} \cong \frac{L}{L+B}\{A_{NN}\bar{P}_t\bar{P}_b + \epsilon_{L_t}A_N\bar{P}_b + \epsilon_{L_b}A_N\bar{P}_t\}, \tag{4.39}$$

The ratio of event yields of the right-reactions is obtained from Equation (4.33) in the same way:

$$\frac{N^R_{\uparrow\uparrow} + N^R_{\downarrow\downarrow} - N^R_{\uparrow\downarrow} - N^R_{\downarrow\uparrow}}{N^R_{\uparrow\uparrow} + N^R_{\downarrow\downarrow} + N^R_{\uparrow\downarrow} + N^R_{\downarrow\uparrow}} \cong \frac{L}{L+B}\left(A_{NN}\bar{P}_t\bar{P}_b - \epsilon_{L_t}A_N\bar{P}_b - \epsilon_{L_b}A_N\bar{P}_t\right). \tag{4.40}$$

T_R (MeV)	$\epsilon_b^{meas}/\epsilon_N^{meas}$ Fit with *Constant* value (χ^2/ndf))	$\epsilon_b^{meas}/\epsilon_N^{meas}$ Accumulate
$0.6-4.7$ (full-deposit protons only)	0.410 ± 0.026 $(9.4/7)$	0.425 ± 0.020
$0.6-17.0$ (all energy range)	0.424 ± 0.023 $(16.5/13)$	0.445 ± 0.017

Table 4.3: The comparison of $\epsilon_b^{meas}/\epsilon_N^{meas}$ in several ways. A_{NN} results are consistent either way.

Taking the average of Equation (4.39) and (4.40), A_{NN} is obtained :

$$\begin{aligned}\epsilon_{NN}^{meas} &= \frac{1}{2}\left(\frac{(N_{\uparrow\uparrow}^L+N_{\downarrow\downarrow}^L)-(N_{\uparrow\downarrow}^L+N_{\downarrow\uparrow}^L)}{(N_{\uparrow\uparrow}^L+N_{\downarrow\downarrow}^L)+(N_{\uparrow\downarrow}^L+N_{\downarrow\uparrow}^L)}+\frac{(N_{\uparrow\uparrow}^R+N_{\downarrow\downarrow}^R)-(N_{\uparrow\downarrow}^R+N_{\downarrow\uparrow}^R)}{(N_{\uparrow\uparrow}^R+N_{\downarrow\downarrow}^R)+(N_{\uparrow\downarrow}^R+N_{\downarrow\uparrow}^R)}\right)\\ &\cong \frac{N-BG}{N}A_{NN}\bar{P}_b\bar{P}_t. \qquad (4.41)\end{aligned}$$

Figure 4.6 displays ϵ_{NN}^{meas}, ϵ_N^{meas} and ϵ_b^{meas} as a function of $|t|$.

Thus A_{NN} is obtained:

$$A_{NN} \cong \frac{1}{\bar{P}_t\bar{P}_b}\frac{\epsilon_{NN}^{meas}}{1-R_{(\alpha+beam)}} \qquad (4.42)$$

where we substituted $1/(1-R_{(\alpha+beam)}) = (L+B)/L$. The target polarization is $\bar{P}_t = 0.924 \pm 0.018$, which is measured by BRP. The **averaged** beam polarization during RUN-4 is obtained by use of raw-asymmetries for the beam polarization and the target polarization, and the target polarization,

$$\bar{P}_b = \langle\frac{\epsilon_b^{meas}}{\epsilon_N^{meas}}\rangle\bar{P}_t. \qquad (4.43)$$

Because A_N of elastic *pp* elastic scattering does not depend on the reference frame, we can change the role of which is polarized between target proton and beam proton as we mentioned in Equation (4.17) and (4.18). Figure 4.7 displays the ratio of ϵ_b^{meas} and ϵ_N^{meas} as a function of $|t|$. We tried the four ways to get the ratio of $\langle\epsilon_b^{meas}/\epsilon_N^{meas}\rangle$ as shown in Table 4.3. A_{NN} results are consistent either way we choose.

We adopted the value of this ratio:

$$\langle\frac{\epsilon_b^{meas}}{\epsilon_N^{meas}}\rangle = 0.425 \pm 0.020,$$

where the error is statistical. The $|t|$ dependence of this ratio is accounted as one of the systematic error sources, which will be discussed later.

The statistical error of A_{NN} is obtained as follows:

$$\Delta A_{NN}^{stat} = \frac{1}{\bar{P}_b\bar{P}_t}\frac{(\Delta\epsilon_{NN}^{meas})^{stat}}{1-R_{(\alpha+beam)}}, \qquad (4.44)$$

and

$$(\Delta\epsilon_{NN}^{meas})^{stat} \sim \frac{1}{\sqrt{N}}$$

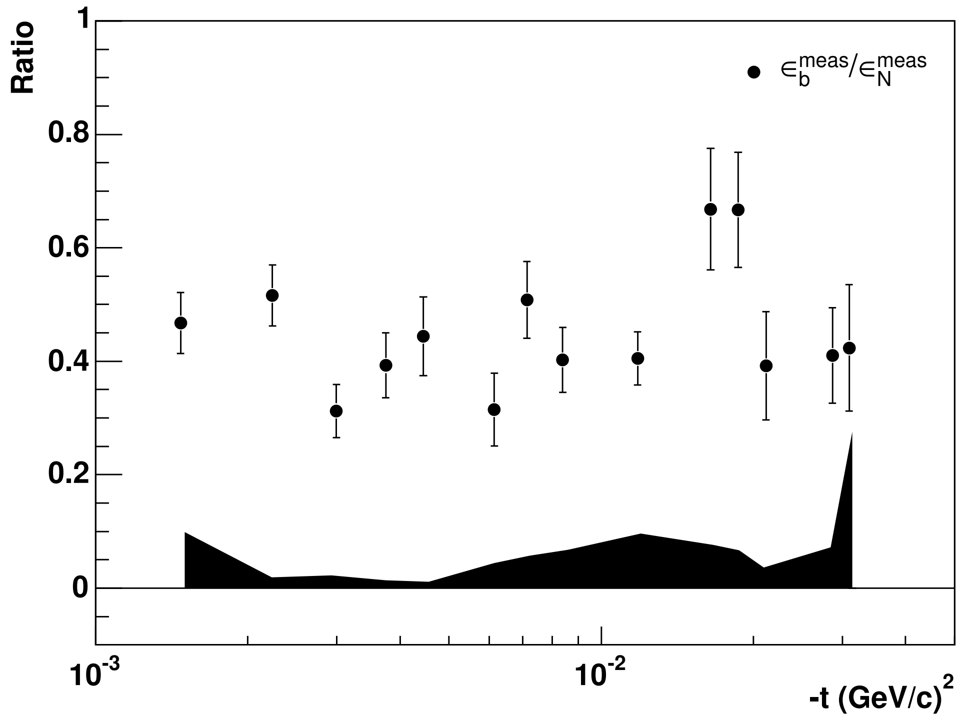

Figure 4.7: The ratio of ϵ_N^{meas} and ϵ_b^{meas} as a function of t. The errors on the data points are statistical. The lower band represents the total systematic error. The $|t|$ dependence is accounted as the systematic uncertainty about the beam polarization in the text.

T_R (MeV)	$-\langle t\rangle$ (GeV^2/c^2)	A_{NN}	ΔA_{NN}^{stat}	$\Delta A_{NN}^{normT} \pm \Delta A_{NN}^{normB}$
0.6 – 1.0	0.0015	-0.0060	0.0042	0.0001 ± 0.0003
1.0 – 1.4	0.0022	-0.0011	0.0050	0.0000 ± 0.0001
1.4 – 1.8	0.0030	-0.0039	0.0055	0.0001 ± 0.0002
1.8 – 2.2	0.0037	-0.0001	0.0059	$< 0.0001 \pm < 0.0001$
2.2 – 2.5	0.0044	-0.0046	0.0068	0.0001 ± 0.0002
3.0 – 3.5	0.0061	-0.0027	0.0064	0.0001 ± 0.0001
3.5 – 4.2	0.0071	0.0058	0.0054	0.0001 ± 0.0003
4.2 – 4.7	0.0084	-0.0093	0.0051	0.0002 ± 0.0004
5.7 – 7.2	0.0118	-0.0022	0.0038	$< 0.0001 \pm 0.0001$
8.0 – 9.3	0.0165	-0.0050	0.0060	0.0001 ± 0.0002
9.3 – 10.6	0.0187	0.0006	0.0051	$< 0.0001 \pm < 0.0001$
10.6 – 12.0	0.0212	0.0006	0.0051	$< 0.0001 \pm < 0.0001$
14.5 – 16.0	0.0287	-0.0032	0.0053	$< 0.0001 \pm 0.0002$
16.0 – 17.0	0.0309	-0.0014	0.0067	$< 0.0001 \pm 0.0001$

Table 4.4: A_{NN}, the normalization errors and the statistical errors as a function of energy bins.

The final values of A_{NN} and the statistical error as a function of $|t|$ are provided in Table 4.4.

The systematic uncertainty in the measurement are in two categories: T_R bin-dependent and overall normalization. These are obtained from the derivation of the first term in Equation (4.42):

$$\Delta A_{NN}^{sys} \cong A_{NN}\left(\frac{\Delta\epsilon_{NN}^{meas}}{\epsilon_{NN}^{meas}} \oplus \frac{\Delta R_{(\alpha+beam)}}{1-R_{(\alpha+beam)}} \oplus \frac{\Delta\bar{P}_t}{\bar{P}_t} \oplus \frac{\Delta\bar{P}_b}{\bar{P}_b}\right), \tag{4.45}$$

where $\oplus$ denotes the quadratic sum. The first and second terms are T_R bin-dependent. The first term is related to the residual component of A_N (ΔA_{NN}^{res}) and the elastic event selection (ΔA_{NN}^{sel}). The second term is related to the background correction (ΔA_{NN}^{BG}). The third and forth terms are the uncertainty about the normalization by $\bar{P}_t$ (ΔA_{NN}^{normT}) and $\bar{P}_b$ (ΔA_{NN}^{normB}). They are provided in Table 4.4. The systematic uncertainty of $\bar{P}_b$ is referred as ΔA_{NN}^{beam}. The spin-dependent luminosity, which is ignored Equation (4.34), is estimated to be small.

⟨ Systematic uncertainty from the residual A_N component ⟩

ΔA_{NN}^{res} is estimated as:

$$\Delta A_{NN}^{res} = \frac{A_N}{\bar{P}_t}\sqrt{(\epsilon_{L_t})^2 + \left(\epsilon_{L_b}\langle\frac{\epsilon_N^{meas}}{\epsilon_b^{meas}}\rangle\right)^2}$$

ΔA_{NN}^{res} is provided in Table 4.5 and is negligible for all T_R bins compared with statistical errors.

⟨ Systematic uncertainty from the elastic event selection ⟩

ΔA_{NN}^{sel} is related to the criteria of the elastic event selection. In Section 3.5, we mentioned the criteria for the recoil proton identification was $|ToF - ToF_{calc}| < 8$ nsec. We consider the ToF-cut width dependence by comparing the A_{NN} results with $|ToF - ToF_{calc}| < 6$ nsec and $|ToF - ToF_{calc}| < 10$ nsec cases.

$$\Delta A_{NN}^{sel} = |A_{NN}^{|ToF-ToF_{calc}|<6} - A_{NN}^{|ToF-ToF_{calc}|<10}| < \Delta A_{NN}^{stat}.$$

ΔA_{NN}^{sel} is provided in Table 4.5 and is ranging between 0.0001 and 0.0034 for all T_R bins. They are small in size to the statistical errors.

⟨ Systematic uncertainty from the background correction ⟩

ΔA_{NN}^{BG} is related to the backgrounds correction.

$$\Delta A_{NN}^{BG} = A_{NN} \cdot \sqrt{\Delta {R_\alpha}^2 + \Delta {R_{beam}}^2}$$

ΔA_{NN}^{BG} is provided in Table 4.5 and is negligible for all T_R bins. The details of ΔR_α and ΔR_{beam} have been discussed in Section 3.6.

⟨ Systematic uncertainty from the RHIC-beam polarization ⟩

The RHIC-beam polarization should be independent of T_R bins. However, as we have seen in Figure 4.7, the ratios of ϵ_b^{meas} and ϵ_N^{meas} are fluctuated as provided in Table 4.3. In order to account for this fluctuation, we rewrite Equation (4.42) in this way:

$$A_{NN}^{fluc} = \frac{1}{\bar{P}_t^2} \frac{\epsilon_N^{meas}}{\epsilon_b^{meas}} \frac{\epsilon_{NN}^{meas}}{1 - R_{(\alpha+beam)}}, \tag{4.46}$$

and we consider the difference between A_{NN} and A_{NN}^{fluc} as the systematic uncertainty about the RHIC-beam polarization:

$$\Delta A_{NN}^{beam} = \frac{\epsilon_{NN}^{meas}}{\bar{P}_t^2 (1 - R_{(\alpha+beam)})} \sqrt{\left(\langle \frac{\epsilon_N^{meas}}{\epsilon_b^{meas}} \rangle - \frac{\epsilon_N^{meas}}{\epsilon_b^{meas}} \right)^2}$$

ΔA_{NN}^{beam} is provided in Table 4.5 and is ranging between 0.0001 and 0.0018 for all T_R bins. They are small compared to the statistical errors.

⟨ Systematic uncertainty from the spin-dependent luminosity ⟩

The effect spin-dependent luminosity is obtained as the product of ϵ_{L_b} and ϵ_{L_t} from Equation (4.34). It is negligible as long as $|\epsilon_{L_b}|$ and $|\epsilon_{L_t}|$ are less than 5×10^{-3}.

In order to estimate ϵ_{L_b} and ϵ_{L_t} in the different way, we tried to use selected elastic proton event yields.

$\epsilon_{L_b}^{eve} = (N_{\uparrow 0}^L + N_{\uparrow 0}^R - N_{\downarrow 0}^L - N_{\downarrow 0}^R)/(N_{\uparrow 0}^L + N_{\uparrow 0}^R + N_{\downarrow 0}^L + N_{\downarrow 0}^R) = 0.0035 \pm 0.0005$

$\epsilon_{L_t}^{eve} = (N_{0\uparrow}^L + N_{0\uparrow}^R - N_{0\downarrow}^L - N_{0\downarrow}^R)/(N_{0\uparrow}^L + N_{0\uparrow}^R + N_{0\downarrow}^L + N_{0\downarrow}^R) = 0.0036 \pm 0.0005,$

thus the product of ϵ_{L_b} and ϵ_{L_t} is in the order of 10^{-5} and negligible.

T_R (MeV)	$-\langle t \rangle$ (GeV/c)^2	total sys. ΔA_{NN}^{sys}	Components $\Delta A_{NN}^{res} \pm \Delta A_{NN}^{sel} \pm \Delta A_{NN}^{BG} \pm \Delta A_{NN}^{beam}$
0.6 – 1.0	0.0015	0.0012	$0.0009 \pm 0.0007 \pm < 0.0001 \pm 0.0005$
1.0 – 1.4	0.0022	0.0034	$0.0005 \pm 0.0034 \pm < 0.0001 \pm 0.0002$
1.4 – 1.8	0.0030	0.0016	$0.0004 \pm 0.0006 \pm < 0.0001 \pm 0.0014$
1.8 – 2.2	0.0037	0.0014	$0.0003 \pm 0.0014 \pm < 0.0001 \pm < 0.0001$
2.2 – 2.5	0.0044	0.0017	$0.0003 \pm 0.0017 \pm < 0.0001 \pm 0.0002$
3.0 – 3.5	0.0061	0.0010	$0.0003 \pm 0.0001 \pm < 0.0001 \pm 0.0009$
3.5 – 4.2	0.0071	0.0022	$0.0002 \pm 0.0020 \pm < 0.0001 \pm 0.0009$
4.2 – 4.7	0.0084	0.0009	$0.0005 \pm 0.0005 \pm < 0.0001 \pm 0.0005$
5.7 – 7.2	0.0118	0.0006	$0.0004 \pm 0.0003 \pm < 0.0001 \pm 0.0001$
8.0 – 9.3	0.0165	0.0020	$0.0002 \pm 0.0006 \pm < 0.0001 \pm 0.0018$
9.3 – 10.6	0.0187	0.0012	$0.0002 \pm 0.0012 \pm < 0.0001 \pm 0.0002$
10.6 – 12.0	0.0212	0.0025	$< 0.0001 \pm 0.0025 \pm < 0.0001 \pm 0.0001$
14.5 – 16.0	0.0287	0.0009	$0.0003 \pm 0.0009 \pm < 0.0001 \pm 0.0001$
16.0 – 17.0	0.0309	0.0003	$0.0002 \pm 0.0002 \pm < 0.0001 \pm < 0.0001$

Table 4.5: Systematic uncertainties on A_{NN} as a function of T_R-bins. The first is total, followed by the components.

Chapter 5

Results and Discussion

5.1 A_N for the H-jet-target Polarization

5.1.1 Results

The resulting A_N is displayed in Figure 5.1 and Table 5.1. The statistical errors, the systematic errors and the normalization errors for 14 T_R bins are listed as well.

The black line is the theoretical prediction with no hadronic spin-flip ($\mathrm{Im}r_5 = 0$ and $\mathrm{Re}r_5 = 0$). [1]. This line is obtained from Equation (1.34) and (1.35) with substituting the parameters from the past experiments: $\sigma_{tot} = 38.4 \pm 0.5$ mb, $\rho = -0.08 \pm 0.02$, $\delta_C = 0.02 \pm 0.01$. And the parameters from the references: $B = 12\ (\mathrm{GeV}/c)^{-2}$ [63] and $\kappa = 1.7938 \pm < 0.0001$.

The A_N data are compared to the theoretical prediction and the χ^2 is 13.4 for 14 degrees of freedom. The major uncertainty in the CNI prediction comes from the parameterization of the hadronic amplitudes and the approximate knowledge of the ρ parameter.

The A_N data are also fitted with the CNI prediction allowing for a hadronic spin-flip contribution. The blue line shows the fitting results without fixing $\mathrm{Im}r_5 = 0$ and $\mathrm{Re}r_5 = 0$. The quality of the fit is similar to the case with no hadronic spin-flip ($\chi^2 = 11.1/12$ d.o.f.). The values obtained for r_5 are:

$$\begin{aligned} \mathrm{Re}\, r_5 &= -0.0008 \pm 0.0091, \\ \mathrm{Im}\, r_5 &= -0.015 \pm 0.029 \end{aligned}$$

and the correlation parameter between $\mathrm{Re}\ r_5$ and $\mathrm{Im}\ r_5$ is -0.92. The results of the r_5 fit are shown in Figure 5.1. The results of r_5 and its associated χ^2 contours are displayed in Figure 5.2.

5.1.2 Effects of ρ, δ_C and σ_{tot} on A_N

The A_N data indicates the tiny deviation in shape and magnitude from the CNI prediction without spin-flip. This deviation is regarded as the r_5 contribution. However, the accuracy of CNI prediction is limited because of the other parameters like σ_{tot}, ρ and δ_C. These were obtained from the past experimental results with finite uncertainties. And these uncertainties bring a deviation on A_N shape, as well as r_5 does. Therefore we estimate the sensitivity for r_5.

B would not affect A_N because it acts as an exponential in very small $-t$. κ is measured very well within 10^{-5}. Thus, we checked the effect on A_N data of ρ, δ and σ_{tot} uncertainties. They

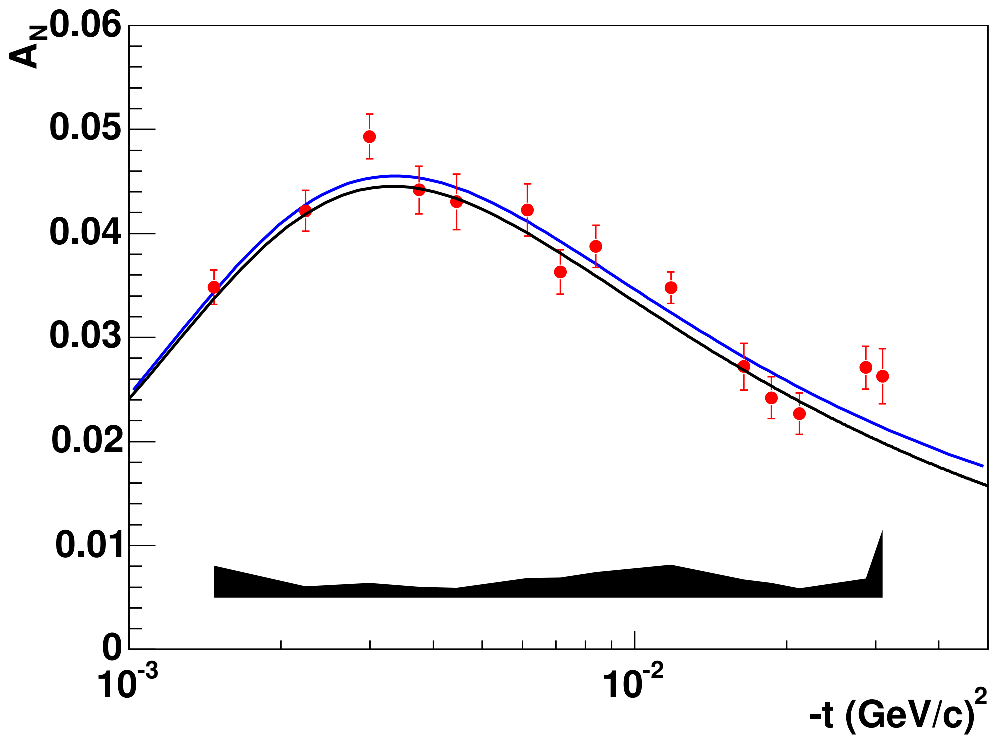

Figure 5.1: A_N as a function of $-t$ for $pp^{\uparrow} \rightarrow pp$. The results of this experiment (at $\sqrt{s}$ = 13.7 GeV). The errors on the data points are statistical. The lower band represents the systematic errors. The prediction for A_N with the electro-magnetic spin-flip only is superimposed to the data (black lane). The blue line is a fit to the data allowing for a hadronic spin-flip contribution to A_N.

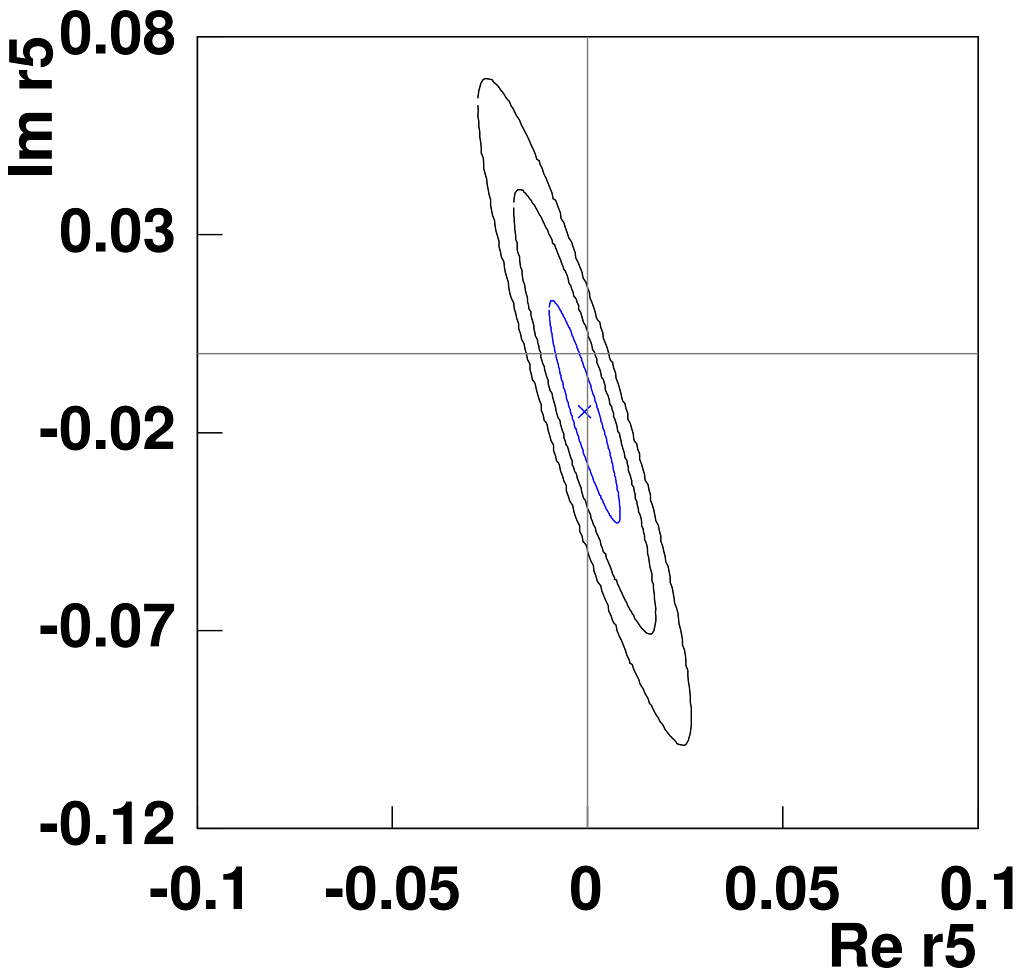

Figure 5.2: r_5 with the 1-σ, 2-σ and 3-σ confidence contours.

T_R (MeV)	$-\langle t \rangle$ (GeV/c)^2	A_N	ΔA_N (stat. $\pm$ sys. $\pm$ norm.)
0.6 – 1.0	0.0015	0.0348	$0.0017 \pm 0.0030 \pm 0.0007$
1.0 – 1.4	0.0022	0.0422	$0.0020 \pm 0.0007 \pm 0.0008$
1.4 – 1.8	0.0030	0.0493	$0.0022 \pm 0.0010 \pm 0.0010$
1.8 – 2.2	0.0037	0.0442	$0.0023 \pm 0.0006 \pm 0.0009$
2.2 – 2.5	0.0044	0.0430	$0.0027 \pm 0.0004 \pm 0.0008$
3.0 – 3.5	0.0061	0.0423	$0.0025 \pm 0.0017 \pm 0.0008$
3.5 – 4.2	0.0071	0.0363	$0.0021 \pm 0.0018 \pm 0.0007$
4.2 – 4.7	0.0084	0.0388	$0.0020 \pm 0.0023 \pm 0.0008$
5.7 – 7.2	0.0118	0.0348	$0.0015 \pm 0.0031 \pm 0.0007$
8.0 – 9.3	0.0165	0.0272	$0.0023 \pm 0.0016 \pm 0.0005$
9.3 – 10.6	0.0187	0.0242	$0.0020 \pm 0.0013 \pm 0.0005$
10.6 – 12.0	0.0212	0.0227	$0.0020 \pm 0.0008 \pm 0.0004$
14.5 – 16.0	0.0287	0.0271	$0.0021 \pm 0.0018 \pm 0.0005$
16.0 – 17.0	0.0309	0.0263	$0.0027 \pm 0.0065 \pm 0.0005$

Table 5.1: A_N as a function of $-t$ in 14 T_R bins. The first error is the statistical one, followed by the systematic error, and the normalization error on P_t.

are independent and the total uncertainty is regarded as the quadratic sum of each components.

$$\Delta A_N^{sum} = \frac{\partial A_N}{\partial \sigma_{tot}}\Delta\sigma_{tot} \oplus \frac{\partial A_N}{\partial \rho}\Delta\rho \oplus \frac{\partial A_N}{\partial \delta_C}\Delta\delta_C, \tag{5.1}$$

$$\frac{\partial A_N}{\partial \sigma_{tot}}\Delta\sigma_{tot} \approx \frac{|A_N(\sigma_{tot}+\Delta\sigma_{tot}) - A_N(\sigma_{tot}-\Delta\sigma_{tot})|}{2}, \tag{5.2}$$

$$\frac{\partial A_N}{\partial \rho}\Delta\rho \approx \frac{|A_N(\rho+\Delta\rho) - A_N(\rho-\Delta\rho)|}{2}, \tag{5.3}$$

$$\frac{\partial A_N}{\partial \delta_C}\Delta\delta_C \approx \frac{|A_N(\delta_C+\Delta\delta_C) - A_N(\delta_C-\Delta\delta_C)|}{2}, \tag{5.4}$$

Here we set $\Delta\sigma_{tot} = 0.05$ mb from Figure 1.2, $\Delta\rho = 0.02$ from Figure A.3 and $\Delta\delta_C = 0.01$ from the experimental results.

Figure 5.3 displays the deviations from the non spin-flip A_N form. Blue solid line corresponds to the deviation, which is obtained from Figure 5.1 comparing blue and black lines (with and without spin-flip amplitude). The black dashed line represents Equation (5.1). The red-dotted line, green-dashed and dotted line and pink-thine solid line correspond to Equation (5.2), (5.3) and (5.4), respectively. Comparing the blue solid line and the black dashed line, the level of the deviation is comparable, ~ 0.0001. Thus we conclude that our A_N data are consistent with no hadronic spin-flip within uncertainties from other parameters. A_N data do not support the presence of a large hadronic spin-flip amplitude at this energy.

This measurement represents the first precise confirmation of the predicted dependence of the analyzing power on the four-momentum transfer squared t in *pp* elastic scattering, due to the proton's anomalous magnetic moment of Schwinger [2], Kopeliovich, and Lapidus [3].

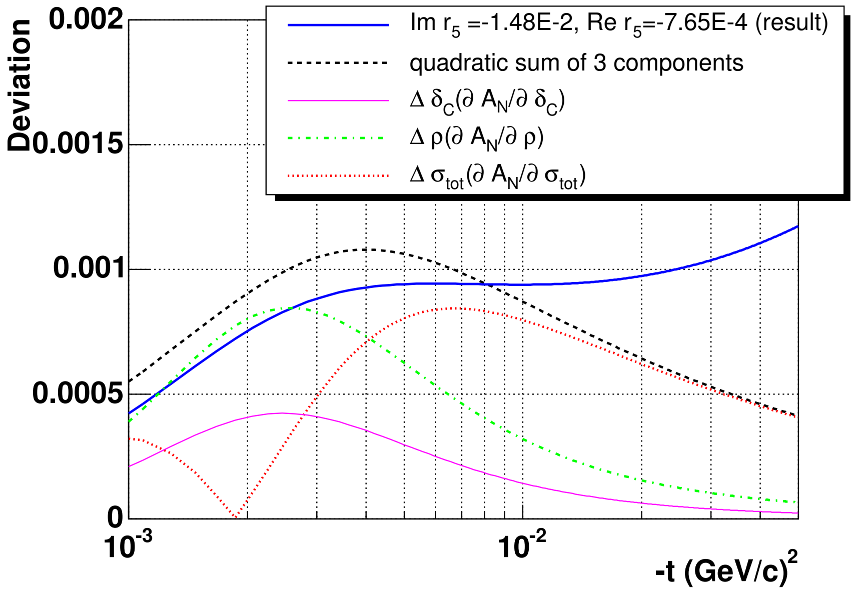

Figure 5.3: Deviations from the non spin-flip A_N form. Blue solid line corresponds to the deviation of A_N shape which is obtained from Figure 5.1 comparing blue and black lines (with/without spin-flip amplitude). The black dashed line represents Equation (5.1). The red-dotted line, green-dotted and dashed line and pink-thin solid line corresponds to Equation (5.2), (5.3) and (5.4), respectively.

5.2 A_{NN} for the H-Jet-target and the RHIC-beam Polarizations

5.2.1 Results

At large $\sqrt{s}$ and small $-t$, A_{NN} is expressed as:

$$\begin{aligned} A_{NN}\frac{\mathrm{d}\sigma}{\mathrm{d}t} &= \frac{4\pi}{s^2}\{2|\phi_5(s,t)|^2 + \mathrm{Re}[\phi_1(s,t)^*\phi_2(s,t) - \phi_3(s,t)^*\phi_4(s,t)]\} \\ &\cong \frac{4\pi}{s^2}\{2|\phi_5^{had}(s,t)|^2 + \mathrm{Re}[\phi_+(s,t)^*\phi_2^{had}(s,t)]\}. \end{aligned}$$

By considering $\phi_5^{had}(s,t)$ is consistent with zero by the A_N measurement, A_{NN} are sensitive to hadronic component of double spin-flip amplitude. The resulting A_{NN} is displayed in Figure 5.4 and Table 5.2 with the statistical errors, the systematic errors and the normalization errors for each energy-bin are listed .

The statistical errors and the systematic errors of ϵ_N, ϵ_b and ϵ_{NN} have been discussed in the previous section.

The results of A_{NN} for each measured points are small and consistent with zero. The mean value of A_{NN} for the region of $0.001 < |t| < 0.032$ (GeV/c)^2 is $< A_{NN} >= -0.0024 \pm 0.0015$, and is consistent with zero.

Thus we conclude that our A_{NN} data are consistent with no hadronic double spin-flip within uncertainties from other parameters. A_{NN} data do not support the presence of a large hadronic double spin-flip amplitude at this energy.

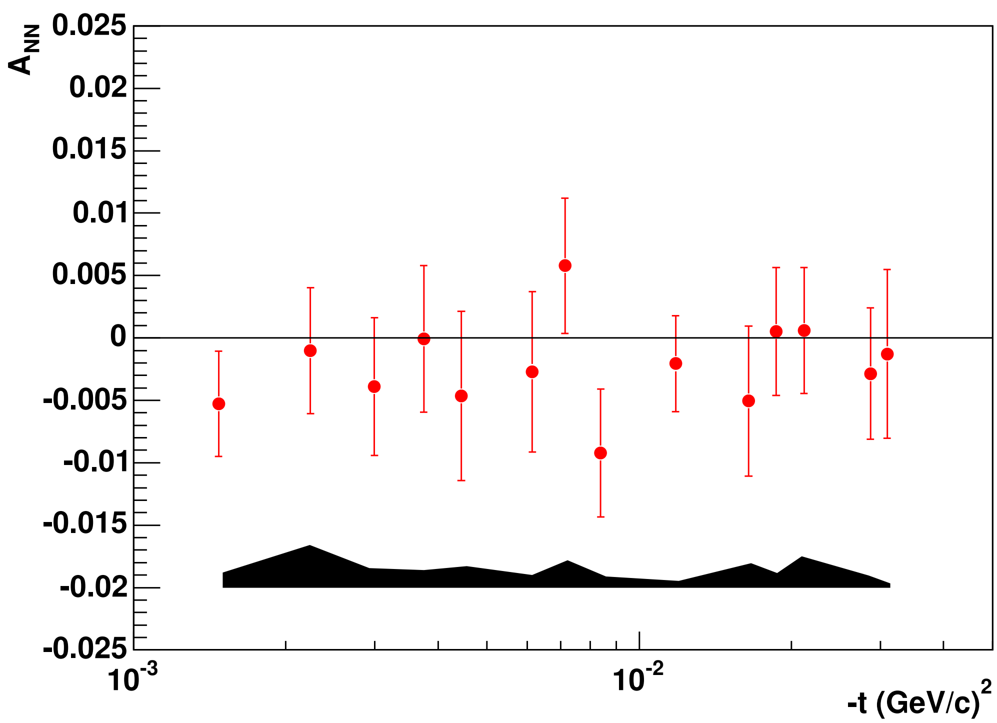

Figure 5.4: A_{NN} as a function of $-t$ for $p^{\uparrow}p^{\uparrow} \rightarrow pp$ at $\sqrt{s} = 13.7$ GeV. The errors on the data points are statistical. The lower band represents the total systematic error.

The A_{NN} are satisfied with the equations which have been discussed in Subsection 1.2.1:

$$\phi_2^{had}(s,t) = -\frac{\{\phi_5(s,t)\}^2}{\phi_+(s,t)},$$

and

$$\phi_2^{had}(s,t) \propto |t| \rightarrow 0.$$

5.2.2 Sensitivity for $\phi_2^{had}(s,t)$

As we have introduced in Subsection 1.3.2, the sensitivity of the A_{NN} to the double spin-flip amplitude have been studied theoretically [43]. The striking difference of A_{NN} values depending on the real-to-imaginary ratio of $\phi_2^{had}(s,t)$ has displayed in Figure 1.13 with assuming the magnitude to $\phi_+^{had}(s,t)$ is 0.05. Because our A_{NN} data are quite small, we can not extract the real-to imaginary ration of $\phi_2^{had}(s,t)$. And the magnitude to $\phi_+^{had}(s,t)$ is estimated to be less than 0.05, even in the extreme case that $\phi_2^{had}(s,t)$ is nearly pure real. In the case that ϕ_2^{had} is nearly imaginary, the magnitude to ϕ_2^{had} must be in the order of 10^{-3}.

Recently, as the result of analysis of the data from the *pp* and *p*C elastic scattering at the AGS and at the RHIC, the new model-dependent estimation of the magnitude and energy dependence of A_{NN} have been discussed [66].

T_R (MeV)	$-\langle t \rangle$ (GeV^2/c^2)	A_{NN}	ΔA_{NN} (stat. $\pm$ sys. $\pm$ norm.)
0.6 – 1.0	0.0015	-0.0060	$0.0042 \pm 0.0012 \pm 0.0003$
1.0 – 1.4	0.0022	-0.0011	$0.0050 \pm 0.0034 \pm 0.0001$
1.4–1.8	0.0030	-0.0039	$0.0055 \pm 0.0006 \pm 0.0002$
1.8 – 2.2	0.0037	-0.0001	$0.0059 \pm 0.0014 \pm < 0.0001$
2.2 – 2.5	0.0044	-0.0046	$0.0068 \pm 0.0017 \pm 0.0002$
3.0 – 3.5	0.0061	-0.0027	$0.0064 \pm 0.0001 \pm 0.0001$
3.5 – 4.2	0.0071	0.0058	$0.0054 \pm 0.0020 \pm 0.0003$
4.2 – 4.7	0.0084	-0.0093	$0.0051 \pm 0.0005 \pm 0.0005$
5.7 – 7.2	0.0118	-0.0022	$0.0038 \pm 0.0003 \pm 0.0001$
8.0 – 9.3	0.0165	-0.0050	$0.0060 \pm 0.0006 \pm 0.0003$
9.3– 10.6	0.0187	0.0006	$0.0051 \pm 0.0012 \pm < 0.0001$
10.6 – 12.0	0.0212	0.0006	$0.0051 \pm 0.0025 \pm < 0.0001$
14.5 – 16.0	0.0287	-0.0032	$0.0053 \pm 0.0009 \pm 0.0001$
16.0 – 17.0	0.0309	-0.0014	$0.0067 \pm 0.0002 \pm 0.0001$

Table 5.2: A_{NN} and the errors are listed as a function of energy bins.

In the limit at $-t \to 0$, the A_{NN} is connected to $\Delta\sigma_T$ and $\mathrm{Im}\phi_2(s,0)$:

$$A_{NN} \to -\frac{\Delta\sigma_T}{\sigma_{tot}} = -\frac{8\pi}{\sqrt{s(s-4m_p^2)}}\frac{\mathrm{Im}\phi_2(s,0)}{\sigma_{tot}},$$

therefore we obtain $\Delta\sigma_T$ at $P_{beam} = 100$ GeV/c:

$$\Delta\sigma_T = 0.092 \pm 0.058 \text{ (mb)},$$

where we use $\sigma_{tot} = 38.4$ mb.

Comparing our data and the past experiments, $\Delta\sigma_T = 0.34 \pm 0.07$ (mb) at $P_{beam} = 6$ GeV/c [32], our data have consistent tendency regarding the beam momentum dependence. (See Figure 1.5.) The first measurement of A_{NN} as a function of $-t$ in the CNI region are consistent with the experimental expectation of $\Delta\sigma_T \to 0$ and $\mathrm{Im}\phi_2(s,0) \to 0$ as $\sqrt{s} \to \infty$.

$\sqrt{s}$ (GeV)	σ_{tot} (mb)	ρ	B (GeV/c)$^{-2}$
13.7	34.0	-0.03	12.0
19.4	38.4	-0.08	12.0
200	41.6	0.13	16.3

Table 5.3: The input parameters for Equation (1.34), (1.35) and (1.36) with different center-of-mass energies.

5.3 Comparison of r_5 with Other Experiments

5.3.1 Elastic $p^{\uparrow}p$ Scattering

Figure 5.5 displays the results of A_N from this experiment, the E704 experiment and the PP2PP experiment. Our A_N data are measured at $\sqrt{s} = 13.7$ GeV. The E704 experiment at FNAL and PP2PP experiment at BNL measured A_N for $p\uparrow p$ elastic scattering in CNI region at $\sqrt{s} = 19.4$ GeV and $\sqrt{s} = 200$ GeV, respectively. The prediction for A_N with electro-magnetic spin-flip only for different center-of-mass energies are superimposed to the data. The red-solid line is for $\sqrt{s} = 13.9$ GeV, the dashed-black line is for $\sqrt{s} = 19.4$ GeV and the dashed-dotted-green line is for $\sqrt{s} = 200$ GeV. The prediction lines are obtained setting $\mathrm{Im}r_5 = 0$ and $\mathrm{Re}r_5 = 0$ in Equation (1.34), (1.35) and (1.36). The some of the other parameters are a function of the center-of-mass energy as we have displayed in Figure 1.2, A.3 and A.4. The values which are used in Figure 5.5 and 5.7 are summarized in Table 5.3.

As we have discussed in Subsection 1.3.1, the presence of a hadronic spin-flip amplitude ($\phi_5^{had}(s,t)$) interfering with the electro-magnetic non-spin-flip one ($\phi_+^{em}(s,t)$) introduces a deviation in shape and magnitude from A_N calculated with no hadronic spin-flip [1].

Figure 5.5 displays the comparison of A_N with different $\sqrt{s}$.

- The results of the PP2PP are consistent with the CNI prediction without hadronic spin-flip amplitude. (However they insisted in the paper that the data indicate a deviation which are suggestive of a hadronic spin-flip amplitude at $\sqrt{s} = 200$ GeV.)
- The results of E704 at $\sqrt{s} = 19.4$ GeV can not provide constraints on a hadronic spin-flip amplitude because of their limited accuracy.
- Our data do not suggest the presence of a large hadronic spin-flip amplitude at $\sqrt{s} = 13.7$ GeV.

The theoretical works in finding a way to understand the $\sqrt{s}$ dependence of hadronic spin-flip are ongoing [64].

We will concentrate on the similar $\sqrt{s}$ region in the following discussions. Figure 5.6 displays the result of r_5 with the 1-σ contour of the associated χ^2 for both results. The fitting results of them are displayed in Figure 5.7. The precision in the A_N and r_5 measurement was significantly improved by this experiment, compared with the results measurement by E704 experiment.

5.3.2 Elastic $p^{\uparrow}$C Scattering

A_N data from proton-carbon elastic scattering over a similar kinematic range at the same [9] and lower [6] energies, on the contrary, deviate substantially from the simple CNI prediction and

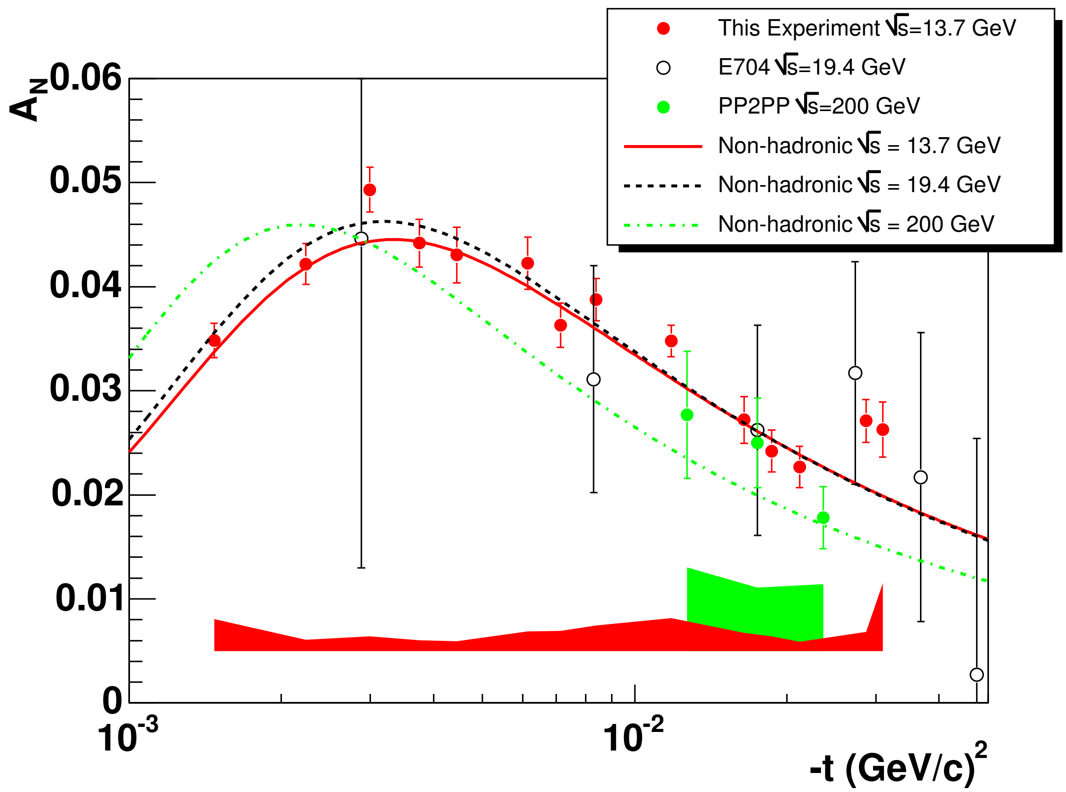

Figure 5.5: A_N as a function of t for $pp \rightarrow pp$. The results of this experiment which are measured at $\sqrt{s}$ = 13.7 GeV are indicated by the filled-red circles. The empty circles are measured at $\sqrt{s}$ = 19.4 GeV by the E704 experiment at FNAL. The filled-green circles are measured at $\sqrt{s}$ = 200 GeV by the PP2PP experiment at BNL. The errors on the data points are statistical. The red solid, black dashed and green dotted-dashed lines are the functions without allowing for a hadronic spin-flip contribution to A_N for these $\sqrt{s}$, respectively.

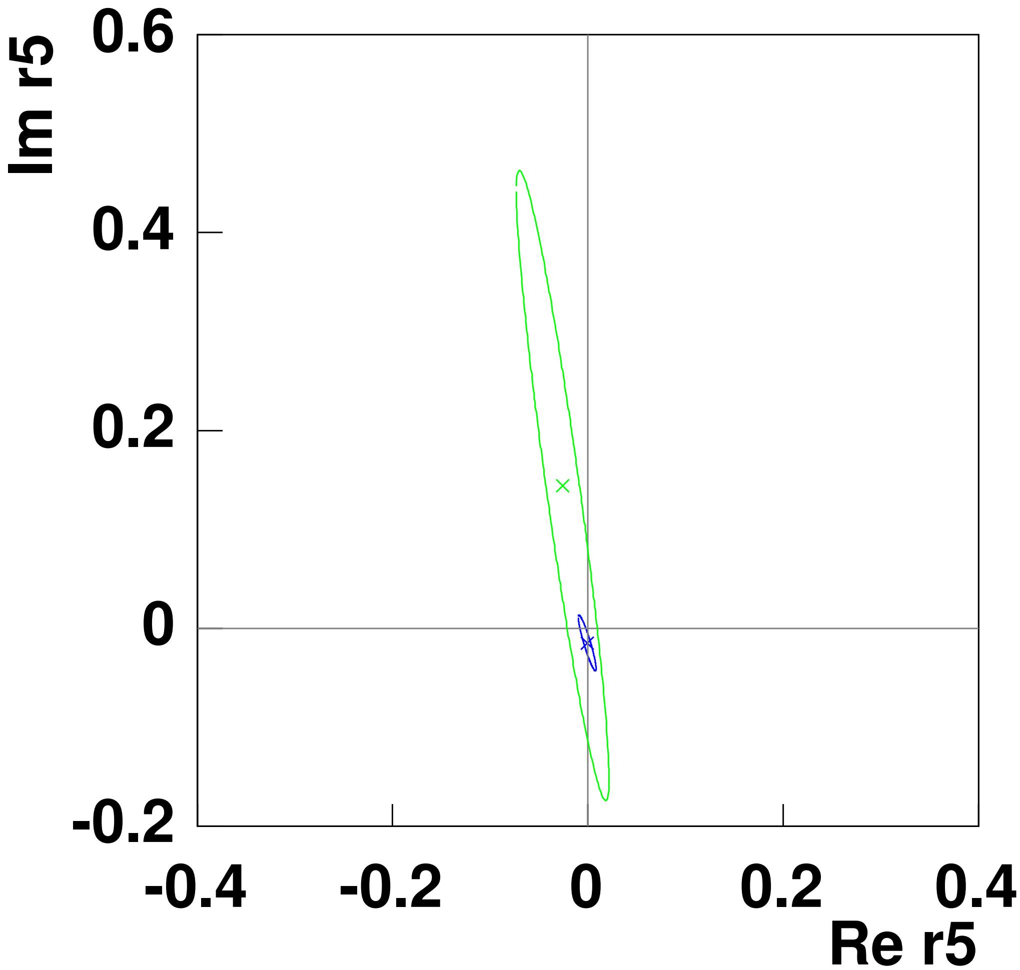

Figure 5.6: Hadronic spin-flip amplitude, r_5, with the 1-σ contour of the associated χ^2 obtained from A_N for *pp* elastic scattering at $\sqrt{s} = 13.7$ GeV (blue line, this experiment) and $\sqrt{s} = 19.4$ (green line, E704), respectively.

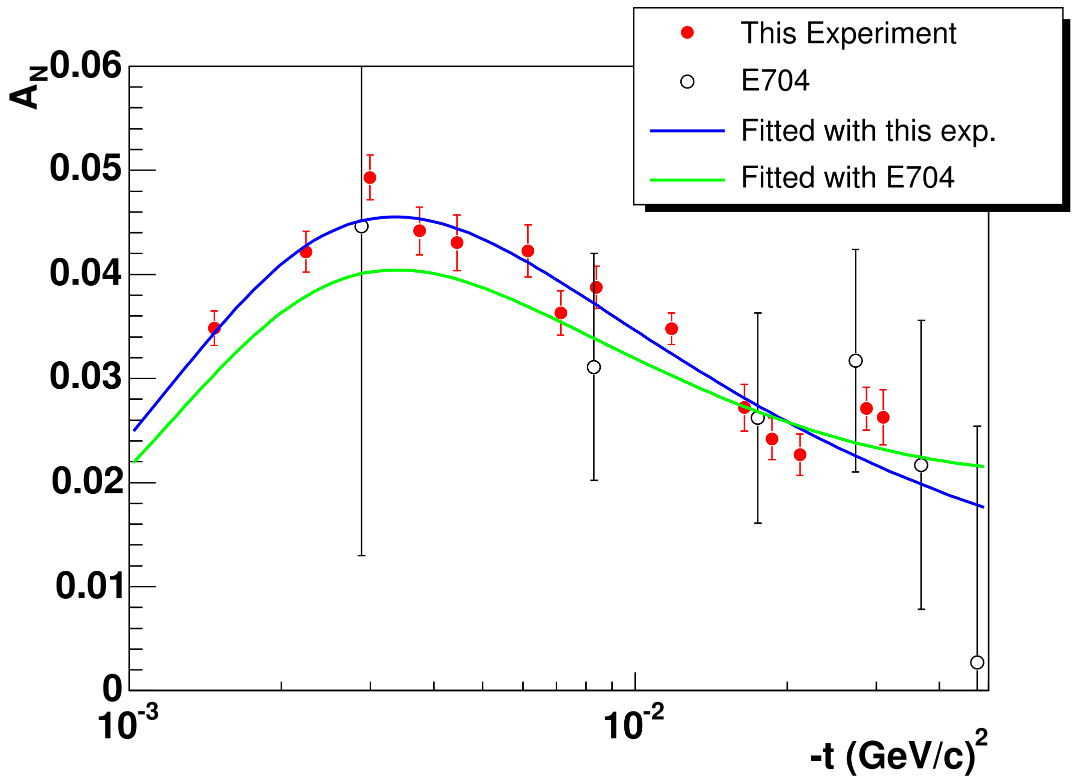

Figure 5.7: A_N as a function of t for $pp \to pp$. The results of this experiment (at $\sqrt{s} = 13.7$ GeV) are indicated by the filled-red circles. The empty circles are measured at $\sqrt{s} = 19.4$ GeV (E704 experiment at FNAL). The errors on the data points are statistical. The blue and green lines are fit to the data allowing for a hadronic spin-flip contribution to A_N for this experiment and E704 [5], respectively.

require a substantial hadronic spin-flip contribution.

The *p*C elastic scattering is described with two independent helicity amplitudes of the spin-nonflip amplitude $F_{++}(s,t)$, and the spin-flip amplitudes, $F_{+-}(s,t)$. The analyzing power, A_N, and the differential cross section, $\mathrm{d}\sigma_{pC}/\mathrm{d}t$, are written as [65]:

$$A_N \frac{\mathrm{d}\sigma_{pC}}{\mathrm{d}t} = 2\mathrm{Im}F_{++}(s,t)F_{+-}(s,t)^*,$$
$$\frac{\mathrm{d}\sigma_{pC}}{\mathrm{d}t} = |F_{++}(s,t)|^2 + |F_{+-}(s,t)|^2. \tag{5.5}$$

Each amplitude, F_j $(j = ++, +-)$, can be decomposed as

$$F_j(s,t) = F_j^{em}(s,t) + e^{-i\delta_{pC}} F_j^{had}(s,t),$$

where $F_j^{em}(s,t)$ and $F_j^{had}(s,t)$ are the electro-magnetic part and hadronic part of each amplitude respectively. δ_{pC} is the Coulomb phase.

The amplitudes are normalized by using total cross-section, σ_{tot}^{pC}, through the optical theorem as

$$\sigma_{tot}^{pC} = 4\sqrt{\pi}\mathrm{Im}F_{++}^{had}(s,0).$$

The hadronic spin-flip amplitude for the *p*C elastic scattering, r_5^{pC}, is defined by

$$r_5^{pC}(t) = \frac{m_p}{\sqrt{-t}} \frac{F_{+-}^{had}(s,t)}{\mathrm{Im}F_{++}^{had}(s,t)}. \tag{5.6}$$

$$\rho_{pC}(t) = \frac{\mathrm{Re}F_{++}^{had}}{\mathrm{Im}F_{++}^{had}}.$$

Figure 5.8 displays the A_N data of the elastic *pC* scattering at 21.7 GeV/c and r_5^{pC} is obtained by fitting the A_N data using Equation (5.6).

Using the relationship between r_5^{pC} and r_5

$$r_5 = \frac{1 - i\rho}{1 - i\rho_{pC}(t)} r_5^{pC}(t),$$

where $\rho_{pC}(t)$ is the ratio of the real-to-imaginary parts of the hadronic amplitude for *p*C elastic scattering, We have r_5 of the elastic *p*C scattering process as displayed in Figure 5.9.

Recently high statistics A_N data for $P_{beam} = 100$ GeV/c were reported [9] as displayed Figure 5.10. A significant strong spin flip has been observed for proton-carbon CNI scattering.

Although A_N^{pC} data from proton-carbon elastic scattering and A_N^{pp} data from proton-proton elastic scattering cover a similar momentum transfer squared $|t|$ range at the similar $\sqrt{s}$, bothering issue is there. It is a surprise because theorists predicted that the proton-proton result should also have a similar hadronic spin flip term. The discrepancy between them is thought to fully come from the target nucleus. Proton is iso-vector ($I = 1$) and Carbon is iso-scalar ($I = 0$). The new theoretical works, which are trying to find a way to understand the "mystery" of hadronic spin-flip, are ongoing [64]. Further measurements are also required to fully disentangle the role of the hadronic spin-flip amplitudes, their energy dependence and the different behavior between proton and nuclear targets.

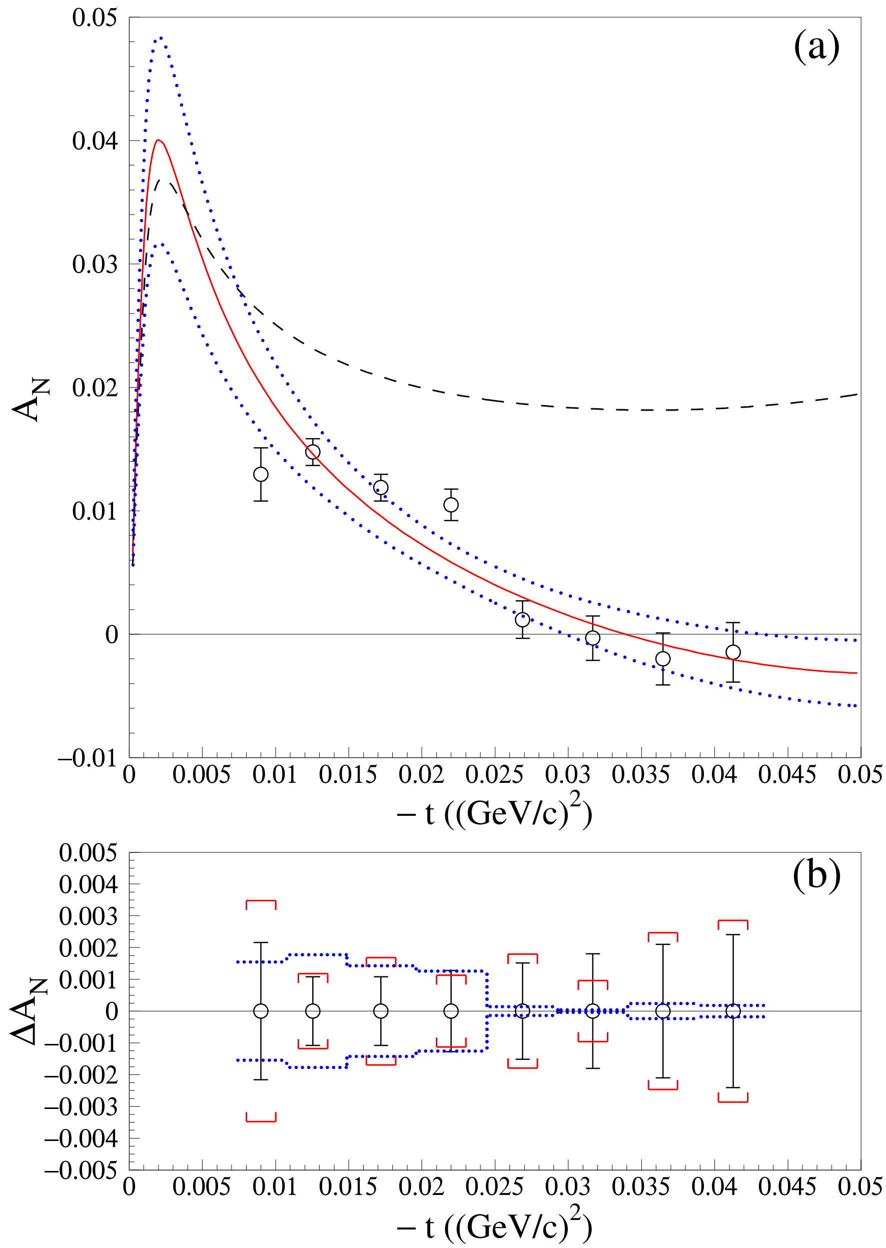

Figure 5.8: (a) The analyzing power, ${A_N}^{pC}$, for $p^{\uparrow}$C elastic scattering in the CNI region at $P_{beam} = 21.7$ GeV/c [6]. The error bars on the data points are statistical only. The solid line is the fitted function from theory [65]. The dotted lines are the 1-σ error band of the fitting result. The dashed line is the theoretical function with no hadronic spin-flip amplitude ($r_5 = 0$). (b) The error bars represent the statistical errors. The brackets represents the systematic errors in the raw asymmetry. The dotted lines represent the systematic error in the beam polarization.

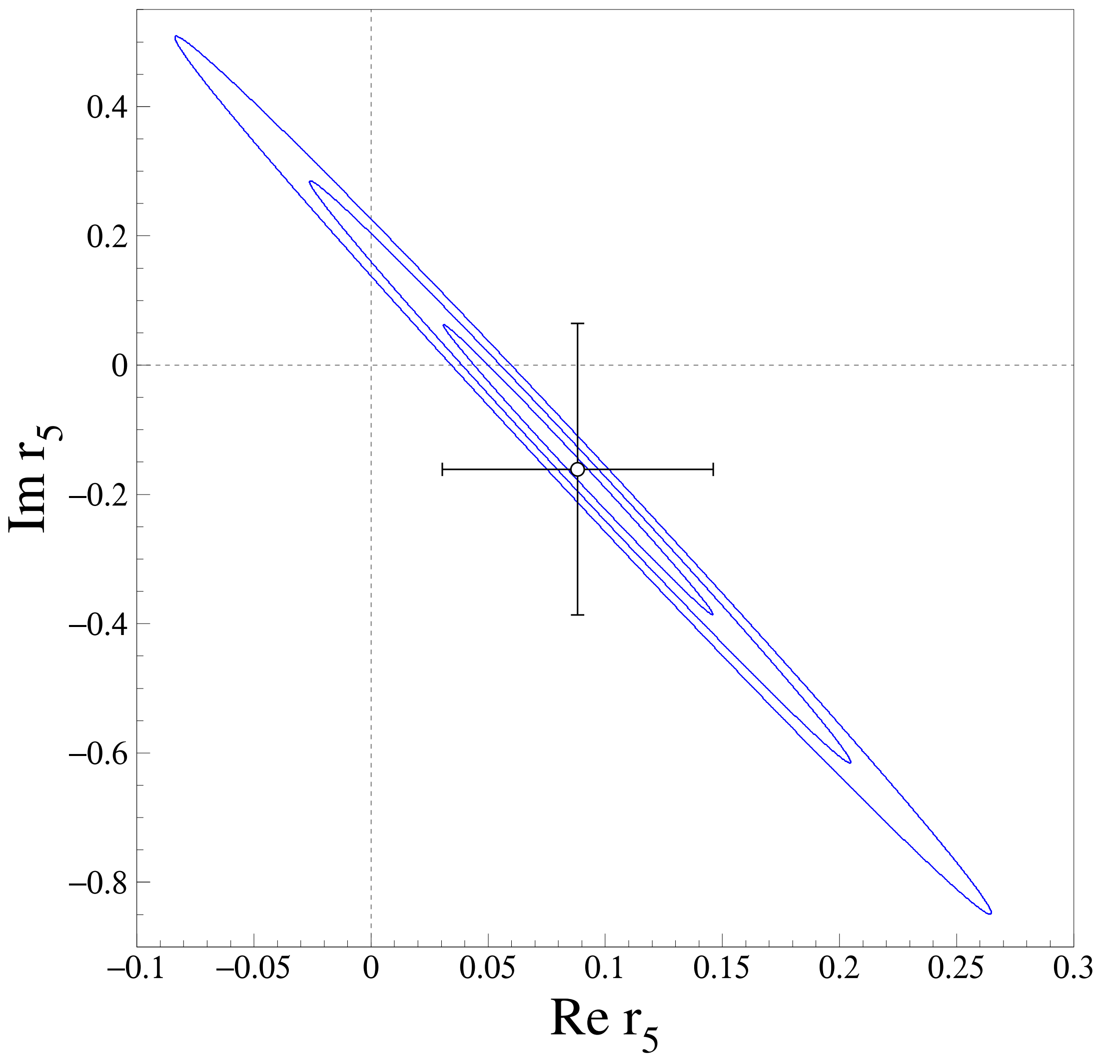

Figure 5.9: Hadronic spin-flip amplitude, r_5, with the 1-σ contour of the associated χ^2 obtained from ${A_N}^{pC}$ for $p^{\uparrow}C$ elastic scattering at $P_{beam} = 21.7$ GeV/c [6].

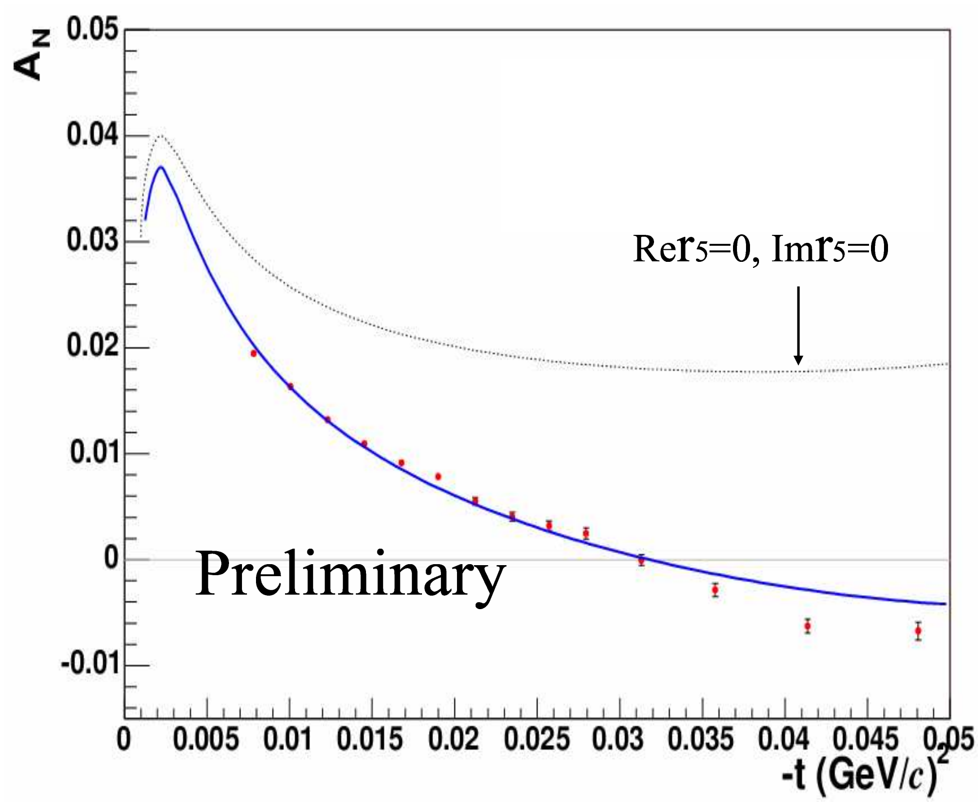

Figure 5.10: ${A_N}^{pC}$ as a function of t for $p^{\uparrow}C \rightarrow pC$ at $P_{beam} = 100$ GeV/c. The errors on the data points are statistical. The blue line is the fit to the data with the theoretical function [11] which is allowing a hadronic spin-flip contribution. The dotted line is the electro-magnetic spin-flip only ($\mathrm{Re}\, r_5 = 0, \mathrm{Im}\, r_5 = 0$).

Chapter 6

Conclusion

The spin-dependent asymmetries, A_N and A_{NN} for *pp* elastic scattering in the small momentum transfer region, $0.001 < -t < 0.032$ (GeV/c)^2, at $\sqrt{s} = 13.7$ GeV were measured using a polarized proton beam and a polarized hydrogen gas jet target. The polarized hydrogen gas jet target system and the recoil spectrometer were installed in the RHIC-ring, and the experiment was carried out in 2004.

In this $-t$ region, the electro-magnetic force and the hadronic force become same in strength and interfere with each others. We call this interference the Coulomb Nuclear Interference (CNI). The A_N and A_{NN} in the CNI region have been studied as the sensitive probe of the hadronic single and double spin flip amplitudes. The A_N is predicted theoretically, however, the accuracy of predicted A_N is limited by poor knowledge of the spin-flip hadronic amplitude. The precise measurements of A_N and A_{NN} in the CNI region were expected to provide significant constraints for various theoretical approaches and models. In addition to the physics interests, the precise measurement for A_N is also extremely important as a calibration tool for the *p*C-CNI polarimeter, which determines the beam polarization at the RHIC.

The hydrogen gas jet target system provided highly polarized atomic hydrogen, $P_t = 0.924 \pm 0.018$. The residual hydrogen molecules in the scattering chamber was measured to be $3.5 \pm 2.0\%$ in terms of hydrogen atoms. The target size was 6.5mm FWHM and the thickness along RHIC beam axis was measured to be $(1.3 \pm 0.2) \cdot 10^{12} \mathrm{atoms/cm^2}$. These values were highly satisfied with the designed values.

The recoil spectrometer, which consisted of the three left-right symmetric pairs of silicon detectors, was newly developed for this experiment. The recoil spectrometer was designed to identify the *pp* elastic scattering inside the RHIC ring by detecting only recoil protons. The covered kinetic energy range for a recoil proton was $0.6 < T_R < 17.5$ MeV ($0.001 < -t < 0.032$ (GeV/c)^2). The flight length of the recoil protons was 0.8 m and ToF ranged between 13 – 80 nsec. The recoil protons were well separated from beam-related backgrounds by ToF. The silicon strip runs along the incident RHIC-beam direction and the hit position was obtained from the channel-number. The covered recoil angle range per one arm was 10 –100 mrad and each read-out channel covered 5.5 mrad.

The off-line data analysis was performed with emphasis on the identification of *pp* elastic scatterings only with the recoil protons. The recoil particle identification was performed by use of ToF and measured kinetic energy T_R. The forward scattered missing particle identification was performed by use of recoil angle and T_R. We had accumulated 4 million elastic *pp* scattering events in $T_R = 0.6$ – 17.5 MeV. The momentum transfer, $-t$, was obtained by the measured kinetic energy T_R. The energy loss in the silicon entrance-window, the detector resolutions

(ToF and recoil angle), the background estimation were studied. Extraction of A_N and A_{NN} from selected signal events were discussed.

A_N for *pp* elastic scattering in the CNI region of $0.001 < -t < 0.032$ (GeV/c)^2 has been measured with high statistical precision $\Delta A_N^{stat}/A_N \sim 0.05$ for each T_R bin. The systematic uncertainty is comparable with the statistical error. We measured the peak shape of A_N due to CNI for the first time. The hadronic spin-flip component was obtained by fitting the data as follows,

$$\begin{aligned} \mathrm{Re}\, r_5 &= -0.0008 \pm 0.0091, \\ \mathrm{Im}\, r_5 &= -0.015 \pm 0.029. \end{aligned}$$

The A_N data are consistent with no hadronic spin-flip at $\sqrt{s} = 13.7$ GeV within uncertainties.

A_{NN} for the *pp* elastic scattering in the CNI region of $0.001 < -t < 0.032$ (GeV/c)^2 has been measured for the first time. A_{NN} is sensitive to the hadronic double spin-flip amplitude ($\phi_2^{had}(s,t)$) but there is no conclusive understanding for its $-t$ dependence nor magnitude to $\phi_+^{had}(s,t)$ [43].

The results of A_{NN} for each measured points are small and consistent with zero. The systematic uncertainty was smaller than the statistical error. The mean value for the region of $0.001 < -t < 0.032$ (GeV/c)^2 is $< A_{NN} >= -0.0024 \pm 0.0015$. Our data do not support the presence of a large double spin-flip amplitude at this energy.

Extrapolating A_{NN} data to the limit of $-t \to 0$, we have extracted the difference between total cross sections for anti-parallel and parallel transverse-spin states, $\Delta\sigma_T = 0.092 \pm 0.058$ (mb). Our $\Delta\sigma_T$ is consistent with zero. The past experimental data, which were measured in the region of small momentum beam up to $P_{beam} = 6$ GeV/c, indicated that $\Delta\sigma_T$ decreased as the beam momentum increased. Our data at $P_{beam} = 100$ GeV/c still keep consistent tendency.

Although our A_N and A_{NN} data for the *pp* elastic scattering do not support the presence of single nor double spin-flip amplitudes, A_N^{pC} data at $P_{beam} = 21.7$ –100 GeV/c for the proton-carbon elastic scattering indicated sizable hadronic spin-flip amplitude. The discrepancy between *pp* and *p*C scattering remind as the open question and the new theoretical works are ongoing [64]. Further measurements are required to fully disentangle the role of the hadronic spin-flip amplitudes, their energy dependence and the different behavior between proton and nuclear targets.

Acknowledgments

First and foremost, I would like to express my gratitude to Prof. Ken'ichi Imai, who has been my supervisor. He has always been ready with wealth of ideas and suggestions whenever I have discussed my work with him. He always encouraged me with his thoughtful advice and sharp physics sense. I have learned from him the way to approach the maximal results and essentials of physics from the data.

I am grateful to Prof. Naohito Saito, who has been my supervisor and gave me candid advice and guidance with infinite patience during my graduate education. Originally He gave me the first suggestion that I join the CNI Polarimetry group. He inspires me to achieve more, to think from a broader perspective what I never have noticed for myself.

I am much obliged to Dr. Gerry Bunce, who has been one of my supervisors at BNL. He has supported, advised and encouraged me to complete the present work and depthful insight has been created by a lot of discussion with him.

I would like to express my sincere thanks to Dr. Alessandro Bravar. I really enjoyed our interaction, and I cannot imagine a better adviser for me. I got a great profit from his thoughtful and concrete advice on my work and I am inspired much from his approach as a physicist.

I would like to thank all the collaborators of the CNI polarimetry Group and the hydrogen jet target team; Dr. I. G. Alekseev, Dr. A. Bravar, Dr. G. Bunce, Dr. S. Dhawan, Dr. R. Gill, Prof. W. Haeberli, Dr. O. Jinnouchi, Dr. A. Khodinov, Dr. Y. Makdisi, Dr. A. Nass, Prof. N. Saito, Prof. Edward J. Stephenson, Dr. D.N. Svirida, Prof. T. Wise, Dr. A. Zelenski, Dr. K.O. Eyser, Dr. H. Huang, Dr. I. Nakagawa and Dr. J. Wood.

I was very fortunate to receive much help and support from all of you.

Special thanks are due to Dr. Tom Wise and Dr. Alexander Nass. I have learned many things about the hydrogen jet target system from them. I would like to thank Dr. Igor G. Alekseev and Dr. Dimitry N. Svirida for developing the DAQ system and providing fruitful discussions on the data analysis. I would like to thank Prof. Edward J. Stephenson for supplying me indispensable advice and suggestions at any stage of the present work. I address my thanks to Dr. Yousef Makdisi for running the experiment and giving me advice and suggestion on the data analysis.

I would like to thank the Collider Accelerator Department and the RHIC / AGS Operation Groups for supporting the experiment. The experiment has not been done without their enormous efforts. I would like to thank the Instrumentation Division for newly developing the silicon detector and the front end electronics for this experiment. Our data in the very small $-t$ region are owing to their great efforts for the low noise read-out electronic chain.

I am grateful to all the members of RIKEN BNL Research Center for their support during my stay at BNL. I would like to thank Ms. Pam Esposito, Ms. Tammy Heinz, Ms. Jane Lysik, Ms. Taeko Ito, Ms. Chiharu Shimoyamada-Kawamura, Mr. Jun Nakamura and Mr. Ryousuke Maruyama for their administrative and secretarial support.

I would like to thank all present and past members of the "Experimental Nuclear and Hadronic

Physics" (NH) Group at Kyoto University. I am grateful to Prof. Masanobu Nakamura, Prof. Haruhiko Funahashi, Prof. Tetsuya Murakami, Prof. Masaru Yosoi and Prof. Kiyoshi Tanida, for valuable discussions. I would like to thank the staff of the Tandem Van de Graaff Accelerator, especially for Mr. Masanori Hirose, Mr. Hiroshi Matsumoto and Mr. Harukazu Nakahama, for their technical support in the test experiments for the detector system. I would like to express my thanks to Ms. Ayako Furumori-Nagaoka, Ms. Ayumi Nakao, Ms. Chika Horiuchi and Ms. Sonoko Chiaki for their secretarial support and hospitality. I would like to thank all present and past graduate students, Dr. Hiroki Sato, Dr. Hisayuki Torii, Dr. Junji Tojo, Mr. Kazuya Aoki, Mr. Kohei Shoji, who have worked together with me for RHIC Spin Collaboration and the PHENIX experiment. I would like to address my sincere thanks to all graduate students, especially in the same grade, Mr. Yoshinori Fukao, Dr. Koji Miwa, Mr. Terunao Nakura, Mr. Shinsuke Ota, Mr. Satoru Terashima, Mr. Manabu Togawa for their friendships and encouragements. They helped keeping my spirits high. I am also indebted to Mr. Yoshinori Fukao for his careful reading of and extensive feedback on earlier drafts of this dissertation; the present version is greatly improved thanks to his thorough comments.

I am grateful to all present and past members of Radiation Laboratory in RIKEN. Special thanks are due to the Chief Scientist, Dr. Hideto En'yo, who gave me a chance to re-start my career in physics. His advice, suggestion, support and encouragement have been crucial for the present work. I would like to address my thanks to Dr. Yasushi Watanabe, Dr. Yasuyuki Akiba, Dr. Yuji Goto, Dr. Atsushi Taketani, Prof. Kazuyoshi Kurita, Dr. Satoshi Yokkaichi, Dr. Itaru Nakagawa and Dr. Kensuke Okada. I would like to special thanks to Dr. Osamu Jinnouchi, who worked together with me as a member of the CNI polarimeter Group. Comments, suggestions and discussions from him have been invaluable. I would like to express my gratitude to Ms. Noriko Kiyama, Ms. Michiko Muroi and Ms. Karen Sakuma for their secretarial support and hospitality.

Finally, I would like to greatly acknowledge the generous support provided by my parents, Aiko Iinuma and Takeo Iinuma; my brother, Hiroo Iinuma. I would like to express my special appreciation to my husband, Dr. Kensuke Okada, for his heartful and continuous support and understanding. I am very lucky to have been surrounded by such a wonderful group of colleagues, family and friends. Thank you all.

Bibliography

[1] N.H. Buttimore *et al.*, Phys. Rev. D **59**, 114010 (1999).

[2] J. Schwinger, Phys. Rev. **69**, 681 (1946).

[3] B.Z. Kopeliovich and L.I. Lapidus, Sov. J. Nucl. Phys. **19**, 114 (1974).

[4] N.H. Buttimore, E. Gotsman, and E. Leader, Phys. Rev. D **18**, 694 (1978).

[5] N. Akchurin *et al.*, Phys. Rev. D **48**, 3026 (1993).

[6] J. Tojo *et al.*, Phys. Rev. Lett. **89**, 052302 (2002).

[7] S. Bültmann *et al.*, Phys. Lett. B **632**, 167 (2006).

[8] C. Aidala *et al.*, *Research Plan for Spin Physics at RHIC*, BNL-73798-2005.

[9] O. Jinnouchi *et al.*, Proc. 16^{th} International Spin Physics Symposium SPIN2004, p. 515.

[10] S.S. Adler *et al.* (PHENIX Collab.) , Phys. Rev. Lett **93**, 202002 (2004). [arXive: hep-ex/0404027];
S.S. Adler *et al.* (PHENIX Collab.) , Phys. Rev. D **73**, 091102 (2006). [arXive: hep-ex/0602004]

[11] T.L. Trueman, *hep-ph/0305085* (2003).

[12] R.N. Cahn, Z. Phys. C **15**, 253 (1982).

[13] V.N. Gribov, Sov. J. Nucl. Phys. **5**, 138 (1967).

[14] G.C. Fox *et al.*, Phys. Rev. Lett **18**, 3241 (1967).

[15] P.D.B Collins, *An Introduction to Regge Theory and High Energy Physics*, Cambridge University Press, Camblidge, 1977.

[16] M. Froissart, Phys. Rev. **123**, 1053 (1961);
A. Martin, Nuovo Cimento **42**, 930 (1966); **44**, 1219 (1966).

[17] http://pdg.lbl.gov/xsect/contents.html

[18] J.R. Cudell *et al.* (CIMPETE Collab.) Phys. Rev. D **65**, 074024 (2002). [arXiv:hep-ph/0107219]

[19] R.E Breedon *et al.*, Phys. Lette. B **216**, 459 (1989).

[20] http://pdg.lbl.gov/xsect/contents.html

[21] http://nuclth02.phys.ulg.ac.be/compete/predictor.html/

[22] U. Amaldi *et al.*, Phys. Lett. B **36**, 504 (1971)

[23] N. Amos *et al.*, Phys. Lett. B **128**, 343 (1983)

[24] M. Holder *et al.*, Phys. Lett. B **36**, 200 (1971)

[25] V. Bartenev *et al.*, Phys. Rev. Lett. **29**, 1755 (1972)

[26] V. Bartenev *et al.*, Phys. Rev. Lett **31**, 1088 (1973)

[27] G. Barbiellini *et al.*, Phys. Lett. B **39**, 663 (1972)

[28] N. Amos *et al.*, Phys. Lett. B **120**, 460 (1983)

[29] K.J. Foley *et al.*, Phys. Rev. Lett. **11**, 425 (1963)

[30] L.A. Fajardo *et al.*, Phys. Rev. D **24**, 46 (1981)

[31] Kh.M. Chernev et *al.*, Phys. Lett. B **36**, 266 (1971)

[32] Ed.K. Biegert *et al.*,Phys. Lett. B **73**, 235 (1978);
W. deBoer *et al.*, Phys. Rev. Lett. **34**, 558 (1975);
W.P. Madigan *et al.*, Phys. Rev. D **31**, 966 (1985);
W.R. Ditzler *et al.*, Phys. Rev. D **27**, 680 (1983);
J.P. Stanley *et al.*, Nucl. Phys. A **403**, 525-552 (1983).

[33] J.P. Stanley *et al.*, Nucl. Phys. A **403**, 525-552 (1983) ;
E. Aprile-giboni *et al.*, Nucl. Phys. A **431**, 637-668 (1984);
I.P. Auer *et al.*, Phys. Rev. Lett. **41**, 354 (1978);
D.P Gronsnick *et al.*, Phys. Rev. D **55**, 1159 (1997);
I.P. Auer *et al.*, Phys. Rev. D **29**, 2435 (1984);
J. Bystricky *et al.*, Phys. Lett. **142**, 130 (1984);
I.P. Auer *et al.*, Phys. Rev. Lett. **62**, 2649 (1989).

[34] A.D. Krisch and S.M Troshin, [35], p830.

[35] T.L. Trueman, in *Spin96*, Proceedings of 12th International Symposium in High Energy Spin Physics, Amsterdam, 1996,
edited by C.W. de Jager *et al.* (Word Scientific, Singapore, 1997), p. 833, hep-ph/9610429;RHIC/DET Note 18,1996,hep-ph/9610316

[36] D.G. Crabb *et al.*, Phys. Rev. Lett **65**, 3241 (1990).

[37] D.G. Crabb *et al.*, Nucl. Phys. **B121**, 231 (1977).

[38] J. Antille *et al.*, Nucl. Phys. **B185**, 1 (1981).

[39] P.H. Hansen et al, PRL50, 802 (1993).

[40] D.C. Peaslee *et al.*, Phys. Rev. Lett. **51**, 2359 (1983);
P.R. Cameron *et al.*, Phys. Rev. **D32**, 3070 (1985).

[41] K. Abe *et al.*, Phys. Lett. B **63**, 239 (1976);
J.R. O'Fallon *et al.*, Phys. Rev. Lett. **39**, 733 (1977);
D.G. Crabb *et al.*, Phys. Rev. Lett. **41**, 1257 (1978).

[42] D.G. Crabb *et al.*, Phys. Rev. Lett. **60**, 2351 (1988)

[43] E. Leader *et al.*, Phys. Rev. D **61**, 077504 (2000).

[44] Y. Akimov *et al.*, Sov. Phys. -JETP **21**, 507 (1965);
G. Beznogikh *et al.*, Phys. Lett. B **30**, 274 (1969).

[45] G. Beznogikh *et al.*, Phys. Lett. B **39**, 274 (1972).

[46] V. Bartenev *et al.*, Phys. Rev. Lett. **29**, 1755 (1972), and **31**, 1088 (1973), and **31**, 1367 (1973).

[47] V. Bartenev *et al.*, Sov. J. Nucl. Phys **23**, 400 (1976).

[48] W. K. Pitts *et al.*, Phys. Rev. C **45**, R1 (1992).

[49] A. Nass *et al.*, Nucl. Inst. Meth. A**505**,633 (2003).

[50] A. Nass *et al.*, in *Spin04*, Proceedings of 16th International Symposium in High Energy Spin Physics, Trieste, 2004.

[51] A. Zelenski *et al.*, Nucl. Inst. and Meth. A **536**, 248 (2005);
T. Wise *et al.*, Nucl. Inst. and Meth. A **559**, 1 (2006).

[52] P.R. Cameron *et al.*, *Proc. 95 Particle Accel. Conf.*, 1995, p. 2458, IEEE Cat. No. 95CH35843.

[53] P.R. Cameron *et al.*, Nucl.Instrum.Meth. **A345**, 226-229 (1994).

[54] I. Alekseev *et al.*, Nucl.Instrum.Meth. **A499**, 392-414 (2003).

[55] I. Alekseev *et al.*, *Configuration Manual Polarized Proton Collider at RHIC* (2001), http://www.agsrhichome.bnl.gov/RHIC/Spin/design/CMan/CMan.pdf

[56] M. Bai *et al.*, Phys. Rev. Lett. **96**, 174801 (2006).

[57] M. Froissart *et al.*, Nucl. Instr. Meth. **1**, 297 (1960).

[58] T. Kohe *et al.*, Part. Accel. **6**, 213 (1975);
H. Sato *et al.*, Nucl. Instr. Meth., Phys. Res. Sec. A **272**, 617 (1988);
F.Z. Khirai *et al.*, Phys. Rev. D **39**, 45 (1989).

[59] Jeff Dr. Thesis

[60] http://www.ipl.isotopeproducts.com/new..ipl..site/html/products..stand.asp

[61] http://physics.nist.gov/PhysRefData/Star/Text/contents.html

[62] C.F. Williamson, J.P. Boujot, and J. Picards, CEA report, **CEA-R-3042**, 1966.

[63] M.M. Block and R.N. Cahn, Rev. Mod. Phys. **57**, 563 (1985).

[64] T.L. Trueman, in *Spin04*, Proceedings of 16th International Symposium in High Energy Spin Physics, Trieste, 2004,
hep-ph/0412242

[65] B.Z. Kopeliovich and T.L. Trueman, Phys. Rev. D **64**, 034004 (2001).

[66] T.L. Trueman, RHIC Spin Note, September 27, (2005).
hep-ph/0604153

[67] G.G. Ohlsen and P.W. Keaton, Nucl. Inst. Meth. **109**, 41 (1973).

[68] E. Predazzi and O.V. Selyugin, Eur. Phys. J. A **13**, 471 (2002);
A.F. Martin and E. Predazzi, Phys. Rev. D **66**, 034029 (2002).

[69] B.Z. Kopeliovich and B.G. Zakharov, Phys. Lett. B **226**, 156 (1989).

[70] C. Bourelly, J. Soffer, and T.T. Wu, Phys. Rev. D **19**, 3249 (1979); Nucl. Phys B. **247**, 15 (1984).

[71] M. Anselmino and S. Forte, Phys. Rev. Lett. **71**, 223 (1993).

[72] Messiah. A, *Quantum Mechanics*, North Holland, 1958.

[73] E.L Berger *et al.*, Phys. Rev. D**17**, 2971 (1978).

[74] S.L Kramer *et al.*, Phys. Rev. D**17**, 1709 (1978).

[75] A. Lin *et al.*, Phys. Lett. B **74**, 273 (1978);
E.A. Crosbie *et al.*, Phys. Rev. D **23**, 600 (1981).

[76] M.J. Berger *et al.*, NIST database
http://physics.nist.gov/PhysRefData/Star/Text

Appendix A

Transition Amplitudes

A.1 Helicity amplitudes and Transversity amplitudes

The helicity amplitudes are the simplest, useful and urged by the parity restrictions. However transition amplitudes are also valuable, in particular transversity amplitudes. Both amplitudes are consist from five independent amplitudes. Five independent "helicity" amplitudes are displayed in Figurefig:Helicty. Five independent "transversity" amplitudes are displayed in Figurefig:Transversity. In this section, we write helicity amplitudes as ϕ_i instead $\phi_i(s,t)$ (i=1 –5) for simplicity.

The relationships between helicity amplitudes and transverse amplitudes are given as follows:

$$\begin{aligned}
\phi_1 &= \frac{1}{4}\{\alpha+\beta+2(\gamma-\delta-\epsilon)\}, \\
\phi_2 &= \frac{1}{4}\{\alpha+\beta+2(\gamma+\delta+\epsilon)\}, \\
\phi_3 &= \frac{1}{4}\{\alpha+\beta+2(-\gamma-\delta+\epsilon)\}, \\
\phi_4 &= \frac{1}{4}\{-\alpha-\beta+2(\gamma-\delta+\epsilon)\}, \\
\phi_5 &= \frac{i}{4}\{\alpha-\beta\}. \qquad \text{(A.1)}
\end{aligned}$$

$$\begin{aligned}
A_N &= \frac{\sigma_{\uparrow 0}-\sigma_{\downarrow 0}}{\sigma_{\uparrow 0}+\sigma_{\downarrow 0}} \\
&= \frac{\sigma_{\uparrow\uparrow\to\uparrow\uparrow}-\sigma_{\downarrow\downarrow\to\downarrow\downarrow}}{\sigma_{\uparrow\uparrow\to\uparrow\uparrow}+2\sigma_{\uparrow\uparrow\to\downarrow\downarrow}+2\sigma_{\uparrow\downarrow\to\uparrow\downarrow}+2\sigma_{\uparrow\downarrow\to\downarrow\uparrow}+\sigma_{\downarrow\downarrow\to\downarrow\downarrow}} \\
&= \frac{|\alpha|^2-|\beta|^2}{|\alpha|^2+|\beta|^2+2(|\gamma|^2+|\epsilon|^2+|\delta|^2)} \\
&= \frac{-2\mathrm{Im}\phi_5^*(\phi_1+\phi_2+\phi_3-\phi_4)}{|\phi_1|^2+|\phi_2|^2+|\phi_3|^2+|\phi_4|^2+4|\phi_5|^2}, \qquad \text{(A.2)}
\end{aligned}$$

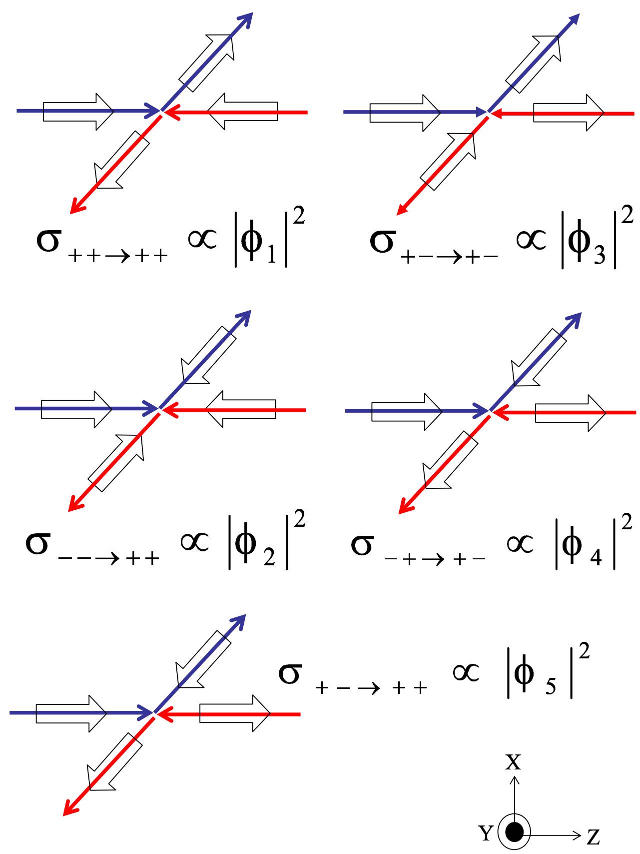

Figure A.1: Five independent helicity amplitudes: ϕ_1 and ϕ_3 are non-spin-flip amplitudes. ϕ_2 and ϕ_4 are double-spin-flip amplitudes. ϕ_5 is single-spin-flip amplitude

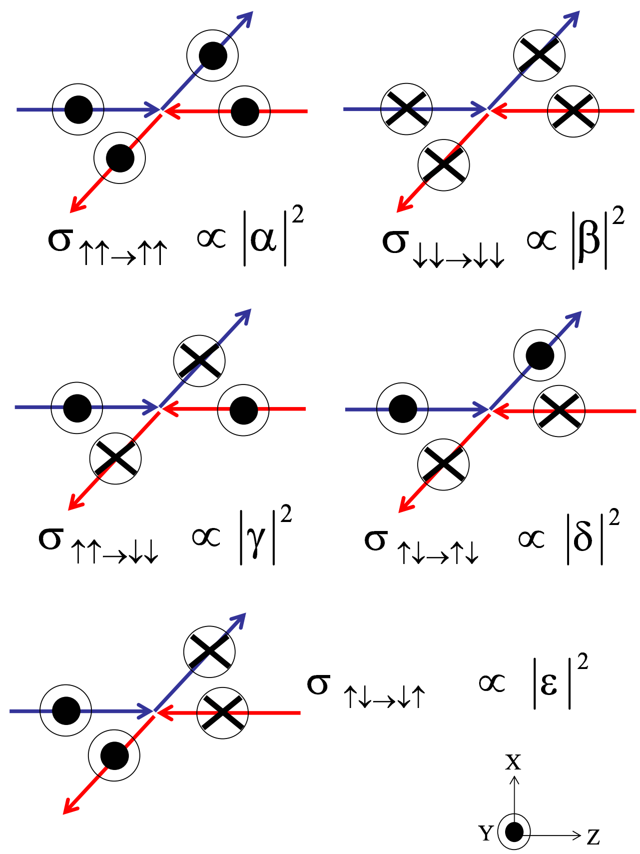

Figure A.2: Five independent transverse amplitudes where

$$
\begin{aligned}
\sigma_{\uparrow 0} &= \sigma_{\uparrow\uparrow} + \sigma_{\uparrow\downarrow} \\
\sigma_{\uparrow\uparrow} &= \Sigma_{kl}\sigma_{\uparrow\uparrow\to kl} = \sigma_{\uparrow\uparrow\to\uparrow\uparrow} + \sigma_{\uparrow\uparrow\to\downarrow\downarrow} \\
\sigma_{\uparrow\downarrow} &= \Sigma_{kl}\sigma_{\uparrow\downarrow\to kl} = \sigma_{\uparrow\downarrow\to\uparrow\downarrow} + \sigma_{\uparrow\downarrow\to\downarrow\uparrow} \\
\sigma_{\downarrow 0} &= \sigma_{\downarrow\downarrow} + \sigma_{\downarrow\uparrow} \qquad \text{(A.3)} \\
\sigma_{\downarrow\downarrow} &= \Sigma_{kl}\sigma_{\downarrow\downarrow\to kl} = \sigma_{\downarrow\downarrow\to\uparrow\uparrow} + \sigma_{\downarrow\downarrow\to\downarrow\downarrow} \\
\sigma_{\downarrow\uparrow} &= \Sigma_{kl}\sigma_{\downarrow\uparrow\to kl} = \sigma_{\downarrow\uparrow\to\uparrow\downarrow} + \sigma_{\downarrow\uparrow\to\downarrow\uparrow} = \sigma_{\uparrow\downarrow}. \qquad \text{(A.4)}
\end{aligned}
$$

Therefore

$$
\begin{aligned}
\sigma_{\uparrow 0} - \sigma_{\downarrow 0} &= \sigma_{\uparrow\uparrow\to\uparrow\uparrow} - \sigma_{\downarrow\downarrow\to\downarrow\downarrow} \\
\sigma_{\uparrow 0} - \sigma_{\downarrow 0} &= \sigma_{all} = \sigma_{\uparrow\uparrow\to\uparrow\uparrow} + 2\sigma_{\uparrow\uparrow\to\downarrow\downarrow} + 2\sigma_{\uparrow\downarrow\to\uparrow\downarrow} + 2\sigma_{\uparrow\downarrow\to\downarrow\uparrow} + \sigma_{\downarrow\downarrow\to\downarrow\downarrow}
\end{aligned}
$$

$$
\begin{aligned}
A_{NN} &= \frac{(\sigma_{\uparrow\uparrow} + \sigma_{\downarrow\downarrow}) - (\sigma_{\uparrow\downarrow} + \sigma_{\downarrow\uparrow})}{\sigma_{all}} \\
\text{nominator} &= \sigma_{\uparrow\uparrow\to\uparrow\uparrow} + \sigma_{\downarrow\downarrow\to\downarrow\downarrow} + 2(\sigma_{\uparrow\uparrow\to\downarrow\downarrow} - \sigma_{\uparrow\downarrow\to\uparrow\downarrow} + \sigma_{\uparrow\downarrow\to\downarrow\uparrow} \\
&= |\alpha|^2 + |\beta|^2 + 2(|\gamma|^2 - |\epsilon|^2 - |\delta|^2) = \mathrm{Re}[\phi_1^*\phi_2 - \phi_3^*\phi_4] + 2|\phi_5|^2. \qquad \text{(A.5)}
\end{aligned}
$$

A.2 Spin-dependent asymmetries

Using only initial state transverse polarization, with one or both particles polarized, we can measure seven spin dependent asymmetries.

$$
\begin{aligned}
A_N\frac{\mathrm{d}\sigma}{\mathrm{d}t} &= -\frac{4\pi}{s(s-4m_p^2)}\mathrm{Im}\,[\phi_5^*(\phi_1+\phi_2+\phi_3-\phi_4)], \qquad \text{(A.6)} \\
A_{NN}\frac{\mathrm{d}\sigma}{\mathrm{d}t} &= \frac{4\pi}{s(s-4m_p^2)}[2|\phi_5|^2 + \mathrm{Re}\,(\phi_1^*\phi_2 - \phi_3^*\phi_4)], \qquad \text{(A.7)} \\
A_{SS}\frac{\mathrm{d}\sigma}{\mathrm{d}t} &= \frac{4\pi}{s(s-4m_p^2)}\mathrm{Re}\,[\phi_1\phi_2^* + \phi_3\phi_4^*], \qquad \text{(A.8)} \\
A_{SL}\frac{\mathrm{d}\sigma}{\mathrm{d}t} &= \frac{4\pi}{s(s-4m_p^2)}\mathrm{Re}\,[\phi_5^*(\phi_1+\phi_2-\phi_3+\phi_4)], \qquad \text{(A.9)} \\
A_{LL}\frac{\mathrm{d}\sigma}{\mathrm{d}t} &= \frac{4\pi}{s(s-4m_p^2)}[|\phi_1|^2 + |\phi_2|^2 - |\phi_3|^2 - |\phi_4|^2]. \qquad \text{(A.10)}
\end{aligned}
$$

A.3 ρ and b-slope

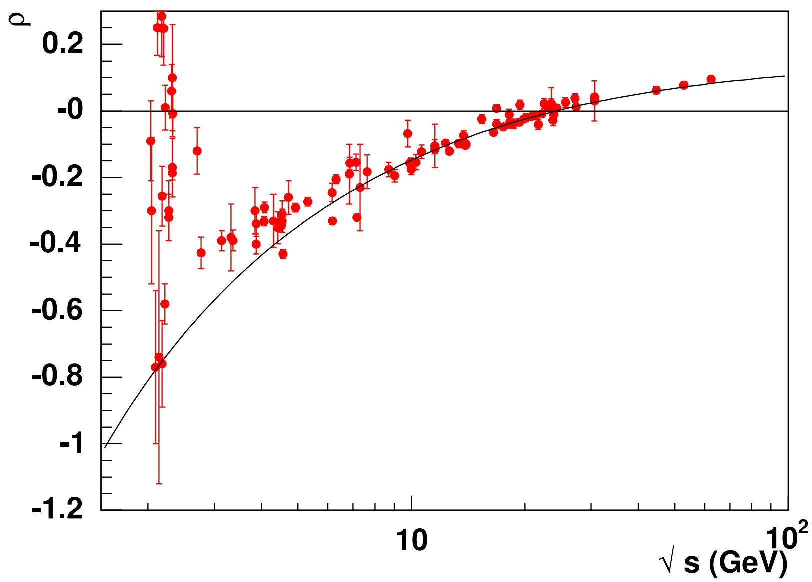

Figure A.3: ρ as a function of $\sqrt{s}$ [20]. The solid curve shows the results of the fitted function [21] suggested by Regge theory.

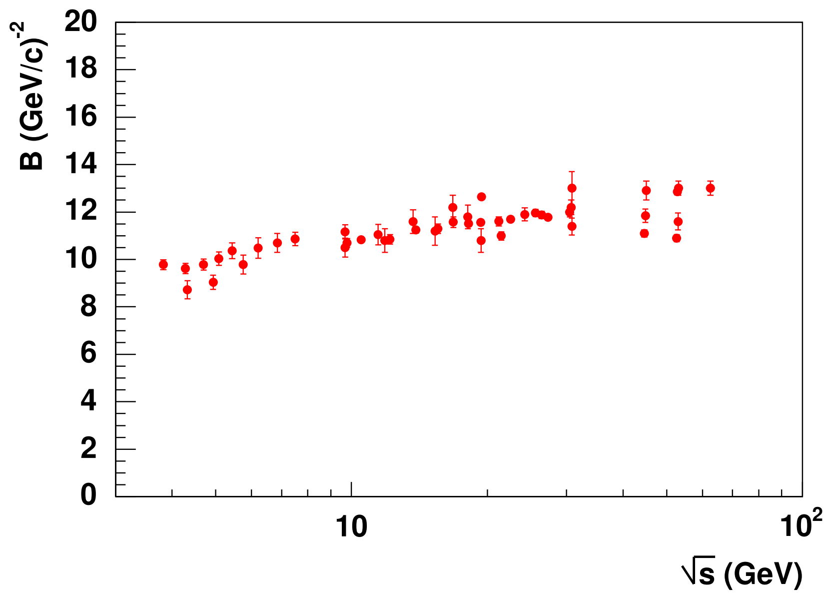

Figure A.4: B as a function of $\sqrt{s}$ [22, 23, 24, 25, 26, 27, 28, 29, 30, 31].

A.4 Read-out electronics in details

A.4.1 Capacitance and leak current of single strip for BNL-type and Hamamatsu-type

As is mentioned before, we employed two different types of silicon detector which were fabricated by the Hamamatsu Photonics, K. K. and fabricated by the BNL Instrumentation Division.

Capacitance Figure A.5 displays an example of single strip capacitance measurement of BNL-type as a function of bias voltage. The measured values varied among strips because of bench-test condition. The detector is full depleted around 160 V and the capacitance is around 20 $\sim$ 25 pF. Then the capacitance of 4strips gathered is $\sim$ 100 pF.

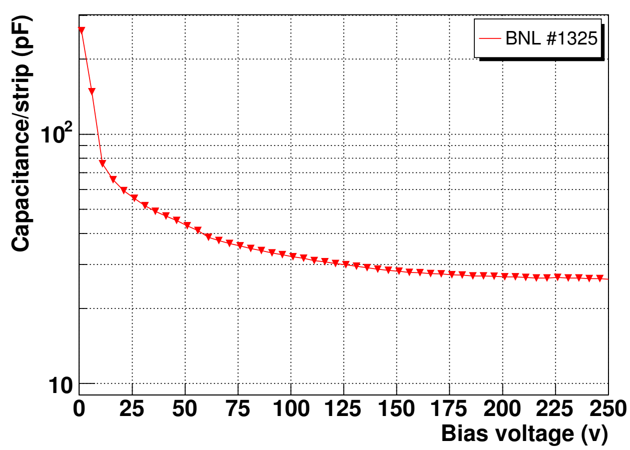

Figure A.5: Single strip capacitance measurement in a function of bias voltage for BNL-type detectors (measured by author)

Figure A.6 displays the capacitance of *the sum of all strips* of BNL-type as a function of bias voltage. From this figure, the detector is full depleted at 70 V and the capacitance of single strip is $\sim$ 1.5 pF (=$\sim$ 1101/720 (pF/strips)). Then the capacitance of 40 strips gathered is $\sim$ 60 pF.

Leak current at operating voltage The operating voltages were set high enough: 160 V for BNL-type and 200 V for Hamamatsu-type. The measured leak current at operating voltage were 5 $\sim$ 10 nA for BNL-type and $\sim$ 10 nA.

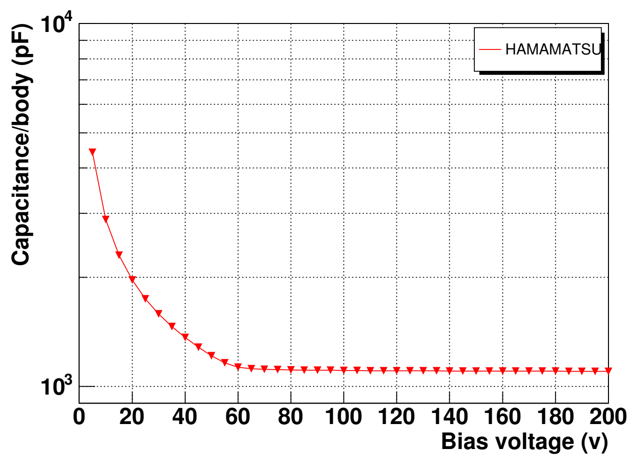

Figure A.6: Detector body capacitance measurement in a function of bias voltage for Hamamatu-type detector (data from Hamamatsu)

A.5 AGS CNI polarimeter

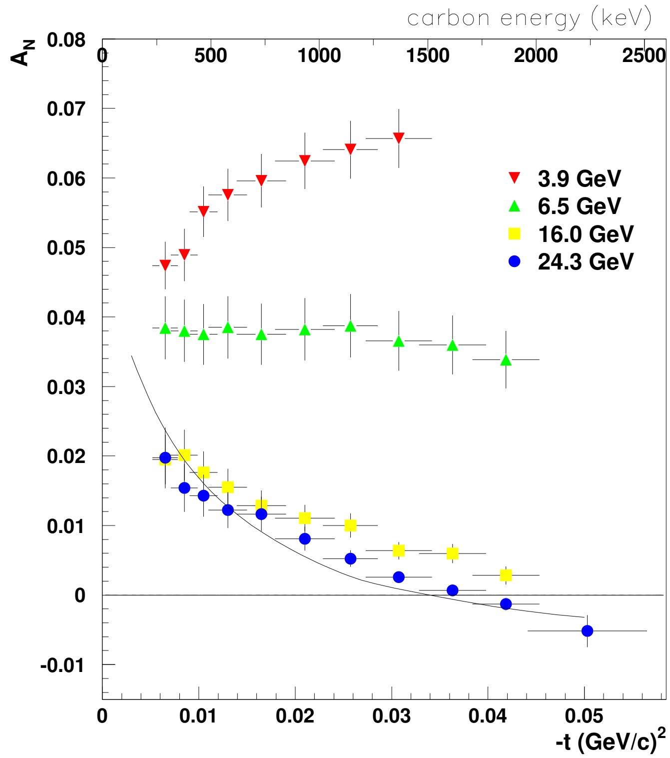

Figure A.7: Analyzing power versus $-t$ (GeV/c)^2 from the 2004 run. The beam energies of each measurement are indicated in the plot. The solid line represents a theoretical fit to E950 data [6]. The error bars are given by the statistical error and systematic error added in quadrature.

A.6 How to make *reference* Waveform

Figure A.8 and A.9 explained the detailed method for making *averaged* waveform. We made 96 waveforms for every independent read-out channel extracted from $\sim$ 1000 Waveform samples. The method of *averaged* waveform shape for each independent read-out channel is:

1. Collect about 1000 waveform sample for each channel. (We sampled 1000 Waveforms which passed rough eye selection in order to reject discernibly bad waveforms.)
2. Divide 1 bin digit into 10 bins. Waveform has 90 digits as an original. Then it changes to 90×10 digits waveform.(1 digit $\sim$ 2.38 nsec)
3. Calculate the center of gravity (G) from 900 digits

$$G = \frac{\sum_{i=1}^{900} i \times ph(i)}{\sum_{i=1}^{900}}$$

4. Normalize the pulse-height of Waveform by area from (G-17) to (G+13) integration.
5. Accumulate all Waveforms (more than 1000 samples)
6. Slice along the x-axis and apply Gaussian fit in the y-axis. (Repeat Gaussian fitting for 900 times)
7. Extract the mean values for 900 points of Gaussian fitting results.
8. Repeat above steps for all read-out channels.

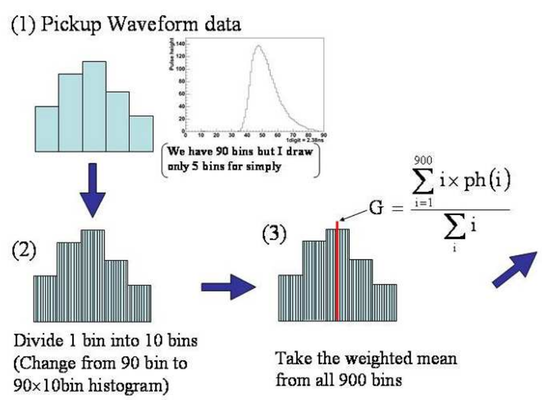

Figure A.8: The procedure of making averaged Waveform

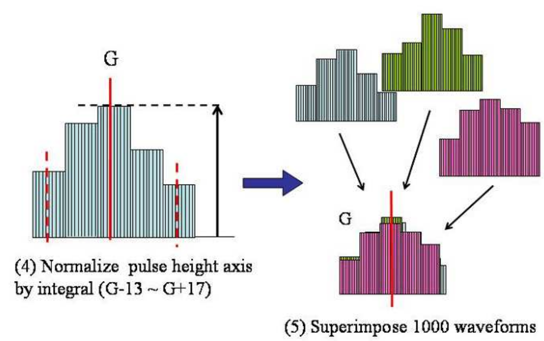

Figure A.9: Continued

The top left plot in Figure A.10 displays the accumulated Waveforms more than 1000 samples.

A.7 $INTG - T_{meas}$ plots of background study run

Figure A.11 displays the correlation of $INTG$ and T_{meas} of the empty-target run. Figure A.12 displays the correlation of $INTG$ and T_{meas} of the empty-target and no-beam run.

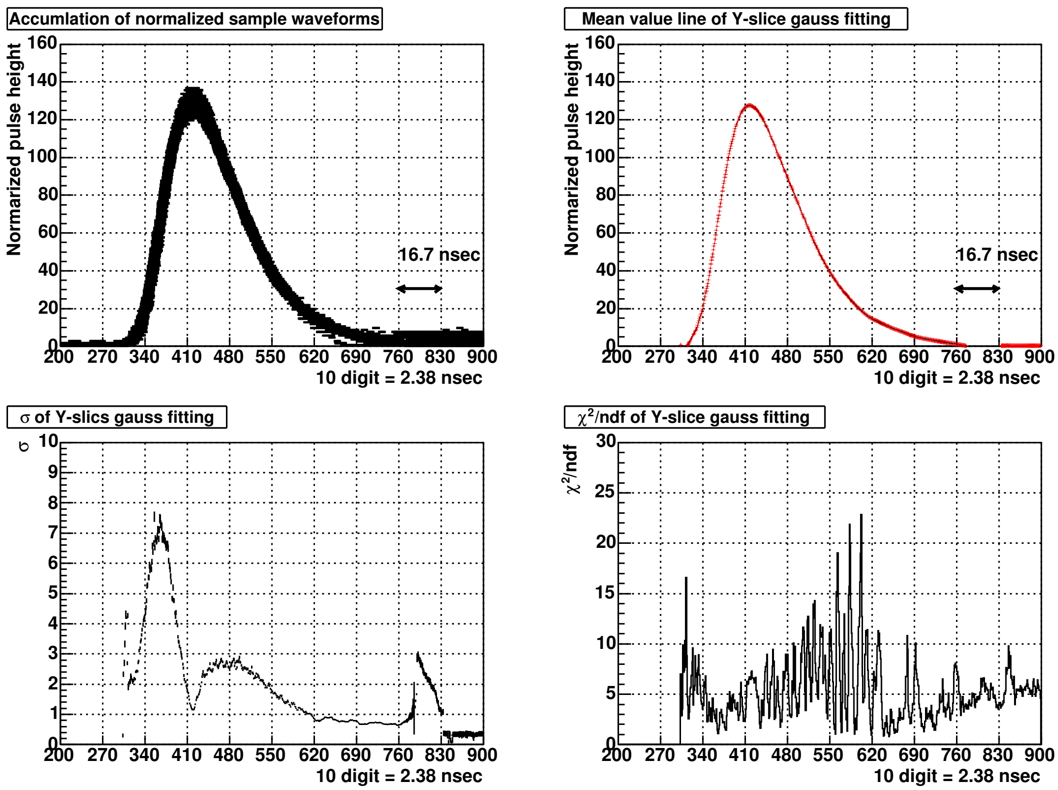

Figure A.10: Slice y-axis of accumulated waveform

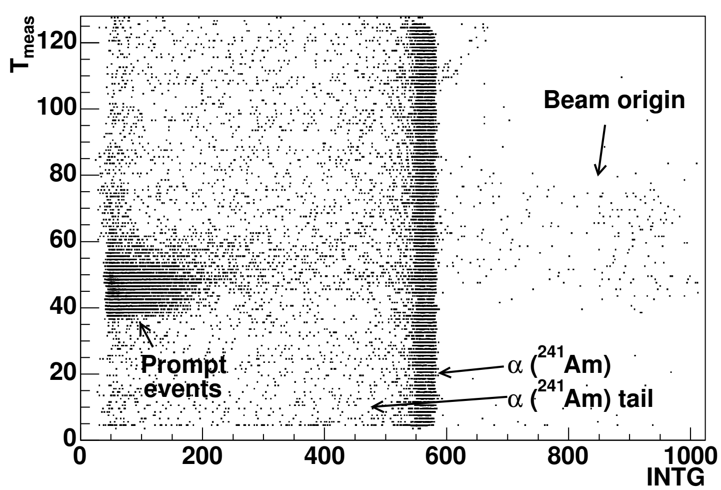

Figure A.11: *EMPTY* target . $INTG$ vs. T_{meas} from channel $\#3$

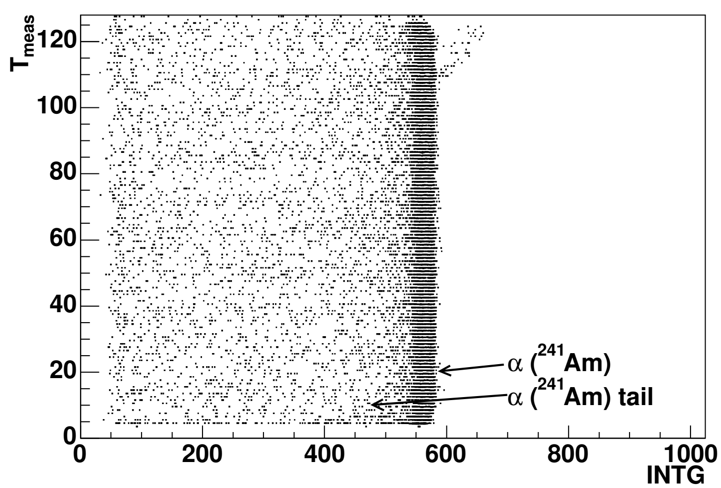

Figure A.12: textitEmpty target nor No Beam, $INTG$ vs. T_{meas} from channel $\#3$

A.8 Angle estimation

The angle data is obtained from the silicon detector channel number (position). We set the incident RHIC-beam direction as the z-axis. The silicon strip runs along the z-axis. In principle the channel number is linear to the angle from the x-axis.

Actually, the angle have some offset value because of the H-Jet target chamber rotate slightly from the correct direction as displayed in green θ_{offset} in Figure A.13. The base axis of the detector is also rotated to the x'-axis. Therefore, if proton is recoiled to θ direction from the x-axis, the left-side detector measures the recoiled angle as $\theta_{Left} = \theta - \theta_{offset}$. θ_{Left} is colored in red.

If proton is recoiled to $\pi - \theta$ direction from the x-axis, the right-side detector measures the recoiled angle as $\theta_{Right} = \pi - \theta + \theta_{offset}$, colored in blue.

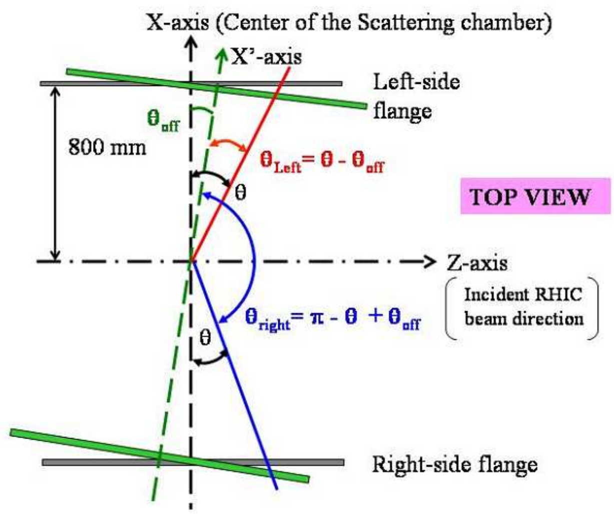

Figure A.13: Misalignment of H-Jet target system

In addition to the alignment offset, the angle data especially for low energy recoiled proton is bent by the Holding-Magnet field.

$$\theta_{offset} = \theta_{align} + \theta_{field}$$

Thus, the accuracy of the absolute angle is limited by the detector alignment and the holding magnetic field effect. To evaluate the degree of misalignment and the holding magnetic field, we changed the holding magnetic field configuration and took data of *NO*-field and *REVERSED*-field to compare with *NORMAL*-field data.

A.8.1 The offset angle estimation from the Holding Magnetic field study

Figure A.14 displays the left-right pair detectors comparison at *NO*-field condition. This figure tell us the degree of misalignment. θ_{align} is evaluated to same as 1channel (~ 5 mrad). Actually, we found this misalignment in the middle of run4-period, but we could not rotate the H-Jet target system. As for run5 case, we made the most of this studies. We examined the same study at the early stage and correct the alignment in the beginning of the run5 period.

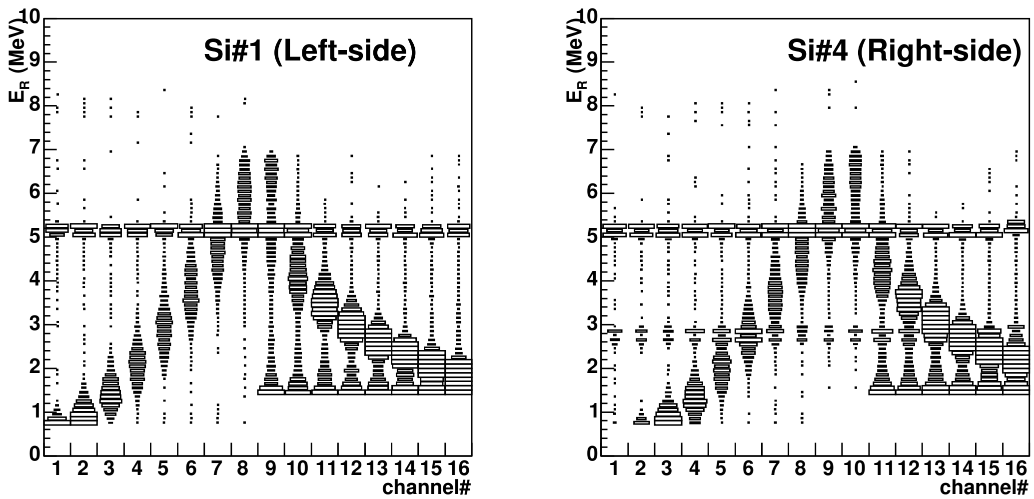

Figure A.14: Left-Right sides comparison at Non-Holding magnetic field OFF

Figure A.15 displays the left-right pair detectors comparison at *NORMAL*-field condition. This figure tell us the sum of misalignment and the holding magnetic field. Comparing *NORMAL*-field and *NO*-field cases, it seems that the effects of the holding magnetic field are not symmetrical for the left-right sides detectors. θ_{offset} is evaluated be 2channel ($\sim$ 10 mrad) for protons of less than 1 MeV.

This behavior replicates by comparing *REVERSED*-field and *NO*-field cases. Figure A.16 displays the left-right pair detectors comparison at *REVERSED*-field condition. The effect of the holding-magnetic field is not symmetrical and θ_{field} of right-side is lager than left-side one. θ_{field} of right-side is evaluated to be 5 mrad for protons less than 1 MeV.

Originally, the angle data is intended to use to distinguish between the elastic events and the inelastic events. In both case, the recoiled particles are proton and would be bent in the same way. Therefore, we do not need a precise absolute angle but need a fine resolution.

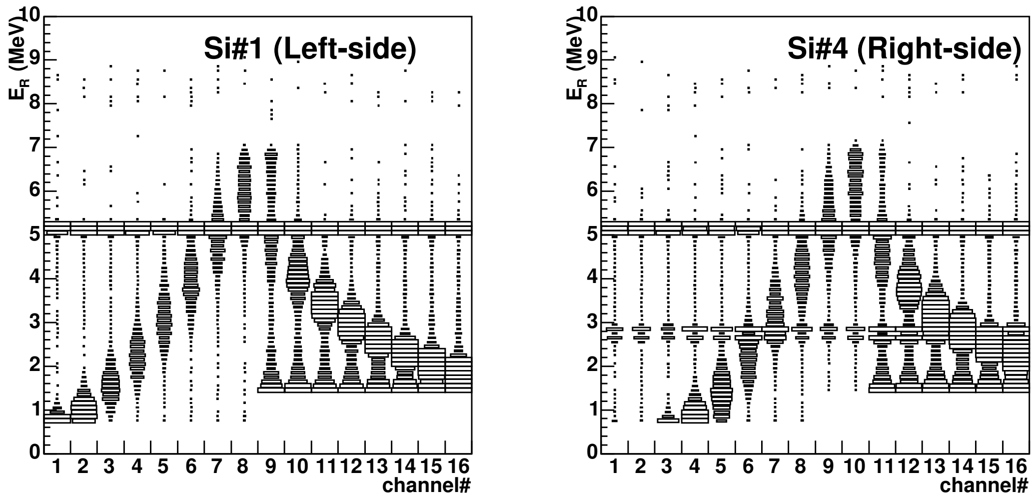

Figure A.15: Left-Right sides comparison at Normal-Holding magnetic field

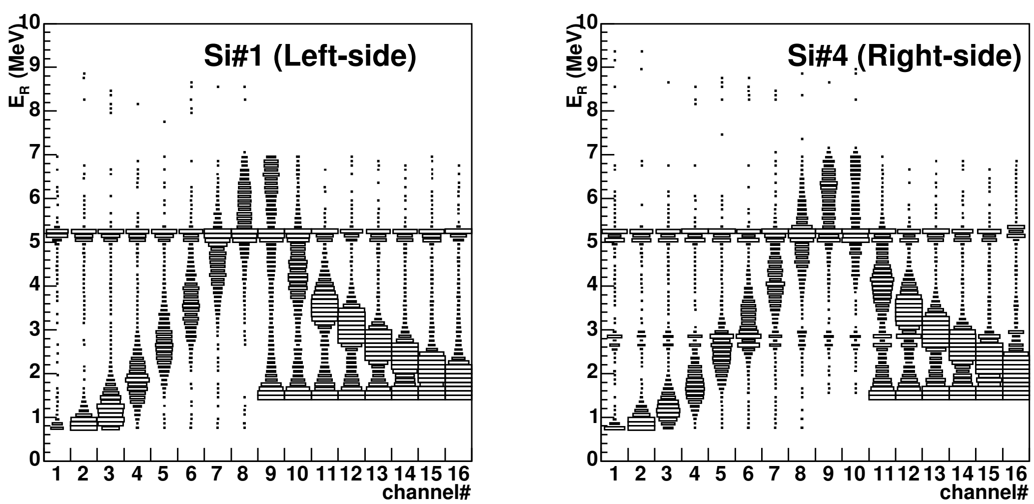

Figure A.16: Left-Right sides comparison at Reversed-Holding magnetic field

A.9 Conversion from Deposit to Incident Energy Conversion Table

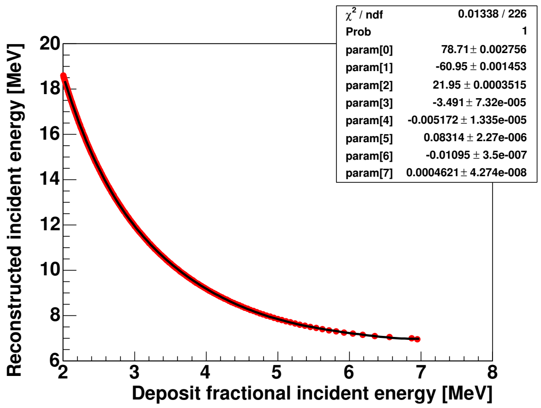

Figure A.17: Conversion function from deposit energy to incident energy

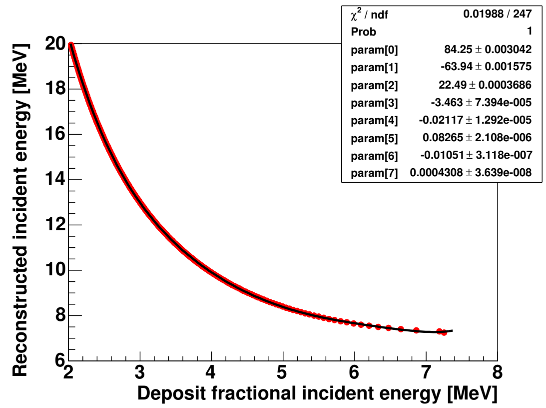

Figure A.18: Incident energy reconstruction function for BNL type

A.10 procedure B

The procedure using the *fractional* deposit energy and angle ; B

The second procedure B is using measured *fractional* deposit energy of several channels and *predicted* incident energy from angle. As shown fig 3.24, ch# 9-16 detected deposit energy fraction. By use of rough angle data which is estimated from ch#, we calculated the ”predicted” incident energy of these channels. Comparing the ”predicted” incident proton energy (Ein) and measured ”fractional” proton energy (Emes), we estimated the actual detector thickness.

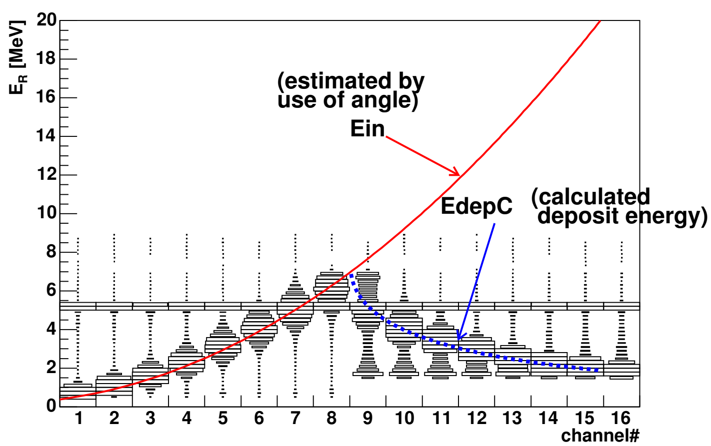

Figure A.19: channel# vs. energy correlation with rough ToF cut ($\triangle ToF \leq 10$ nsec)

$\mathrm{d}E/\mathrm{d}x$ is the stopping power of proton in silicon as shown in fig 3.20. Thus, each of detector thickness is calculated from *punched-through* channels independently. Figure A.20 displays the detector thickness distribution of Si# 1. And Figure A.21 displays the same for Si# 2. The estimated actual detector thickness from several *punched-through* channels agree very well.

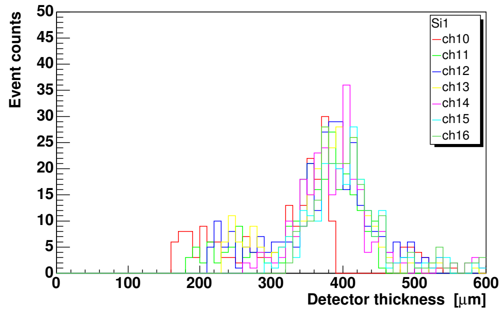

Figure A.20: The thickness of each independent channels of Si# 1 by procedure B

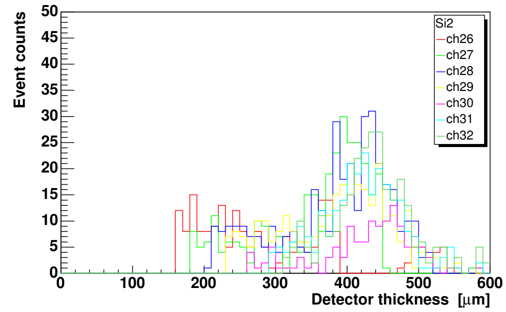

Figure A.21: The thickness of each independent channels of Si# 2 by procedure B

The sum of the thickness distribution of these *punched-through* channels, we have the averaged detector thickness as shown Figure A.22 for Si# $1-3$ and Figure A.23 for Si# $4-6$, respectively. The peaks around 400 μm are the estimated thickness from punched through proton events. The tail on the left side is of prompt events. The results of procedure B are 380 ± 10 μm for Hamamatsu-type detectors and 420 ± 10 μm for BNL-type detectors.

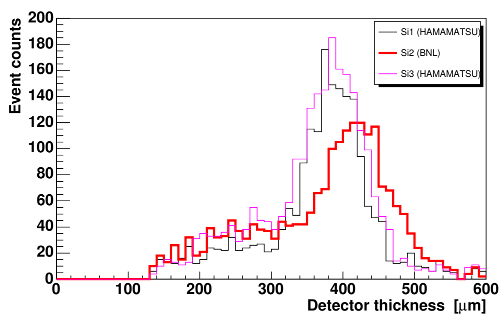

Figure A.22: The thickness of Si# $1-3$ by procedure B

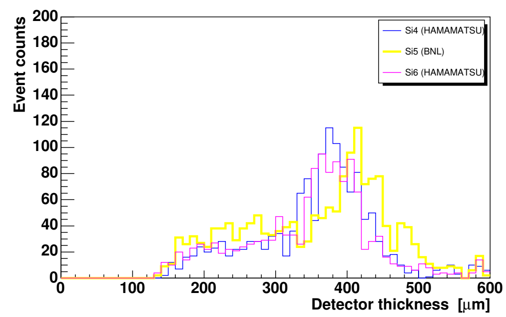

Figure A.23: The thickness of Si# $4-6$

A.11 Event Selection

The selected events count are listed in the table below.

T_R Bin #	Total	Si# 1	Si# 2	Si# 3	Si# 4	Si# 5	Si# 6
1	450112	71373	64948	70761	80694	87235	75101
2	309650	52533	55109	49139	51378	55601	45890
3	258166	41571	46907	40452	41309	47974	39953
4	229871	36808	44586	33979	35658	44999	33841
5	172815	25028	39081	22716	25240	39557	21193
6	194095	6826	25519	34591	36690	26882	33587
7	270279	43935	49783	42434	43291	50043	40793
8	305383	42598	75247	40546	43258	68513	35221
9	449352	86196	120174	78244	71621	93117	74087
10	217921	50468	–	58439	60344	–	8670
11	297811	76781	–	74562	76519	–	69949
12	304399	73674	–	75440	79028	–	76257
13	283075	78609	–	71068	78525	–	54873
14	171338	56185	–	50062	40113	–	24978

The above event have been already discard strange Waveforms. The ratio of the *good* waveforms to the events which passed the kinematical cuts.

A.12 $t0$ estimation

$t0$ distribution for all 96 channels are listed in Appendix. The mean values and the sigma values for all 96 read-out channels are displayed in Figure A.24 and Figure A.25. Red points are from non-good read-out channels which we do not use for the asymmetry calculation.

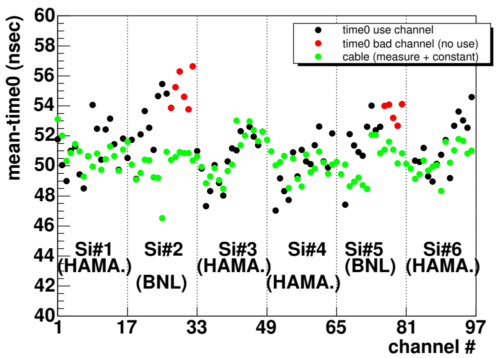

Figure A.24: mean $t0$ distributions

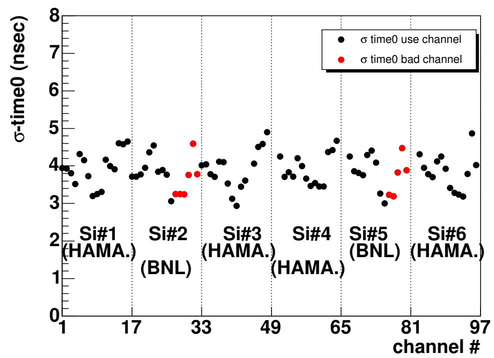

Figure A.25: σ_{t0} distribution

The mean values of $t0$ for channel-by channel

The mean values of $t0$ are fluctuated around 50 ± 4 nsec. Each of $t0$ are quite stable and do not change more than 1 nsec for whole run period. This agrees the postulation of $t0$. Then we can calculate $t0$ backwardly and fix them for further analysis.

There are two reasons why $t0$ fluctuate channel-by-channel. One is the read-out cable length and the other is *Risetime*. To confirm how much the cable length is fluctuated channel-by-channel, I tried to measure the cable length using the signal reflection of the rectangle shaped pulse. Figure A.24 displays the fluctuation of the cable length. (To compare with $t0$ distribution, 50 nsec offset is added.)

The cable length difference between channel-by-channel can explain the fluctuation of $t0$. But the some discrepancy remains in Si# 2 which are not explained by the cable length difference. The reasonable explanation is found in *Risetime* distribution of channel by channel. If *Risetime* is bigger than other channels, $t0$ can be estimated bigger qualitatively. In the waveform analysis in Section 3.2, *Risetime*of Si# 2 were obviously bigger than the others.

Appendix B

Square Root Formula

B.1 Raw Physics Asymmetry

The first quantity of square root formula is obtained as follows.

$$\frac{\sqrt{N^L_{0\uparrow}N^R_{0\downarrow}}-\sqrt{N^L_{0\downarrow}N^R_{0\uparrow}}}{\sqrt{N^L_{0\uparrow}N^R_{0\downarrow}}+\sqrt{N^L_{0\downarrow}N^R_{0\uparrow}}} \cong A_N\bar{P}_t\left(1-\frac{B}{L}\right)-A_N\bar{P}_t\epsilon_{A_N}\epsilon_{P_t}+{\delta_1}^4... \tag{B.1}$$

where $L=(L_{0\uparrow}+L_{0\downarrow})/2$.

As for complements:

$$\begin{aligned}\sqrt{N^L_{0\uparrow}N^R_{0\downarrow}} &= C_0\left[L_{0\uparrow}\{1+A_N\bar{P}_t(1+\epsilon_{A_N})(1+\epsilon_{P_t})\}+B\right]^{\frac{1}{2}}\cdot\left[L_{0\downarrow}\{1+A_N\bar{P}_t(1-\epsilon_{A_N})(1-\epsilon_{P_t})\}+B\right]^{\frac{1}{2}} \\ &\cong C_0\sqrt{L_{0\uparrow}L_{0\downarrow}}\left[(1+A_N\bar{P}_t)+A_N\bar{P}_t\epsilon_{A_N}\epsilon_{P_t}+{\delta_1}^4+\frac{B}{L}\right] \qquad \text{(B.2)} \\ \sqrt{N^L_{0\downarrow}N^R_{0\uparrow}} &\cong C_0\sqrt{L_{0\uparrow}L_{0\downarrow}}\left[(1-A_N\bar{P}_t)+A_N\bar{P}_t\epsilon_{A_N}\epsilon_{P_t}+{\delta_1}^4+\frac{B}{L}\right] \qquad \text{(B.3)}\end{aligned}$$

(B.4)

where $C_0=N_0\sqrt{d\Omega_L d\Omega_R}$ and we have ignored the forth order of the products $A_N\bar{P}_t$, ϵ_{A_N}, ϵ_{P_t}, $(L_{0\uparrow}-L_{0\downarrow})/(L_{0\uparrow}-L_{0\downarrow})$ and B/L.

Thus, A_N is obtained as one of the quantities of the square root formula, we call Raw Physics Asymmetry: $\epsilon_{\text{ PHYS}}$. Conventionally one writes $\epsilon_{\text{PHYS}} = \epsilon_N$.

Except for backgrounds dilution, the accuracy of this procedure is estimated to be third order of δ_1. δ_1 can be $\epsilon_{A_N}, \epsilon_{P_t}$ or $\bar{P}_t A_N$. The Raw physics asymmetry and the estimated error on this procedure are:

$$\epsilon_N=\frac{\sqrt{N^L_{0\uparrow}N^R_{0\downarrow}}-\sqrt{N^L_{0\downarrow}N^R_{0\uparrow}}}{\sqrt{N^L_{0\uparrow}N^R_{0\downarrow}}+\sqrt{N^L_{0\downarrow}N^R_{0\uparrow}}},\ \delta\epsilon_N\sim A_N\bar{P}_t({\epsilon_{A_N}}^2+{\epsilon_{P_t}}^2). \tag{B.5}$$

where, we set $\delta\epsilon_N>{\delta_1}^3\sim A_N\bar{P}_t\epsilon_{A_N}\epsilon_{P_t}$ for the conservative.

The statistical error of ϵ_N is obtained as:

$$\Delta\epsilon_N=\frac{\sqrt{N^L_{0\uparrow}N^R_{0\downarrow}N^R_{0\uparrow}N^R_{0\downarrow}}}{\left(\sqrt{N^L_{0\uparrow}N^R_{0\downarrow}}+\sqrt{N^R_{0\uparrow}N^R_{0\downarrow}}\right)^2}\sqrt{\frac{1}{N^L_{0\uparrow}}+\frac{1}{N^L_{0\downarrow}}+\frac{1}{N^R_{0\uparrow}}+\frac{1}{N^R_{0\downarrow}}}$$

Here, 4 independent numbers are huge and similar : $N^L_{0\uparrow} \sim N^L_{0\downarrow} \sim N^R_{0\uparrow} \sim N^R_{0\downarrow}$.

$$\Delta\epsilon_N \sim \frac{1}{\sqrt{N^L_{0\uparrow} + N^R_{0\downarrow} + N^R_{0\uparrow} + N^R_{0\downarrow}}} \tag{B.6}$$

B.2 Luminosity Asymmetry

We ignore the background components for simplifications. The second quantity of square root formula is obtained as follows.

$$\begin{aligned} \epsilon_{Lumi.} &= \frac{\sqrt{N^L_{0\uparrow}N^R_{0\uparrow}} - \sqrt{N^L_{\downarrow}N^R_{\downarrow}}}{\sqrt{N^L_{\uparrow}N^R_{\uparrow}} + \sqrt{N^L_{\downarrow}N^R_{\downarrow}}} && \text{(B.7)} \\ &\cong \frac{I_t(\uparrow) - I_t(\downarrow)}{I_t(\uparrow) + I_t(\downarrow)} + A_N\bar{P}_t\epsilon_{A_N} + {\delta_2}^4. && \text{(B.8)} \end{aligned}$$

where,

$$\begin{aligned} \sqrt{N^L_{0\uparrow}N^R_{0\uparrow}} &= C_0\sqrt{[I_t(\uparrow)d\Omega_L(1 + A_N\bar{P}_t)] \cdot [I_t(\uparrow)d\Omega_R(1 - A_N\bar{P}_t]} \\ &\cong C_0 I_t(\uparrow)\sqrt{d\Omega_L d\Omega_R}\sqrt{1 + 2A_N\bar{P}_t\epsilon_A A_N - {\bar{P}_t}^2 {A_N}^2 + {\delta_2}^4} \\ &\cong C_0 I_t(\uparrow)\sqrt{d\Omega_L d\Omega_R}[1 + A_N\bar{P}_t\epsilon_A A_N - \frac{1}{2}{\bar{P}_t}^2 {A_N}^2 + {\delta_2}^4)] \\ \sqrt{N^L_{0\downarrow}N^R_{0\downarrow}} &\cong C_0 I_t(\downarrow)\sqrt{d\Omega_L d\Omega_R}[1 - A_N\bar{P}_t\epsilon_A A_N - \frac{1}{2}{\bar{P}_t}^2 {A_N}^2 + {\delta_2}^4)] \end{aligned}$$

where, ϵ_2 can be ϵ_{A_N} or $\bar{P}_t A_N$.

Thus, the second quantity is related to the geometrical asymmetry : $\epsilon_{\mathrm{LUMI.}}$, which is in the amount of intensity for two polarization states.

The accuracy of this procedure is estimated to be third order of δ_1. δ_1 can be $\epsilon_{A_N}, \epsilon_{P_t}$ or $\bar{P}_t A_N$. The Raw physics asymmetry and the estimated error on this procedure are:

$$\begin{aligned} \Delta\epsilon_{lumi.} &= \frac{\sqrt{N^L_{\uparrow T}N^R_{\downarrow T}N^R_{\uparrow T}N^R_{\downarrow T}}}{\left(\sqrt{N^L_{\uparrow T}N^R_{\downarrow T}} + \sqrt{N^R_{\uparrow T}N^R_{\downarrow T}}\right)^2}\sqrt{\frac{1}{N^L_{\uparrow T}} + \frac{1}{N^L_{\downarrow T}} + \frac{1}{N^R_{\uparrow T}} + \frac{1}{N^R_{\downarrow T}}} \\ &\sim \frac{1}{\sqrt{N^L_{\uparrow T} + N^R_{\downarrow T} + N^R_{\uparrow T} + N^R_{\downarrow T}}} && \text{(B.9)} \end{aligned}$$

In this case, δ_b can be ϵ_{BT}.

B.3 Acceptance Asymmetry

The third quantity of square root formula is obtained as follows.

$$\frac{\sqrt{N^L_{\uparrow}N^L_{\downarrow}} - \sqrt{N^R_{\downarrow}N^R_{\uparrow}}}{\sqrt{N^L_{\uparrow T}N^L_{\downarrow}} + \sqrt{N^R_{\downarrow}N^R_{\uparrow}}} = \frac{d\Omega_L - d\Omega_R}{d\Omega_L + d\Omega_R} + A_N\bar{P}_t\epsilon_{P_t} + A_N\bar{P}_t{\delta_3}^2. \tag{B.10}$$

where,

$$
\begin{aligned}
\sqrt{N^L_{0\uparrow}N^L_{0\downarrow}} &= \sqrt{[I_b I_t(\uparrow) d\Omega_L(1+A_N\bar{P}_t)]\cdot[I_b I_t(\downarrow) d\Omega_L(1-A_N\bar{P}_t)]} \\
&= I_b d\Omega_L\sqrt{I_t(\uparrow)I_t(\downarrow)}\sqrt{1-2A_N P_t(\uparrow)\epsilon_{P_t}{A_N}^L-{\bar{P}_t}^2{A_N}^2(1-\epsilon{P_t}^2)} \\
&\cong I_b d\Omega_L\sqrt{I_t(\uparrow)I_t(\downarrow)}[1-A_N\bar{P}_t\epsilon_{P_t}A_N-\frac{1}{2}{\bar{P}_t}^2{A_N}^2+\delta({\epsilon_3}^4)] \\
\sqrt{N^R_{0\uparrow}N^R_{0\downarrow}} &\cong I_b d\Omega_R\sqrt{I_t(\uparrow)I_t(\downarrow)}[1+A_N\bar{P}_t\epsilon_{P_t}A_N-\frac{1}{2}{\bar{P}_t}^2{A_N}^2+\delta({\epsilon_3}^4)]
\end{aligned}
$$

where, ϵ_3 can be ϵ_{I_t}.

The third quantity is related to the acceptance asymmetry, we call it ϵ_{GEOM}, which is in the solid angle times efficiency for two-sides detectors.

The statistical error of ϵ_{GEOM} is obtained as follows:

$$
\begin{aligned}
\Delta\epsilon_{GEOM} &= \frac{\sqrt{N^L_{\uparrow T}N^R_{\downarrow T}N^R_{\uparrow T}N^R_{\downarrow T}}}{\left(\sqrt{N^L_{\uparrow T}N^R_{\downarrow T}}+\sqrt{N^R_{\uparrow T}N^R_{\downarrow T}}\right)^2}\sqrt{\frac{1}{N^L_{\uparrow T}}+\frac{1}{N^L_{\downarrow T}}+\frac{1}{N^R_{\uparrow T}}+\frac{1}{N^R_{\downarrow T}}} \\
&\sim \frac{1}{\sqrt{N^L_{\uparrow T}+N^R_{\downarrow T}+N^R_{\uparrow T}+N^R_{\downarrow T}}} \qquad \text{(B.11)}
\end{aligned}
$$

In the three square root asymmetries ,ϵ_N, ϵ_{GEOM} and ϵ_{LUM}, the quantities $\bar{P}_t A_N$, ϵ_{A_N}, ϵ_{I_t}, $\epsilon_{d\Omega}$ and $\epsilon_{P_t}$are all assumed small and about the same magnitude. The physically interesting asymmetry is ϵ_{PHYS}.